

---

Masters Theses

Student Theses and Dissertations

---

Summer 2019

## Passively-coded embedded microwave sensors for materials characterization and structural health monitoring (SHM)

Katelyn Rose Brinker

Follow this and additional works at: [https://scholarsmine.mst.edu/masters\\_theses](https://scholarsmine.mst.edu/masters_theses)



Part of the [Electromagnetics and Photonics Commons](#)

Department:

---

### Recommended Citation

Brinker, Katelyn Rose, "Passively-coded embedded microwave sensors for materials characterization and structural health monitoring (SHM)" (2019). *Masters Theses*. 7904.

[https://scholarsmine.mst.edu/masters\\_theses/7904](https://scholarsmine.mst.edu/masters_theses/7904)

This thesis is brought to you by Scholars' Mine, a service of the Missouri S&T Library and Learning Resources. This work is protected by U. S. Copyright Law. Unauthorized use including reproduction for redistribution requires the permission of the copyright holder. For more information, please contact [scholarsmine@mst.edu](mailto:scholarsmine@mst.edu).

PASSIVELY-CODED EMBEDDED MICROWAVE SENSORS FOR MATERIALS  
CHARACTERIZATION AND STRUCTURAL HEALTH MONITORING (SHM)

by

KATELYN ROSE BRINKER

A THESIS

Presented to the Faculty of the Graduate School of the  
MISSOURI UNIVERSITY OF SCIENCE AND TECHNOLOGY

In Partial Fulfillment of the Requirements for the Degree  
MASTER OF SCIENCE IN ELECTRICAL ENGINEERING

2019

Approved by:

Dr. Reza Zoughi, Advisor  
Dr. Kristen Donnell  
Dr. Mohammad Al Qaseer

© 2019

Katelyn Rose Brinker

All Rights Reserved

## ABSTRACT

Monitoring and maintaining civil, space, and aerospace infrastructure is an ongoing critical problem facing our nation. As new complex materials and structures, such as multilayer composites and inflatable habitats, become ubiquitous, performing inspection of their structural integrity becomes even more challenging. Thus, novel nondestructive testing (NDT) methods are needed. Chipless RFID is a relatively new technology that has the potential to address these needs. Chipless RFID tags have the advantage of being wireless and passive, meaning that they do not require a power source or an electronic chip. They can also be used in a variety of sensing applications including monitoring temperature, strain, moisture, and permittivity. However, these tags have yet to be used as embedded sensors. By embedding chipless RFID tags in materials, materials characterization can be performed via multi-bit sensing; that is, looking at how the multi-bit code assigned to the response of the tag changes as a function of material. This thesis develops this method through both simulation and measurement. In doing so, a new coding method and tag design are developed to better support this technique. Furthermore, inkjet-printing is explored as a manufacturing method for these tags and various measurement methods for tags including radar cross-section and microwave thermography are explored.

## ACKNOWLEDGMENTS

This work was supported by a NASA Space Technology Research Fellowship. I would like to thank this program for their support and aiding me in both my academic and career pursuits. I would also like to thank my fellowship research collaborator, Dr. William C. Wilson for his support of my research and for hosting me at NASA Langley Research Center in the summer of 2018.

Next, I would like to thank my Advisor, Dr. Reza Zoughi, guidance, kindness, and support he has provided me with during my master's degree. Additionally, I would like thank my committee members Dr. Kristen Donnell and Dr. Mohammad Al Qaseer and my colleagues in the Applied Microwave Nondestructive Testing Laboratory (*amntl*) for always being willing to help me. Lastly, thank you to my friends and family for their support.

## TABLE OF CONTENTS

	Page
ABSTRACT.....	iii
ACKNOWLEDGMENTS .....	iv
LIST OF ILLUSTRATIONS.....	ix
LIST OF TABLES.....	xvii
NOMENCLATURE .....	xviii
 SECTION	
1. INTRODUCTION.....	1
1.1. PROBLEM STATEMENT.....	1
1.2. BACKGROUND .....	1
1.2.1. Overview of Chipless RFID.....	1
1.2.1.1. Chipless RFID tag architectures.....	2
1.2.1.2. Response encoding methods.....	5
1.2.1.3. Tag metrics.....	7
1.2.1.4. Tag fabrication methods.....	10
1.2.1.5. Examples of tag applications.....	10
1.2.2. Materials Characterization Overview.....	24
1.3. OBJECTIVES.....	25
2. EMBEDDED CHIPLESS RFID PROOF OF CONCEPT.....	27
2.1. PREMISE.....	27
2.2. SIMULATION RESULTS .....	27

2.3. MEASUREMENT RESULTS.....	32
2.4. DISCUSSION.....	40
3. CODING METHOD DEVELOPMENT.....	41
3.1. MOTIVATION.....	41
3.2. CODING METHOD.....	41
3.3. IMPLEMENTATION OF CODING METHOD.....	43
3.4. REMARKS.....	48
4. TAG DESIGN METHODOLOGY.....	50
4.1. PREMISE.....	50
4.2. TAG DESIGN METHODOLOGY.....	50
4.2.1. Environmental Concerns.....	51
4.2.2. Method.....	54
4.3. DEVELOPED TAG.....	54
4.4. DESIGN GUIDELINES.....	66
4.4.1. Circular Slot Resonator Design Guidelines.....	67
4.4.2. Ring Resonator Design Guidelines.....	75
4.4.3. Spiral Resonator Design Guidelines.....	82
4.4.4. Design Guidelines for Resonator Combination.....	94
4.5. ASSOCIATING TAG GEOMETRY AND RESPONSE.....	102
4.6. APPLICATION ADAPTATIONS OF TAG.....	105
4.6.1. X-band Version of Tag.....	106
4.6.2. ID Application Tag.....	109
4.6.3. Materials Characterization Application Tag.....	110

4.7. MEASUREMENT OF TAG.....	115
4.7.1. Misalignment Simulations.....	124
4.7.1.1. X translation.....	125
4.7.1.2. Y translation.....	126
4.7.1.3. Z translation. ....	127
4.7.1.4. X-axis rotation. ....	131
4.7.1.5. Y-axis rotation. ....	133
4.7.1.6. Z-axis rotation.....	136
4.8. DISCUSSION.....	140
5. INKJET-PRINTING AS A MEANS OF TAG MANUFACTURING.....	141
5.1. PREMISE.....	141
5.2. PRINTING PAPER DIELECTRIC PROPERTIES .....	141
5.3. CONDUCTIVITY DETERMINATION .....	147
5.3.1. Influences on Conductivity. ....	158
5.3.2. Improving Conductivity. ....	161
5.3.2.1. Thermal sintering.....	161
5.3.2.2. Laser and photonic sintering .....	162
5.3.2.3. Electrical sintering. ....	163
5.3.2.4. Plasma sintering.....	163
5.4. SIMULATION WITH PRINTING PARAMETERS.....	163
5.5. MEASUREMENT OF PRINTED TAGS.....	169
5.6. DISCUSSION.....	171
6. TAG MEASUREMENT METHODS .....	172



6.1. MOTIVATION.....	172
6.2. RADAR CROSS-SECTION (RCS) MEASUREMENTS.....	173
6.2.1. RCS Determination Methods. ....	174
6.2.1.1. Method 1.....	174
6.2.1.2. Method 2.....	176
6.2.1.3. Method 3.....	176
6.2.1.4. Method 4.....	177
6.2.1.5. Method 5.....	177
6.2.1.6. Method 6.....	178
6.2.2. Employment of Method 6.....	180
6.3. BISTATIC MEASUREMENTS.....	199
6.4. MICROWAVE THERMOGRAPHY.....	202
6.5. EMBEDDED TAG MEASUREMENTS.....	204
7. SUMMARY AND FUTURE WORK.....	208
7.1. BACKGROUND.....	208
7.2. MATERIALS CHARACTERIZATION METHODOLOGY.....	208
7.3. APPLICATION-ADAPTABLE DESIGN METHODOLOGY.....	209
7.4. FUTURE WORK.....	210
BIBLIOGRAPHY.....	212
VITA.....	228

## LIST OF ILLUSTRATIONS

	Page
Figure 1.1. Tx/Rx frequency-based tag [17].	3
Figure 1.2. Backscatter frequency-based tag [23].	4
Figure 1.3. RCS vs. frequency response for tag in Figure 1.2 [23].	4
Figure 1.4. Spatial-based chipless RFID tag [28].	5
Figure 1.5. Illustration of FSE coding method [32].	6
Figure 2.1. 8 circular slot resonator tag model.	28
Figure 2.2. Free space RCS vs. frequency response of 8 circular slot resonator tag.	28
Figure 2.3. Response of tag embedded in a material of $\epsilon_r' = 4$ .	29
Figure 2.4. Comparison of tag in free-space and half size tag in material of $\epsilon_r' = 4$ .	30
Figure 2.5. Response of tag in low loss materials.	31
Figure 2.6. Response of tag as loss is increased.	31
Figure 2.7. Tag for embedded measurement proof of concept.	32
Figure 2.8. Free-space RCS response of tag from Figure 2.7.	34
Figure 2.9. Plane-wave $S_{11}$ simulation setup.	34
Figure 2.10. Simulated plane-wave $S_{11}$ result of the tag.	35
Figure 2.11. Waveguide $S_{11}$ simulation setup.	35
Figure 2.12. Simulated waveguide $S_{11}$ result of the tag.	36
Figure 2.13. Comparison of RCS and $S_{11}$ simulation results.	36
Figure 2.14. Measurement setup for embedded tag measurements.	37
Figure 2.15. Processed measurement results of tag embedded in sand.	38

Figure 2.16. Processed measurement results of tag embedded in wet sand. ....	39
Figure 2.17. Comparison of measurement results for tag embedded in materials.....	39
Figure 3.1. Illustration of proposed coding method.....	43
Figure 3.2. Encoded response of 8 slot tag in free-space.....	44
Figure 3.3. Encoded response for 8 slot tag in a material of $\epsilon_r = 4$ .....	45
Figure 3.4. Encoded response for 8 slot tag in a material of $\epsilon_r = 8$ .....	46
Figure 3.5. Encoded response for 8 slot tag in a material of $\epsilon_r = 8$ with limited bandwidth.....	47
Figure 4.1. Simulation setup for tag pasted on dielectric slab of varying sizes.....	52
Figure 4.2. RCS vs. frequency response for tag when it is on a dielectric slab of varying sizes.....	53
Figure 4.3. No spiral configuration of tag.....	55
Figure 4.4. RCS vs. frequency response of tag in Figure 4.3. ....	55
Figure 4.5. Tag configurations for demonstrating ring resonator dependence. ....	57
Figure 4.6. RCS vs frequency responses of tag configurations in Figure 4.5.....	58
Figure 4.7. Orientations of spiral resonator. ....	59
Figure 4.8. RCS vs frequency responses for different orientations. ....	60
Figure 4.9. Diagram of spiral resonator location designations. ....	61
Figure 4.10. RCS vs frequency responses for different spiral locations.....	62
Figure 4.11. Configurations of tag design. ....	63
Figure 4.12. RCS vs frequency response of four spiral tag. ....	63
Figure 4.13. RCS vs frequency response of the eight spiral tag. ....	64
Figure 4.14. Effect on response when a tag with a ground plane is placed on a dielectric slab of varying sizes.....	65

Figure 4.15. Circular slot resonator [118].....	67
Figure 4.16. Slot resonator annotated with simulation parameters.....	69
Figure 4.17. Effect of radius on resonance frequency of circular slot resonator. ....	69
Figure 4.18. Effect of ring width on magnitude of slot resonator resonance.....	70
Figure 4.19. Effect of gap and ring width on resonance frequency.....	71
Figure 4.20. Effect of gap and ring width on resonance frequency.....	72
Figure 4.21. Annotated tag used in multi-slot simulations. ....	73
Figure 4.22. Effect of slot 2 gap and ring width on resonance frequency of slot 2. ....	74
Figure 4.23. Effect of slot 2 gap and ring width on slot 1 resonance frequency. ....	74
Figure 4.24. Ring resonator diagram. ....	76
Figure 4.25. Ring resonator equivalent circuit of [121] for microwave filters.....	76
Figure 4.26. Effect of radius on resonance frequency of ring resonator.....	78
Figure 4.27. Effect of radius on depth of notch. ....	78
Figure 4.28. Effect of ring thickness on resonance frequency of ring resonator. ....	79
Figure 4.29. Effect of ring radius and thickness on resonance frequency with patch. ....	81
Figure 4.31. RCS vs. frequency response for tag with and without ground plane. ....	82
Figure 4.32. Equivalent circuit for spiral resonator from [123].....	83
Figure 4.33. Equivalent circuit for spiral resonator coupled to microstrip line [124]. ....	84
Figure 4.34. Section designations for transmission line model [12].....	86
Figure 4.35. Transmission line model for spiral resonator coupled to microstrip [12]. ...	87
Figure 4.36. Microwave filter layout from [110].....	88
Figure 4.37. Diagram of spiral resonator. ....	88
Figure 4.38. Example design curve from [110]. ....	88

Figure 4.39. Effect of removing length from the outside of a spiral resonator.....	89
Figure 4.40. Effect of removing length from the inside of a spiral resonator.....	90
Figure 4.41. Example of non-resonance condition of spiral resonator when removing length from outside of spiral. ....	91
Figure 4.42. Effect of width and gap on resonance frequency of spiral resonator. ....	92
Figure 4.43. Illustration of effect of increasing the width of a spiral resonator. ....	92
Figure 4.44. Simulation layout for Tx/Rx configuration using spiral resonator.....	93
Figure 4.45. Comparison of configurations with spiral resonator. ....	94
Figure 4.46. Diagram of increasing distance between spiral and ring resonators. ....	95
Figure 4.47. RCS vs. frequency plots for increasing distance between spiral and ring resonators. ....	95
Figure 4.48. Effect of increasing distance on resonance frequency of spiral resonator. ..	96
Figure 4.49. Effect of increasing distance on Q-factor of resonance frequency of spiral resonator.....	96
Figure 4.50. Effect of increasing distance on resonance frequency of ring resonator.....	97
Figure 4.51. X-band version of eight spiral tag. ....	102
Figure 4.52. RCS vs. frequency response of X-band eight spiral tag. ....	103
Figure 4.53. Surface current density simulations.....	103
Figure 4.54. Single spiral version of X-band tag. ....	104
Figure 4.55. RCS vs. frequency response of single spiral X-band tag. ....	105
Figure 4.56. Surface current density simulations for single spiral X-band tag.....	105
Figure 4.57. Four spiral X-band tag.....	106
Figure 4.58. Simulated $S_{11}$ response for four spiral tag.....	107
Figure 4.59. Simulation setup for $S_{11}$ of tag with waveguide.....	108
Figure 4.60. Simulated rotation sensing results for four spiral tag. ....	108

Figure 4.61. Simulated directional rotation sensing for four spiral tag. ....	109
Figure 4.62. RCS vs. frequency responses of ID application optimized tag. ....	111
Figure 4.63. Simulation setup for embedded materials characterization. ....	112
Figure 4.64. RCS vs frequency response for tag embedded in materials with different permittivities. ....	113
Figure 4.65. RCS vs. frequency response for tag embedded in materials with different complex dielectric constants. ....	113
Figure 4.66. Simulation setup for $S_{11}$ of tag. ....	115
Figure 4.67. Simulation results for $S_{11}$ of eight spiral and single spiral tags. ....	116
Figure 4.68. Fabricated eight spiral and single spiral tags. ....	116
Figure 4.69. Measurement setup for fabricated spiral tags. ....	117
Figure 4.70. Measurement and simulation results for single spiral tag. ....	119
Figure 4.71. Measurement and simulation results for eight spiral tag. ....	119
Figure 4.72. Measurement and simulation results for Tag 3.1. ....	120
Figure 4.73. Measurement and simulation results for Tag 4.1. ....	120
Figure 4.74. Comparison of processed measurements of five copies of Tag 1. ....	121
Figure 4.75. Comparison of processed measurements of five copies of Tag 2. ....	121
Figure 4.76. Comparison of processed measurements for five copies of Tag 3. ....	122
Figure 4.77. Comparison of processed measurements for five copies of Tag 4. ....	122
Figure 4.78. Spirals modified for simulation of manufacturing defects. ....	123
Figure 4.79. Simulation of modified tag in comparison to original tag simulation and measurement. ....	123
Figure 4.80. Comparison of measured responses of four tag configurations. ....	124
Figure 4.81. Translation of tag in $-x$ direction. ....	125
Figure 4.82. Translation of tag in $+x$ direction. ....	126

Figure 4.83. Translation of tag in $-y$ direction.....	127
Figure 4.84. Translation of tag in $+y$ direction. ....	127
Figure 4.85. Translation of tag along $z$ -direction.....	128
Figure 4.86. Depiction of $x$ -axis rotation of tag.....	131
Figure 4.87. $x$ -axis tag rotation for $-1^\circ$ , $0^\circ$ , and $1^\circ$ . ....	132
Figure 4.88. $x$ -axis tag rotation for $-10^\circ$ to $-7^\circ$ . ....	132
Figure 4.89. $x$ -axis tag rotation for $7^\circ$ to $10^\circ$ . ....	133
Figure 4.90. Depiction of tag rotation about $y$ -axis. ....	134
Figure 4.91. $y$ -axis tag rotation for $-1^\circ$ , $0^\circ$ , and $1^\circ$ . ....	134
Figure 4.92. $y$ -axis tag rotation for $-10^\circ$ to $-7^\circ$ . ....	135
Figure 4.93. $y$ -axis tag rotation for $7^\circ$ to $10^\circ$ . ....	135
Figure 4.94. Simulation of $z$ -axis tag rotation.....	136
Figure 4.95. Comparison of simulation and measurement for $z$ -axis tag rotation. ....	137
Figure 4.96. $z$ -axis tag rotation for $45^\circ$ and $225^\circ$ . ....	138
Figure 4.97. $z$ -axis tag rotation for $135^\circ$ and $315^\circ$ . ....	138
Figure 4.98. $z$ -axis tag rotation for $0^\circ$ to $10^\circ$ . ....	139
Figure 4.99. $z$ -axis tag rotation for $-5^\circ$ to $5^\circ$ . ....	139
Figure 5.1. Setup for measurement of dielectric properties of paper.....	145
Figure 5.2. Measurement and recalculation for dielectric property determination.....	146
Figure 5.3. Printed microwave short. ....	148
Figure 5.4. Comparison of printed short to calibration kit short. ....	148
Figure 5.5. CST Microwave Studio® model of resonant cavity. ....	150
Figure 5.6. Operation of cavity at TE <sub>012</sub> mode.....	151

Figure 5.7. Simulated $S_{21}$ response of resonant cavity. ....	151
Figure 5.8. Simulated effect of conductivity on Q-factor. ....	152
Figure 5.9. $S_{21}$ as a function of conductivity. ....	153
Figure 5.10. Examples of printed samples for conductivity measurement. ....	153
Figure 5.11. Measurement setup for conductivity measurements. ....	154
Figure 5.12. Measurement comparison of different papers with reference. ....	155
Figure 5.13. Effect of handling samples. Left: un-smearred. Right: Smearred. ....	159
Figure 5.14. Effect of conductivity on skin depth. ....	160
Figure 5.15. Sintered prints. Left: photo paper. Right: Mitsubishi paper. ....	162
Figure 5.16. Microscope images of effect of thermal sintering. ....	162
Figure 5.17. Example of printable tag. ....	164
Figure 5.18. Response of printable tag. ....	164
Figure 5.19. Response of tag on different printing substrates. ....	165
Figure 5.20. Response of simulated printed tag with non-ideal conductor. ....	166
Figure 5.21. X-band spiral tag response with variable conductivity. ....	167
Figure 5.22. Discretized circular slot resonator. ....	167
Figure 5.23. Ideal circular slot resonator. ....	168
Figure 5.24. Comparison of response for discretized and ideal circular slot resonator. .	168
Figure 5.25. Measurement setup for measurement of PCB and printed tags. ....	169
Figure 5.26. Simulation setup for tag $S_{11}$ . ....	170
Figure 5.27. Simulated $S_{11}$ responses of PCB and printed tags. ....	170
Figure 5.28. Measurement results of PCB and printed tags. ....	171
Figure 6.1. Diagram of RCS measurement model for Method 6. ....	179



Figure 6.2. Measured RCS for a split ring resonator based tag [91]. .....	180
Figure 6.3. Simulation setup for RCS calculation. ....	182
Figure 6.4. $S_{11}$ of the tag at a distance of 5 cm. ....	182
Figure 6.5. Reconstructed RCS of tag from simulation data using 8 x 8 cm plate as reference.....	183
Figure 6.6. Calculated RCS of tag from simulation data using 20 x 20 cm plate as reference.....	183
Figure 6.7. Calculated RCS of tag from simulation data using 30 x 30 cm plate as reference.....	184
Figure 6.8. Bistatic measurement setup. ....	200
Figure 6.9. PCB and inkjet-printed tag arrays. ....	200
Figure 6.10. Simulated response of 4 x 4 PCB tag array.....	201
Figure 6.11. Measured response of 4 x 4 PCB tag array. ....	201
Figure 6.12. Measured response of 4 x 4 unsintered inkjet-printed tag array. ....	201
Figure 6.13. Measured response of 4 x 4 sintered inkjet-printed tag array. ....	202
Figure 6.14. 8 spiral tag microwave thermography results.....	203
Figure 6.15. Single spiral tag microwave thermography results. ....	204
Figure 6.16. Embedded tag measurement setup. ....	205
Figure 6.17. Embedded tag measurement setup for tag embedded 0 cm in oil. ....	206
Figure 6.18. Responses for tag embedded 0 cm in free-space, oil, and sand. ....	207
Figure 6.19. Responses for tag embedded 0.5 cm in free-space, oil, and sand. ....	207

## LIST OF TABLES

	Page
Table 1.1. Chipless RFID tags for ID applications.....	11
Table 1.2. Chipless RFID tags for sensing applications.....	19
Table 1.3. Chipless RFID tags with dual sensing and ID capabilities.....	23
Table 3.1. Codes for different embedding materials permittivities for 8 slot tag.....	44
Table 3.2. Codes for different embedding material loss factors for 8 slot tag.....	47
Table 3.3. Codes for different embedding materials permittivities for 8 slot tag with limited interrogation bandwidth.....	48
Table 4.1. Tag metrics for different coding methods.....	64
Table 4.2. Responses of tag configurations with multiple of the same spiral.....	98
Table 4.3. Codes for ID tag using coding method 2.....	110
Table 4.4. Effect of z-direction translation on measurement and simulation.....	129
Table 5.1. Reported dielectric properties of printing papers.....	142
Table 5.2. Printing paper thicknesses.....	144
Table 5.3. Dielectric properties of papers.....	146
Table 5.4. Measured $S_{21}$ of different inkjet-printed samples.....	156
Table 5.5. Summary of conductivity measurement results.....	157
Table 5.6. Effect of handling prints on conductivity.....	159
Table 6.1. $S_{11}$ of eight spiral tag for different distances.....	185
Table 6.2. Reconstructed RCS for measured plate reference target.....	189
Table 6.3. Reconstructed RCS with plate simulation for reference.....	194

**NOMENCLATURE**

Symbol	Description
$\epsilon_r$	Relative Complex Dielectric Constant
$\epsilon_r'$	Relative Permittivity
$\tan\delta$	Loss Tanget
$\lambda_{mat}$	Wavelength in Material
$c$	Speed of Light
$\epsilon_{eff}$	Effective Permittivity
$\sigma$	Conductivity (S/m)

# 1. INTRODUCTION

## 1.1. PROBLEM STATEMENT

Monitoring and maintaining civil, space, and aerospace infrastructure is an ongoing critical problem facing our nation. As new complex materials and structures, such as multilayer composites and inflatable habitats, become ubiquitous, performing inspection of their structural integrity becomes even more challenging. Thus, novel nondestructive testing (NDT) methods are needed that can effectively address a multitude of needs, such as being low cost, broadly applicable, and user friendly [1-5]. This work seeks to address this through the development of miniaturized embedded wireless passive microwave sensors for materials characterization and structural health monitoring (SHM). Specifically, this work is in the field of chipless radio frequency identification (RFID) and lays the foundation for a new way to perform materials characterization.

## 1.2. BACKGROUND

**1.2.1. Overview of Chipless RFID.** RFID is a growing technology with a wide variety of applications. As a technology, RFID is a method for retrieving data through electromagnetic transmissions. An RFID system typically consists of a tag and a reader. In a traditional system, the tag contains a unique ID number as well as memory that can store additional information. The reader is then able to read or write data to the tags through wireless transmission [6, 7]. This technology was mainly developed for the purpose of object tracking and management, but has also been adapted to other applications by integrating sensors into the RFID tags and by using different types of tags [7-9]. Tags can be active, semi-active, passive, and chipless. Active tags have a battery

and an integrated circuit (IC) that stores their information, while semi-active tags rely on RF energy from the reader to activate the tag which is then battery powered. Passive tags have similar functionality to active and semi-active tags, but they are fully powered by RF energy from the reader. Lastly, chipless tags are tags that do not have a power source and do not have an IC. Instead, their information is “stored” in their structure, in the sense that they produce a frequency response that is dependent on their physical geometry after they are interrogated with an electromagnetic wave [7, 10-12]. Chipless RFID is a relatively new field, with the first tag report in 2007. However, the field has been growing rapidly due to the low cost and versatile nature of chipless tags [13]. Over the last decade there have been many developments within the field, especially in the tag characteristic aspects of this technology. More specifically, these developments have been primarily in the areas of tag architectures, encoding methods, fabrication methods, metrics, and applications.

**1.2.1.1. Chipless RFID tag architectures.** Chipless RFID tags typically fall into one of three architectural categories: time-domain, frequency-domain, or spatial-domain. In all cases a binary code is assigned to the response of the tag. This code is then used for identification or occasionally in a sensing modality. When using time-domain tags, a pulse is sent to the tag and the backscattered signal is analyzed. The received data is often filtered and time-gated to isolate the antenna mode from the structural mode. Then, the shape and time of occurrence of response signatures are analyzed to extract the code of the tag [14-16].

Frequency-domain tags, also sometimes referred to as spectral-based tags, have their response as a function of frequency. Typically, this response is in terms of radar

cross-section (RCS) vs. frequency (in dBsm) or the log magnitude plot of a scattering parameter ( $S_{11}$  or  $S_{21}$ ) (in dB). Within the frequency-based tag category, there are two main sub-categories: Tx/Rx and backscatter tags. Tx/Rx tags contain two antennas that are cross-polarized with respect to each other and then a collection of resonators between the antennas that create notches in the response. These resonators are often spiral

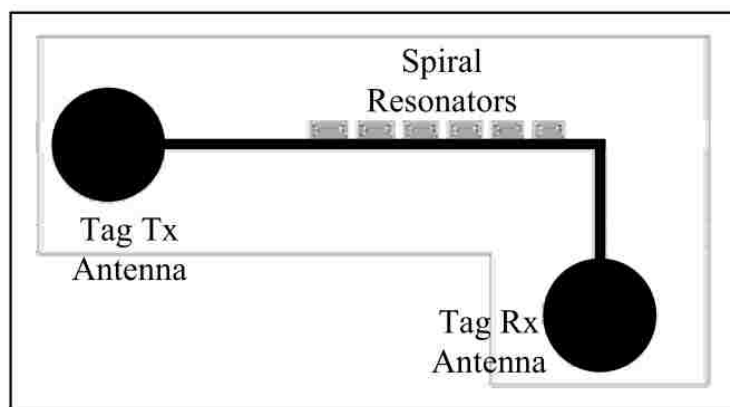


Figure 1.1. Tx/Rx frequency-based tag [17].

resonators, but open loop and hairpin resonators have also been used [17-22]. A configuration of this type of tag is shown in Figure 1.1.

In backscatter tags, the geometry of the tag causes it to scatter in a specific way when it is interrogated with an electromagnetic wave, creating a specific frequency response. To create these tags, a variety of resonators such as, slots, rings, spirals, U-shaped, and C-shaped, can be used. These resonators can be used individually or combined in order to engineer different tag responses [23-27]. Figure 1.2 shows an example of a backscatter frequency-based tag from [23] and Figure 1.3 shows an RCS vs. frequency response for the tag in Figure 1.2.



Figure 1.2. Backscatter frequency-based tag [23].

The tag in Figure 1.2 is associated with the red curve in Figure 1.3. As can be seen from Figure 1.3, there are 4 notches in the response in the 6 to 15 GHz frequency range. Each of these notches corresponds to one of the circular slot resonators of the tag, with the slot with the largest radius being associated with the lowest resonant frequency notch in the response [23].

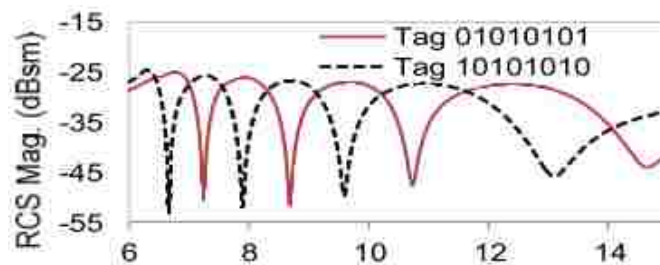


Figure 1.3. RCS vs. frequency response for tag in Figure 1.2 [23].

Spatial-based tags rely on imaging methods to measure them. They consist of a collection of conductive features on a dielectric substrate. These conductive features can be depolarizing, but are not always, and are typically lines or meander lines spaced based on the resolution of the imaging system. The image that is created then has a binary code assigned to it. This tag type has the benefit of being easier to use at higher frequencies.

However, it requires a more complicated reader system than time-domain or frequency-domain based tags. Additionally, spatial-based tags are limited by the resolution of the reader system and are thus difficult to achieve high bit density (the number of bits in the binary code per  $\text{cm}^2$  of tag area) with [28]. Figure 1.4 shows an example of a spatial based tag.



Figure 1.4. Spatial-based chipless RFID tag [28].

Given the relative simplicity and versatility of frequency-based tags, they are the most popular type of tag and have been used in this work. Consequently, the subsequent background sections focus on additional aspects of frequency-based chipless RFID tags.

**1.2.1.2. Response encoding methods.** As previously mentioned, a binary code is often assigned to the spectral response of the frequency-based tags. This binary code can be assigned in a variety of ways including the following:

- Method 1: notches are 1s, removing a notch shortens the code [19].
- Method 2: notches are 1s, removing a notch adds a 0 to the code [23].
- Method 3: notches are 1s, elsewhere are 0s [17, 29].



- Method 4: Frequency Shift Encoding (FSE) – bit sequences are assigned to each notch depending on its position state. Position states refer to the user defined set of resonant frequencies a notch can have in a response. The assigned bit sequences are concatenated together [30-32]. This method is illustrated in Figure 1.5.
- Method 5: extends Method 3 by adding error-correcting Golay, BCH, or majority-rule based codes [33].
- Method 6: applies FSE to both amplitude and phase data. This is often referred to as a hybrid coding scheme [27].
- Method 7: Extends FSE to exploit the width of notches. Wider notches are associated with more bits than narrower notches [34].

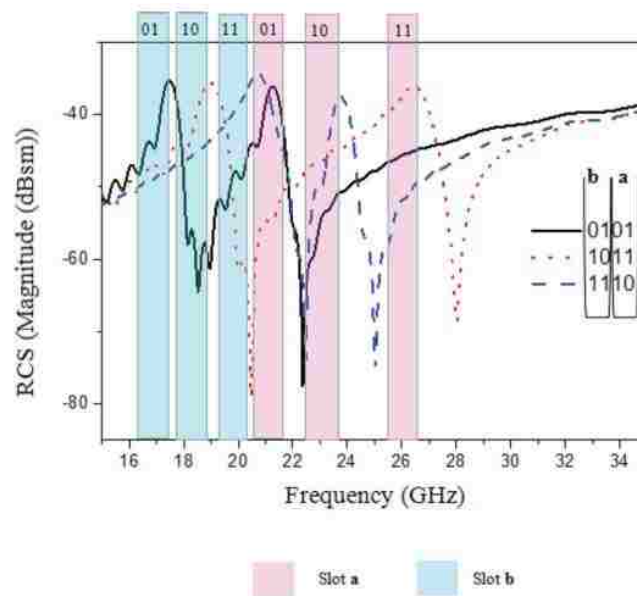


Figure 1.5. Illustration of FSE coding method [32].

A new coding method based off of Method 7, will be discussed in Section 3. This coding method has been specifically designed with embedded chipless RFID for materials characterization in mind. Many of these coding methods are subject to user bias (i.e., two code assigners using the same method will not always produce the same results). The effects of which coding method is selected and how it is implemented are seen in the calculation of tag metrics and thus affect how tags are compared to each other. Which coding method is used in practice is dependent on the application, tag design, and in many cases user preference.

**1.2.1.3. Tag metrics.** A variety of metrics have been developed for chipless RFID. The primary metrics used are bit density, coding capacity, data capacity, and spectral bit density. These metrics are usually only used for ID applications and not sensing applications due to codes typically not being assigned to sensing based tags. However, when tags are used for sensing applications, measurand sensitivity has also been used as a metric.

Bit density is the number of bits in the binary code of a tag per  $\text{cm}^2$  of tag area. The number of bits is dependent on the coding method used. Thus, a tag can have a range of bit densities. This makes it difficult to directly compare reported bit densities of tags. Coding capacity is another metric that suffers from a similar coding method dependency, while also having multiple reported definitions.

The first definition refers to coding capacity as it relates to the number of total combinations, which is mathematically expressed as:

$$2^C = T \quad (1)$$

In Equation (1)  $C$  is the coding capacity and  $T$  is the total number of code combinations.  $T$  can be determined by multiplying the number of possible positions for each resonance (i.e., multiplying the number of possible defined positions for the first notch in the frequency response by the number of possible positions for the second notch in the response and so on). Equation (1) can be rearranged to get the following expression for coding capacity:

$$C = \frac{\log(T)}{\log(2)} \quad (2)$$

The definition in Equation (2) takes into account the multiple positions a notch can take in the frequency response of a tag (see Figure 1.5), but is also dependent on how the code generator determines what constitutes a different position for a resonance [35].

The second definition of coding capacity simply provides the total number of possible combinations for the code. It can be expressed as:

$$C = 2^n \quad (3)$$

In Equation (3),  $n$ , refers to the number of bits in the code [36]. This definition is the simplest to calculate of those provided and provides insight into how many unique IDs a tag design can possess, which succinctly describes capability of the tag for ID applications.

The third definition of coding capacity involves cases where Method 4 for response coding is used. This definition incorporates the number of resonators, the bandwidth used for the tag response, and the average bandwidth of the notches in the response to determine the coding capacity. This definition can be expressed as follows:

$$C = \log_2 \left( \frac{f}{\Delta f} \right)^n \quad (4)$$

In Equation (4),  $f$ , represents the bandwidth of the tag response,  $\Delta f$  represents the frequency difference between two coding locations in the response,  $n$  represents the number of resonances, and  $C$  again represents the coding capacity. This definition is dependent on using coding Method 4 and cannot easily be extended to scenarios where other coding methods are used [30].

A fourth definition divides the tag response bandwidth by the number of positions a single resonance in the spectral response of the tag can take. In this sense, coding capacity is the maximum possible number of resonances that could be achieved using a collection of a single resonator type within a certain bandwidth. The context in which this definition was proposed is a scenario where a coding method similar to that of Method 4 was used [31].

Data density and spectral density are less commonly used metrics than bit density and coding capacity. In the cases where data density has been used, it has been referred to as the number of bits in the code [37]. This definition does not take into account the size of the tag as bit density does or the bandwidth usage as some definitions of coding capacity do. It is, however, still highly dependent on the code generation method used, similar to the previously-presented bit density and coding capacity definitions. Spectral density, is similarly dependent on the coding method and is the number of bits in the code per bandwidth needed for encoding [38]. All four of these metrics were designed for measuring the suitability of a tag for ID applications and therefore are not typically used for sensing-based tags.

As previously mentioned, in sensing applications measurement sensitivity is sometimes used as a metric for tags. Sensitivity is how significantly a measured

parameter changes as a function of the parameter being sensed. An example of this is how drastically a measured voltage changes as a function of temperature for a temperature sensor. This metric provides insight into how small of changes in the sensing parameter a sensor can detect. It can also provide the user with useful information as to what ranges of the sensing parameter are best measured [39]. All five of these metrics along with new proposed metrics will be further discussed in Section 4.

**1.2.1.4. Tag fabrication methods.** Tags are often made as printed circuit boards (PCBs) or through photolithography processes. Inkjet-printing with conductive ink has also garnered interest as a method for tag fabrication due to its cost effectiveness and quick production features. It is believed that in order for chipless RFID to become ubiquitous, tags will need to be manufactured extremely inexpensively through inkjet-printing [37, 40-45]. Inkjet printing and its practicality for embedded chipless RFID will be discussed further in Section 6.

Additional fabrication methods include, Flexography, gravure printing, screen printing, micro-contact printing, transfer printing, and nano-imprinting [46-49]. With all of the printing methods previously mentioned, the substrate can be a chemical interactive material (CIM). By making the substrate a CIM, chipless tags can easily be turned into sensors [50]. An additional manufacturing method involves using direct thermal transfer of conductive ribbon to a substrate. This can be done with a SATO printer [37].

**1.2.1.5. Examples of tag applications.** The primary applications of chipless RFID are identification and sensing. In ID applications, the goal is to create a tag that essentially performs the function of a barcode, but with greater security. Thus, ID applications desire tags with high bit densities and large coding capacities so that more

items can have unique IDs [12, 25]. In order to provide insight into the state of the chipless RFID tag field in terms of tags for ID applications, Table 1.1 shows a variety of tags that have been reported. The table is in chronological order of published date to shows the evolution of this technology.

Table 1.1. Chipless RFID tags for ID applications.

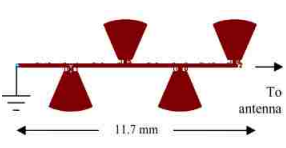
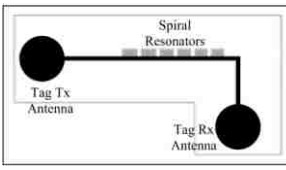

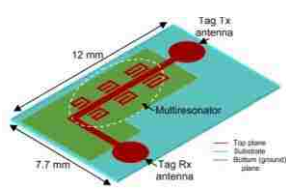

Tag	Application	Coding Method	Frequency (GHz)	Bit Density (bits/cm <sup>2</sup> )	Year	Ref.
	ID	N/A	6.9 – 7.9	N/A	2007	[13]
	ID	2	1.9 – 2.6	No tag size given	2008	[17]
	ID	2	3 - 7	0.61	2009	[51]
	ID	2	20 - 40	6.49	2011	[18]
	ID	6	2 - 7	2.86	2011	[27]

Table 1.1. Chipless RFID tags for ID applications (cont.).

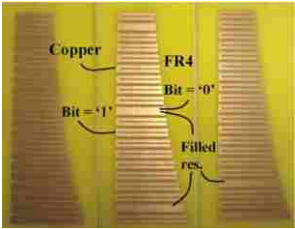

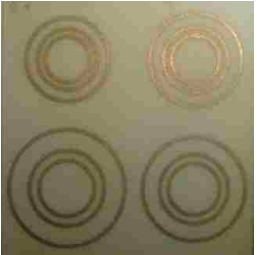
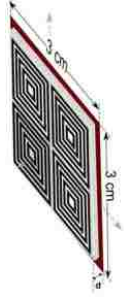
Tag	Application	Coding Method	Frequency (GHz)	Bit Density (bits/cm <sup>2</sup> )	Year	Ref.
	ID	2	2 - 4	1.14	2012	[52]
	ID	2	6-15	4.19	2012	[23]
	ID	4	3 - 9	2.5	2012	[25]
	ID	2	2 - 8	0.56	2013	[26]

Table 1.1. Chipless RFID tags for ID applications (cont.).

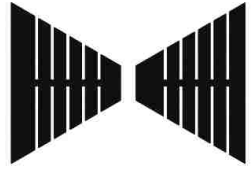
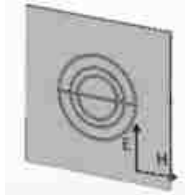
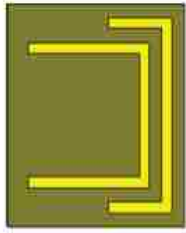

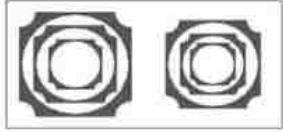
Tag	Application	Coding Method	Frequency (GHz)	Bit Density (bits/cm <sup>2</sup> )	Year	Ref.
	ID	2	4 - 10	1.04	2014	[53]
	ID	4	3.1 – 7.6	No Code Assigned	2015 6	[31]
	ID	4	17 – 27	28.57	2016	[32]
	ID	2	3 – 10	4.23	2016	[54]
	ID	4	3 – 9	3.56	2016	[35]



Table 1.1. Chipless RFID tags for ID applications (cont.).


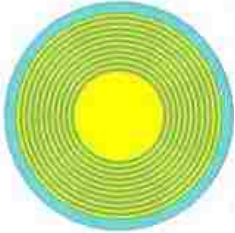

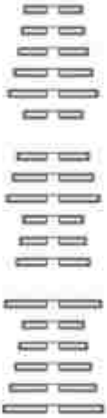
Tag	Application	Coding Method	Frequency (GHz)	Bit Density (bits/cm <sup>2</sup> )	Year	Ref.
	ID	2	2 - 4	1.14	2016	[55]
	ID	N/A	4 - 11	No Code Assigned	2016	[56]
	ID	4	8 - 14	19	2017	[57]
	ID	2	1.8 - 3.6	1.77	2017	[58]

Table 1.1. Chipless RFID tags for ID applications (cont.).

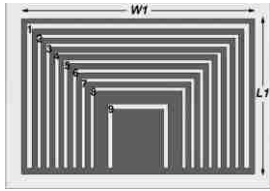
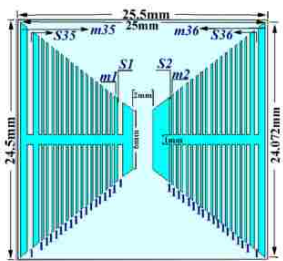
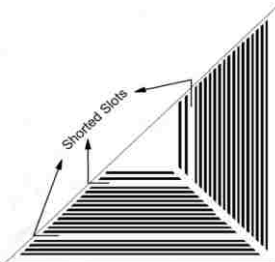
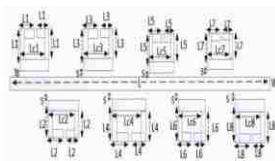

Tag	Application	Coding Method	Frequency (GHz)	Bit Density (bits/cm <sup>2</sup> )	Year	Ref.
	ID	2	8 - 20	5.71	2017	[24]
	ID	2	5 - 19	5.76	2017	[59]
	ID	2	4.6 – 14.6	9.03	2017	[60]
	ID	2	3.3 – 5.8	No tag size given	2017	[20]
	ID	2	1 – 5	No tag size given	2017	[61]

Table 1.1. Chipless RFID tags for ID applications (cont.).

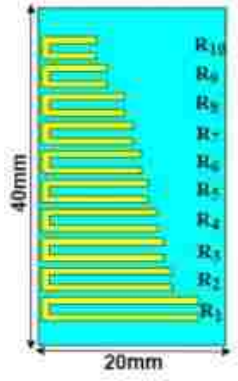



Tag	Application	Coding Method	Frequency (GHz)	Bit Density (bits/cm <sup>2</sup> )	Year	Ref.
	ID	2	2.5 – 5.5	1.25	2017	[36]
	ID	4	4 – 9.5	No code given	2017	[30]
	ID	2	3.1 – 3.9	0.56	2017	[62]
	ID	2	2 – 5	1.11	2017	[21]

Table 1.1. Chipless RFID tags for ID applications (cont.).

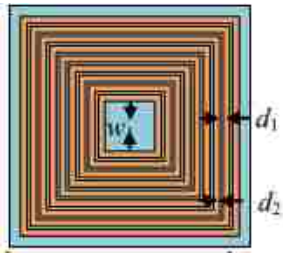
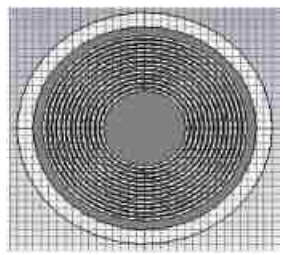
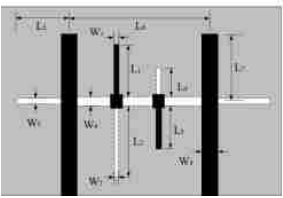
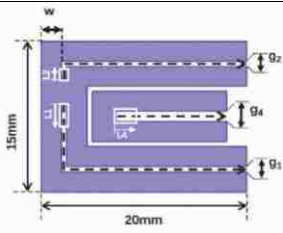

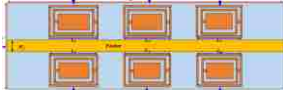
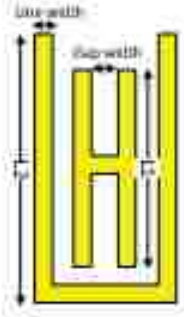

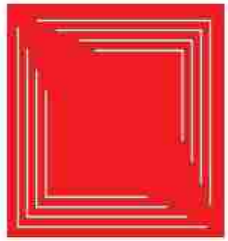
Tag	Application	Coding Method	Frequency (GHz)	Bit Density (bits/cm <sup>2</sup> )	Year	Ref.
	ID	2	1.9 – 7.1	2.78	2017	[63]
	ID	2	3.1 - 10	2.11	2018	[64]
	ID	2	2 – 10	0.64	2018	[65]
	ID	4	2 – 5.5	No Code Given	2018	[66]
	ID	1	0.85 – 1	0.028	2018	[67]

Table 1.1. Chipless RFID tags for ID applications (cont.).

Tag	Application	Coding Method	Frequency (GHz)	Bit Density (bits/cm <sup>2</sup> )	Year	Ref.
	ID	2	6.1 – 6.6	1.771	2018	[68]
	ID	2	3 - 8	5.13	2018	[69]
	ID	2	1.8 - 3.6	0.7	2018	[38]
	ID	2	3 - 6	2	2019	[70]

As can be seen, the highest reported bit density found is 28.57 bits/cm<sup>2</sup>. However, it is worth noting that this tag only has two notches in its response and by virtue of using FSE-based encoding, achieves a 4 bit code with a small tag area [32]. Methods 2 and 4

are the most common coding mechanisms, but the frequency ranges used to encode the information vary widely from tag to tag.

Chipless RFID tags can also be used as sensors. In these cases, the response changes as a function of a sensing parameter. An example of this is a humidity sensor in which the notches in the response shift as a function of the relative humidity [50]. The magnitude of a singular notch in the response has also been used to indicate changes in a sensing parameter [71]. In regards to SHM, strain, displacement, rotation, cracks, corrosion, and dielectric properties have been sensed with chipless RFID [71-76]. Sensing based tags tend to not have codes associated with them and therefore do not typically have bit densities. Table 1.2 provides an overview of the reported chipless RFID tags for sensing. As can be seen, the frequency range used for interrogating the tag varies widely and so do the parameters being sensed.

Table 1.2. Chipless RFID tags for sensing applications.

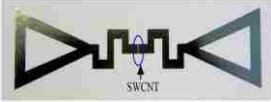
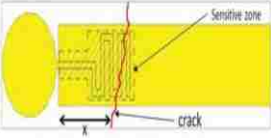
Tag	Application	Coding Method	Frequency (GHz)	Bit Density (bits/cm <sup>2</sup> )	Year	Ref.
	Gas Sensor	N/A	0.6 - 1	N/A	2009	[77]
	Surface Crack Sensor	N/A	1 - 4	N/A	2012	[78]

Table 1.2. Chipless RFID tags for sensing applications (cont.).

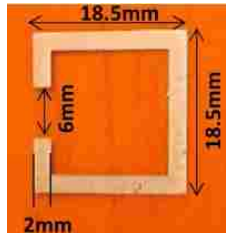
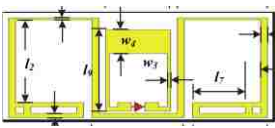
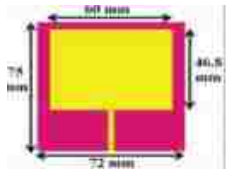
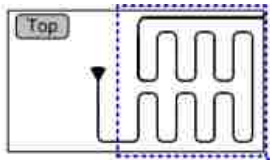

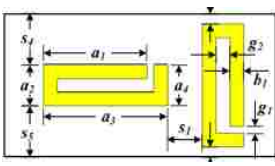
Tag	Application	Coding Method	Frequency (GHz)	Bit Density (bits/cm <sup>2</sup> )	Year	Ref.
	Strain and Crack Sensing	N/A	2.3 – 2.5	N/A	2014	[73]
	Dielectric Property Sensor	N/A	0.9225	N/A	2015	[79]
	Strain Sensor	N/A	2.2 – 2.7	N/A	2015	[72]
	Dielectric Property Sensor	N/A	3.1 – 5.6	N/A	2015	[16]
	Permittivity Sensor	N/A	1 - 6	N/A	2016	[80]
	Permittivity Sensor	N/A	0.9225	N/A	2016	[81]

Table 1.2. Chipless RFID tags for sensing applications (cont.).



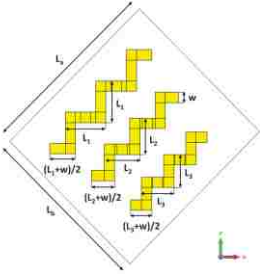
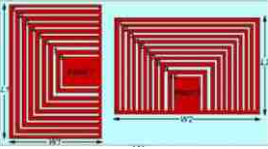
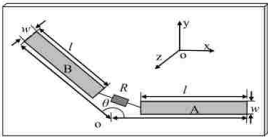
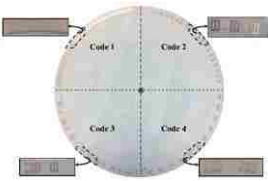
Tag	Application	Coding Method	Frequency (GHz)	Bit Density (bits/cm <sup>2</sup> )	Year	Ref.
	Corrosion Sensor	N/A	0.5 – 3	N/A	2016	[76]
	Rotation Sensor	N/A	3 – 6	N/A	2017	[75]
	Temperature Sensor	N/A	3.6 – 5.6	N/A	2017	[82]
	Humidity Sensor	2	4 – 14	5.54	2017	[83]
	Resistance sensor	N/A	1.8 - 3	N/A	2017	[84]
	Angular Velocity Sensor	2	3.3 – 4.5	No tag size given	2017	[15]



Table 1.2. Chipless RFID tags for sensing applications (cont.).

Tag	Application	Coding Method	Frequency (GHz)	Bit Density (bits/cm <sup>2</sup> )	Year	Ref.
	Displacement Sensor	N/A	2 - 8	N/A	2017	[74]
	Humidity Sensor	N/A	2 - 9	N/A	2017	[50]
	Dielectric Property Sensing	N/A	3.5 – 4.5	N/A	2018	[71]
	Pressure Sensor	N/A	20 - 23	N/A	2018	[85]
	Dielectric Property Sensor	N/A	1 - 6	N/A	2018	[86]
	Salt Water Concentration Sensor	N/A	3.5 – 3.6	N/A	2018	[87]

Some chipless RFID tags combine ID and sensing functionality. In these cases, a sensing bit is added to the ID tag to account for the effect of the material the tag is attached to, or ID bits are added to a sensing tag to distinguish multiple sensing tags from each other [19, 52, 88-91]. These combinational cases are less common than cases where the tag is designed for a singular application. Tags of this type are shown in Table 1.3.

Table 1.3. Chipless RFID tags with dual sensing and ID capabilities.

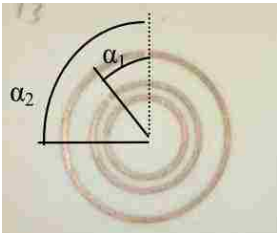
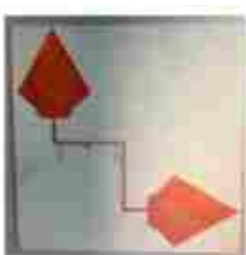
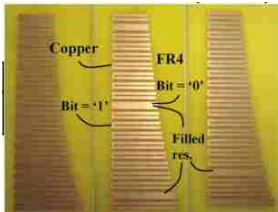
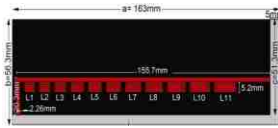
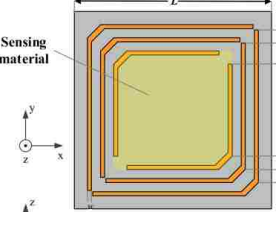
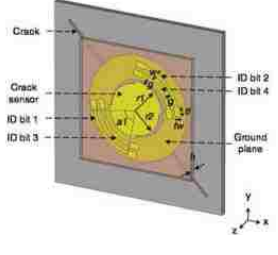
Tag	Application	Coding Method	Frequency (GHz)	Bit Density (bits/cm <sup>2</sup> )	Year	Ref.
	Rotation Sensing and ID	4	3.4 – 7.1	0.67	2012	[91]
	Permittivity Sensor with ID bit	N/A	1.4 - 6	N/A	2012	[88]
	ID with Sensing Bits	2	2 – 4	1.14	2012	[52]
	ID with Sensing Bit	1	1.5 – 3.5	0.13	2016	[19]

Table 1.3. Chipless RFID tags with dual sensing and ID capabilities (cont.).

Tag	Application	Coding Method	Frequency (GHz)	Bit Density (bits/cm <sup>2</sup> )	Year	Ref.
	Humidity Sensor with ID Bits	4	4 – 7.5	2.67	2018	[89]
	Metal Crack Sensor with ID Bits	1	2 – 6	No tag size given	2018	[90]

**1.2.2. Materials Characterization Overview.** For the applications being considered, materials characterization involves determining the dielectric properties of the material (assuming non-magnetic materials). At microwave frequencies, dielectric materials are characterized by their complex dielectric constant. When the dielectric constant is referenced to free-space it is referred to as the relative dielectric constant. The relative dielectric constant can be expressed as follows:

$$\epsilon_r = \epsilon_r' - j\epsilon_r'' \quad (5)$$

For this intrinsic electrical property, the real part (relative permittivity) in Equation 6,  $\epsilon_r'$ , represents the ability of the material to store microwave energy, while the imaginary part (loss factor),  $\epsilon_r''$ , represents how well the material absorbs microwave energy [92]. The loss tangent,  $\tan\delta$ , is another quantity used to describe material properties [93]. It can be expressed as follows:

$$\tan\delta = \frac{\epsilon_r''}{\epsilon_r'} \quad (6)$$

There are a variety of methods to determine dielectric properties of materials including: open-ended waveguide, loaded waveguide, modulated scatterer technique, loaded transmission lines, coaxial probes, ring resonators, and co-planar waveguides. Each method has its own advantages and drawbacks depending on the geometry of the material under test (MUT), accuracy needed, and ability to manipulate (i.e., cut or destroy) the sample [1, 2, 94-101]. As can be seen from Tables 1.2 and 1.3, there are also a variety of chipless RFID tags that have been designed to sense dielectric properties. All of these tags look at changes in a singular resonance in the response in terms of both resonance frequency shift and change in magnitude [16, 71, 79-81, 86, 88, 102]. In practice, this requires very careful measurements so that results are properly associated with the correct dielectric properties of the material. Additionally, manufacturing errors which cause changes in resonant characteristics can lead to incorrect sensor results. Therefore, by moving to a multi-resonant response and looking at changes in the binary code of the tag as a function of material rather than a single resonance, greater sensing capabilities can be achieved. This will be shown in Section 2 and then further explored in Sections 3, 4, and 5.

### **1.3. OBJECTIVES**

This work seeks to utilize chipless RFID in order to perform embedded microwave materials characterization by associating a multi-bit binary code with material properties. This goal involves developing an embedded tag measurement methodology, examining coding mechanisms, designing new tags optimized for this

application, investigating manufacturing methods for the tags, and finally performing measurements to show the utility of this novel NDT technique. In doing so, contributions will be made to the fields of chipless RFID and NDT in the areas discussed in Sections 1.2.1.1 to 1.2.2 of this introduction. To accomplish this, first a proof-of-concept was conducted as this technique has never been explored before. This is presented in Section 2. Next, a coding method and a tag design methodology were developed. These are presented in Sections 3 and 4, respectively. In Section 5, a tag designed for embedded materials characterization that can also be used for ID applications is presented. Section 6 then looks at inkjet-printing as a means of fabricating chipless RFID tags. Section 7 looks at measurement methods for tags both in free space and embedded in materials, and lastly, Section 8 provides a summary of the work as well as future work.

## 2. EMBEDDED CHIPLESS RFID PROOF OF CONCEPT

### 2.1. PREMISE

There is an ever growing need for new and innovative sensing technologies for SHM that are easily deployable, inexpensive, minimally invasive, and user friendly. Embedded sensors can meet this need and chipless RFID sensors are one such technology that has the potential to greatly add to the microwave embedded sensor “toolbox.” Yet, prior to this work, embedding chipless RFID tags in order to perform materials characterization has not previously been explored. To this end, a proof of concept of this novel approach to materials characterization was conducted. Simulations utilizing a tag previously presented in [23] are used to show the utility of this method. Then, a modified version of the tag was fabricated and measured to corroborate the simulation results. The results in this section were previously presented in [103].

### 2.2. SIMULATION RESULTS

To begin, a tag from [23] was modeled in CST Microwave Studio® as is shown in Figure 2.1. The tag consists of a TLX-9 low loss substrate disk ( $\epsilon_r' = 2.5$ ,  $\tan\delta = 0.0019$ ) of thickness 0.5 mm and radius 9 mm with 8 circular slot resonators etched onto the top conductor. The tag design does not include a ground plane. Then, a monostatic RCS simulation was conducted using linearly polarized plane-wave excitation in the 1-20GHz frequency range and an RCS probe placed 100 mm in front of the tag in free space. The free space RCS vs. frequency response is shown in Figure 2.2 with the RCS expressed in decibels per square meter (dBsm). With the reference response established, the tag was then embedded in a lossless material with  $\epsilon_r = 4$  and the simulation setup

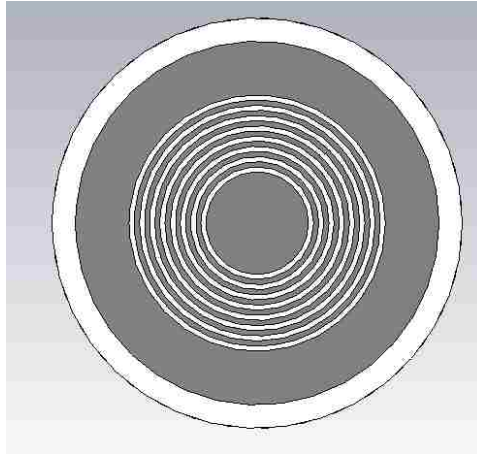


Figure 2.1. 8 circular slot resonator tag model.

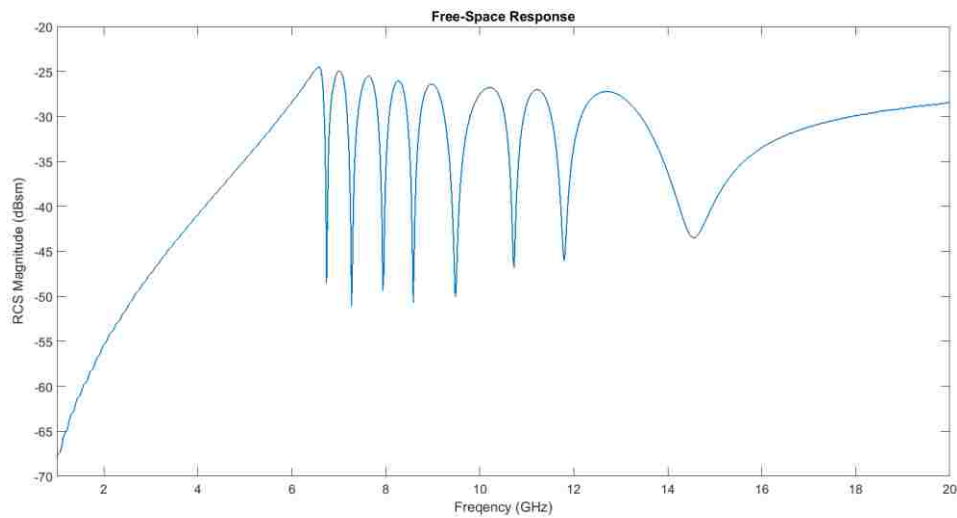


Figure 2.2. Free space RCS vs. frequency response of 8 circular slot resonator tag.

used previously was used again with the tag, plane-wave, and probe inside the material in order to isolate the effect of the material on the tag response. Figure 2.3 shows the response of the embedded tag. As can be seen, there is a clear down shift in frequency of the response as compared to Figure 2.2 – the first notch in Figure 2.2 moves from ~6

GHz to  $\sim 4.5$  GHz in Figure 2.3. This can be explained by the wavelength in the material,  $\lambda_{mat}$ , being smaller than it is in free space by a factor of  $1/\sqrt{\epsilon_r}$ , which makes the tag appear electrically larger and operate at lower frequencies. This illustrates how a change in response could then be associated with the properties of the material that the tag is embedded in.

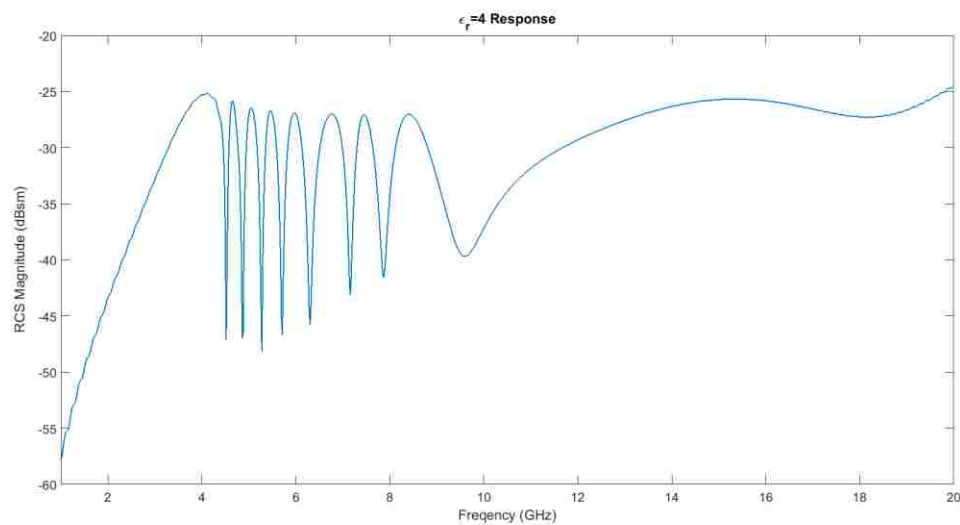


Figure 2.3. Response of tag embedded in a material of  $\epsilon_r' = 4$ .

To further understand this phenomena, another simulation was conducted. For this case, the tag was scaled to half of its original size and then again embedded in a material with  $\epsilon_r = 4$ . In this case, the response of this simulation was expected to be similar to that of the free space response shown in Figure 2.2. However, Figure 2.4 shows that this is not the case. There is a difference between the two responses and this difference is believed to be attributed to the effective permittivity between the tag substrate and the embedding material. These initial results show the effect of a change in permittivity on



the response of the tag, confirming that the response is a function of the material the tag is embedded in.

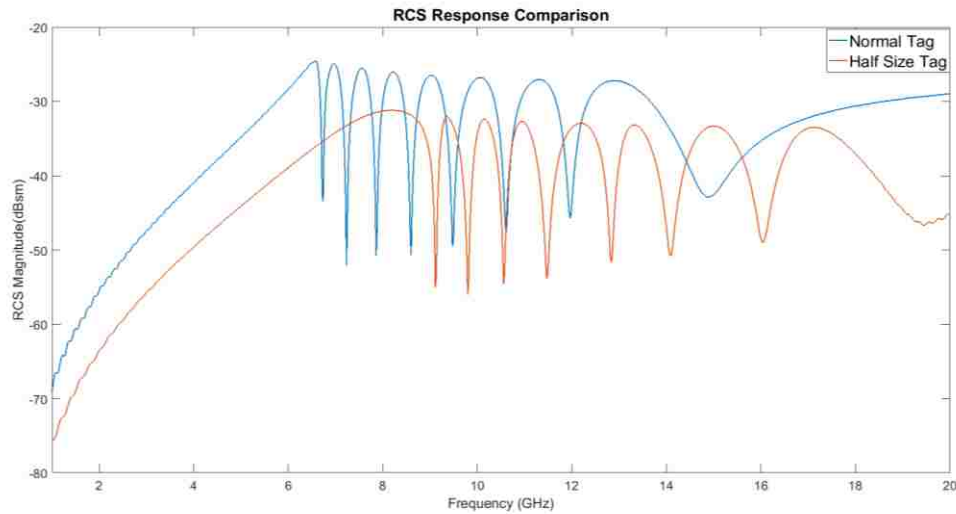


Figure 2.4. Comparison of tag in free-space and half size tag in material of  $\epsilon_r' = 4$ .

To further this investigation, the effect of loss on the response was also examined via simulation. First, the tag was embedded in materials with dielectric properties that resemble those of ceramics which are low loss. The results in Figure 2.5 show how small amounts of loss affect the response: there is a slight distortion of the response especially at higher frequencies. Next, another case where the permittivity was held constant while the loss increased was simulated. The results of this simulations, shown in Figure 2.6 show that as loss is increased, the response of the tag experiences greater distortion and reduction in the magnitude of the notches in the response.

All of these changes in response as a function of the material the tag is embedded in, would cause a change in the binary code that would be associated with the response. These changes in code could then be correlated back to the material properties. With the

initial proof of concept complete through simulation, a tag was then manufactured and measured to corroborate the simulation results.

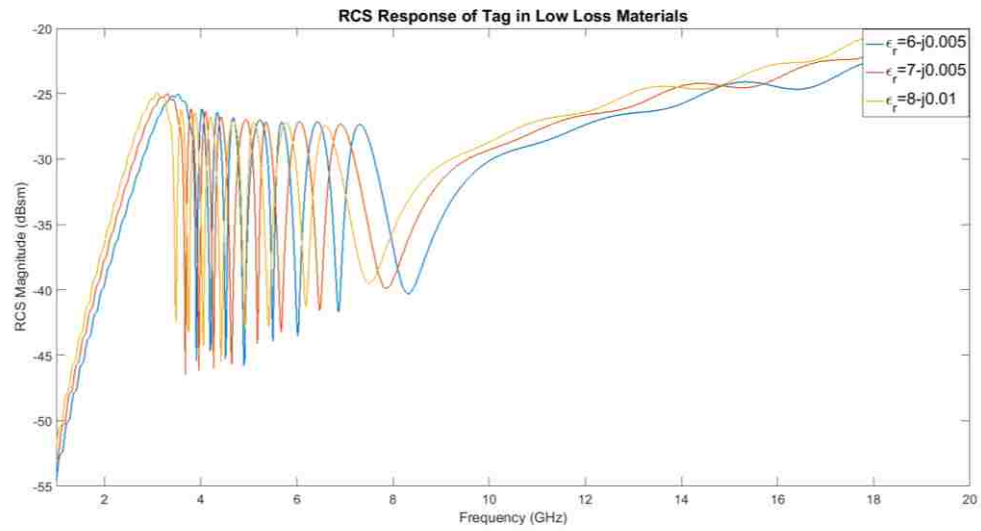


Figure 2.5. Response of tag in low loss materials.

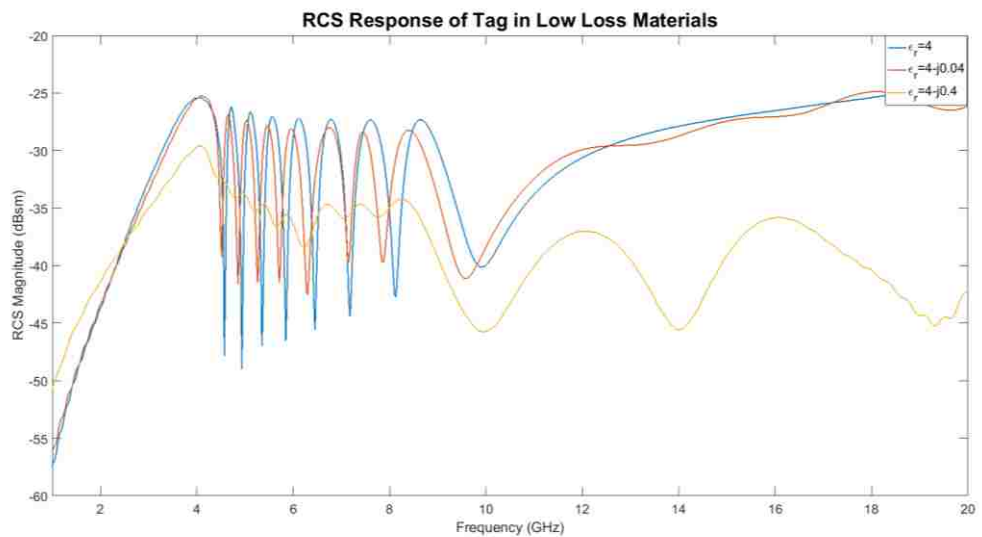


Figure 2.6. Response of tag as loss is increased.

### 2.3. MEASUREMENT RESULTS

To provide further evidence for the utility of this method, a tag was fabricated and then measured. The fabricated tag was made larger than the original design so that it could be milled in the Missouri S&T ECE Department Machine Shop and it was fabricated on Rogers 4003C. The manufactured tag was 36 mm in diameter with 4 circular slot resonators of 0.8 mm width. Only 4 resonators were used rather than 8 due to manufacturing limitations. Due to its larger size, the tag operates at lower frequencies (2 - 5 GHz) than the tag presented in Section 2.2. The CST model of the tag and fabricated tag are shown in Figure 2.7 and the simulated free-space RCS response of the tag is shown in Figure 2.8. Figure 2.8 was created through an RCS simulation with plane-wave excitation and RCS probe, like was done in Section 2.2 above.

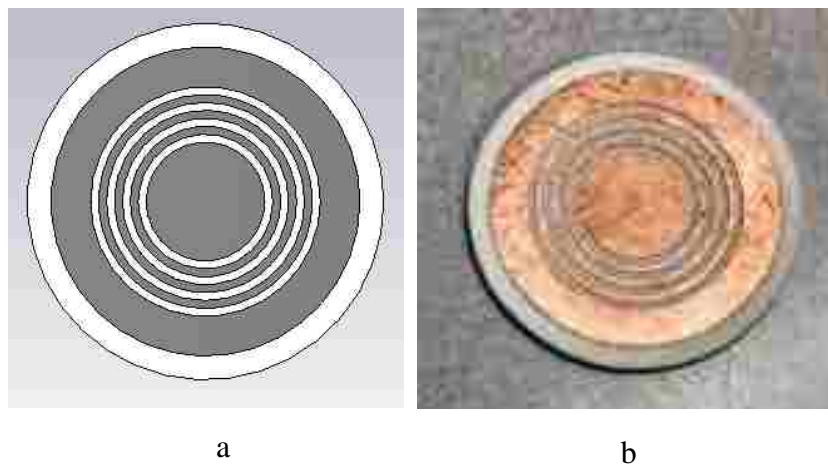


Figure 2.7. Tag for embedded measurement proof of concept. a) CST Microwave Studio® model. b) Manufactured tag.

The tag was measured in both air and embedded in different materials at different depths. The materials used were sand ( $\epsilon'_r \cong 2.5 - 3$ ) and wet sand for easy embedding with large differences in dielectric properties. For measuring the tag, an S-band (2.6 – 3.95 GHz) waveguide was used to measure  $S_{11}$  with an HP8510 vector network analyzer (VNA).  $S_{11}$  was measured rather than RCS because it is a simpler measurement to perform and produces similar results to RCS. To show this, the  $S_{11}$  of the tag was simulated using a plane-wave excitation to allow for the full frequency range to be simulated. To create a plane-wave, the boundaries were set in simulation so that the sides of the bounding box normal to the  $x$ -axis have  $E_t = 0$  and the sides normal to the  $y$ -axis have  $H_t = 0$ . These boundary conditions force a TEM wave to propagate from the waveguide port that is put in front of the tag. This simulation setup is shown in Figure 2.9 and the results are shown in Figure 2.10. As can be seen, the result in Figure 2.10 is very similar to the RCS simulation in Figure 2.8.

To examine the effect of using a waveguide rather than an ideal plane-wave (i.e., the physical measurement setup) to interrogate the tag, a third simulation was conducted with the waveguide exciting the tag. This simulation setup is shown in Figure 2.11 and the results are shown in Figure 2.12. In Figure 2.12, the strange behavior from 1-2 GHz can be attributed to this frequency range being below the cutoff frequency of the waveguide so there is no propagation at these frequencies. The three simulations are compared in Figure 2.13 with the RCS simulation normalized to make comparison easier. From Figure 2.13, it can be seen that all three cases produce fairly similar results with the waveguide simulation response being slightly downshifted in frequency from the others.

These results provide justification for measuring  $S_{11}$  rather than performing the more complex RCS measurement.

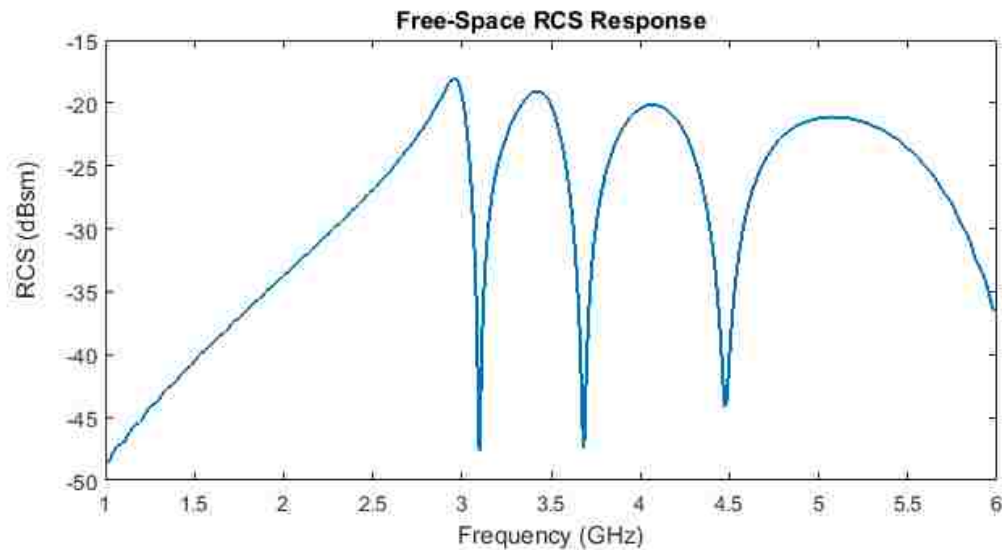


Figure 2.8. Free-space RCS response of tag from Figure 2.7.

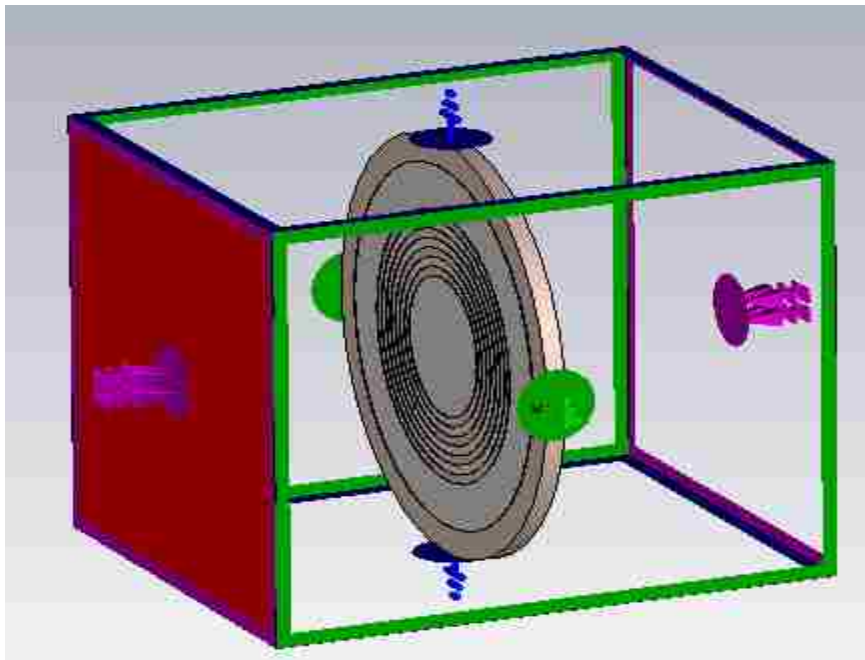


Figure 2.9. Plane-wave  $S_{11}$  simulation setup.

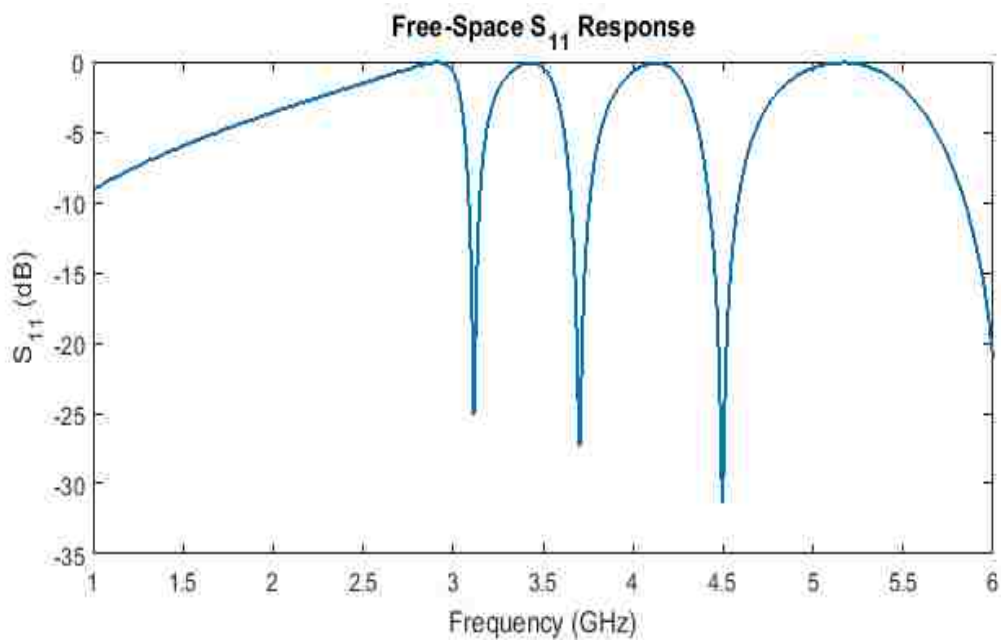


Figure 2.10. Simulated plane-wave  $S_{11}$  result of the tag.

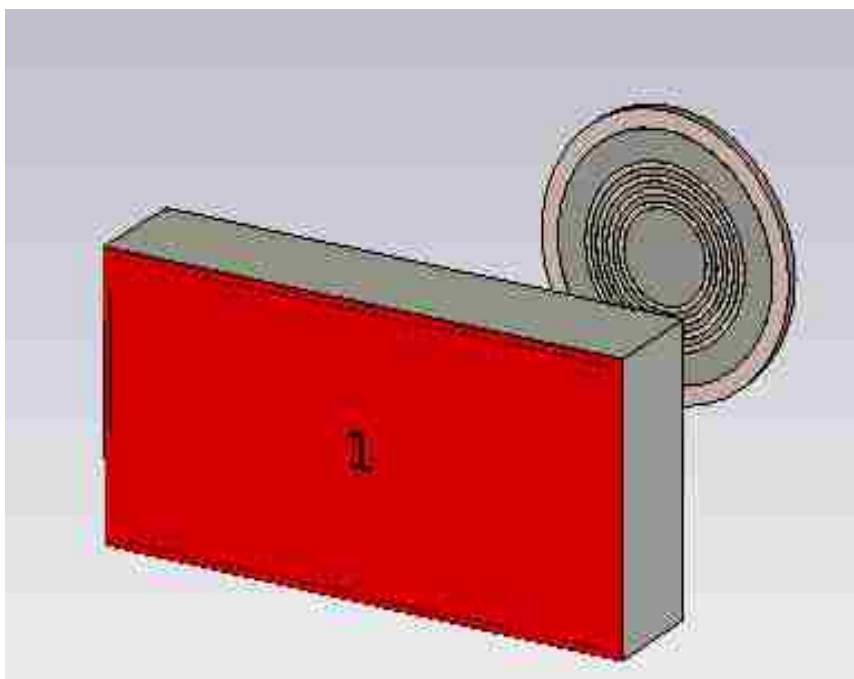


Figure 2.11. Waveguide  $S_{11}$  simulation setup.

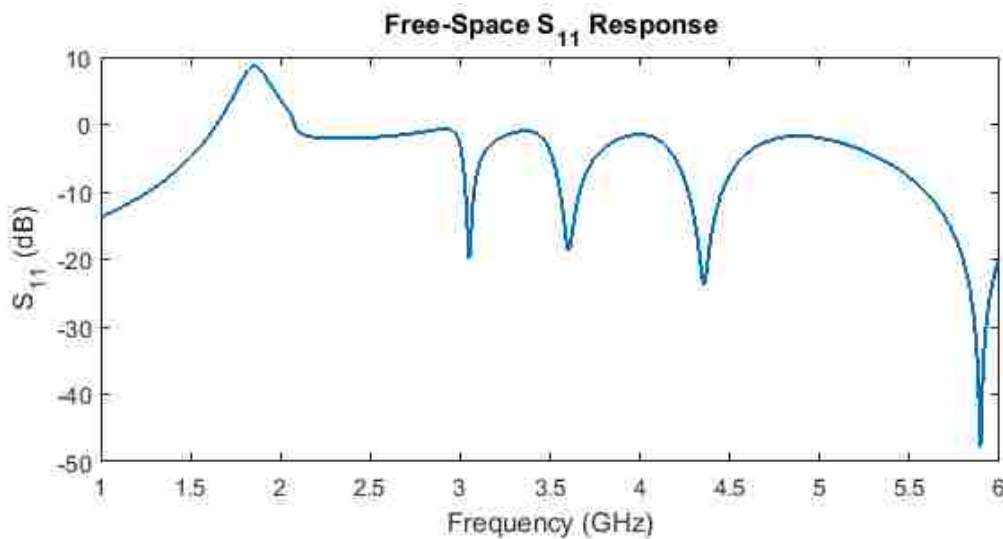


Figure 2.12. Simulated waveguide  $S_{11}$  result of the tag.

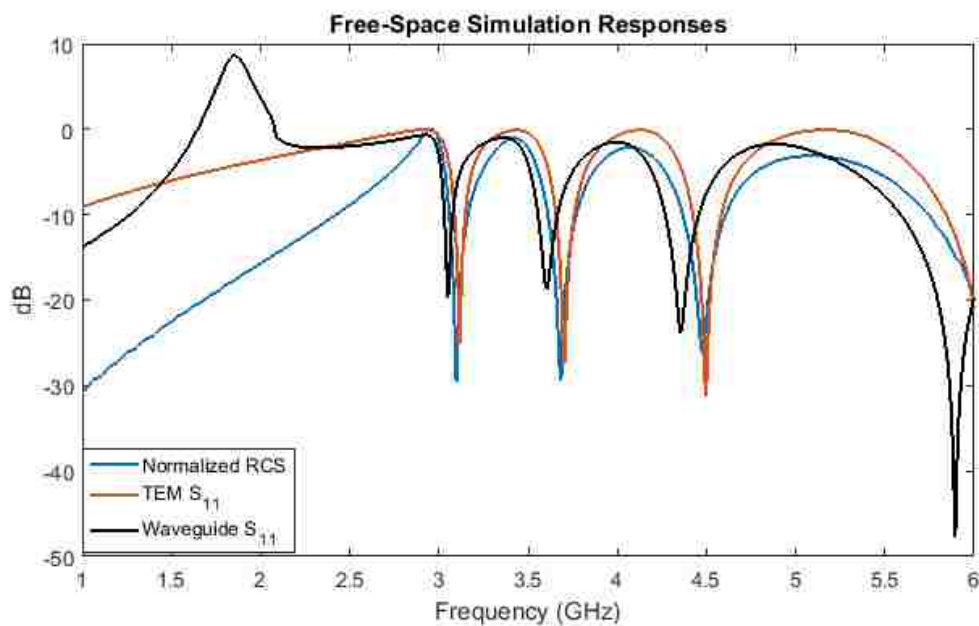


Figure 2.13. Comparison of RCS and  $S_{11}$  simulation results.

All measurements were performed with the waveguide kept stationary and pointing into a box lined with microwave absorbers. A box of the embedding material

was then placed inside this setup to perform the embedded measurements. In the cases of both the embedded and air measurements, the tag was kept the same distance from the waveguide aperture (6cm when the tag was on top of the material). The measurement setup is shown in Figure 2.14.

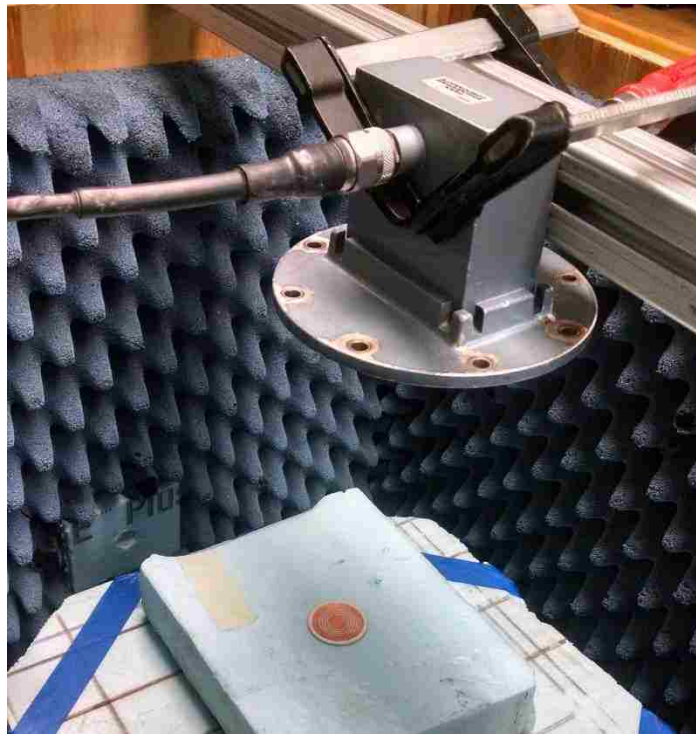


Figure 2.14. Measurement setup for embedded tag measurements.

For making the measurements, the material the tag was to be embedded in was first measured without the tag. Then, the tag was measured embedded in the materials at depths of 0cm (i.e., on top of the material), 1cm, and 2cm due to  $S_{11}$  measurements being distance dependent. For each material and depth, multiple measurements were performed and results were averaged to remove some of the measurement inconsistencies. The response of just the material was then subtracted from the response of the tag in the



material. The processed measurement results (i.e., results with material response subtracted) of the tag being embedded in sand and wet sand at different depths are shown in Figures 2.15 and 2.16, respectively. Due to the tag not having a ground plane, a difference can be seen between the results for different materials even when the tag is placed on top of the material rather than embedded inside.

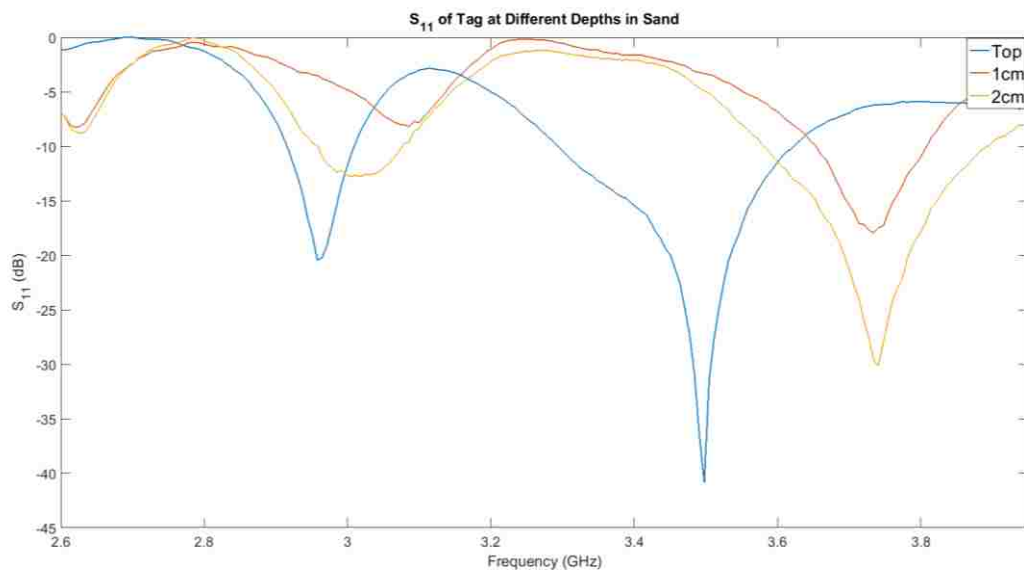


Figure 2.15. Processed measurement results of tag embedded in sand.

Figure 2.17 shows a comparison of the processed measurement results for the tag in air, sand, and wet sand for an embedding depth of 1cm. As can be seen, the responses for the three materials are different. If a binary code were to be assigned to these responses, the different codes could then be associated to the properties of the different materials.

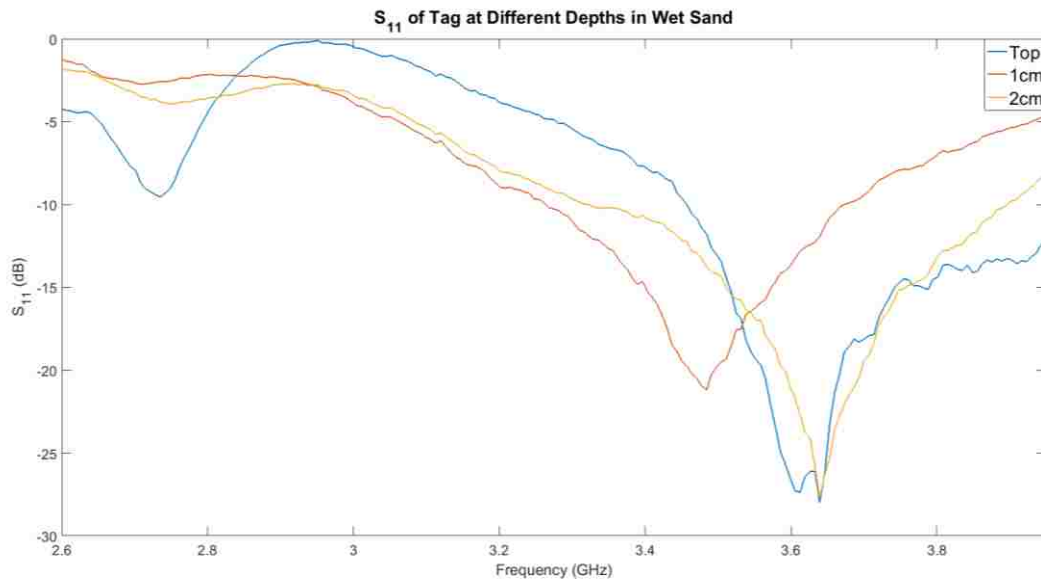


Figure 2.16. Processed measurement results of tag embedded in wet sand.

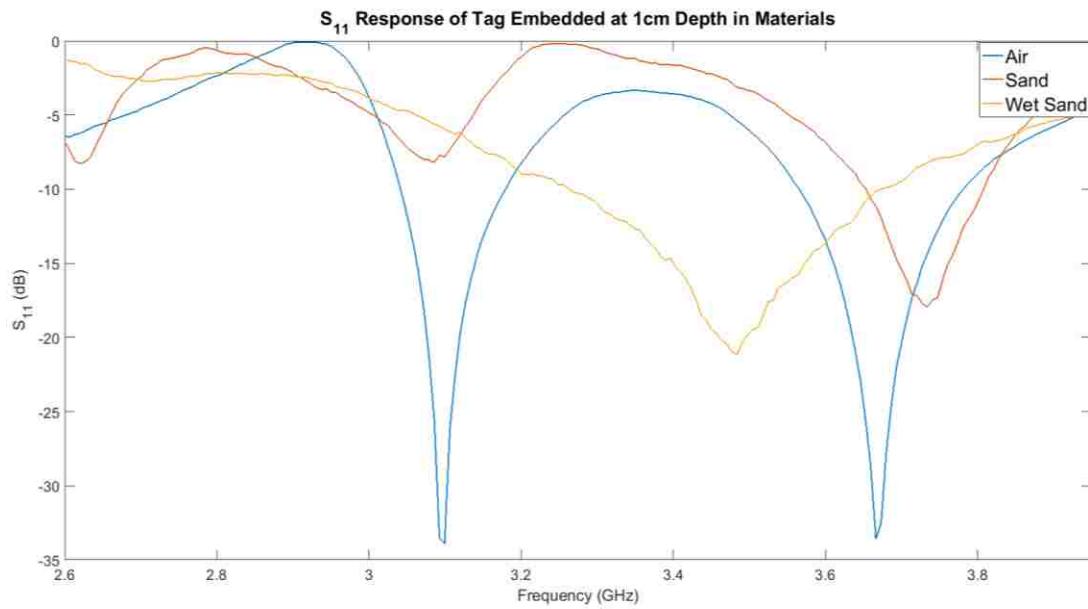


Figure 2.17. Comparison of measurement results for tag embedded in materials.

## **2.4. DISCUSSION**

Through simulation and measurement, the utility of the proposed technique for materials characterization was shown. It was demonstrated that the response of the tag changes as a function of the material by shifting in frequency, compressing, and distorting. These response changes can then be translated into binary codes that could then be associated with the embedding material's properties.

### 3. CODING METHOD DEVELOPMENT

#### 3.1. MOTIVATION

In Section 1.2.1.2, seven different coding methods were presented. However, these coding methods were designed for use in ID applications where the response changes in a very predictable manner and so, these methods are not ideal for sensing applications. When performing materials characterization by embedding chipless RFID tags, the response of the tag shifts, compresses, and distorts as a function of the material in which it is embedded in. Therefore, in order to perform dielectric property sensing by using a code associated with the response of the tag, this code needs to be sufficiently sensitive to reflect small changes in the response. To this end, a new coding method was developed. This method was previously presented in [103].

#### 3.2. CODING METHOD

By taking into consideration the benefits and limitations of the current coding methods, a new coding method has been developed. This new coding method can be used for both RCS and  $S_{11}$  measurements and can capture small changes in the response, like those that occur when performing embedded tag measurements. The proposed coding method, illustrated in Figure 3.1 for the response of the tag used in Section 2.2, is as follows:

- I. Use the “normalized” version of the free-space response of the tag, as the reference response. A portion of this response is shown in Figure 3.1 for illustration purposes.

- II. Establish a *threshold* based on the tag's reference response. For this tag the threshold is set at -5dB. This is depicted by the red horizontal line in Figure 3.1 which illustrates the basic approach.
- III. Identify intersection points (P1 and P2 on Figure 3.1) between the response and the threshold for the *narrowest* peak or notch, to set the frequency window width.

$$\text{Frequency Window Width} = \text{Frequency} [(P2) - (P1)] \quad (7)$$

- IV. Divide the frequency spectrum of the response from left to right into windows with the established window width. The dashed vertical lines in Figure 3.1 show the window divisions.
- V. Consider the amount of the RCS signal above and below the threshold in each window to assign 1s and 0s to the code. A '1' is assigned to a window if the signal is primarily above the threshold (i.e., when the signal is moved up in magnitude so the threshold is at 0 dB, integration of the signal over the window produces a positive result). A '0' is assigned to a window if the signal is primarily below the threshold. The assignments are shown at the top of each window in Figure 3.1.
- VI. Concatenate the binary values of the windows to form the full code.

One thing to note about this coding method is that whether the narrowest notch or peak is used is dependent on the reference response and the sensing resolution needed. In general, using the narrowest notch will produce smaller windows and therefore longer codes. This coding method creates codes that tend to be longer than those produced by

other coding methods, but also provides a mechanism to capture small changes in the response. The following section provides examples of this coding method in use.

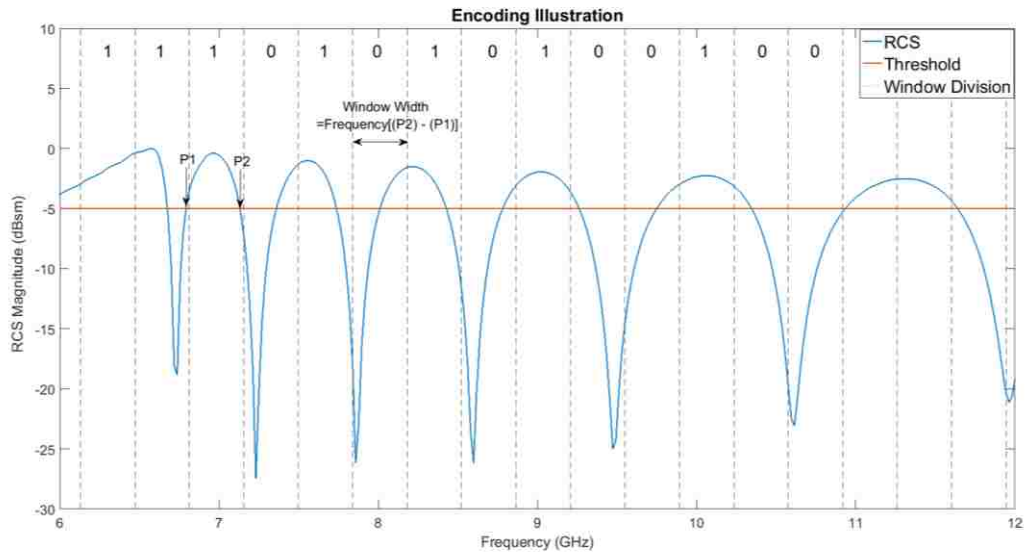


Figure 3.1. Illustration of proposed coding method.

### 3.3. IMPLEMENTATION OF CODING METHOD

To show the utility of this coding method, it is applied to the 8 slot tag presented in Section 2. The tag has the encoded normalized RCS vs. frequency response shown below in Figure 3.2. Using the proposed coding method and coding the full 1 – 20 GHz response, it has the following 55 bit code:

[000000000000000011110101010010011001111000000000000000011]

The extra bandwidth before the first resonance of the reference response is utilized in generating the code so that when the tag is embedded in a material and the response shifts, that shift is captured in the code. Figure 3.3 shows the encoded response for the 8



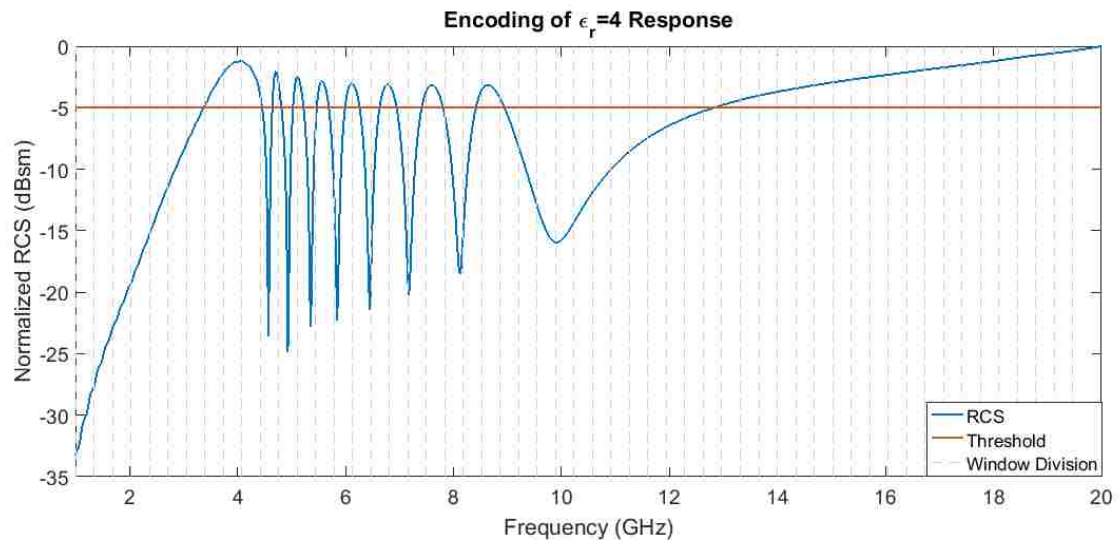


Figure 3.3. Encoded response for 8 slot tag in a material of  $\epsilon_r = 4$ .

By examining Table 3.1, it can be seen that the number of bit differences does not change drastically as permittivity is varied, but the locations of the bit differences do change in each case. As the permittivity increases, not as much variation is seen in the first half of the code. This is due to the normalized response causing a majority of the notches to be below the threshold. This is shown in Figure 3.4. This could mean that there is a limit to what range of permittivities this technique can determine or that a more limited bandwidth needs to be considered in order to address this normalization issue. Figure 3.5 shows the response for the tag when it is embedded in a material with  $\epsilon_r = 8$  and only 1 - 16 GHz is used rather than 1 - 20 GHz. As illustrated, the normalized response in Figure 3.5 contains more peaks above the threshold than that in Figure 3.4. Because of these results, Table 3.3 was constructed that shows the codes for the same tag when 1 – 16 GHz is considered rather than 1 – 20 GHz. This limited bandwidth produces 43 bit codes that tend to have more bit differences from the entries above and below them



in Table 3.3. This means that material properties could be more accurately sensed with shorter codes by using less bandwidth. Another method for achieving higher sensing accuracy would be to use the narrowest notch in terms of 3dB bandwidth to set the window width rather than the narrowest peak. This would provide a finer coding resolution and could possibly allow for better capturing of smaller changes in material properties at the cost of longer codes.

These factors along with the expected needed sensing range (i.e., what range of dielectric constants could potentially need to be measured) need to be balanced when selecting a tag to be used for this method and the interrogation bandwidth of the reader for that tag. This coding method can then be adjusted to be optimal for the scenario at hand.

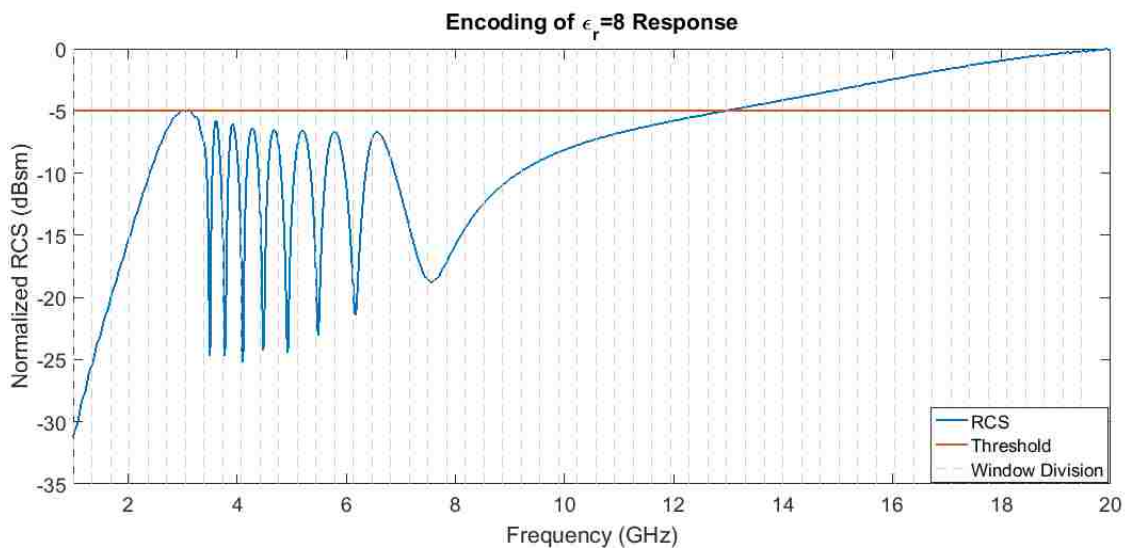


Figure 3.4. Encoded response for 8 slot tag in a material of  $\epsilon_r = 8$ .

Table 3.2. Codes for different embedding material loss factors for 8 slot tag.

Dielectric Constant	Code	Bit Diff. to Ref.	Bit diff to Er=4.
$\epsilon_r = 1$	0000000000000011111010101001001100111100000000000000011	0	N/A
$\epsilon_r = 4$	0000000111000100000100100000000001111111111111111111111	32	0
$\epsilon_r = 4 - j0.004$	0000000111000010100001000000000001111111111111111111111	27	7
$\epsilon_r = 4 - j0.04$	0000000111000010100001000000000111111111111111111111111	27	9
$\epsilon_r = 4 - j0.4$	0000000111111000000001000000000000000000000000000000000	21	27

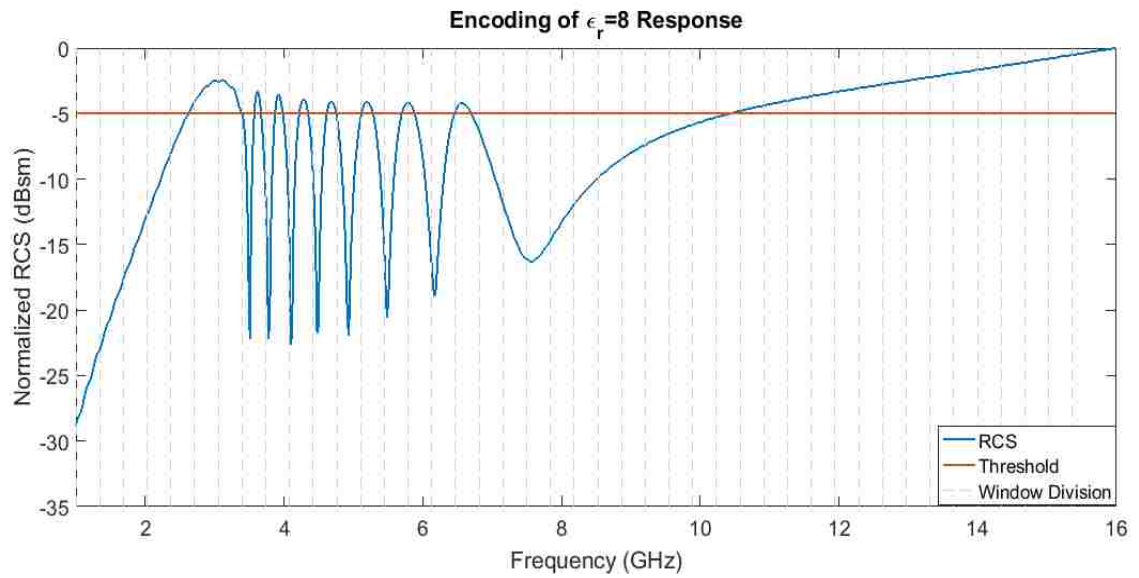


Figure 3.5. Encoded response for 8 slot tag in a material of  $\epsilon_r = 8$  with limited bandwidth.

Table 3.3. Codes for different embedding materials permittivities for 8 slot tag with limited interrogation bandwidth.

Dielectric Constant	Code	Bit Difference to Reference
$\epsilon_r = 1$	0000000000000011110101010010011001111000000	N/A
$\epsilon_r = 1.5$	00000000000111110010000100110011100000000000	16
$\epsilon_r = 2$	00000000000111001010101010100111000000000111	19
$\epsilon_r = 2.5$	000000000001110010010010101001100000000011111	21
$\epsilon_r = 3$	000000000111001001010010011000000000011111111	23
$\epsilon_r = 3.5$	000000001111000010101001100000000111111111	18
$\epsilon_r = 4$	0000000011100000010010100000000011111111111	18
$\epsilon_r = 4.5$	000000011100010010010100000000111111111111	21
$\epsilon_r = 5$	00000001110000101010100000000111111111111	18
$\epsilon_r = 5.5$	00000001100000010100100000000111111111111	15
$\epsilon_r = 6$	0000001110000100000100000000111111111111	22
$\epsilon_r = 6.5$	0000001110000010100100000000111111111111	21
$\epsilon_r = 7$	0000001100000000001000000000111111111111	18
$\epsilon_r = 7.5$	0000001100000001000000000000111111111111	18
$\epsilon_r = 8$	0000001100000000010000000000111111111111	18

### 3.4. REMARKS

The results in Tables 3.1, 3.2, and 3.3 and in Figures 3.3, 3.4, and 3.5 show that unique codes depending on the material that the tag is embedded in can be produced with this method. Changes in both permittivity and loss factor can be captured by this coding method, and by comparing the codes to the references it could be possible to extract these material properties from the codes themselves. This capability is not afforded by the other

current coding methods and thus, there is usefulness in this method. Moving forward, this coding method could be further optimized so that it is even more sensitive to changes in material properties while having a code that is only as long as is needed.

## **4. TAG DESIGN METHODOLOGY**

### **4.1. PREMISE**

Chipless RFID tags are typically designed with a specific application in mind, namely: they are to be used for either ID or Sensing. In a few cases, these applications have combined, but this is done to enhance performance for the main application rather than to give the tag a multifaceted purpose [34, 52]. In all cases, the tags tend to utilize a single type of resonator. This is limiting both in terms of versatility and practicality since it limits how customizable the response of the tag may become. Alternatively, by using multiple types of resonators in combination, greater response diversity and customizability can be achieved. The subsequent section presents a tag design methodology that is based around the combination of multiple types of resonators. This design methodology is also presented in a journal article that is under review at the time this is being written [104].

### **4.2. TAG DESIGN METHODOLOGY**

By applying a methodical approach, chipless RFID tags can be designed to combine multiple types of resonators and be easily adapted to a variety of applications. This design methodology involves taking into account the environments the tag could be in, understanding the design requirements driven by the potential applications, and utilizing design guidelines, like equivalent circuits and equations, to engineer the tag's response.

**4.2.1. Environmental Concerns.** The environments in which a tag may be in and the scenarios it may be in can greatly affect how it performs. One factor to consider is what the tag will be attached to, which lends itself to if it is beneficial for the tag to have a ground plane or not. It has been shown that if the tag is to be pasted to an object (e.g., a product's packaging), it is beneficial for the tag to have a ground plane so that the object does not influence the response of the tag [34, 90]. However, integrating a ground plane is difficult with some manufacturing methods such as inkjet-printing, which has found popularity in the chipless RFID community for its ability to produce inexpensive tags. To illustrate the difference of using tags with and without ground planes in this scenario, simulations were conducted.

For these simulations, the tag used in [103] was used again except the substrate was changed to be Mitsubishi paper, which is a common substrate for inkjet-printed tags. As an aside, the parameters used in inkjet-printing will be explored more in depth in Section 6. This tag, shown in Figure 2.1 was placed on a dielectric slab with  $\epsilon_r = 4$  and a thickness of 0.5cm. This permittivity was used so that there would be a more dramatic shift in response and the point of these simulations could be better illustrated. The simulation setup is shown in Figure 4.1.

Then, in CST Microwave Studio® the size of the slab was increased in the lateral ( $xy$ ) directions behind the tag as the RCS response was simulated using a plane-wave excitation and an RCS probe in a monostatic radar setup. The results of these simulations are shown in Figure 4.2, which was also presented in [104]. From Figure 4.2, it can be seen that the response is shifted down in frequency as compared to its free-space response when the tag is on the slab, similar to how it shifted down when the tag was embedded in

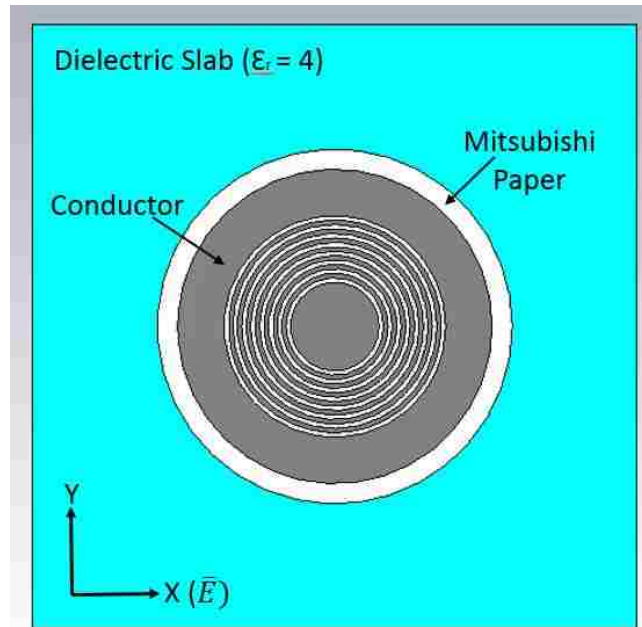


Figure 4.1. Simulation setup for tag pasted on dielectric slab of varying sizes.

a material with  $\epsilon_r = 4$  in Section 2.2. This effect is especially noticeable when comparing the free space response to the response when the tag is pasted on a 20 mm x 20 mm slab. It can also be seen from Figure 4.2 that as the dimensions of the slab increase, it becomes more difficult to discern the response of the tag (i.e., the resonance characteristics) from the response of the slab. This masking of the response by the material behind the tag is a result of the slab scattering more than the tag and the RCS response, which can be thought of as the superposition of the scattering of the slab and the tag, becomes dominated by the scattering of the slab. This overall makes performing measurements challenging. In order to address this issue, depolarizing tags, various measurement techniques, and array strategies have been previously employed. However, the challenges still persist [21, 25, 105-107].

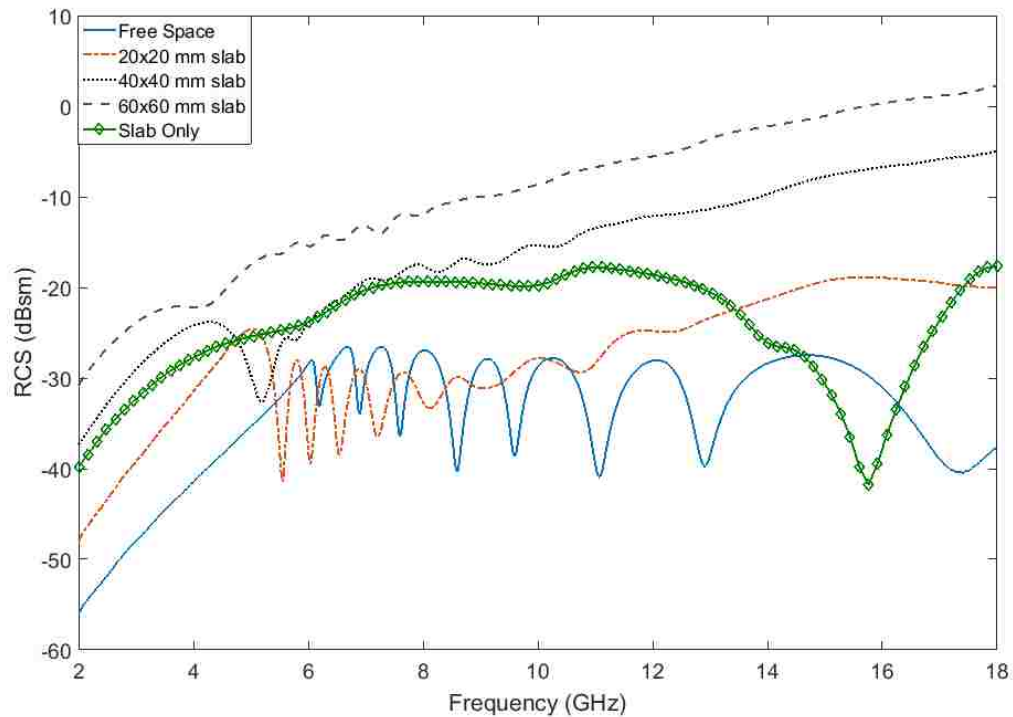


Figure 4.2. RCS vs. frequency response for tag when it is on a dielectric slab of varying sizes.

Another environmental situation to consider is when a tag without a ground plane is to be placed in front of an electrically conductive surface (e.g. metal or carbon composites). If the tag is sufficiently close to the conductive surface, it can act as a ground plane for the tag causing the response of the tag to be dramatically different. In the case of the tag in Figure 4.1, the conductor portion will become ring resonators while the slots will no longer resonate, which will result in a different from expected response.

In addition to the previously discussed environmental factors, other factors like temperature and humidity can also affect the tag and therefore need to be taken into consideration when designing the tag. Inkjet-printed tags are often printed on Mitsubishi paper, which turns out to be a material that is sensitive to humidity to the point that



humidity sensor tags have been made on it [50, 89]. This means that if a tag were to be fabricated on this material, the designer would need to be cognizant of this humidity dependency so that responses are correctly interpreted.

**4.2.2. Method.** The practices discussed above can be summarized in a three step design methodology that is focused towards the design of frequency-based backscatter tags. The three steps are as follows:

- I. Define tag requirements: size, manufacturing method, bit density, etc. Understand the current application and possible future applications.
- II. Select resonators and resonator combinations that satisfy the requirements determined in step I.
- III. Utilize the design guidelines (i.e., equations, equivalent circuits, design curves, etc.) to purposefully modify the resonator geometries to create a desired tag response.

### 4.3. DEVELOPED TAG

Utilizing the above design methodology, a tag was designed through simulation in CST Microwave Studio®. First presented in [108], this tag combines ring and spiral resonators in order to achieve a high bit density tag. Features of the tag can then be added or removed to manipulate the response of the tag. The base of the tag consists of a ground plane backed substrate disk of diameter 6.8 mm made of TLX-9 ( $\epsilon_r = 2.5$  and  $\tan\delta = 0.0019$ ). In its most simple configuration, the tag is shown in Figure 4.3. This configuration with just a circular patch and a ring resonator produces two distinct notches in the response, shown in Figure 4.4, which act as the *start* and *stop* bits (~21 and ~34

GHz, respectively) of the 18 – 35 GHz response of this tag. This frequency range was selected so that the tag could be small and minimally invasive for embedded materials characterization applications.

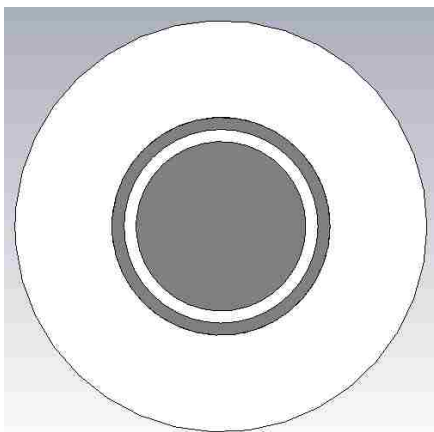


Figure 4.3. No spiral configuration of tag.

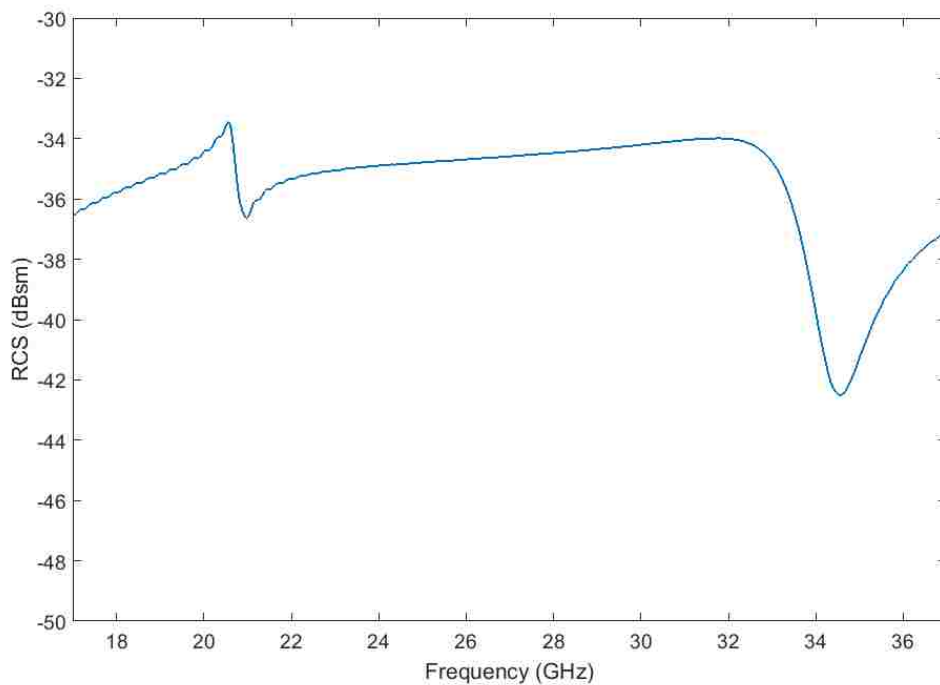


Figure 4.4. RCS vs. frequency response of tag in Figure 4.3.

In creating the spiral elements, first the spiral in top position (see Figure 4.5a) was developed. This spiral resonator was designed to have a resonant frequency near that of the ring resonator. In order to achieve this, the length, width, and distance of the spiral resonator from the ring resonator were manipulated. These manipulations affect the effective inductance/capacitance of the resonator and the ability of the ring resonator to couple signal into the spiral resonator. Larger effective inductances and capacitances are achieved by having longer length spirals and this in turn produces lower resonant frequencies [109, 110].

The first spiral resonator has a resonance frequency of ~18.5 GHz when it is the only spiral resonator on the tag. When additional spiral resonators are added, the interactions between the tag features causes this first spiral resonator notch to shift in between that of the start and stop bit notches. With the configuration in Figure 4.5a, the circular patch can be removed, however, the ring resonator needs to remain if the spiral resonator is going to be used. This is because, as previously mentioned, the ring resonator is used to couple signal into the spiral resonators. Without the ring resonator, the spiral resonators do not add notches to the response. This design constraint is illustrated in Figures 4.5 and 4.6. Figure 4.5 shows three different configurations of the tag and Figure 4.6 shows the responses for each of these configurations. Figure 4.6a shows the response for the configuration in Figure 4.5a. As can be seen, there is a notch in the response that corresponds with each feature of the tag – the patch, ring, and spiral. Figure 4.6b then shows the response for when the patch is removed. In this figure, there are still notches for the spiral and ring resonators but the notch associated with the patch at ~34 GHz is

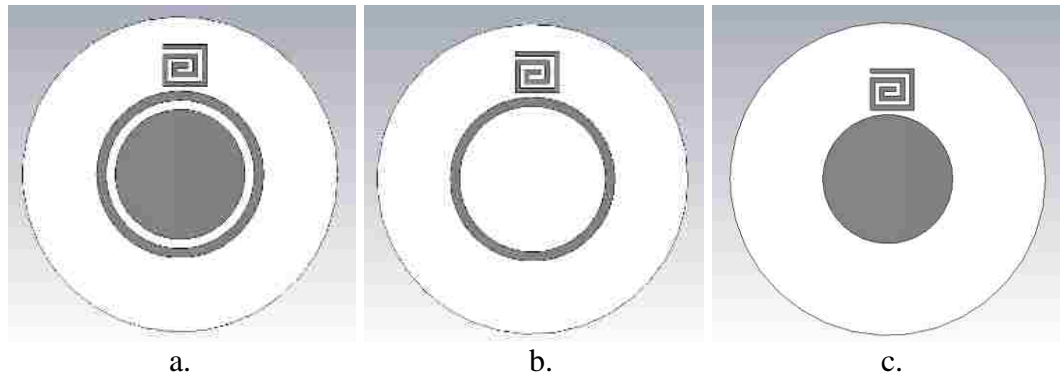
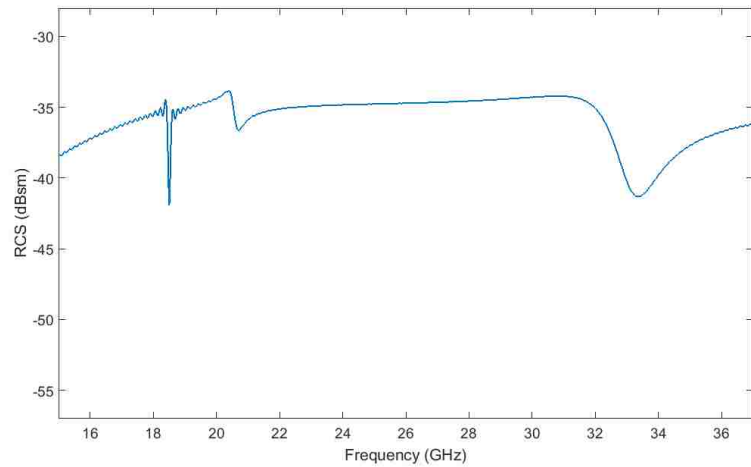


Figure 4.5. Tag configurations for demonstrating ring resonator dependence. a) Patch, ring, and spiral configuration. b) Ring and spiral configuration. c) Patch and spiral configuration.

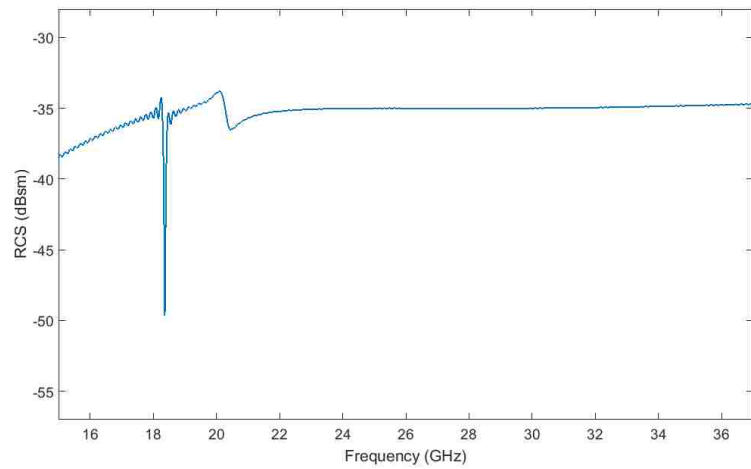
gone. Lastly, in Figure 4.6c only one notch at  $\sim 34$  GHz can be seen in the response despite there being a spiral resonator, as shown in Figure 4.5c, present in the tag configuration. These results demonstrate that the ring resonator is necessary when the spiral resonators are being used.

When the spiral resonator is present in this tag design, rotating the spiral around the ring resonators or in its position can result in different responses. Figure 4.7 shows the four different orientations a spiral can reside in, while Figure 4.8 shows the responses for these different orientations. As can be seen, there are four different responses depending on the orientation and these different responses could produce different binary codes.

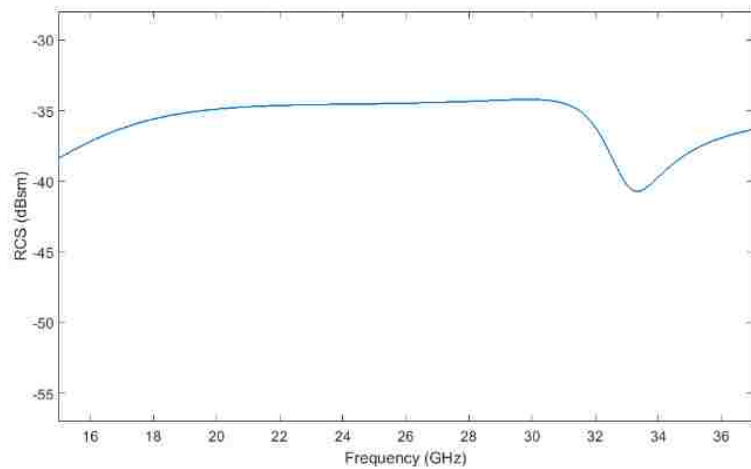
Different responses are also produced when the spiral is moved to different locations with the orientation maintained. Figure 4.9 provides a diagram for the different locations the spiral can reside in and in all cases Orientation 1 (Figure 4.8a) is used. Figure 4.10 shows the three different responses that can occur depending on the location. As can be seen, Locations 1 and 5, which are located directly across from each other,



a.



b.



c.

Figure 4.6. RCS vs frequency responses of tag configurations in Figure 4.5. a) Response for patch, ring, and spiral configuration. b) Response for ring and spiral configuration. c) Response for patch and spiral configuration.

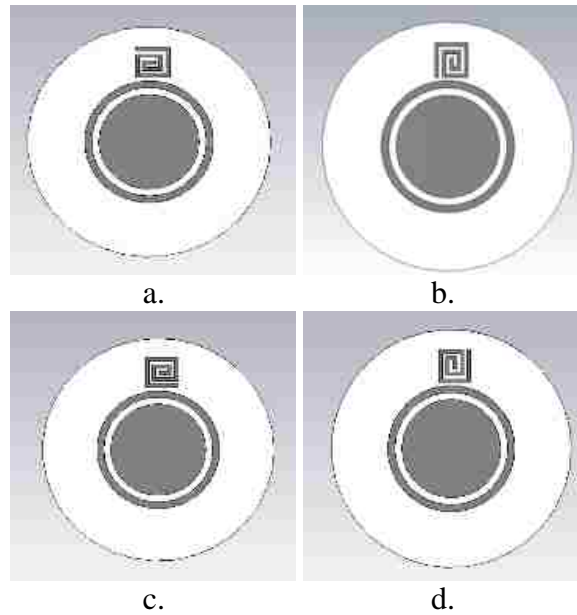
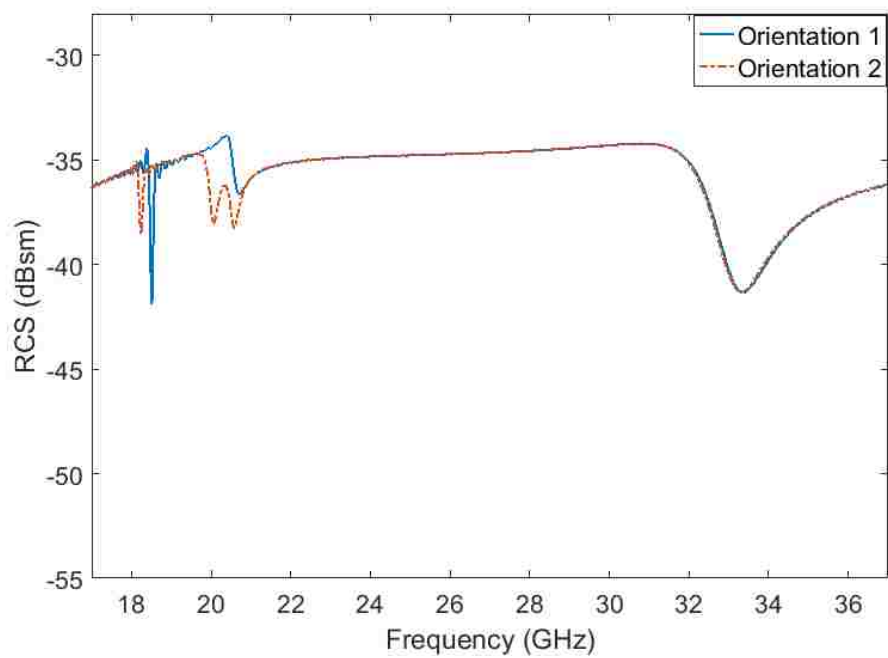
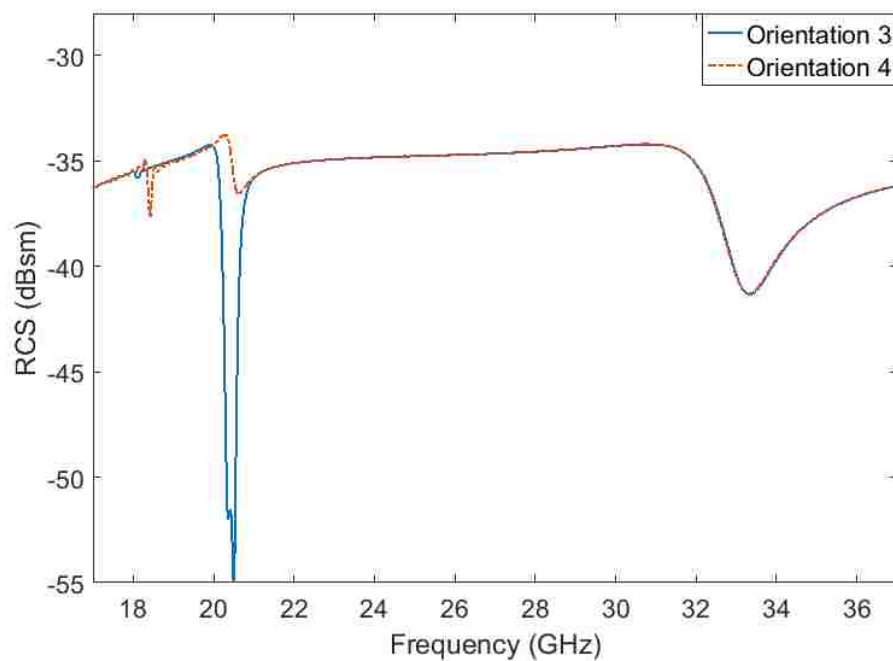


Figure 4.7. Orientations of spiral resonator. a) Orientation 1. b) Orientation 2. c) Orientation 3. d) Orientation 4.

produce the same response. Location 3 and 7 also produce the same response. Lastly, locations 2, 4, 6, and 8 produce the same response. Having multiple locations produce the same response is due to how the polarization of the interrogating wave (i.e., a linearly polarized plane-wave with the E-field along the  $x$ -direction as specified in Figure 4.1) interacts with the tag. These response dependencies on orientation and location in relation to the interrogating wave's polarization can make understanding how changes in tag configuration or feature geometry can affect the response. However, these dependencies can also be exploited to create greater response diversity and to potentially perform rotation sensing [75]. With this insight into how location and orientation affect the response of the tag, the remaining spiral resonator features of the tag were also designed.



a.



b.

Figure 4.8. RCS vs frequency responses for different orientations. a) Responses for orientations 1 and 2. b) Responses for orientations 3 and 4.

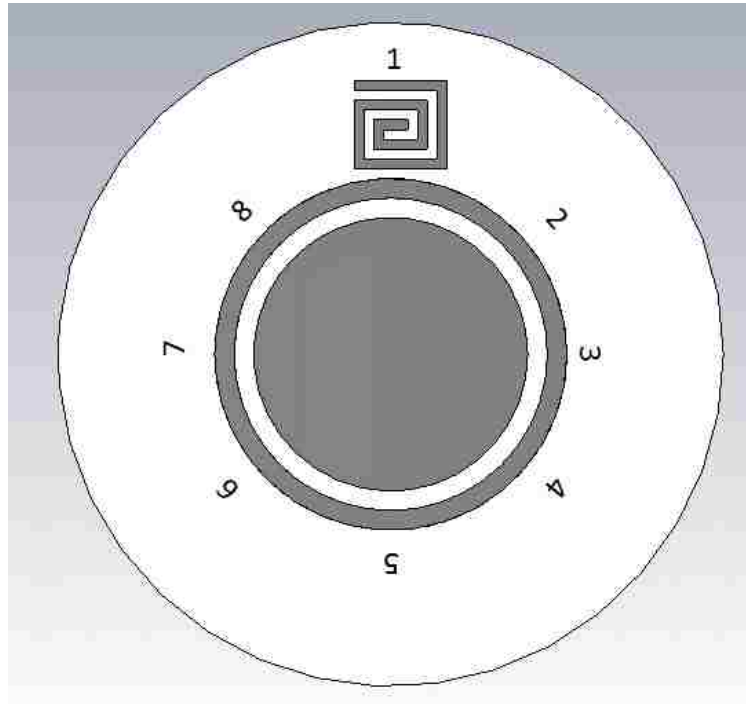
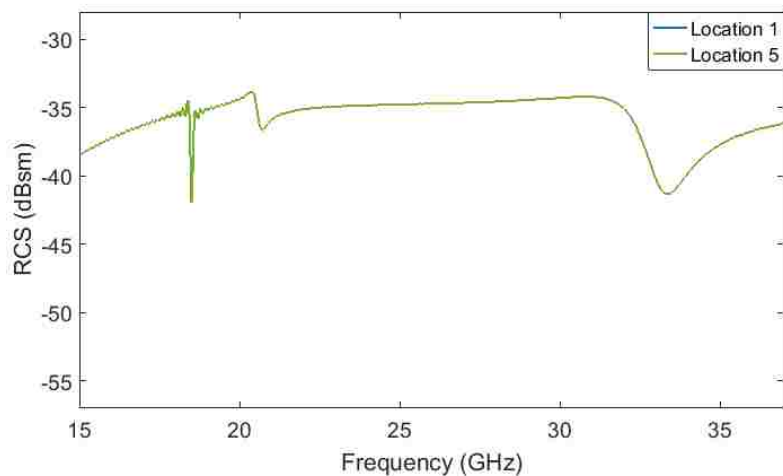


Figure 4.9. Diagram of spiral resonator location designations.

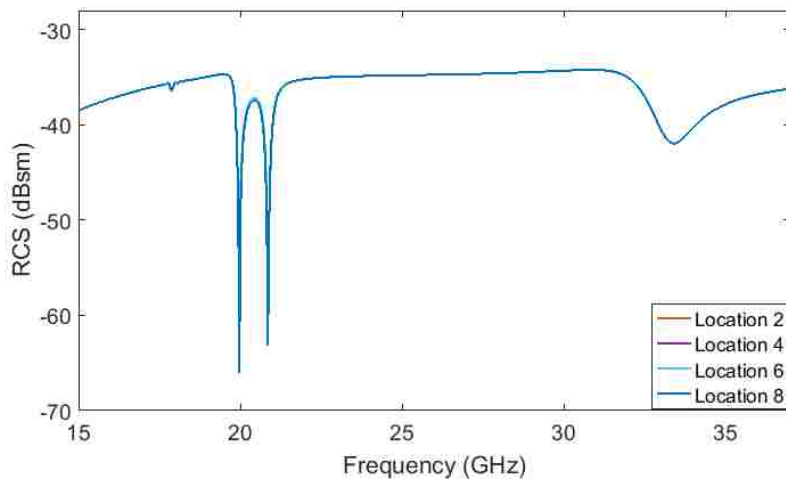
Four spiral and eight spiral configurations of the tag are shown in Figure 4.11. The four spiral configuration of the tag was designed first with the additional spirals being added so that there would be more notches between the start and stop bit notches in the response. The remaining four spirals were then designed to add additional notches among the existing one to increase the bit density of the tag. The responses of the four and eight spiral tag configurations are shown in Figure 4.12 and Figure 4.13, respectively.

This tag can achieve an extremely high bit density and coding capacity due to its small form factor and large number of notches. To illustrate this, Table 4.1 presents the bit density and the coding capacity of this tag for four different coding methods described

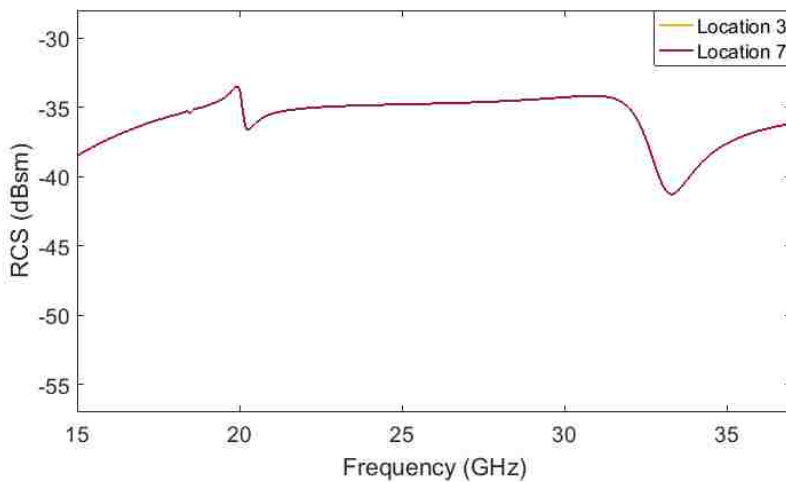




a.



b.



c.

Figure 4.10. RCS vs frequency responses for different spiral locations. a) Responses for spiral in locations 1 and 5. b) Responses for spiral in locations 2, 4, 6, and 8. c) Responses for spiral in locations 3 and 7.

in Section 1.2.1.2. In this table the coding capacity definition expressed in Equation (3) is used. As can be seen, both of these metrics vary widely depending on the coding method used. Thus, one needs to be sure to express metrics in the context of the coding method used to properly compare the merit of tags, as was discussed in Section 1.2.1.3.

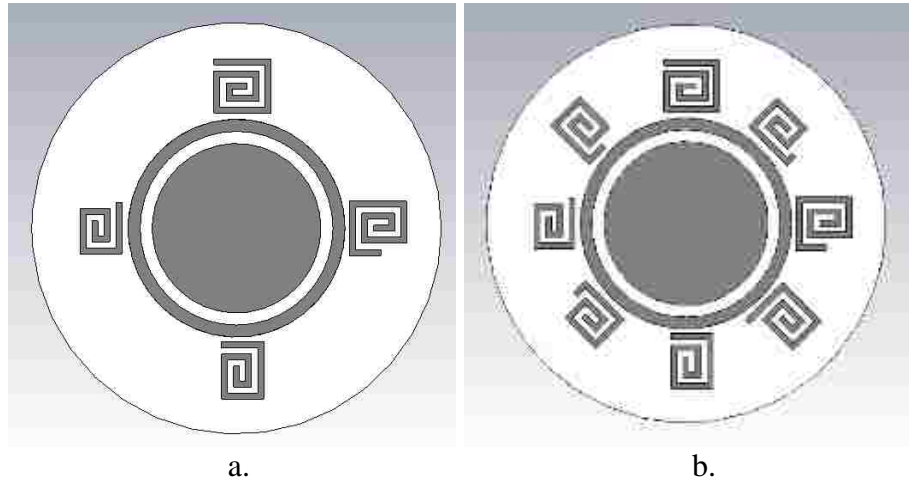


Figure 4.11. Configurations of tag design. a) Four spiral tag configuration. b) Eight spiral tag configuration.

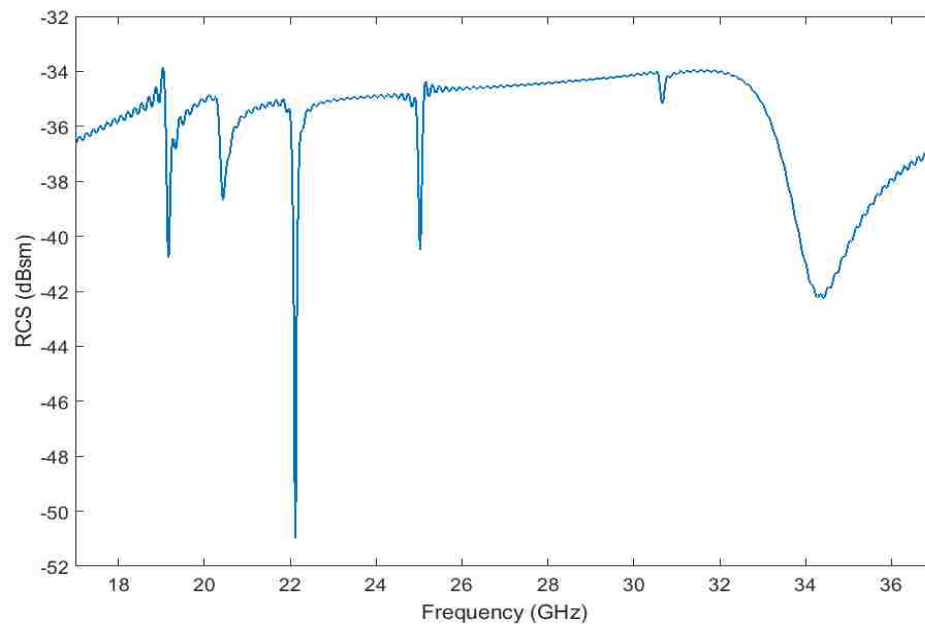


Figure 4.12. RCS vs frequency response of four spiral tag.

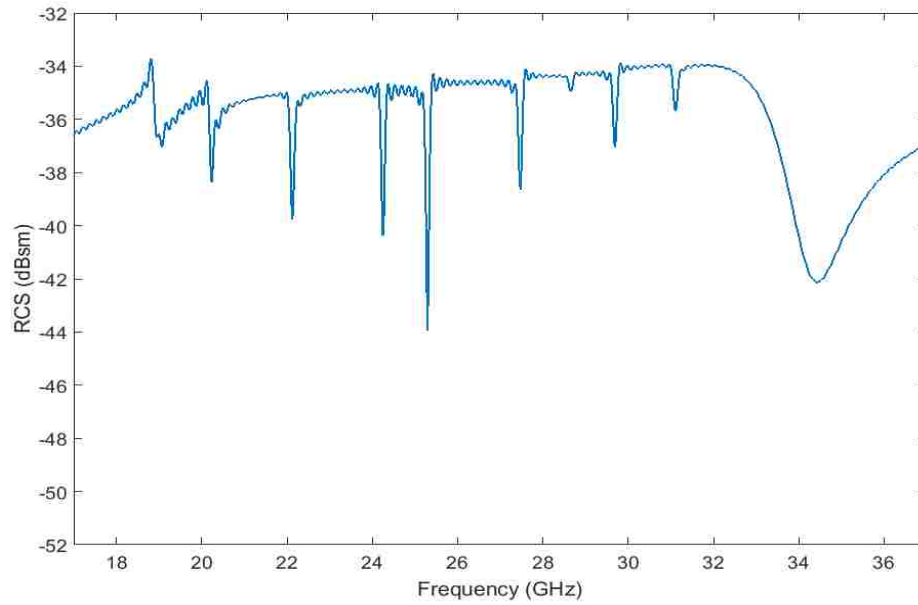


Figure 4.13. RCS vs frequency response of the eight spiral tag.

Table 4.1. Tag metrics for different coding methods.

Method	Bit Density (bits/cm <sup>2</sup> )	Coding Capacity
1	27.54	1024
2	27.54	1024
3	55.07	1048576
4	55.07	1048576

Due to this tag having a ground plane, it is less sensitive to the material it is placed on than tags that do not have a ground plane (i.e., that used for Figure 4.2), are. To provide evidence for this claim, simulations with the designed eight spiral tag on a dielectric slab were conducted. These simulations were done in the same way as those for Figure 4.2 were done and the results of the simulations are shown in Figure 4.14. As can be seen from Figure 4.14, the response does not shift down in frequency as much as the

results in Figure 4.2 did when the tag is placed on the dielectric slab. Another difference between these two cases is that in the case of the tag with the ground plane, there seems to be defined notches in the response for larger slab sizes. In summary, tags with ground planes are less sensitive to the materials they are pasted on, but the tradeoff for this is that manufacturing tags with ground planes tends to be more expensive because inkjet-printing is not as feasible for this type of tag.

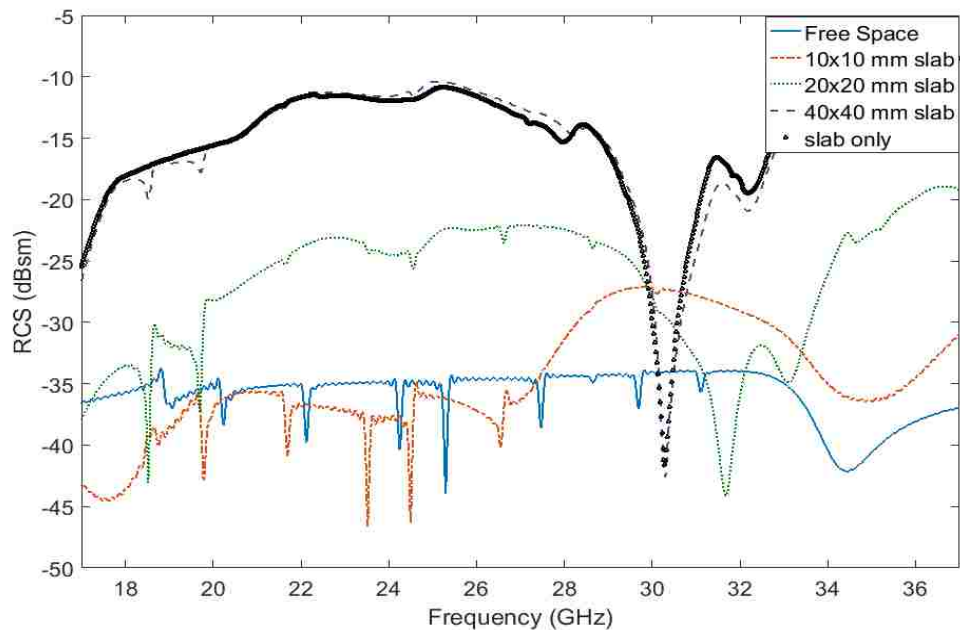


Figure 4.14. Effect on response when a tag with a ground plane is placed on a dielectric slab of varying sizes.

In making measurements of this tag, a wide variety of wideband antennas could be used to capture the entire response. Alternatively, less bandwidth could be used for certain applications like embedded materials characterization because as the material the tag is embedded in changes, new notches could shift into the interrogation bandwidth changing the code. In the cases simulated above, a linearly polarized plane-wave was

used and therefore, linearly polarized antennas would be sufficient for reading the tag. However, circularly polarized antennas could also possibly be used if they can capture both co-pole and cross-pole measurements. This could help overcome the alignment dependency of the tag and the reader antenna encountered in chipless RFID tag measurements for tags that are not orientation insensitive.

In order to adapt this tag's response to different applications in an informed manner, design guidelines are necessary. The subsequent section presents a collection of design guidelines for various types of resonators used and their complementary resonators (i.e., the type of resonators that is used when there is not a ground plane).

#### **4.4. DESIGN GUIDELINES**

As previously mentioned, design guidelines, which commonly take the form of equations, equivalent circuits, and graphs, are extremely useful for developing tag designs. These guidelines can be used to make modifications to tag resonator geometry in order to manipulate the tag's response in a controlled and purposeful manner.

Additionally, guidelines that compare different types of resonators, like those presented in [111], can be helpful when selecting which type or types of resonators to use in a tag design. Design guidelines are not prevalent among chipless RFID tag designs. However, they are prevalent in microwave filter designs [110, 112-117]. These filter-based guidelines can be used to understand basic trends of how the response of a resonator is affected by a change in geometry, but they cannot be directly applied to chipless RFID tag design. This is due to the resonators being fed in a different manner in filter applications than they are in backscatter frequency-based tags. Design guidelines are

presented here for resonators that are relevant to the tag design presented in Section 4.3. This includes circular slot resonators, ring resonators, and spiral resonators.

**4.4.1. Circular Slot Resonator Design Guidelines.** Circular slot resonators, similar to those used in Section 2, have been used for a few different tag designs [23, 56, 118-120]. However, in only one case are design guidelines presented and used to justify the choice of tag dimensions [118]. An example of circular slot resonators is shown in Figure 4.15. These resonators are orientation independent and do not have a ground plane. When a ground plane is added, the conductive structure that makes the circular slot resonators turns into a set of ring resonators. Circular slot resonators are characterized by their radius and width (i.e., these are the primary parameters that affect the resonance frequency of the resonator). Other factors, such as the substrate material, conductor thickness, conductor width between slots, conductivity of the conductor, idealness of the circular shape, and proximity to other circular slot resonators can also affect the resonance frequency of the resonator [23, 37, 56, 57, 64].

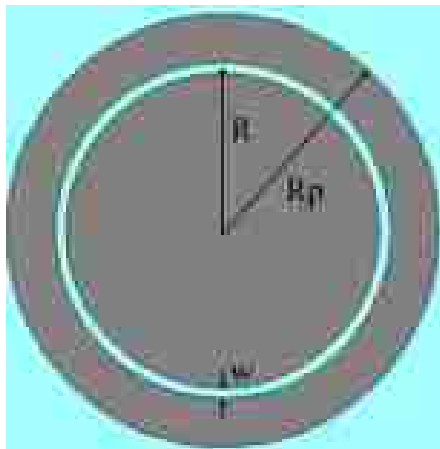


Figure 4.15. Circular slot resonator [118].

In [118], the following equation is provided for the resonance frequency of a circular slot resonator:

$$f_r = \frac{c}{2\pi R_i} \sqrt{\frac{2}{\epsilon_{eff} + 1}} \quad (8)$$

In this equation,  $c$ , is the speed of light and  $\epsilon_{eff}$  is the effective permittivity of the substrate. It is not clear, however, if  $R_i$  is the inner, center, or outer radius of the slot resonator and the width of the slot is not taken into consideration. Due to how uncomprehensive this equation is and the lack of other design guidelines in literature, simulations were performed in CST Microwave Studio®. Figure 4.16 shows the slot resonator used for the simulations and the nomenclature used in the subsequent figures. In Figure 4.16, the substrate disk is made of Taconic TLX-9 ( $\epsilon_r' = 2.5, \tan\delta = 0.0019$ ) and its dimensions are 6.8 mm in diameter and 0.5 mm thick. The conductor is PEC and is 0.035 mm thick, which is the thickness of 1 oz. copper. For these simulations, a monostatic radar simulation setup with plane-wave irradiation and RCS probe interrogation were used in the 14 – 40 GHz frequency range.

First, the gap was set at 0.1 mm and the ring thickness was set to 0.1 mm. This gap width was chosen since it was found to be the minimum gap width that will produce a resonance for this simulation. The inner radius of the slot was then increased while the gap width and ring thickness were maintained (see Figure 4.16). The effect of increasing the inner radius of the circular slot resonator on the resonance frequency is shown in Figure 4.17. As can be seen, as the radius is increased the resonance frequency decreases. This is consistent with what you would expect from Equation (8).

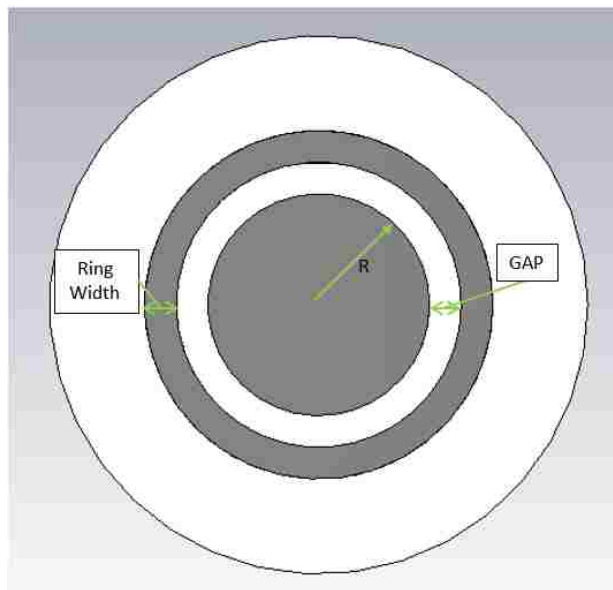


Figure 4.16. Slot resonator annotated with simulation parameters.

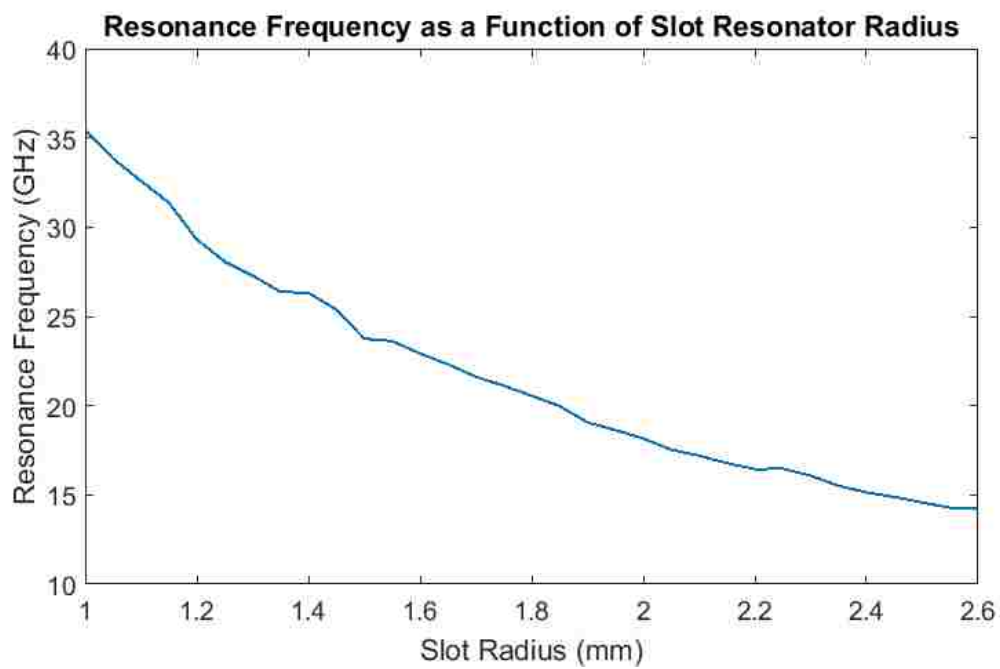


Figure 4.17. Effect of radius on resonance frequency of circular slot resonator.



Next, the gap was again set at 0.1 mm and the ring width was increased rather than the inner radius. The inner radius was maintained at 1.4 mm, which corresponds to a resonance frequency of  $\sim 26.4$  GHz. This radius was chosen because it produces a resonance frequency that is in the middle of the interrogation bandwidth of 14 – 40 GHz, allowing for both increases and decreases in the resonance frequency to be examined as different parameters are manipulated. It was seen that increasing the thickness of the ring with constant gap width and slot radius tends to increase the resonance frequency. This is illustrated in Figures 4.18.

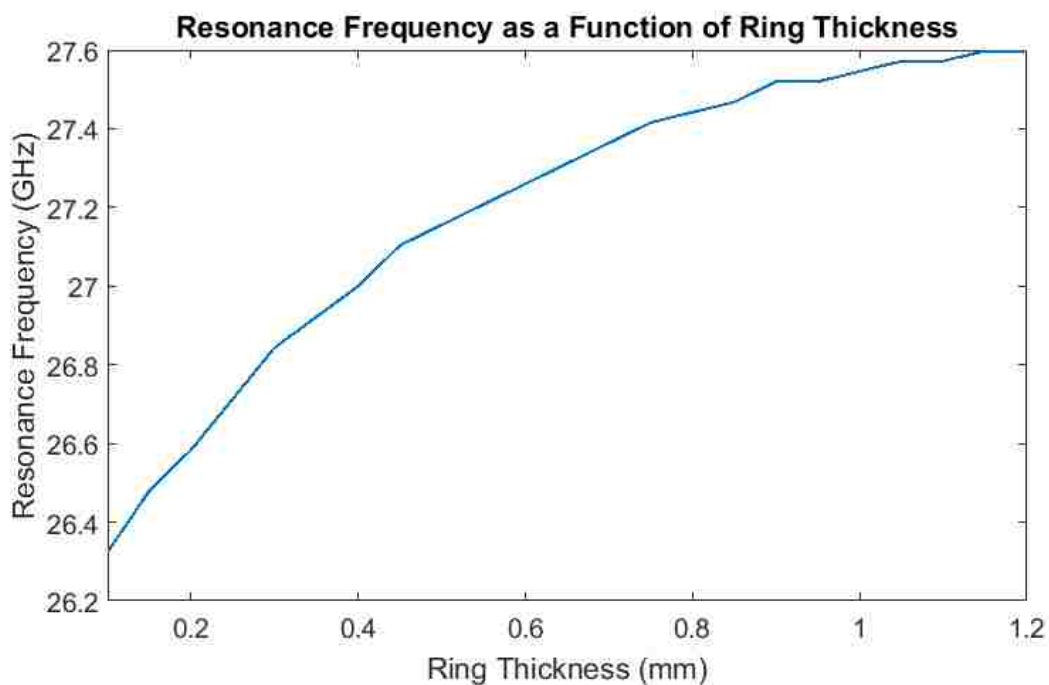


Figure 4.18. Effect of ring width on magnitude of slot resonator resonance.

The next simulation involved increasing the gap width for a variety of ring thicknesses. The results of these simulations are shown in Figures 4.19 and 4.20. Figure

4.19 shows the dependency of the resonant frequency on the ring thickness that Figure 4.18 did while also showing how increasing the gap tends to decrease the resonance frequency. Figure 4.20 represents this data in a different manner. In using these design guidelines, one can select a desired ring width and see how varying the gap will affect the resonance frequency by using Figure 4.19 or vice versa by using Figure 4.20. This allows the tag designer to easily work within their requirements. The demonstrated dependence on gap width and ring width illustrates how Equation (8) is not sufficient for describing the resonance behaviors of circular slot resonators.

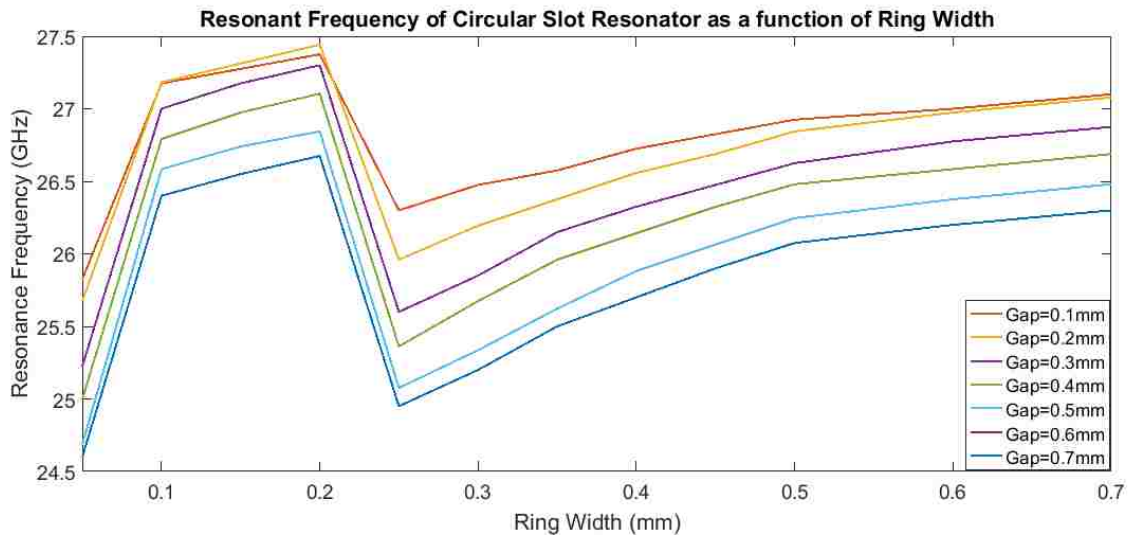


Figure 4.19. Effect of gap and ring width on resonance frequency.

Circular slot resonators can also couple to each other, affecting each other's resonance frequencies. This phenomenon has been briefly mentioned in [23], but has not been characterized. To this end, simulations were performed to see the effect of one circular slot resonator on another. Figure 4.21 shows the tag used in these simulations.

This tag has the same dimensions and substrate characteristics as the tag in Figure 4.16, but two slot resonators are present instead of one. The innermost slot is referred to as slot 1 and the outermost slot is referred to as slot 2.

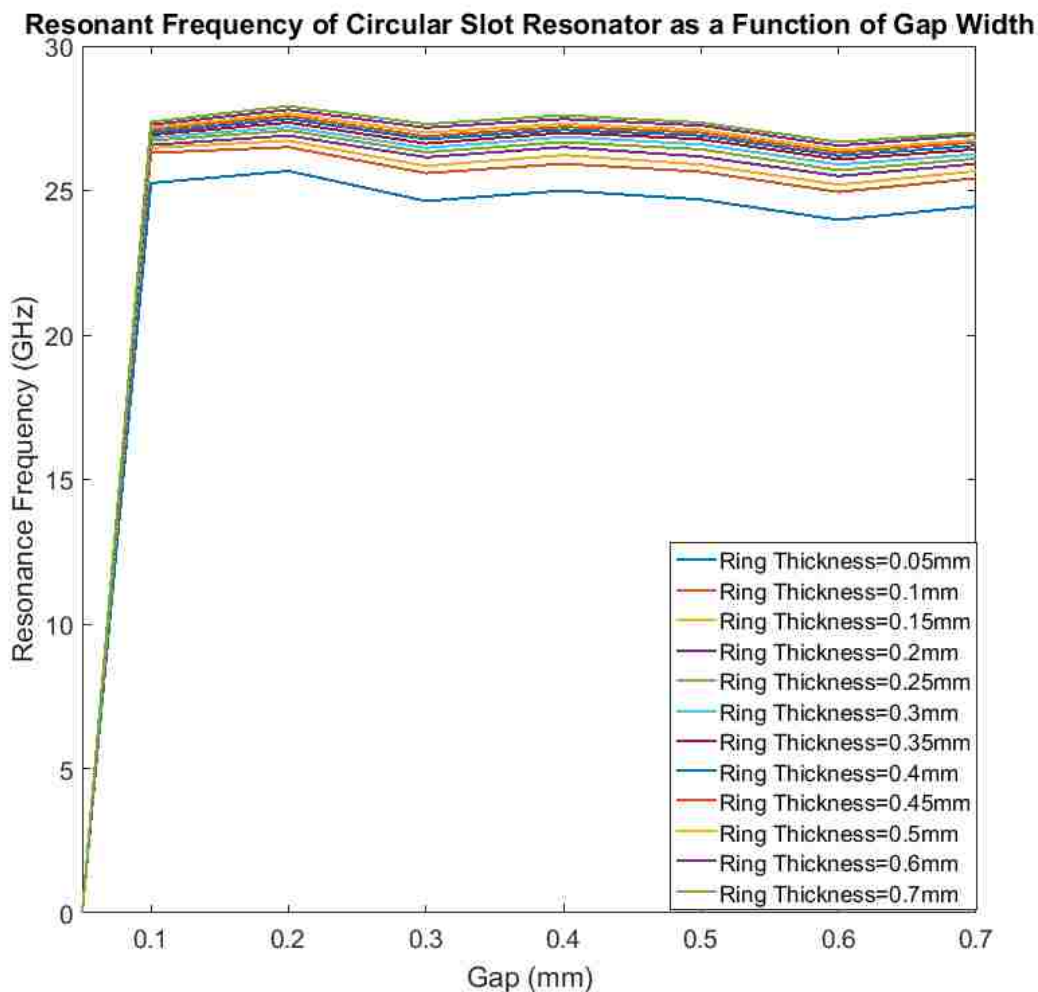


Figure 4.20. Effect of gap and ring width on resonance frequency.

In the first case, the dimensions of slot 1 were chosen to be as space efficient as possible based on the results in Figures 4.19 and 4.20. The gap was chosen to be 0.1 mm and the ring thickness was also chosen to be 0.1mm. This combination corresponds to a

resonance frequency of  $\sim 27.2$  GHz when only one slot is present. The gap and ring thickness for slot 2 were then increased. Figure 4.22 shows how the resonance frequency of slot 2 changes as the gap and ring width of slot 2 are manipulated. It can be seen from Figure 4.22 that the resonance frequency change follows a similar trend as to when there is only one slot resonator present.

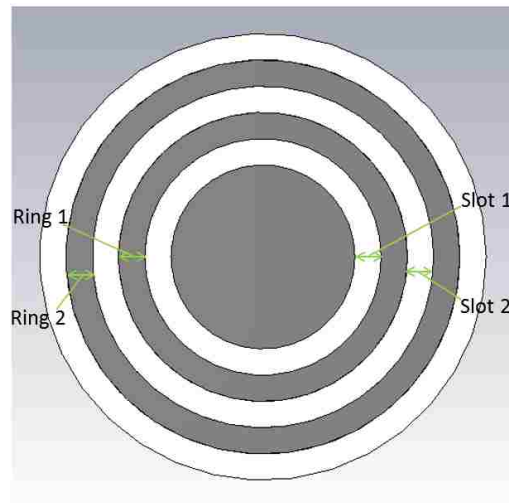


Figure 4.21. Annotated tag used in multi-slot simulations.

Next, the effect of changing slot 2 on slot 1 was examined. Figure 4.23 shows how the resonance frequency of slot 1 changes as these slot 2 parameters are manipulated. This shows up to 1 GHz of variation in resonance frequency of a slot resonator, slot 1, which is not changing in geometry due to changes in another slot resonator. This shows that coupling between slot resonators cannot be ignored when designing tags to have specific responses.

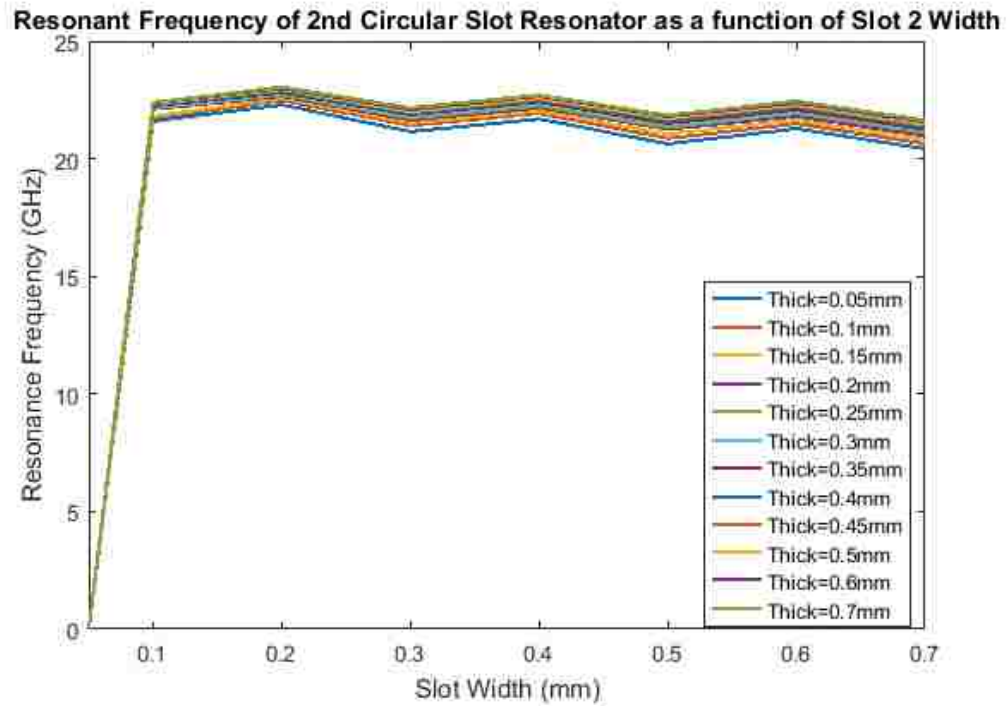


Figure 4.22. Effect of slot 2 gap and ring width on resonance frequency of slot 2.

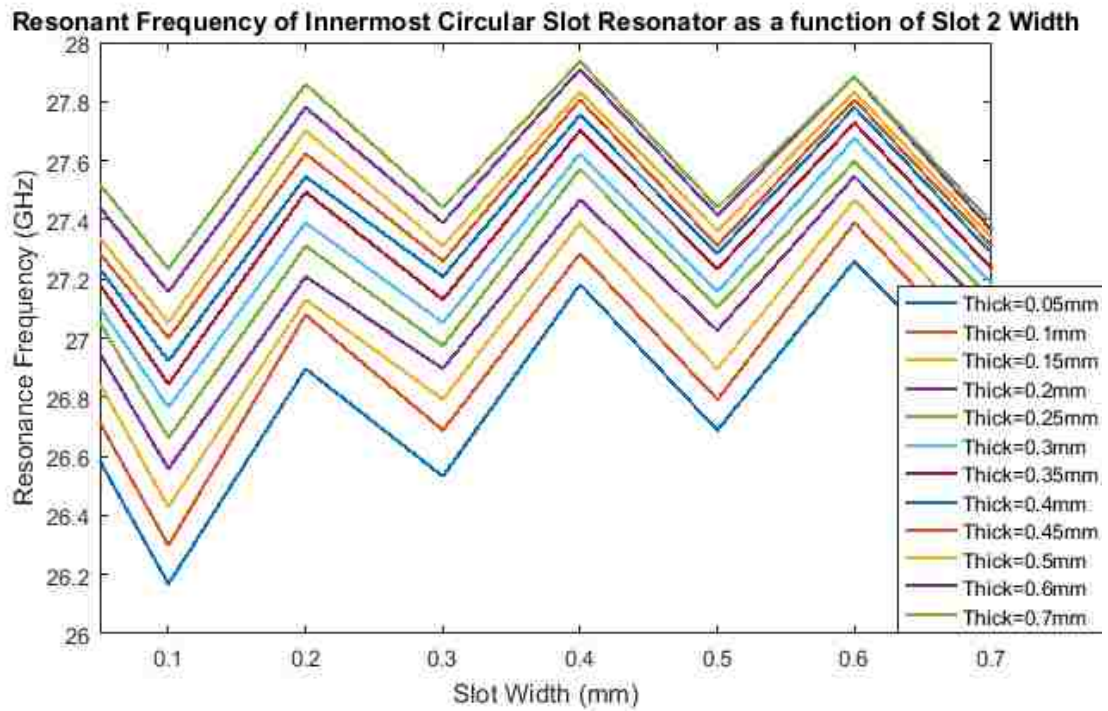


Figure 4.23. Effect of slot 2 gap and ring width on slot 1 resonance frequency.

Typically, eight or more concentric circular slot resonators are used in tag designs, meaning that there are a lot of interactions between slot resonators to consider. However, the gap and ring thickness of each resonator are usually constant amongst all of the resonators which can simplify analysis. In general, if the radius of the slot is increased, the resonance frequency will decrease. For a given radius and ring width if the gap is increased the resonance frequency will also decrease. Lastly, for a given radius and gap, if the ring width is increased, the resonance frequency will increase. All of these trends needs to be considered along with the effects of resonator interaction when designing tags with circular slot resonators.

**4.4.2. Ring Resonator Design Guidelines.** Ring resonators have also been frequently used in chipless RFID tag designs [25]. These resonators require a ground plane and are often used in concentric configurations to save space. The parameters that characterize a ring resonator are its radius and its width. An annotated ring resonator is shown in Figure 4.24. This resonator is also used in the tag presented in Section 4.3 to set the *start* bit of the coded response.

In terms of design guidelines, [25] presents the following equation:

$$f_r = \frac{c}{2\pi R[0.965+19.2R-1372R^2]\sqrt{\epsilon_{eff}}} \quad (9)$$

In Equation (9),  $R$  is the mean radius of the ring resonator. This is an empirical equation, which has an experimental basis, and is considered valid for  $R$ 's in the range of 4 to 9 mm and a ring width of 0.5 mm. This equation is derived from the equivalent circuit of [121] shown in Figure 4.25 and it does not take into account the width of the ring or the interactions between ring resonators.



Figure 4.24. Ring resonator diagram.

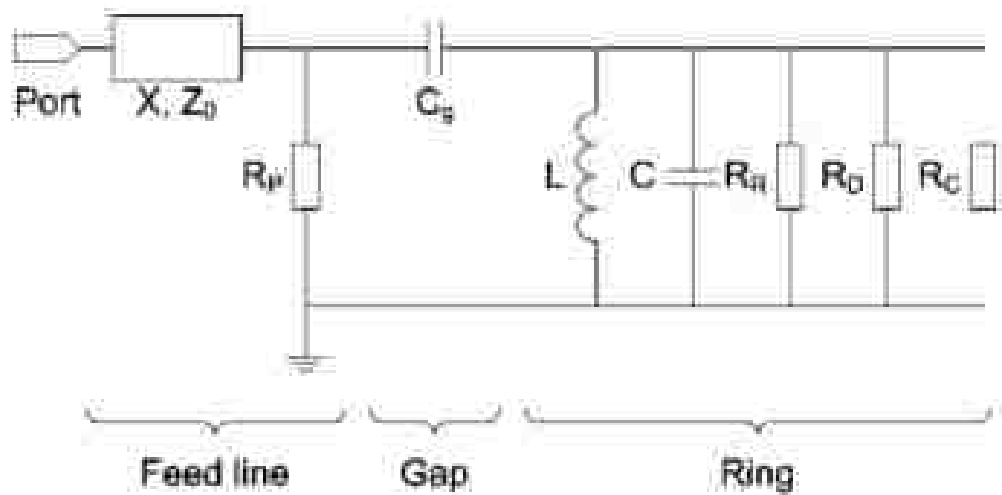


Figure 4.25. Ring resonator equivalent circuit of [121] for microwave filters.

In Figure 4.25, the ring portion of the equivalent circuit is relevant to the backscatter-based chipless RFID tags being considered here. In the ring portion of the

circuit, the three resistances correspond to radiation, dielectric, and conductor losses. The inductance and capacitance,  $L$  and  $C$ , are chosen within limits based on expected Q-factor so that the resonance frequency of the circuit is that of the ring resonator. The transmission line equations on which Figure 4.25 is based on can be used to calculate the resonance frequency of the ring resonator and the circuit components can be assigned values. Equation (10), shown below, can be used for this purpose:

$$f_r = \frac{c}{l\sqrt{\epsilon_{eff}(f)}} \quad (10)$$

In Equation (10),  $l$  is the mean circumference of the ring [121]. This equation and therefore the equivalent circuit above do not take into account the width of the ring or the interactions between concentric ring resonators. Due to these limitations, simulations were again conducted to characterize ring resonator behavior for changes in a variety of parameters.

First, the ring thickness was set at 0.1 mm and the mean radius was increased from 1 mm to 3 mm. Figure 4.26 shows the effect of change in the radius on the resonance frequency of the ring resonator. As can be seen, as the radius increases, the resonance frequency decreases. This aligns with what one would expect from both Equation (9) and Equation (10). However, as the radius increases the depth of the notch tends to decrease for a given thickness, as illustrated in Figure 4.27.

Next, the radius of the ring resonator was maintained at various values from 1 mm to 1.3 mm while the ring thickness was increased. As the thickness is increased from 0.1 mm to 0.5 mm, Figure 4.28 shows that the resonance frequency tends to decrease slightly (average decrease of 440 MHz over the plotted ring thickness range). However, as the



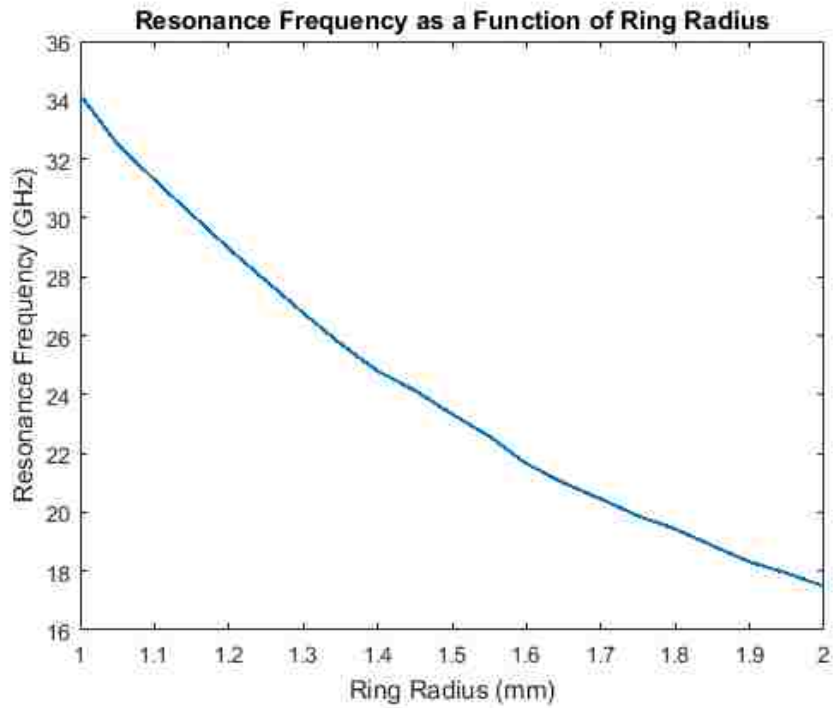


Figure 4.26. Effect of radius on resonance frequency of ring resonator.

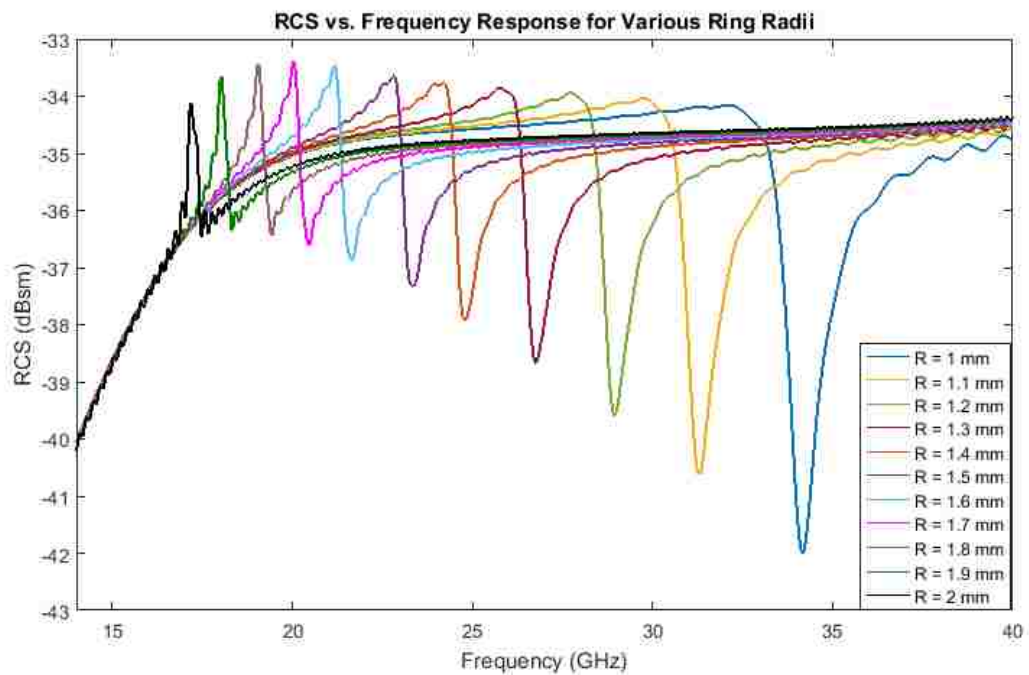


Figure 4.27. Effect of radius on depth of notch.

radius gets larger, it the resonance frequency decreases less as thickness increases (i.e., the slope of the line gets shallower as the radius increases). While this effect is small in comparison to that of changing the radius of the ring resonator, it can still produce changes in the expected resonance frequency. Therefore, Equations (9) and (10) are not sufficient for characterizing the behavior of a ring resonator.

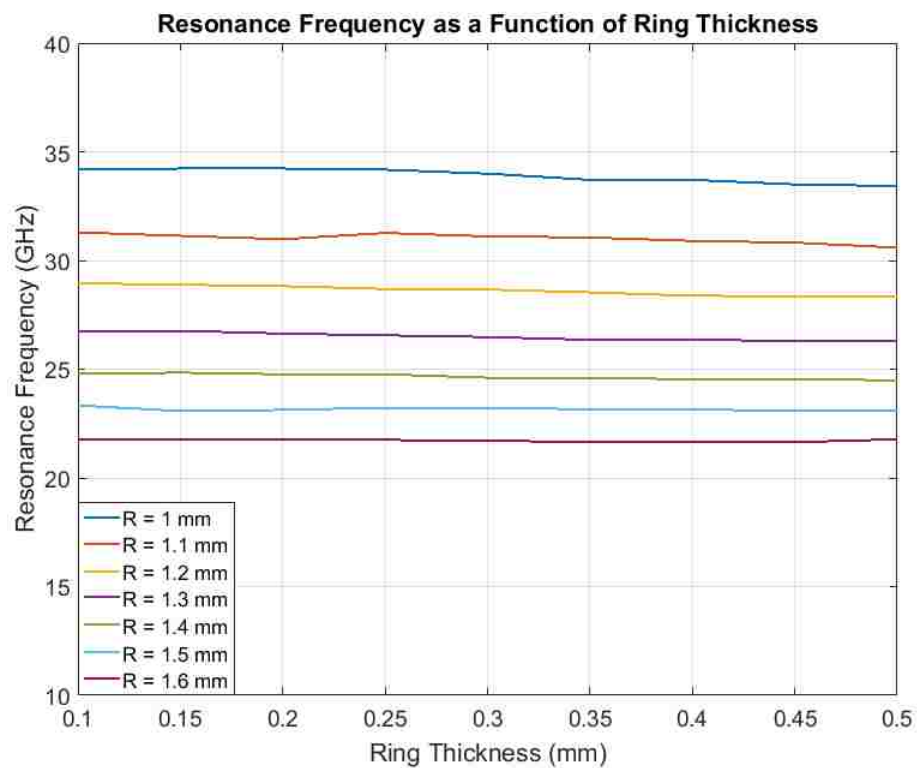
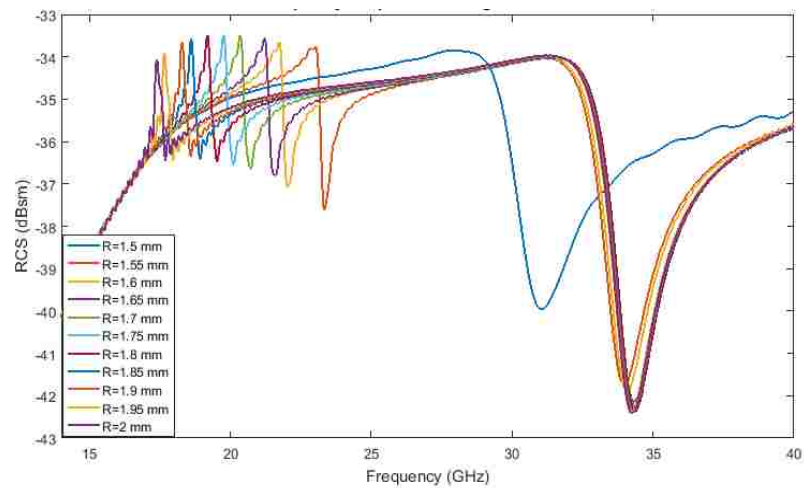


Figure 4.28. Effect of ring thickness on resonance frequency of ring resonator.

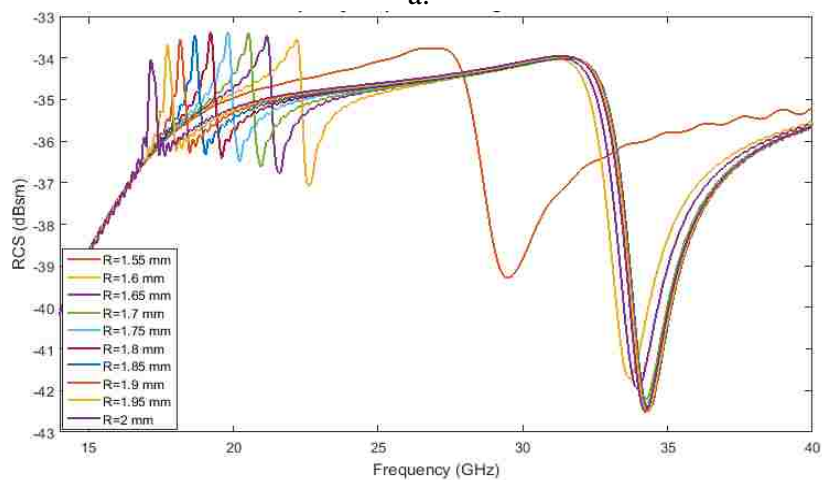
As the ring resonator is used with a circular patch in the tag presented above (see Figure 4.3), next the effects of radius and ring thickness were examined together with the patch present. The patch was maintained with a radius of 1.4 mm as this is the radius in the full spiral tag design. Then, for various mean radii of the ring, the thickness was

increased from 0.1 mm to 0.3 mm. The results of these simulations are shown in Figure 4.29. In Figure 4.29a, the result for  $R = 1.5$  mm has the resonance associated with the patch shifted up in frequency and no resonance associated with the ring, despite the ring and patch not being joined together. When the distance between the ring and patch is increased (i.e., the radius of the ring is increased), the resonance associated with the ring appears in the responses. For various radii equal to and greater than 1.55 mm, the resonance associated with the patch tends to shift down in frequency slightly as the radius is increased. This means that there is some interaction between the ring and patch. By comparing Figure 4.29 to Figure 4.28, it can also be seen that for the same ring thickness and radius, the presence of the patch affects the resonance frequency of the ring resonator, as well. In Figure 4.29b,  $R=1.55$  mm is the first radius used because a radius of 1.5 mm causes the ring and patch to be conjoined. Similarly, the first radius in Figure 4.29c used is 1.6 mm. The results in Figures 4.29b and 4.29c follow similar trends as that of Figure 4.29a. From these results, it can be concluded that the interaction between the patch and the ring resonator cannot be discounted when attempting to engineer a specific response.

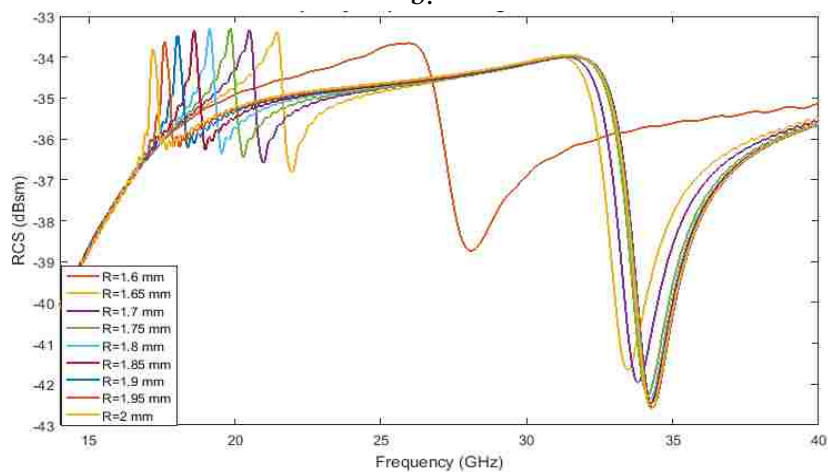
Lastly, the relationship between ring resonator and circular slot resonators was explored since a slot resonator based tag placed on a metallic surface could act like a tag with ring resonators. To this end, the tag shown in Figure 4.30 was simulated with and without a ground plane. This tag, which is the same as that shown in Figure 4.3, has a patch of radius 1.4 mm and a ring of mean radius 1.7 mm and thickness 0.2 mm. This corresponds to a slot resonator with a gap width of 0.2 mm and a ring thickness of 0.2 mm when the ground plane of the tag is removed. Figure 4.31 shows the RCS vs.



a.



b.



c.

Figure 4.29. Effect of ring radius and thickness on resonance frequency with patch. a) RCS vs. frequency responses for ring thickness of 0.1 mm. b) RCS vs frequency responses for ring thickness of 0.2 mm. c) RCS vs frequency responses for ring thickness of 0.3 mm.

frequency response for these two tag configurations. As can be seen, the responses for these two configurations are dramatically different. Thus, this relationship between tags having a ground plane and not having a ground plane is also important to understand.

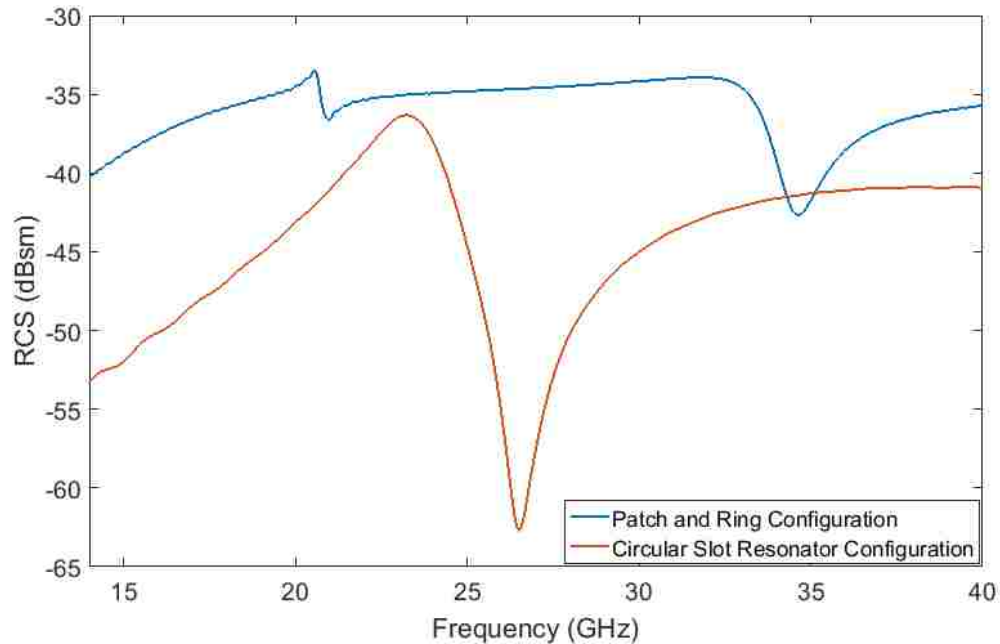


Figure 4.31. RCS vs. frequency response for tag with and without ground plane.

**4.4.3. Spiral Resonator Design Guidelines.** Spiral resonators have been used in many Tx/Rx based tags, like the one shown in Figure 1.1, as well as in microwave filters [18, 19, 110, 122, 123]. This has led to design guidelines in the form of equivalent circuits, a transmission line model, and design curves. The principle behind operation of spiral resonators is that by changing the effective inductance and capacitance of the spiral resonator, the resonance frequency is changed. Longer spiral resonators have higher effective inductance and capacitance and therefore have a lower resonance frequency.

Other factors, though, like the width of the spiral legs and the spacing between the spiral legs, can also play a role in determining the resonance characteristics of the of the spiral resonator. The equivalent circuit from [123] is shown in Figure 4.32. In this equivalent

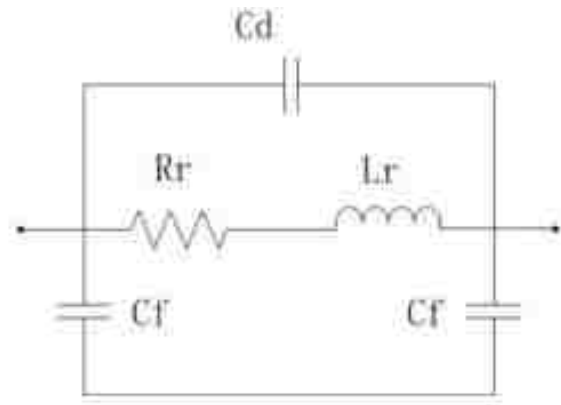


Figure 4.32. Equivalent circuit for spiral resonator from [123].

circuit,  $C_d$  refers to the distributed capacitance,  $C_f$  refers to the dispersion capacitance,  $L_r$  to the distributed inductance, and  $R_r$  to the resistance of the spiral. The resonance frequency can then be determined by Equation (11) from [123]:

$$f_r = \frac{1}{2\pi} \sqrt{\frac{1}{L_r C_r}} \quad (11)$$

In this equation,  $C_r$  is the sum of the distributed and dispersion capacitances. [123] does not, however, provide a means for extracting the circuit values from the geometry of the spiral resonator, which is needed in order to use this circuit as a design guideline. Thus, there is not much engineering intuition to be gain from this equivalent circuit.

Another equivalent circuit model as well as a transmission line model are provided in [12] for the case of a spiral resonator coupled to a microstrip line as is the

case in many Tx/Rx based tags. The equivalent circuit model, originally presented in [124], is shown in Figure 4.33. In Figure 4.33,  $C_r$  and  $L_r$  are the distributed capacitance and inductance, respectively, while  $R_r$  is the resistive loss of the element. Using techniques from [125], [12] presents equations for finding the distributed capacitance based on the charge distribution on the spiral resonator. This charge distribution can be determined using the method of moments or from an EM simulator like CST Microwave Studio®. The distributed inductance of the spiral resonator can then be found using an approach presented in [126]. By combining the equations and approaches in [125] and [126], the values of the circuit in Figure 4.33 can be found and related to the geometry of the spiral resonator. This allows this circuit and its associated equations to be used as design guidelines.

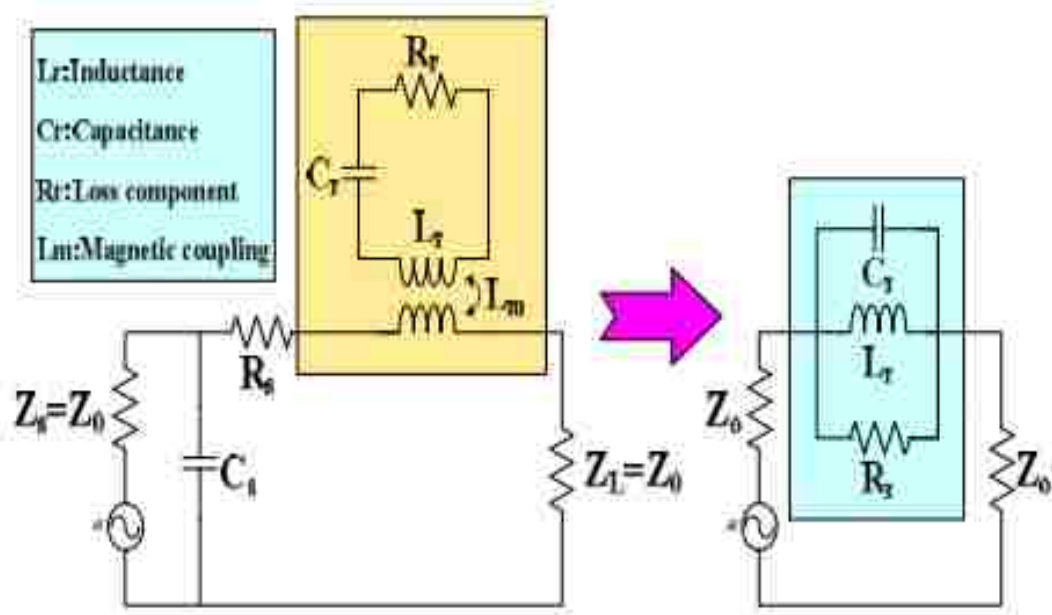


Figure 4.33. Equivalent circuit for spiral resonator coupled to microstrip line [124].

As previously mentioned, [12] also presents a transmission line model of a spiral resonator coupled to a microstrip line. This model was developed to address the issue of the above equivalent circuits not allowing for bends in the microstrip line of Tx/Rx tags, which provide for greater bit density in the tag design since more spiral resonators can then be placed along the microstrip line. The designations used for the transmission line model are shown in Figure 4.34 and the model itself is shown in Figure 4.35. According to the author of [12], by using this model optimization can be done more quickly than is allowed by full wave EM simulators.

In terms of design curves, [110] presents a set for microwave filters that operate in the 0.5 to 3.5 GHz range. The layout of these resonators is shown in Figure 4.36. These design curves cover the effect of changing width ( $w$ ), gap ( $g$ ), length ( $L$ ), and distance between spirals ( $s$ ). Figure 4.37 shows an annotated diagram of a spiral resonator that indicates these geometric parameters, while Figure 4.38 shows an example of one of these design curves from [110]. These design curves cannot be applied directly to the tag under consideration, however, because of the different feeding mechanism they use and their different frequency range of operation.

Another set of design curves for a Tx/Rx based tag is presented in [12]. These design curves are produced for the 0 to 3 GHz range and cover the effects of length, width, gap, spacing, and distance from the microstrip line. These design curves again are for a different frequency range and feeding mechanism than is used in the tag in Section 4.3. This means that these design guidelines again cannot be directly applied to the tag at hand. To this end, simulations were conducted to show how one should expect spiral



resonators to behave in a backscatter based tag design where the spiral resonators have signal coupled into them through a ring resonator.

First a spiral was constructed with orientation 3 in position 1 (see Section 4.3). This spiral resonator has a length of 0.9 mm, a width of 0.05 mm, and a gap of 0.05 mm. It is located 0.1 mm away from the ring resonator. The effect of length was examined first. Length was removed from the spiral resonator from both the inside and the outside.

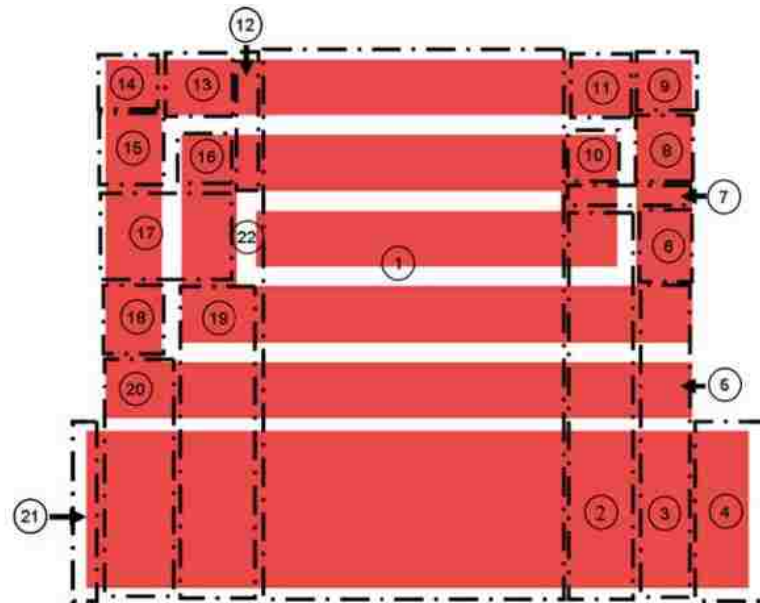


Figure 4.34. Section designations for transmission line model [12].

Figure 4.39 shows the effect of removing length from the outside while Figure 4.40 shows the effect of removing length from the inside. By comparing the figures, it can be seen that there is a similar trend among them (i.e., as length is removed the resonance frequency increases), however, when length from the outside is removed, the coupling between the spiral resonator and the ring resonator is changed which results in some

cases where no resonance is seen due to the spiral resonator. One of these cases is shown in Figure 4.41 where 1.5 mm of spiral length has been removed from the outside of the spiral. Another trend to note from Figure 4.40 is that as the amount of length is increased, the depth of the notch tends to decrease until it becomes not distinguishable, like the case in Figure 4.41b.

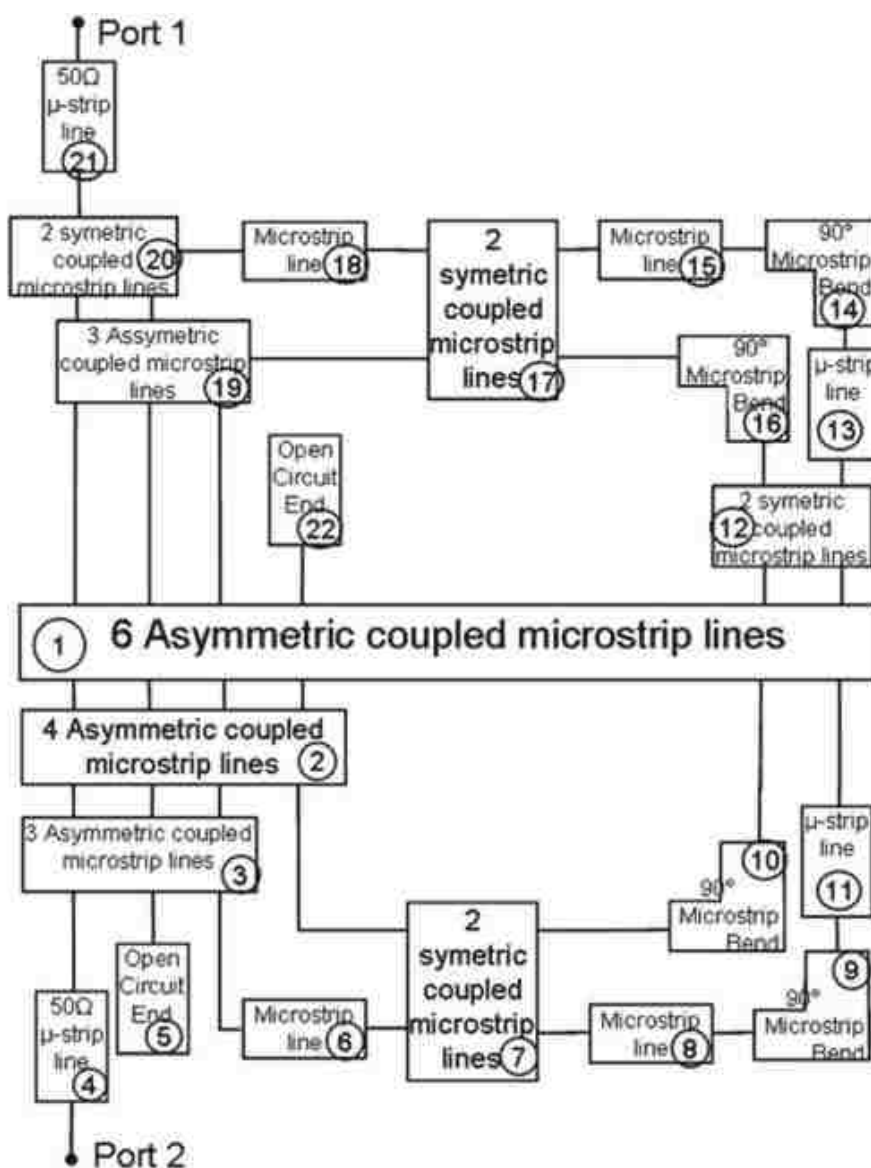
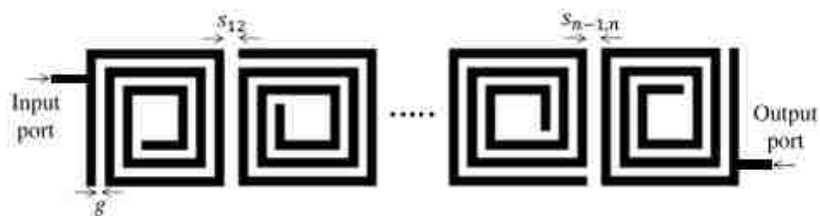


Figure 4.35. Transmission line model for spiral resonator coupled to microstrip [12].



4.36. Microwave filter layout from [110].

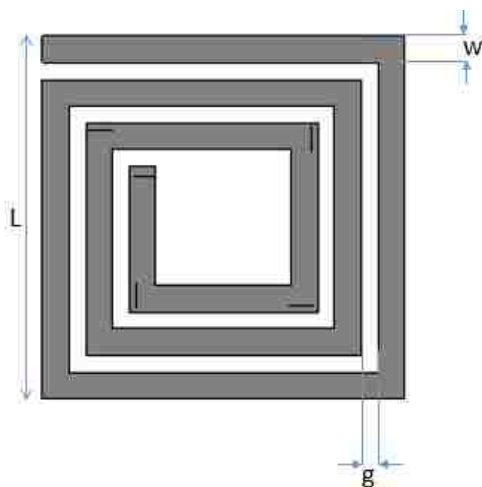


Figure 4.37. Diagram of spiral resonator.

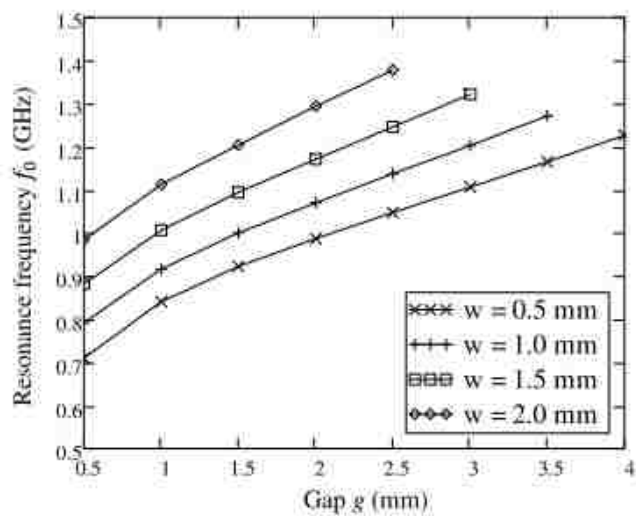
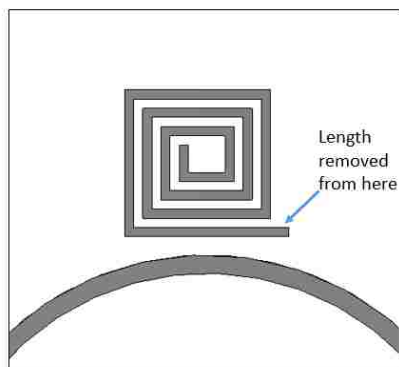
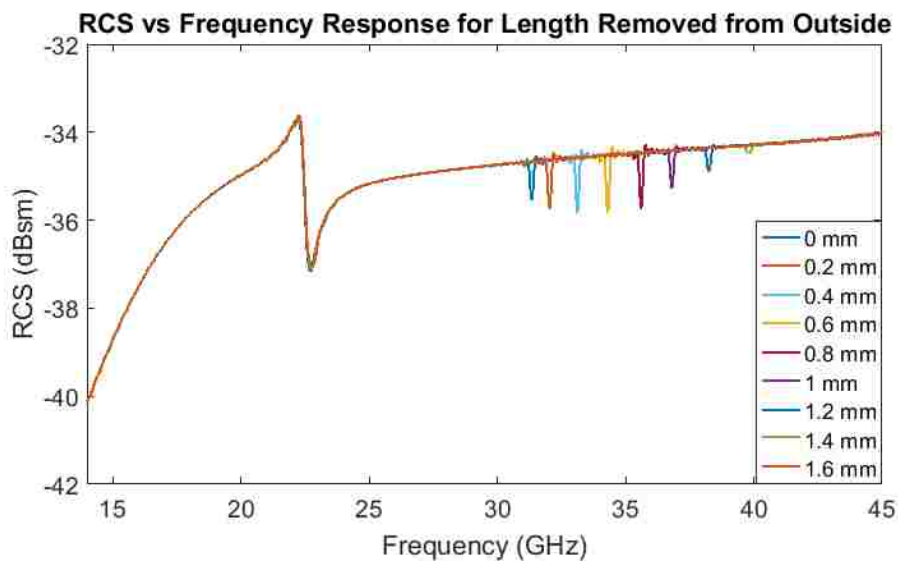


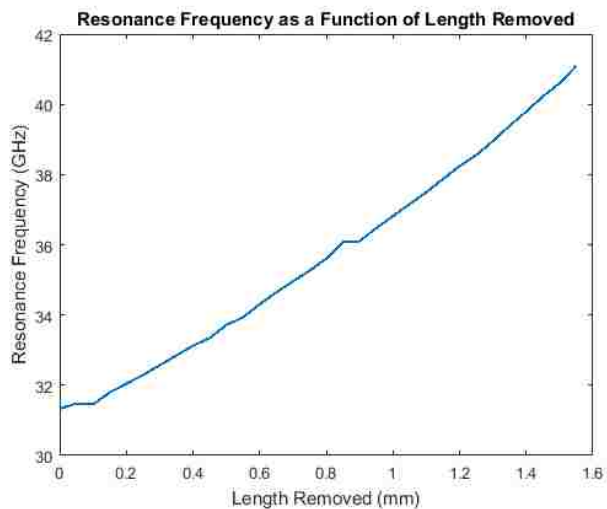
Figure 4.38. Example design curve from [110].



a.

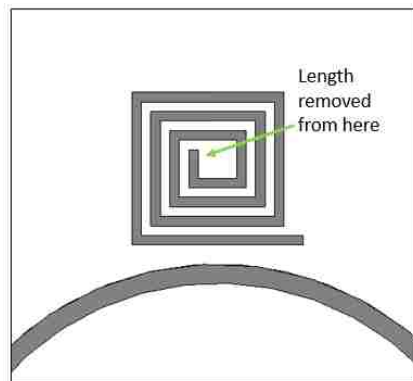


b.

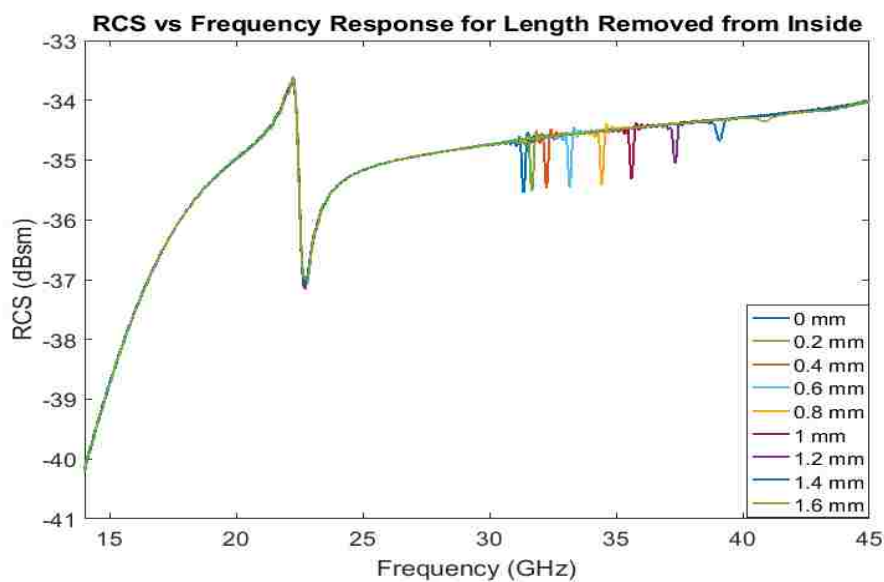


c.

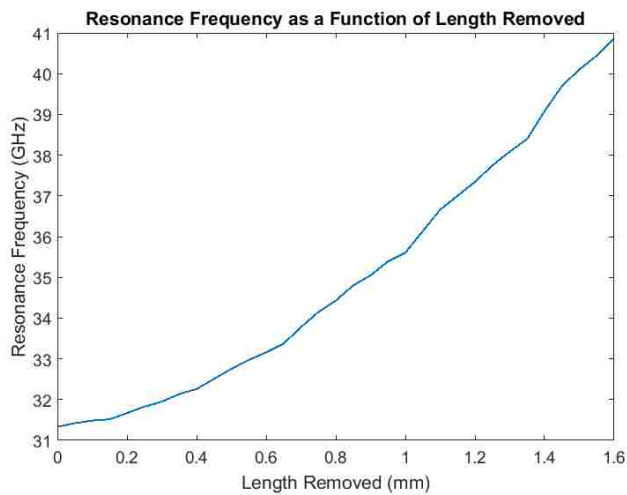
Figure 4.39. Effect of removing length from the outside of a spiral resonator. a) Designation of length removal. b) RCS vs frequency responses for lengths removed. c) Resonance frequency as a function of length removed.



a.

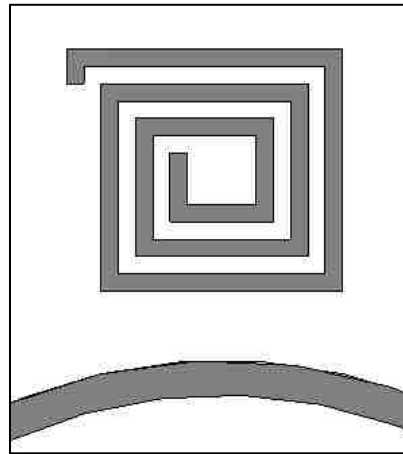


b.



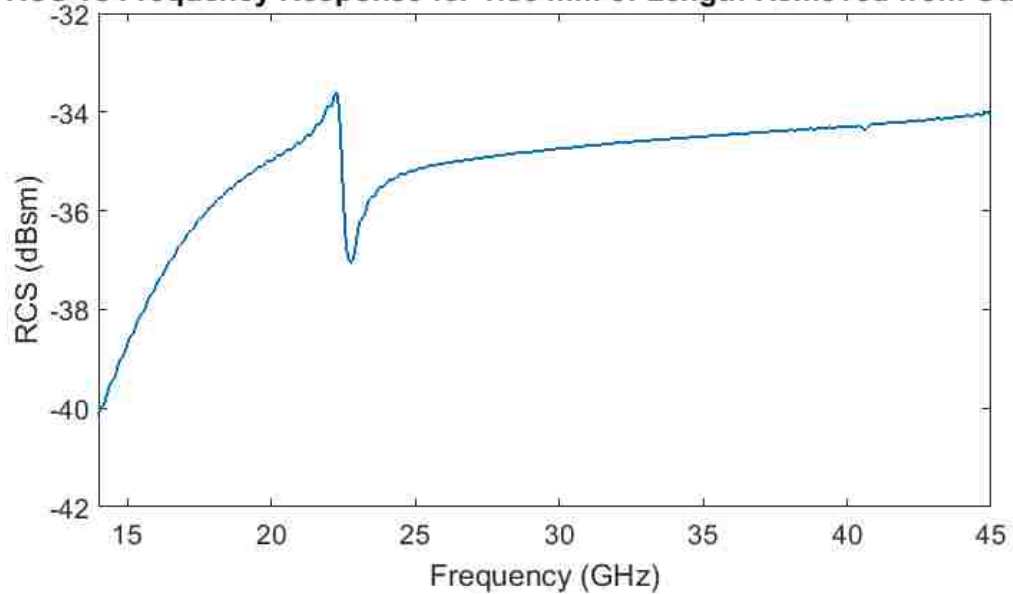
c.

Figure 4.40. Effect of removing length from the inside of a spiral resonator. a) Designation of length removal. b) Response for different lengths removed. c) Resonance frequency as a function of length removed.



a.

**RCS vs Frequency Response for 1.55 mm of Length Removed from Outside**



b.

Figure 4.41. Example of non-resonance condition of spiral resonator when removing length from outside of spiral. a) State of spiral resonator. b) RCS vs frequency response.

Next, the effect of changing width for various gaps was examined. For this, the length was maintained at 0.9 mm. Then, the width of the spiral leg was changed for different gaps. Figure 4.42 shows the results of these simulations. As can be seen from Figure 4.42, as both width and gap are increased the resonance frequency also increases. This is because the same footprint for the spiral resonator is maintained in all cases,

which causes the inner legs of the spiral to be shorter as the width and gap are increased. This effect is illustrated in Figure 4.43. The trends seen in Figure 4.42 are consistent with those presented in [110].

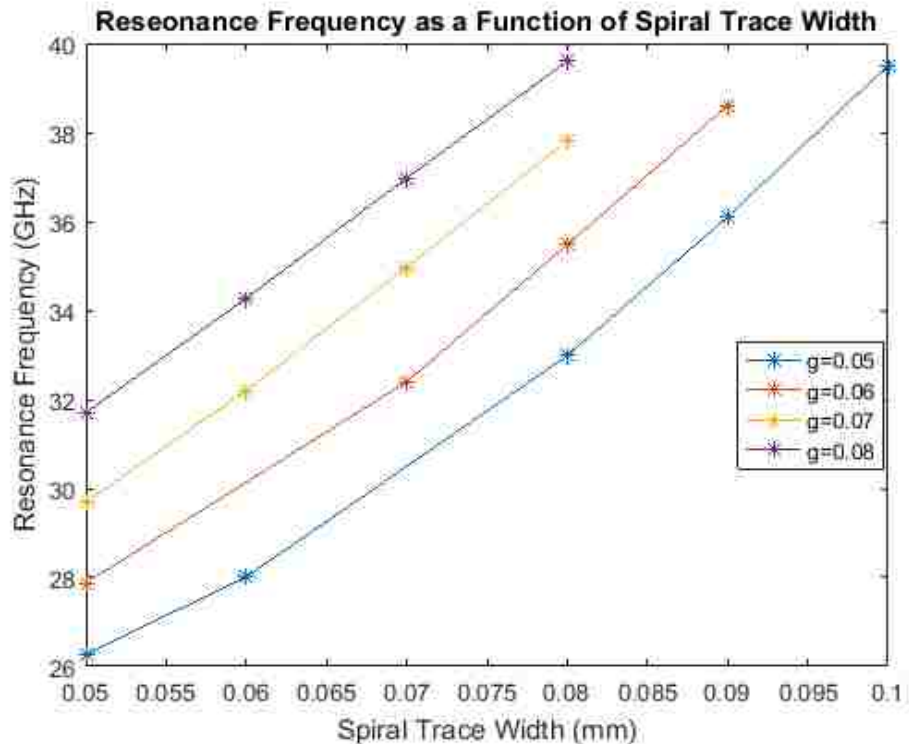


Figure 4.42. Effect of width and gap on resonance frequency of spiral resonator.

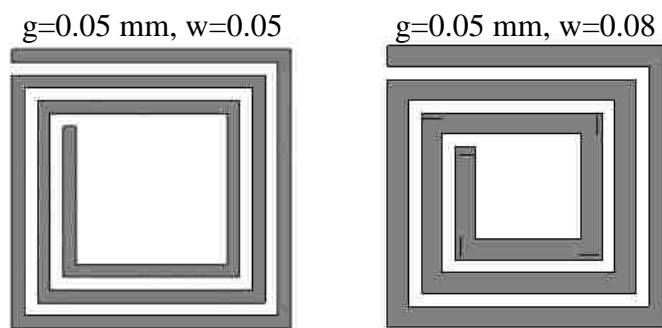


Figure 4.43. Illustration of effect of increasing the width of a spiral resonator.

Lastly, a comparison was conducted for spiral resonators used in Tx/Rx and backscatter configurations. For this, the same spiral resonator was simulated in the configuration used in the form of Figure 4.5a with the spiral shortened slightly to produce a higher resonance frequency that is further away from that of the ring resonator. It was also used in the form shown in Figure 4.44. In Figure 4.44, the spiral resonator is placed 0.1 mm away from a microstrip line of width 1 mm. Waveguide ports were placed on either end of the microstrip line and  $S_{21}$  was simulated. Figure 4.45 shows a comparison of the RCS result produced for the backscatter case with the  $S_{21}$  result produced from the second simulation. Both simulation results are normalized for direct comparison. As can be seen from Figure 4.45, the two different configurations produce different responses with the resonance frequencies even being offset from each other. This shows that design guidelines for backscatter based tags must be developed outside of those for Tx/Rx based tags.

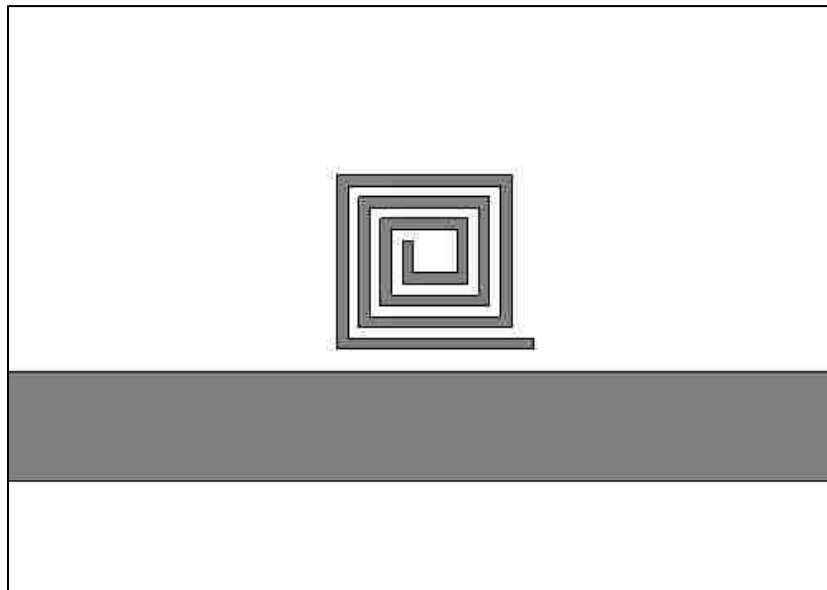


Figure 4.44. Simulation layout for Tx/Rx configuration using spiral resonator.



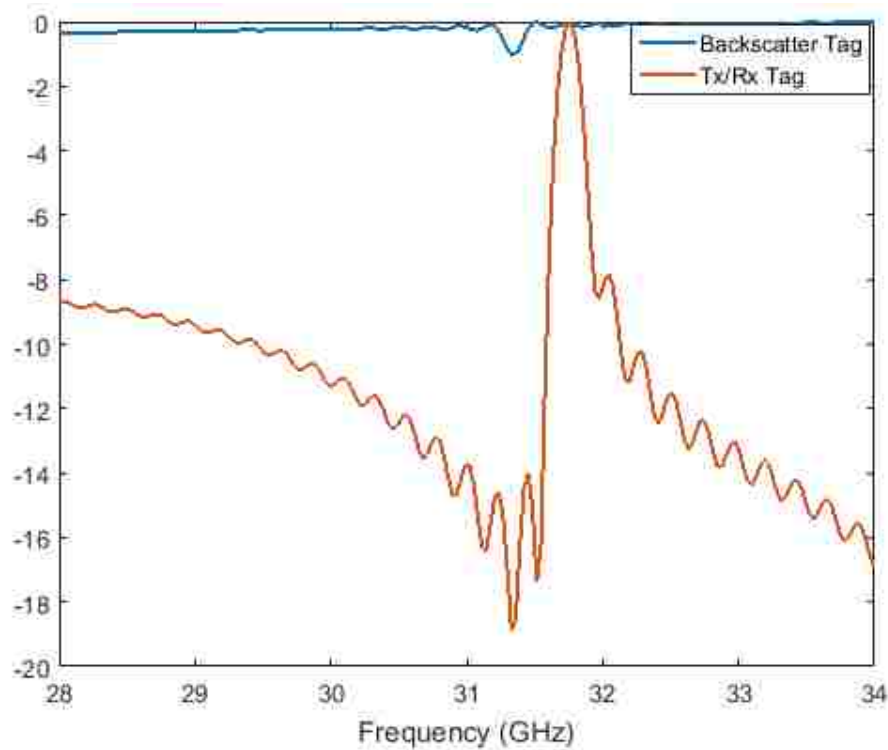


Figure 4.45. Comparison of configurations with spiral resonator.

**4.4.4. Design Guidelines for Resonator Combination.** Previously, the effects of location and orientation of the spiral resonator were shown. It was seen that due to differences in interaction between the polarization of the interrogating wave and the spiral resonator, different responses are produced.

Another factor that affects performance is the distance of the spiral resonator from the ring resonator. Simulations were conducted in which this distance was increased, as is illustrated in Figure 4.46. Figure 4.47 shows the plot of RCS vs. frequency for various distances. As can be seen, there is a change in both the resonance frequency and Q-factor as the distance changes. These effects are captured in Figures 4.48 and 4.49, respectively. From Figure 4.48 it can be seen that as the distance is increased, the resonance frequency

of the spiral resonator tends to increase. However, from Figure 4.49 it can be seen that as the distance increased, the Q-factor of the spiral related resonance also decreases. The distance between the spiral resonator and the ring resonator, also affects the resonance characteristics of the ring resonator. This is evidenced by Figure 4.50, which shows how the resonance frequency of the ring resonator decreases as the distance between the spiral resonator and ring resonator increases.

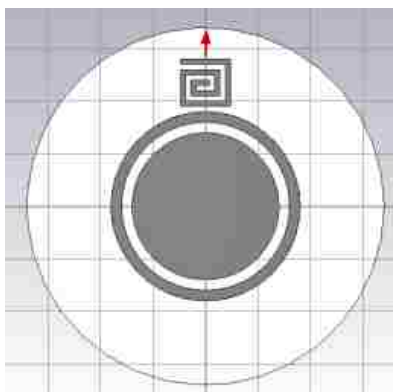


Figure 4.46. Diagram of increasing distance between spiral and ring resonators.

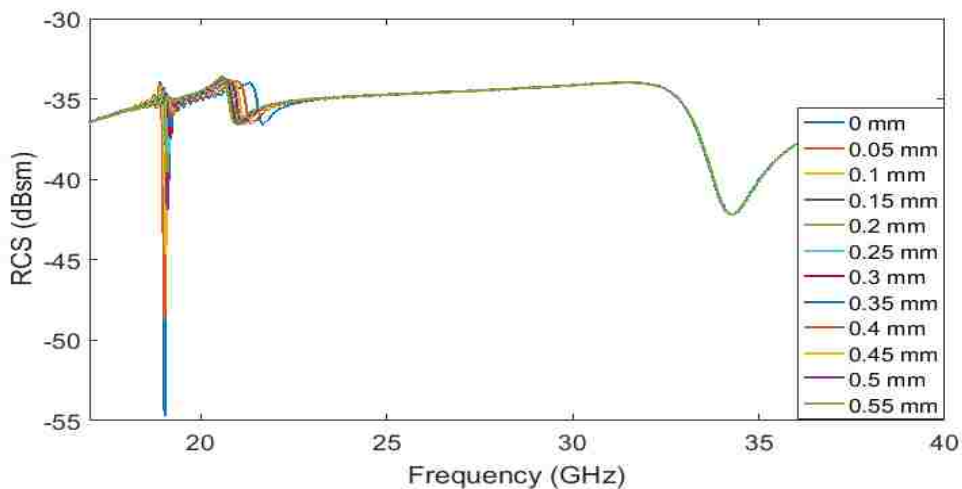


Figure 4.47. RCS vs. frequency plots for increasing distance between spiral and ring resonators.

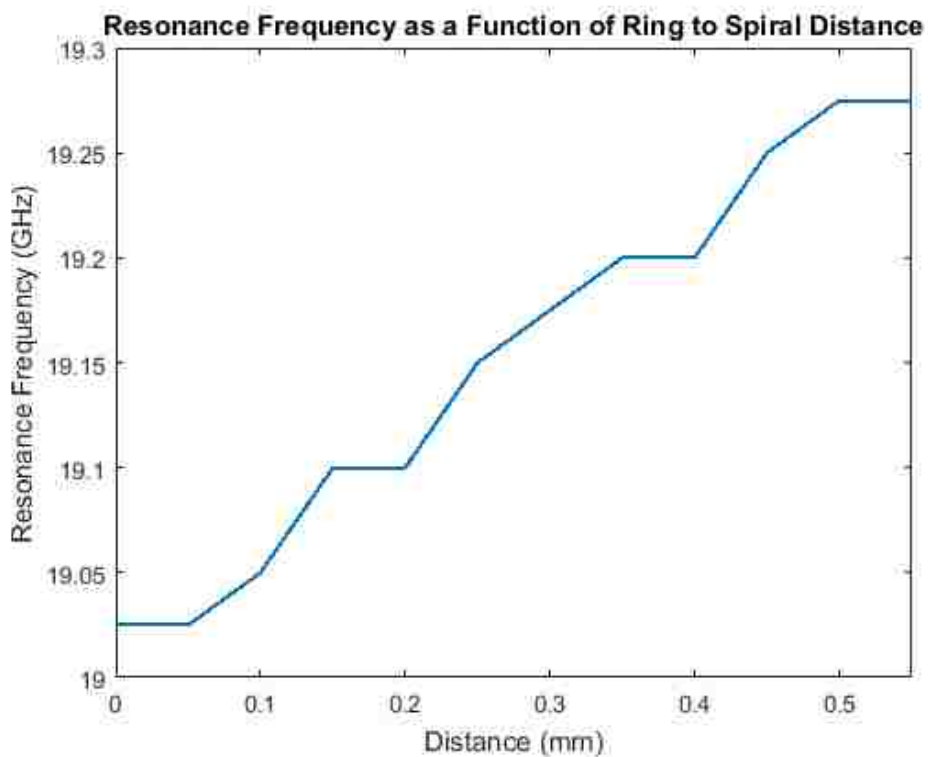


Figure 4.48. Effect of increasing distance on resonance frequency of spiral resonator.

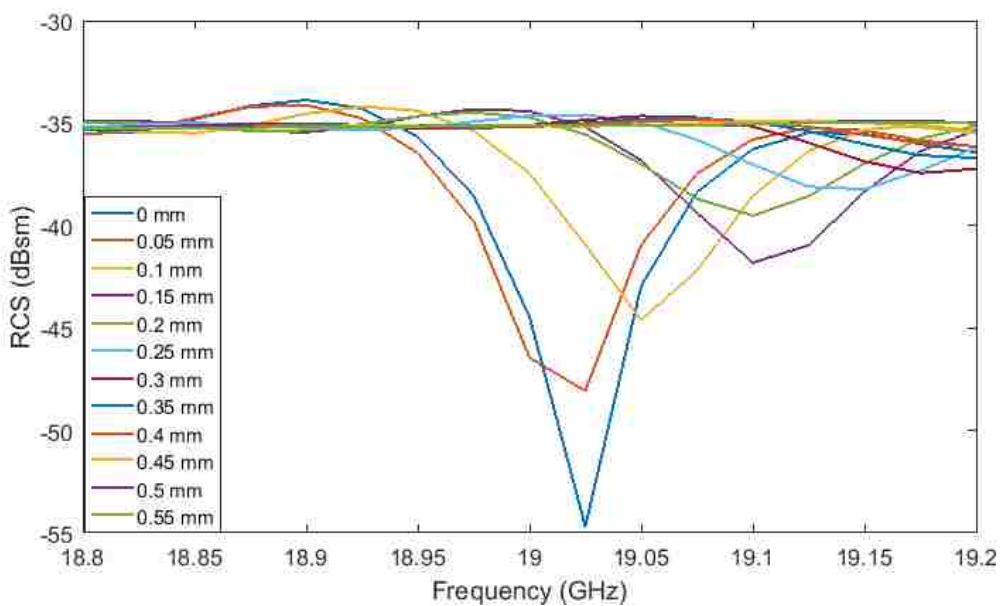


Figure 4.49. Effect of increasing distance on Q-factor of resonance frequency of spiral resonator.

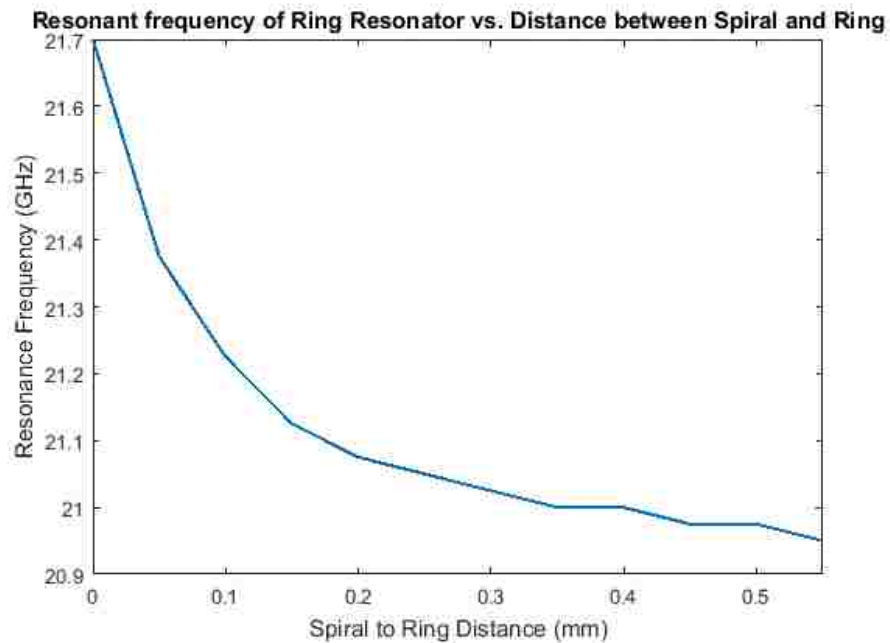


Figure 4.50. Effect of increasing distance on resonance frequency of ring resonator.

According to [12], using multiple spiral resonators of the same dimensions in the same tag can increase the depth of the notch associated with that size spiral resonator. Due to the tag under consideration being a backscatter-based tag rather than a Tx/Rx tag and being more polarization sensitive, an investigation was done to see if this phenomenon would also apply to this case. For this investigation, the same spiral was placed in multiple locations at the same time around the tag. The tag was irradiated with a linearly polarized plane-wave and interrogated with an RCS probe as before. Table 4.2 shows the different configurations and their responses. An inner ring resonator was added to better couple signal into the inner spiral resonators. As can be seen, using multiple of the same spiral does not always result in a deeper notch. This is due to the polarization of the interrogating wave interacting with each spiral on the tag differently.

Table 4.2. Responses of tag configurations with multiple of the same spiral.

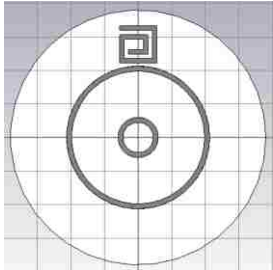
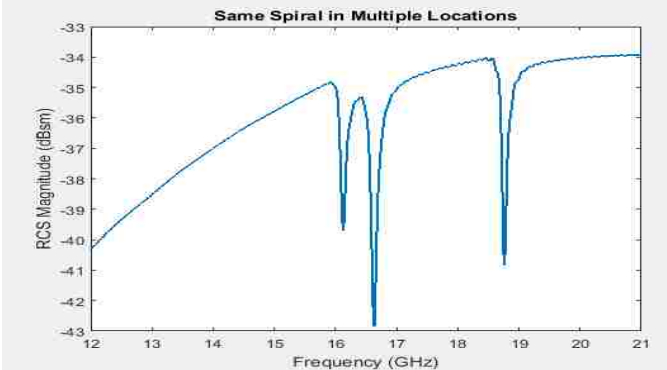
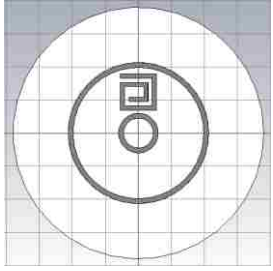
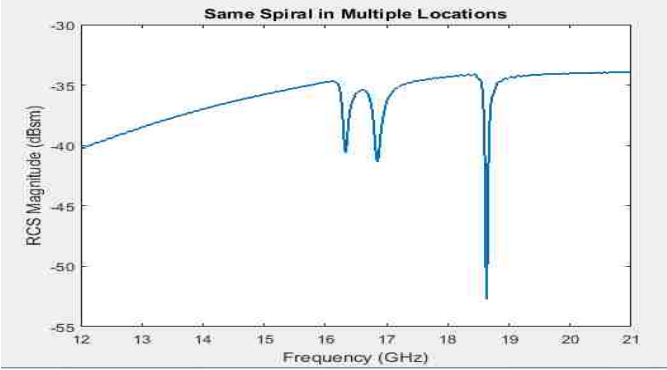
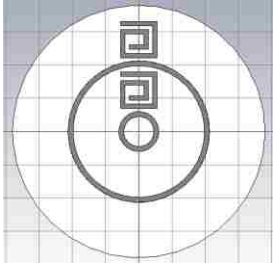
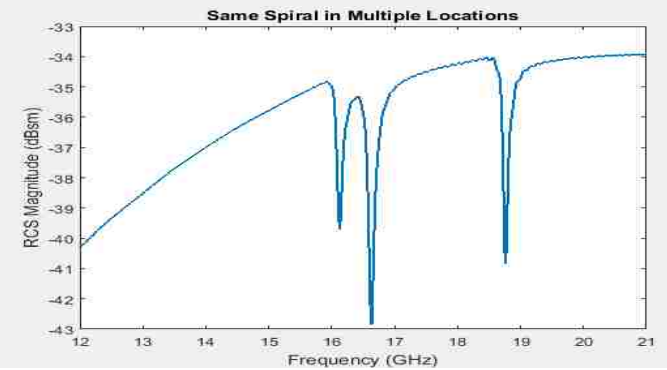
Tag	RCS vs Frequency Response
	
	
	

Table 4.2. Responses of tag configurations with multiple of the same spiral (cont.).

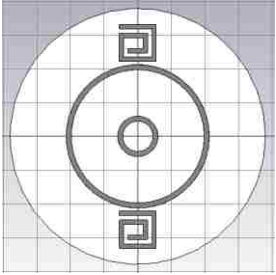
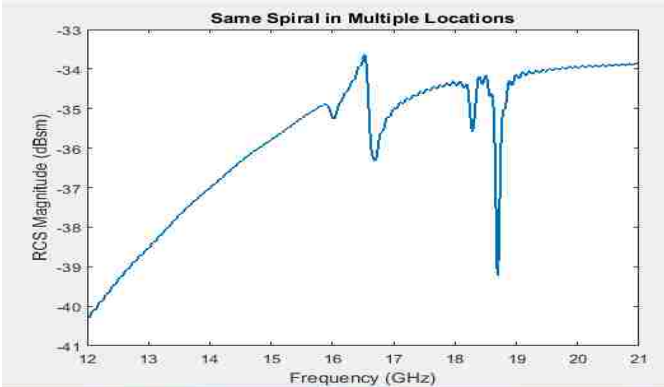
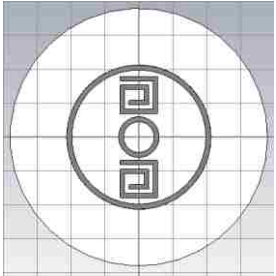
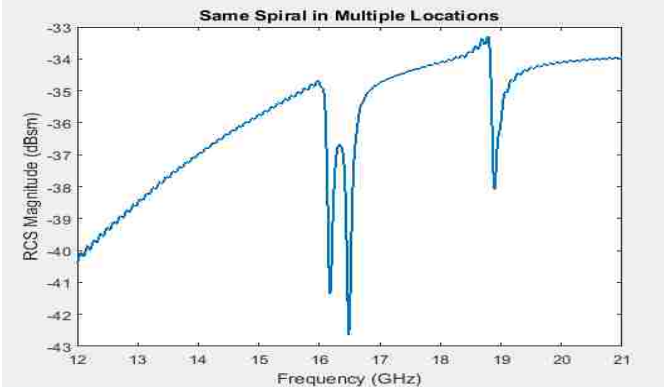
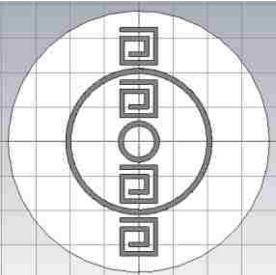
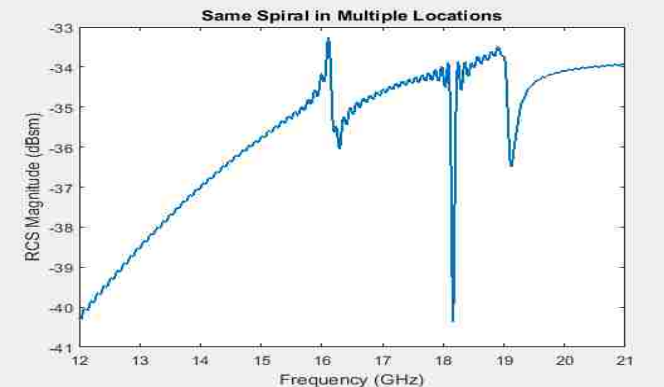
Tag	RCS vs Frequency Response
	
	
	

Table 4.2. Responses of tag configurations with multiple of the same spiral (cont.).

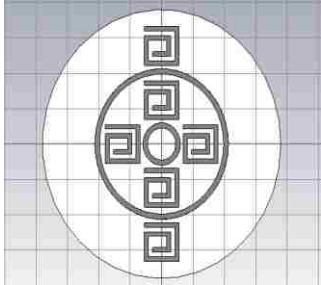
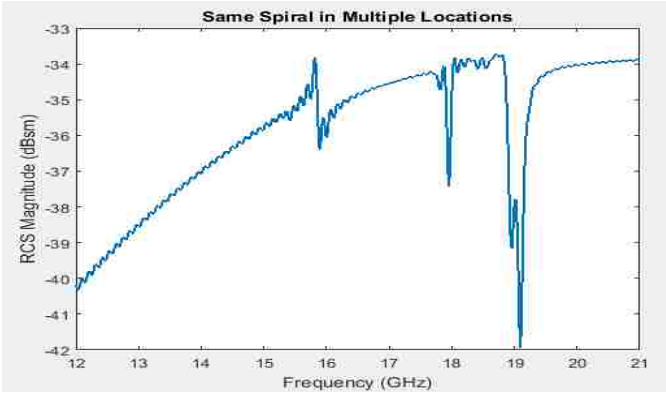
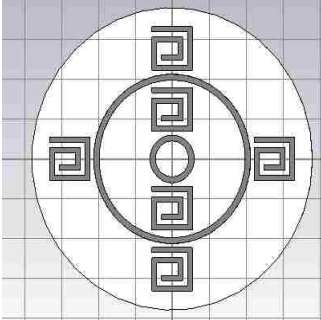
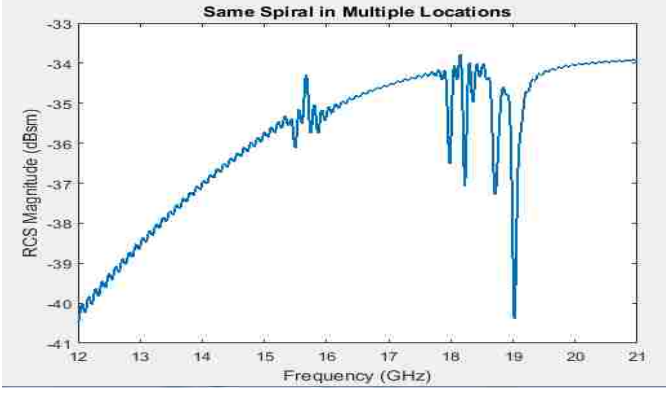
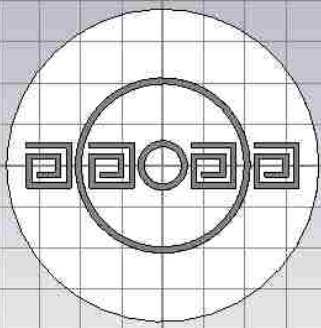
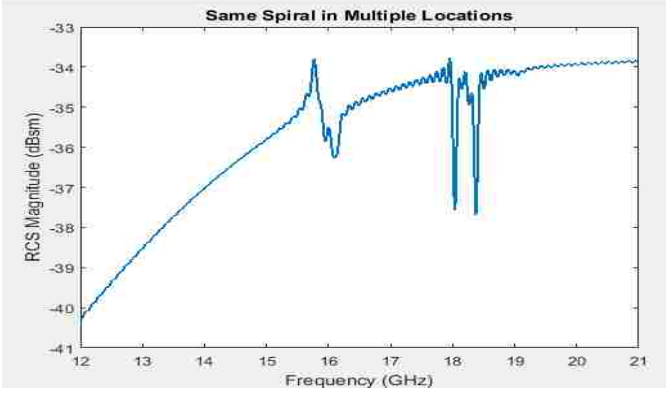
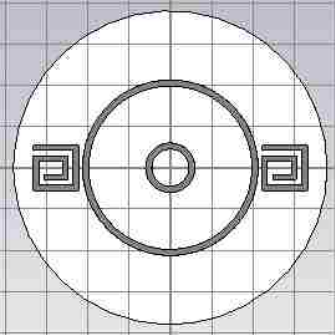
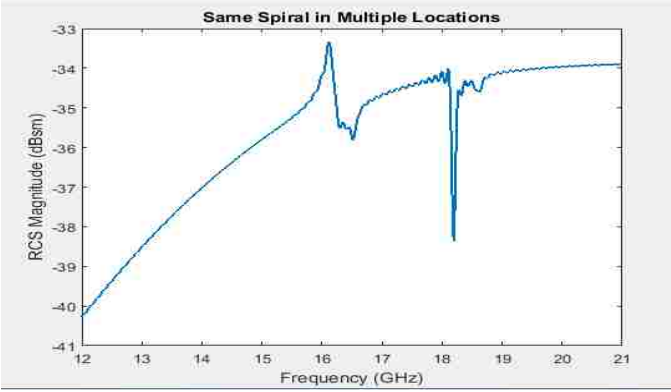
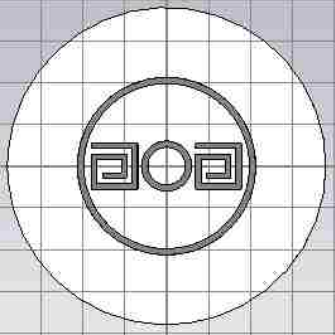
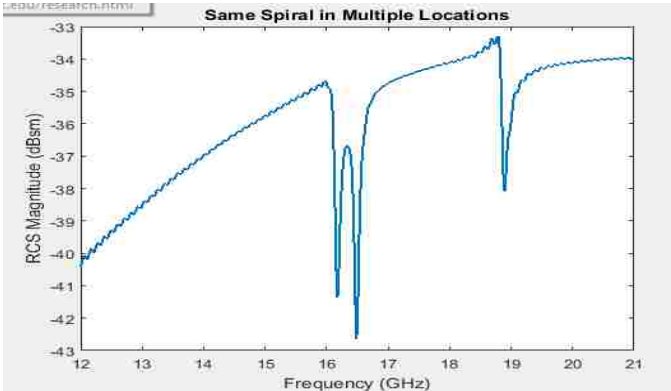
Tag	RCS vs Frequency Response
	
	
	

Table 4.2. Responses of tag configurations with multiple of the same spiral (cont.).

Tag	RCS vs Frequency Response
	
	

From the simulations conducted in Section 4.4, it can be seen that the interactions between multiple types of resonators as well as the effects of changing geometric parameters of a single type of resonator are complex. This makes predicting changes in response as geometry changes rather difficult. However, with design guidelines the tag designer can make informed decisions as to how to change the tag to achieve a desired response.



#### 4.5. ASSOCIATING TAG GEOMETRY AND RESPONSE

When combining multiple types of resonators into a tag design, it can be difficult to discern which tag feature is responsible for which response characteristic. This in turn makes it difficult to know where efforts need to be focused to achieve a desired response. One solution to this issue is to utilize surface current density simulations to associate tag geometry with response characteristics. The results presented in this section were previously shown in [104]. This process is illustrated through the use of an X-band (8.2 – 12.4 GHz) version of the tag shown in Section 4.3 that is also presented in [104]. Figure 4.51 shows this X-band version of the tag, while Figure 4.52 shows its RCS vs. frequency

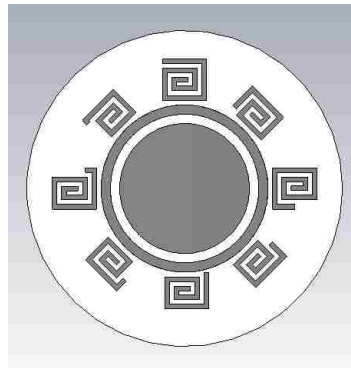


Figure 4.51. X-band version of eight spiral tag.

response. Surface current density simulations were then conducted with this tag. Figure 4.53 shows the results of these simulations for six different frequencies. For all images shown in Figure 4.53, the phase is kept consistent and the amplitude is plotted with a consistent color scale. Figure 4.53a, shows the surface current density on the tag at 10.2 GHz. As can be seen, the spiral resonator in position 1 and the ring resonator have high surface current density, when comparing this with Figure 4.52, it can be seen that there is

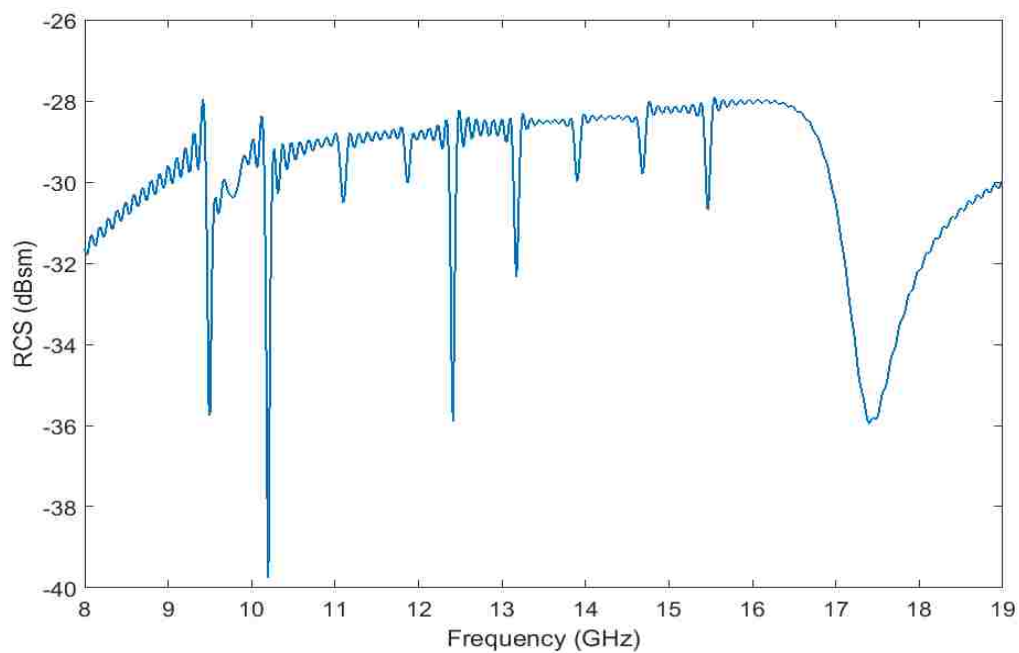


Figure 4.52. RCS vs. frequency response of X-band eight spiral tag.

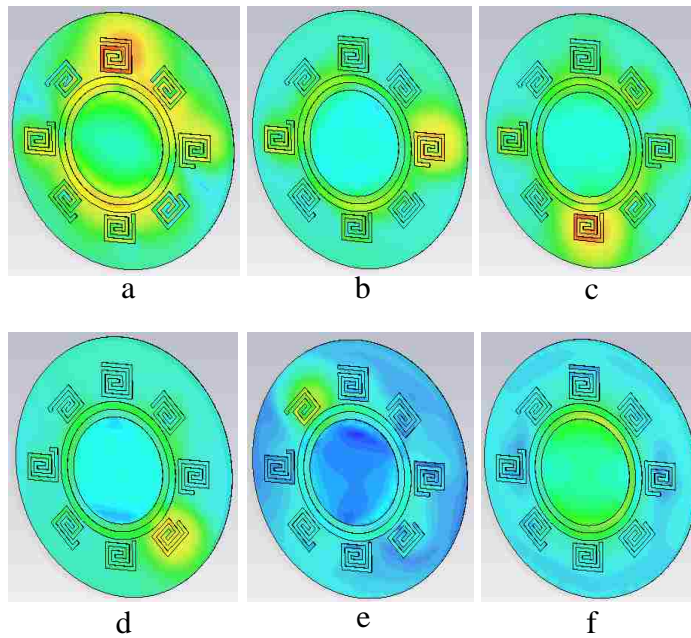


Figure 4.53. Surface current density simulations. a) 10.2 GHz. b) 11.1 GHz. c) 12.4 GHz. d) 13.9 GHz. e) 15.5 GHz. f) 17.4 GHz.

a notch in the response at 10.2 GHz. This means that high surface current density can be correlated to notches in the response. In this way, one can determine which features of the tag are creating which characteristics in the response.

In some cases, multiple tag features contribute to the same characteristic in the response. This is exemplified by the single spiral version of the tag shown in Figure 4.51, which is depicted in Figure 4.54. Figure 4.55 shows the RCS vs. frequency response for this tag and Figure 4.56 show the surface current density simulations. As can be seen from Figure 4.56, both the ring and the spiral possess high surface current densities for both notch frequencies in the response in Figure 4.55. This means that while this method of using surface current density can be used to associate response characteristics with tag features, it cannot necessarily indicate which tag feature should be changed to produce a desired change in the response.

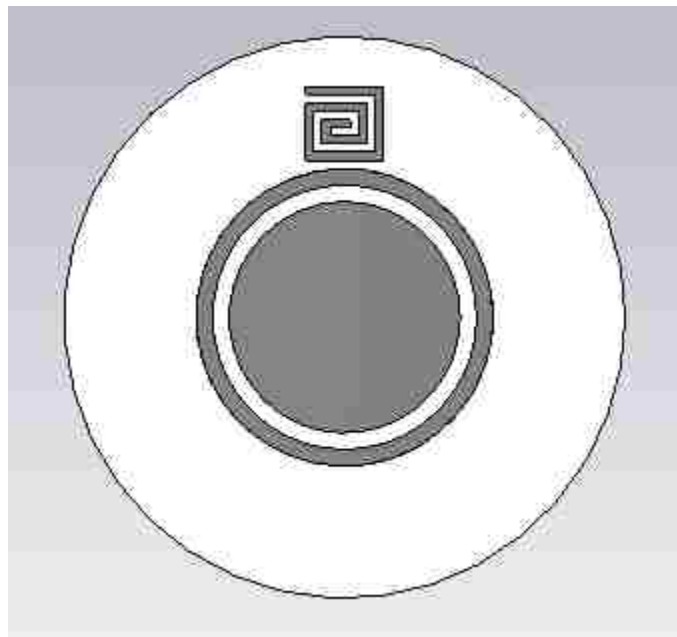


Figure 4.54. Single spiral version of X-band tag.

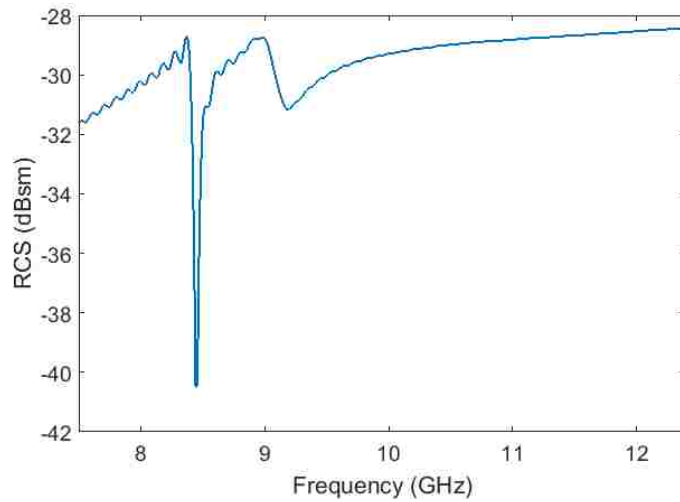


Figure 4.55. RCS vs. frequency response of single spiral X-band tag.

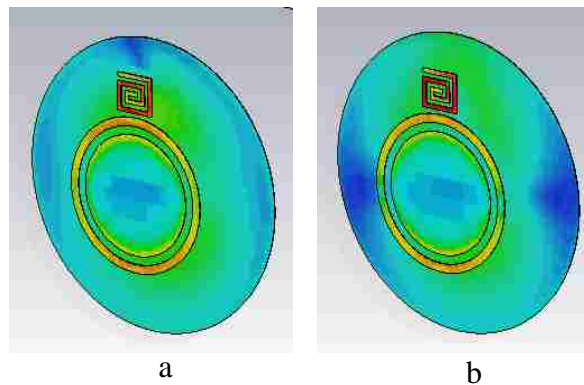


Figure 4.56. Surface current density simulations for single spiral X-band tag. a) 8.4 GHz. b) 8.9 GHz.

#### 4.6. APPLICATION ADAPTATIONS OF TAG

The tag presented in Section 4.3 can be optimized for a variety of applications and scaled to operate in a variety of frequency ranges with the help of the previously presented design guidelines and surface current density simulations. Below three

different versions of the previously presented tag adapted to different applications are shown. These tags and results are also presented in [104].

**4.6.1. X-band Version of Tag.** In Section 4.5, an X-band version of the eight spiral tag was shown. This lower frequency version of the tag was created to allow for easier and less expensive fabrication through a PCB fabrication house. In developing the X-band version, the substrate was changed to Rogers 4350b since this is a low loss substrate available from many PCB manufacturers. The diameter of the tag is 13.6 mm, which is double that of the tag presented in Section 4.3. This tag and its response are shown in Figures 4.51 and 4.52, respectively. In its four spiral configuration, this tag is very sensitive to rotation and could potentially be used as a rotation sensor. The four spiral version is shown in Figure 4.57 and its simulated  $S_{11}$  response is shown in Figure 4.58. Figure 4.58 was generated from a simulation in which the tag is interrogated with an open-ended waveguide. The simulation setup is shown in Figure 4.59. In this setup the aperture of the waveguide is parallel to the  $xy$  plane.

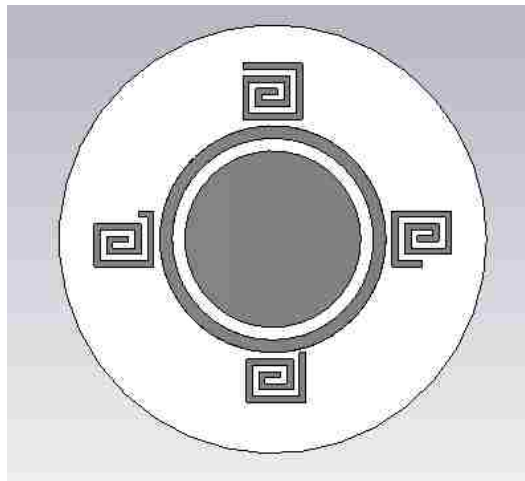


Figure 4.57. Four spiral X-band tag.

From Figure 4.58 it can be seen that there are five deep defined notches in X-band that correspond to the ring and the four spirals. When the tag is rotated about the  $z$ -axis, different responses are created. Codes could be assigned to these responses and then used for multi-bit rotation sensing. Figure 4.60 shows the responses for different amounts of rotation. As can be seen, there is a different response for every five degrees of tag rotation. In Figure 4.61, the effect of rotating the tag in different directions is shown. This figure shows that there are different results for the angles of  $5^\circ$  and  $355^\circ$  ( $-5^\circ$ ), which means that even direction of rotation could potentially be sensing with this tag. These results show promise for potentially using this tag as a rotation sensor.

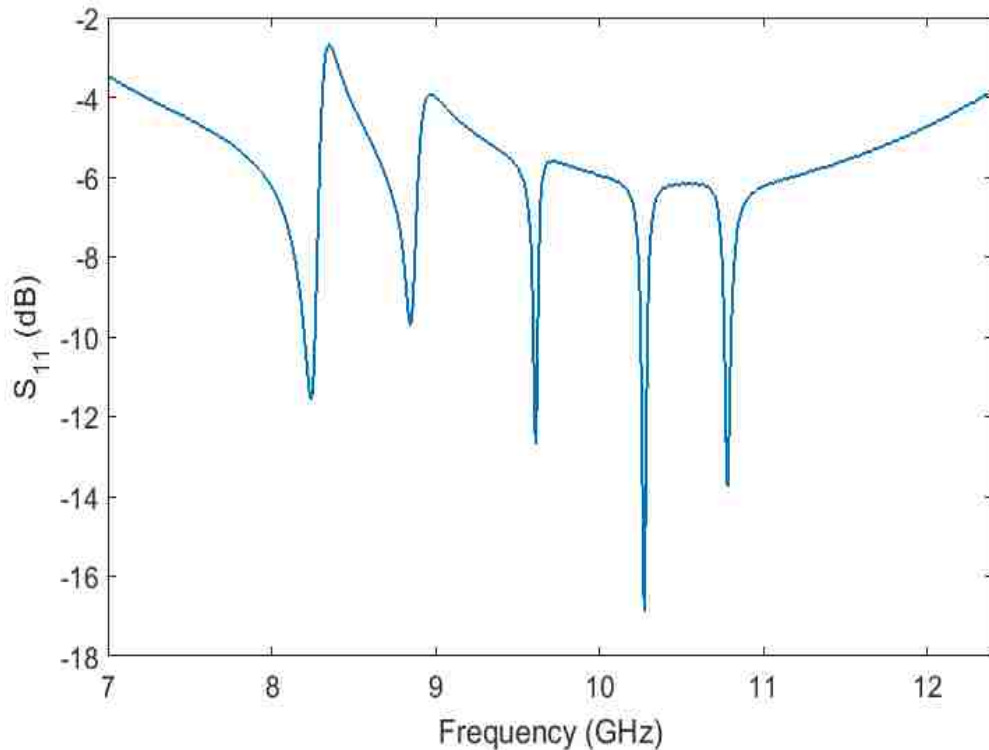


Figure 4.58. Simulated  $S_{11}$  response for four spiral tag.

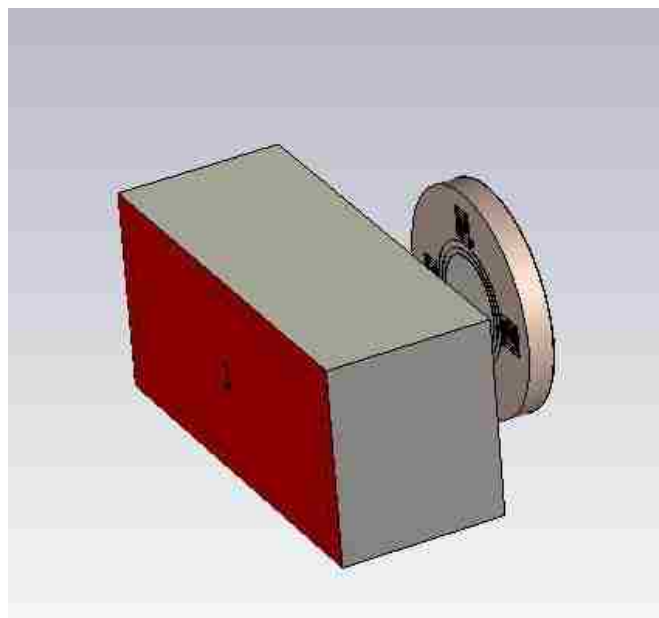


Figure 4.59. Simulation setup for  $S_{11}$  of tag with waveguide.

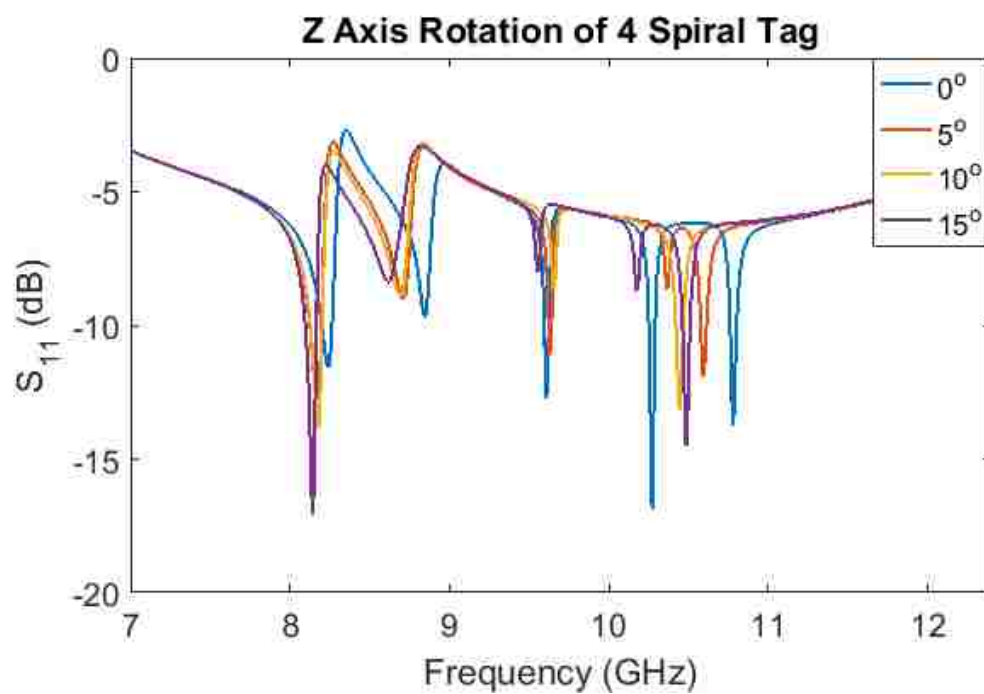


Figure 4.60. Simulated rotation sensing results for four spiral tag.

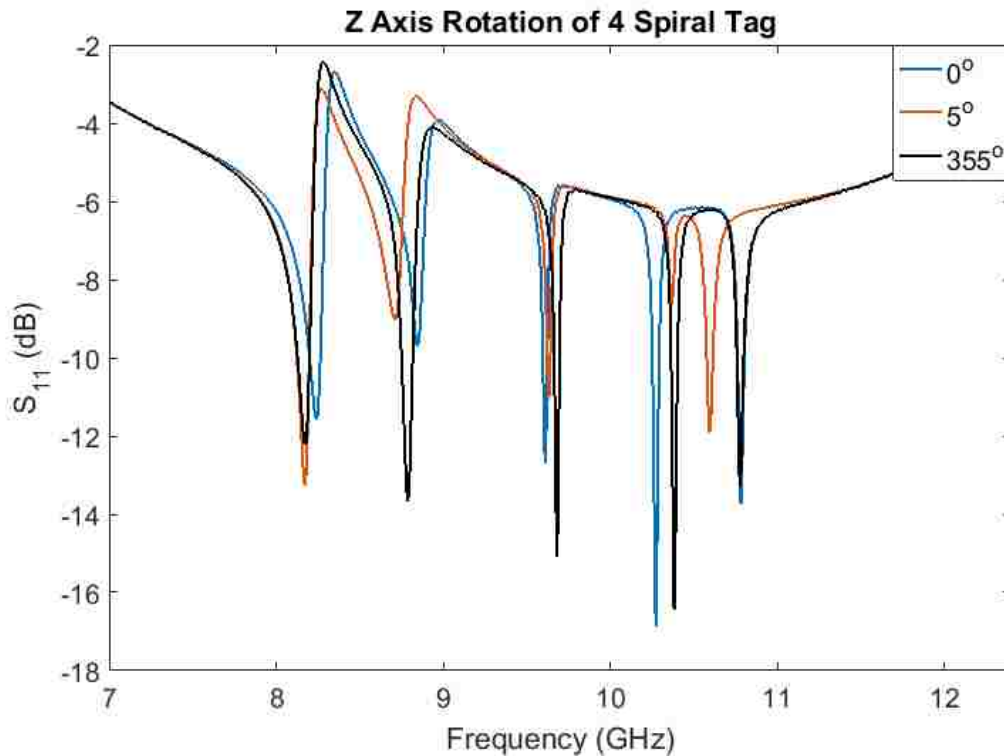


Figure 4.61. Simulated directional rotation sensing for four spiral tag.

**4.6.2. ID Application Tag.** The X-band tag presented in Section 4.6.1 was also optimized for use in ID applications. In order to perform this optimization, spirals with adjacent resonant frequencies (i.e., notches) were not placed adjacently around the ring resonator. By employing this detuning technique first suggested in [52], the response is more robust to the removal of spirals which in turn removes notches from the response. This allows for coding method 2 to be used more reliably. The spirals are numbered with respect to their locations according to Figure 4.9. The responses for when various spirals are removed are shown in Figure 4.62. Figure 4.62b shows a missing notch around 11 GHz as compared to the response in Figure 4.62a. This missing notch corresponds to spiral 2 which has been removed. Figure 4.62c and Figure 4.62d show missing notches in

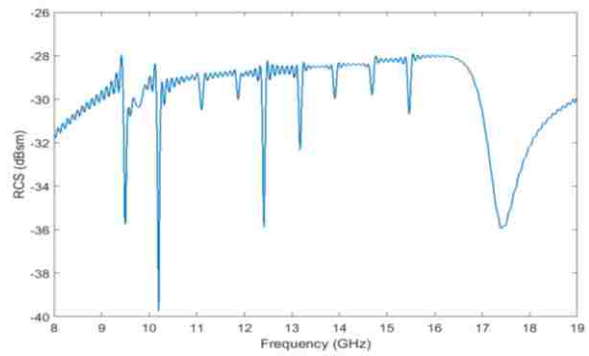


two other locations that correspond to the spiral that has been removed. In all cases shown in Figure 4.62, when a spiral is removed the characteristics of the response not associated with this spiral tend to remain stable (i.e., they do not shift or disappear). The codes using Method 2 are shown for all four of the cases in Figure 4.62 in Table 4.3. By providing so many notches in the response for a relatively small tag area, this tag also has a high bit density (6.89 bits/cm<sup>2</sup>) making it desirable for ID applications.

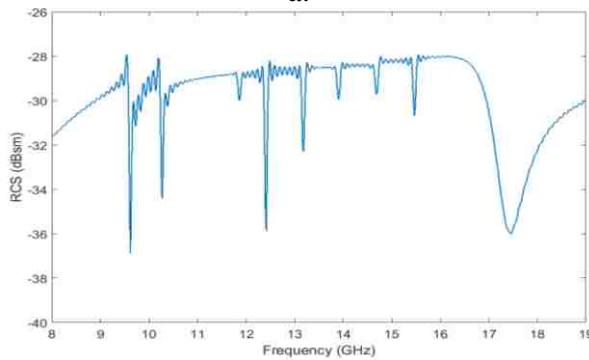
Table 4.3. Codes for ID tag using coding method 2.

Description	Code
Eight spiral configuration (Figure 4.62a)	1111111111
Spiral 2 removed (Figure 4.62b)	1101111111
Spiral 3 removed (Figure 4.62c)	1110111111
Spiral 4 removed (Figure 4.62d)	1111011111

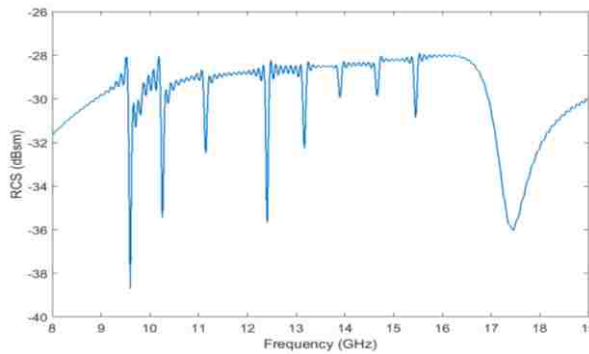
**4.6.3. Materials Characterization Application Tag.** This tag can also be used for materials characterization applications. For this case it is used in its original 18-40 GHz configuration shown in Section 4.3. This is done since as the permittivity of the material in which the tag is embedded increases, the tag response shifts down in frequency. This allows for a K-band (18-26.5 GHz) waveguide to be used for interrogation and as the response shifts down, new notches will enter the interrogation band. Figure 4.63 shows the simulation setup used for testing the utility of this tag for materials characterization. In this monostatic radar simulation, the tag, linearly polarized



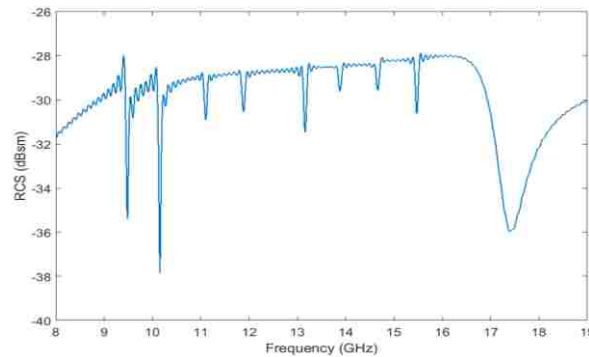
a.



b.



c.



d.

Figure 4.62. RCS vs. frequency responses of ID application optimized tag. a) Eight spiral tag response. b) Response when spiral 2 is removed. c) Response when spiral 3 is removed. d) Response when spiral 4 is removed.

plane-wave used for interrogation, and RCS probe are placed in the material for simplicity. Figures 4.64 and 4.65 show the RCS vs frequency response for various embedding materials. In Figure 4.64 only permittivity is changed where as in Figure 4.65 the complex dielectric constant is manipulated. The trends seen in these figures corroborate what was seen in the proof of concept of embedded chipless RFID in Section 2.

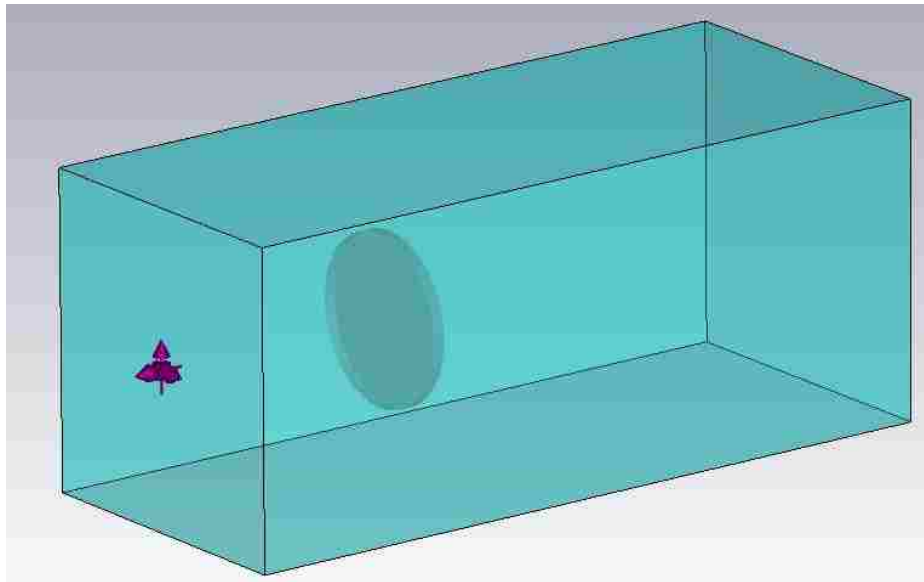


Figure 4.63. Simulation setup for embedded materials characterization.

As previously mentioned, most tag metrics are only applied to ID based tags as codes often are not assigned to the responses of sensing based tags. Additionally, these metrics do not necessarily convey the merit of a tag for a sensing based application. Because of this, three new tag metrics were developed and presented in [104].

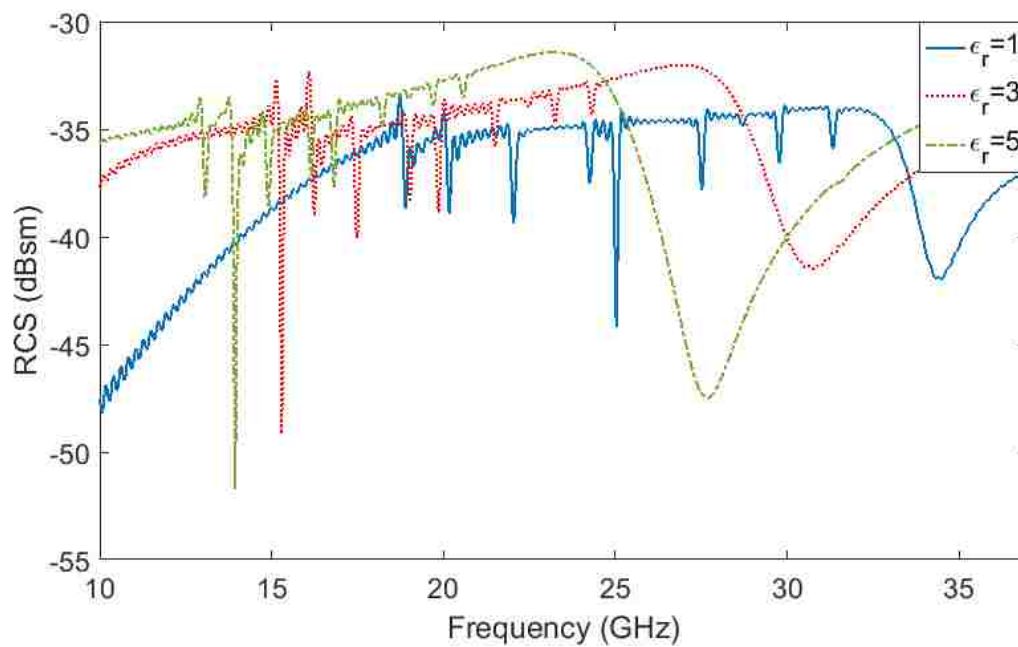


Figure 4.64. RCS vs frequency response for tag embedded in materials with different permittivities.

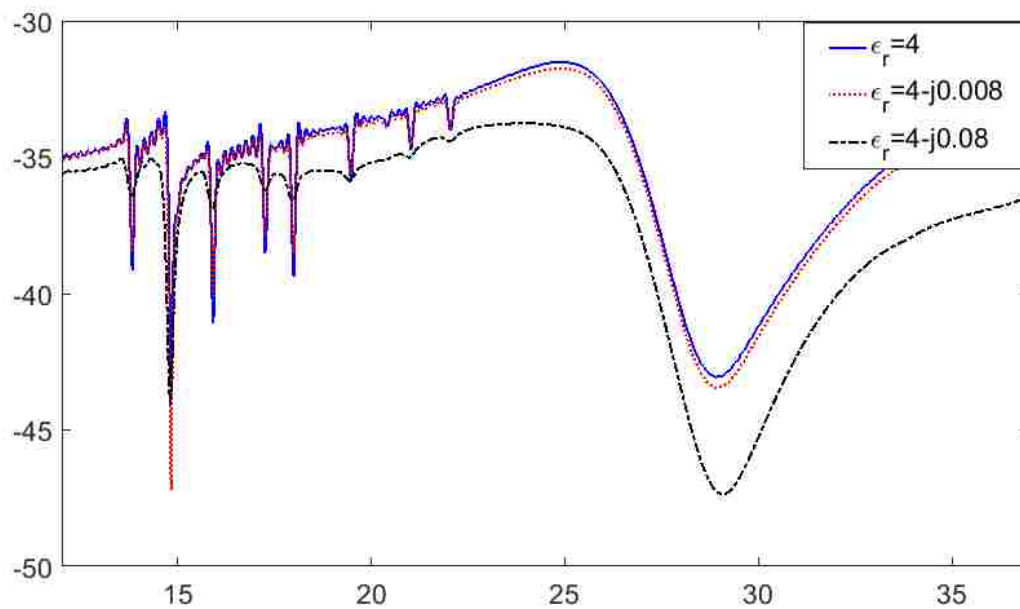


Figure 4.65. RCS vs. frequency response for tag embedded in materials with different complex dielectric constants.

The first of these new metrics is notch density. This metric is a modification of bit density that is defined as the number of response notches per tag area and response bandwidth used. For the case of the tag used above for embedded materials characterization applications, the notch density would be  $10/0.36 \text{ cm}^2/19 \text{ GHz}$ . This metric has the benefit of concisely communicating the coding potential, the size of the tag, and the reader bandwidth specification. Together, this information provides insight into the practicality of the tag. Another benefit of this metric is that it is not coding method dependent as bit density is. However, there can still be some user bias when determining what the reader bandwidth.

A second proposed metric is the average Q-factor which relates to the measurability of a tag in terms of how many frequency points are needed to properly capture the notches in the response. If too few frequency points are used, there is the possibility of missing a notch which will lead to bit generation errors and incorrect codes.

The third proposed metric is the maximum RCS value of the response. The higher the RCS, the more the tag is scattering and the easier it is to capture the response of the tag. Higher RCS's also make it easier to distinguish the response of the tag from the response of the background. Knowing the maximum RCS of a tag will allow the user to know the sensitivity needed in the reader system. Conversely, if there is a specific reader sensitivity, knowing the maximum RCS will allow the user to know if a certain tag is capable of being measured.

#### 4.7. MEASUREMENT OF TAG

This tag was also fabricated in four different configurations and measured. It was fabricated in its X-band version due to limitations of PCB fabrication houses. In doing measurements,  $S_{11}$  was measured rather than RCS due to the complexity of measuring RCS, as was done in Section 2.3. Since  $S_{11}$  was to be measured, first  $S_{11}$  was simulated using a waveguide setup like that shown in Figure 4.66. The response for both the eight spiral (Tag 1) and single spiral (Tag 2) configurations of the tag are shown in Figure 4.67, as both of these configurations were fabricated along with configurations with spiral 3 (Tag 3) missing and spiral 8 (Tag 4) missing. The fabricated tags are shown in Figure 4.68. For all four tag configurations, five copies of each tag were fabricated. The copies of each tag are indicated by a decimal number (i.e., the tags in the eight spiral set are numbered Tag 1.1 to Tag 1.5).

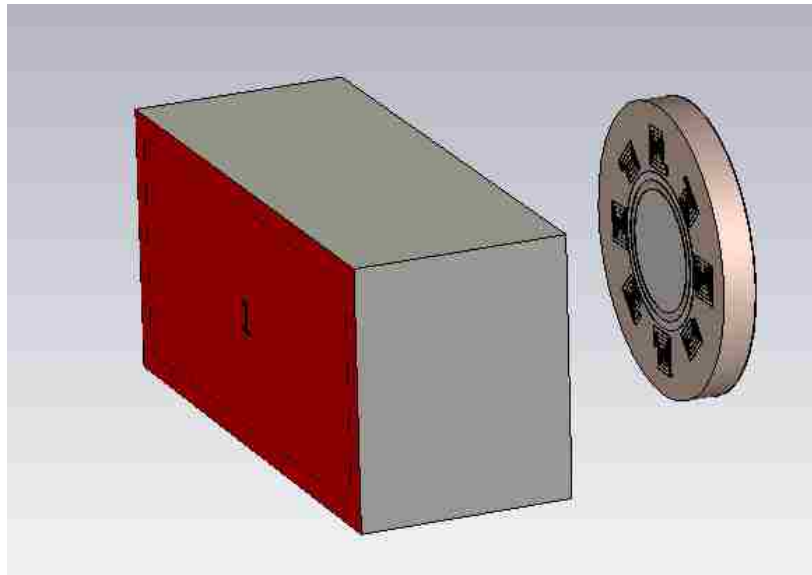


Figure 4.66. Simulation setup for  $S_{11}$  of tag.

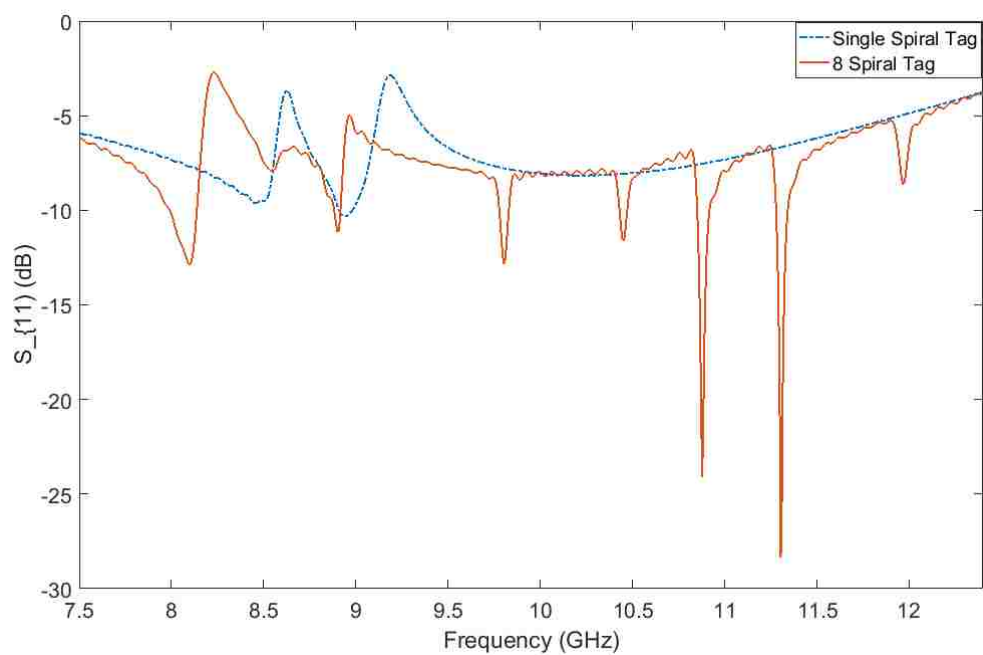


Figure 4.67. Simulation results for  $S_{11}$  of eight spiral and single spiral tags.



Figure 4.68. Fabricated eight spiral and single spiral tags.

In doing the measurements, an X-band open-ended waveguide with a modified flange (described in [127]) was used with a VNA. For the measurements, the waveguide was operated from 7.5 to 12.4 GHz, which is outside its normal 8.2 to 12.4 GHz range, to better capture the lower frequency notches. To this end, 3001 points were also used in the measurements. The measurement setup is shown in Figure 4.69.



Figure 4.69. Measurement setup for fabricated spiral tags.

All tags were measured at a distance of 0.5 cm from the waveguide aperture. It should be noted, that  $S_{11}$  measurements are distance dependent so measurements at different distances produce different results. 0.5 cm was used as the distance here because it produces the strongest response. In processing the measurements, a measurement of the foam that the tag was attached to was subtracted from the measurement of the tag with



the foam. This was done to remove the effects of the foam and isolate the response of the tag so it could be more directly compared to the free-space simulation. The processed measurement results in comparison to the simulation results are shown in Figures 4.70, 4.71, 4.72, and 4.73. In all cases the associated measurement and simulation notches are indicated with ovals. From Figure 4.70 it can be seen that for the single spiral tag the measurement and the simulation results agree. However, in Figure 4.71 there is not as good of agreement between the simulation and the measurement. This is believed to be due to manufacturing defects and misalignment between the waveguide and the tag, as this tag is extremely sensitive to misalignment. In Figures 4.72 and 4.73, similar disagreement between measurement and simulation can be seen. It should be noted that all five copies of the eight spiral tag produced similar measurement results, as is exemplified by Figure 4.74. Figures 4.75, 4.76, and 4.77 show comparisons of measurements for all five copies of Tag 2, Tag 3, and Tag 4, respectively. For Tags 3 and 4 all five copies produce similar results. However, for Tag 2, the measurement for Tag 2.2 is shifted up in frequency from the measurements of the other four tags. This is believed to be from a slight manufacturing defect of this particular tag, which was verified by examining Tag 2.2 under a microscope.

It is possible that all five copies of Tags 1, 3, and 4 are subject to the same manufacturing inaccuracies (i.e., slight differences in spiral length or placement from the simulation model), which could cause changes in response characteristics. To show that this could be the case, further simulation was conducted. In these simulations, spirals in positions 1, 3, and 5, indicated in Figure 4.78, had 0.076 mm (the manufacturing tolerance of the PCB manufacturer used) of length removed from their outside legs.

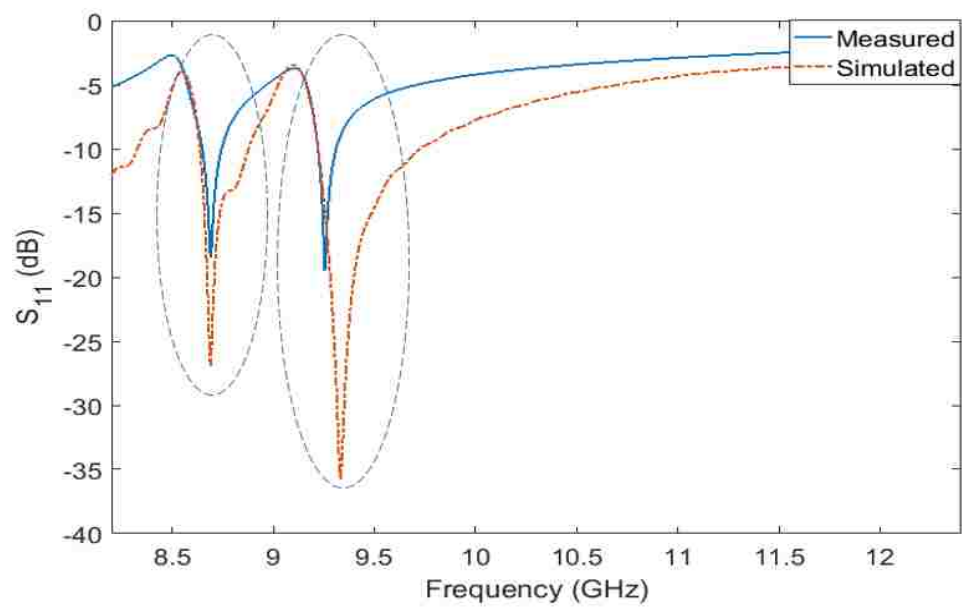


Figure 4.70. Measurement and simulation results for single spiral tag.

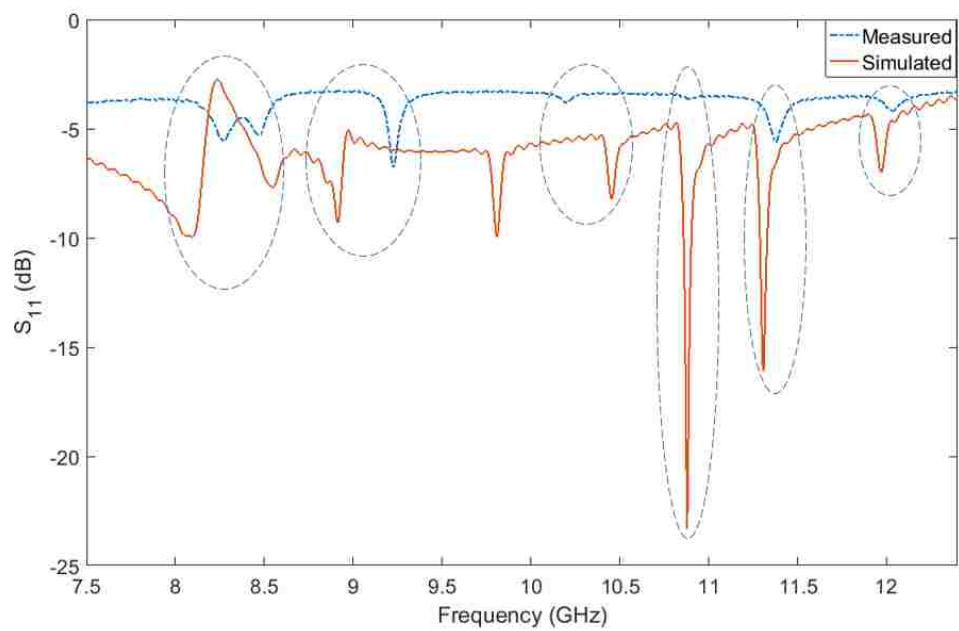


Figure 4.71. Measurement and simulation results for eight spiral tag.

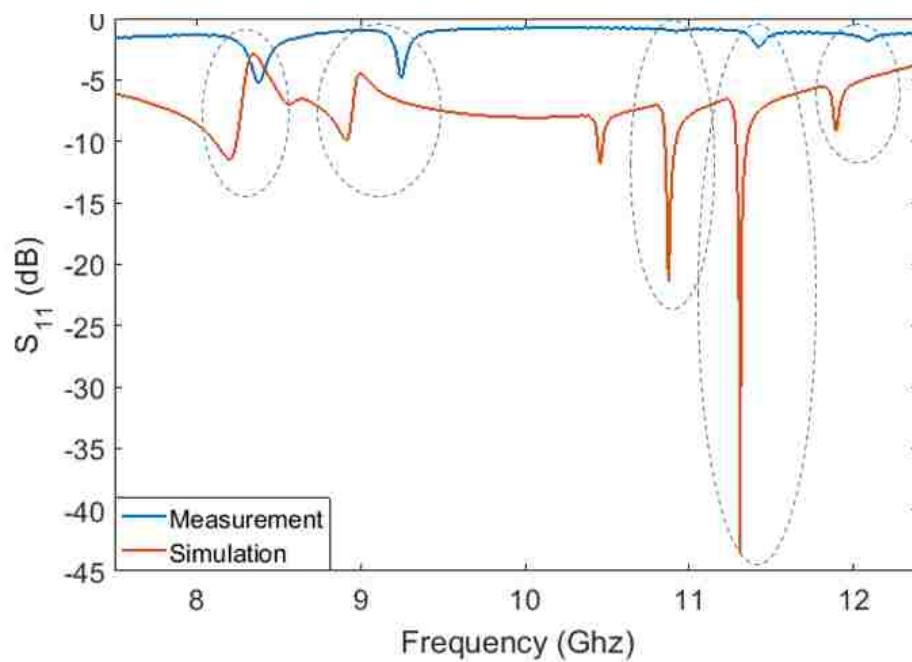


Figure 4.72. Measurement and simulation results for Tag 3.1.

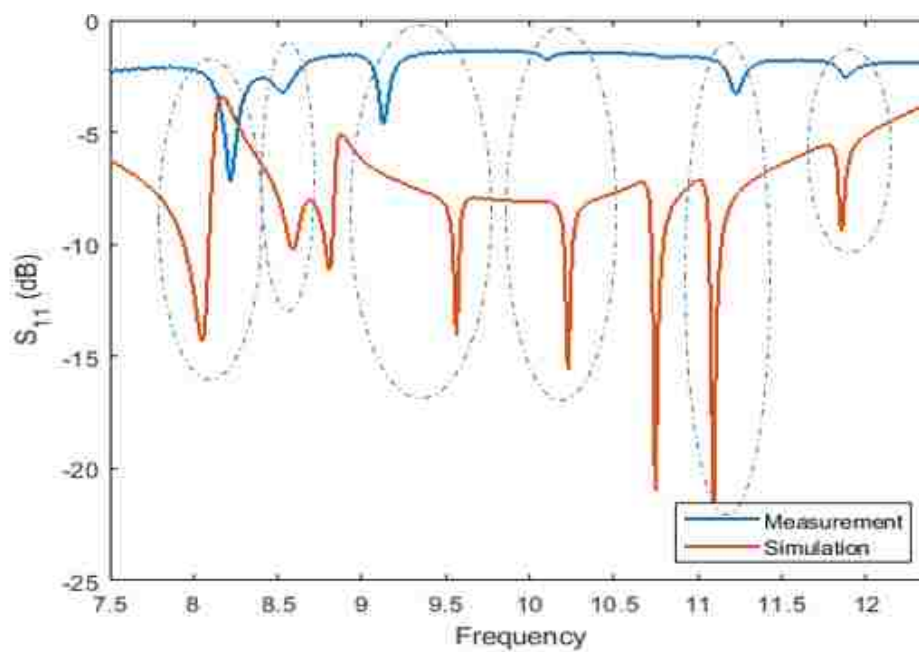


Figure 4.73. Measurement and simulation results for Tag 4.1.

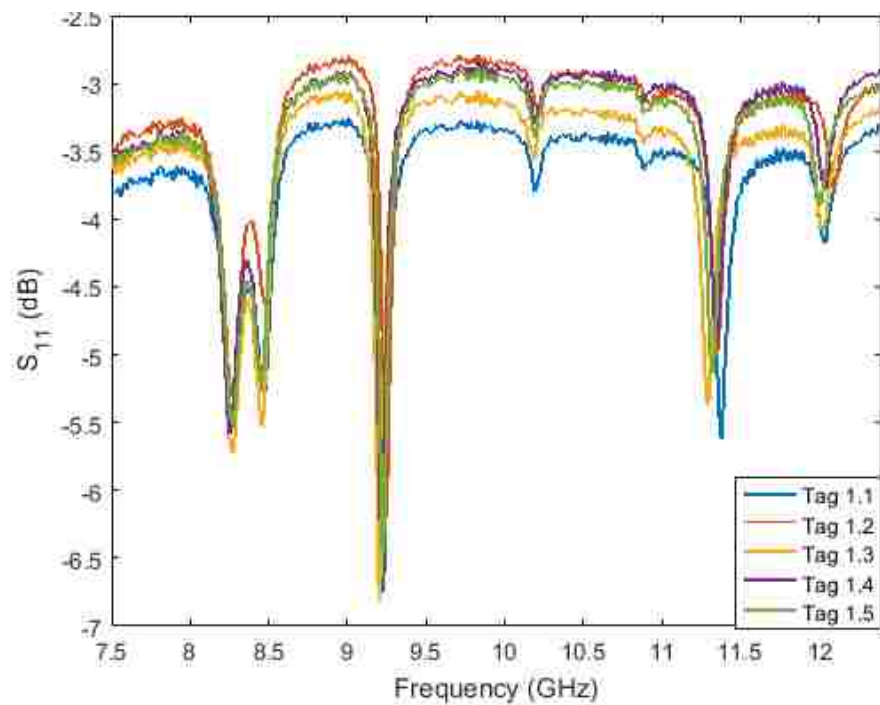


Figure 4.74. Comparison of processed measurements of five copies of Tag 1.

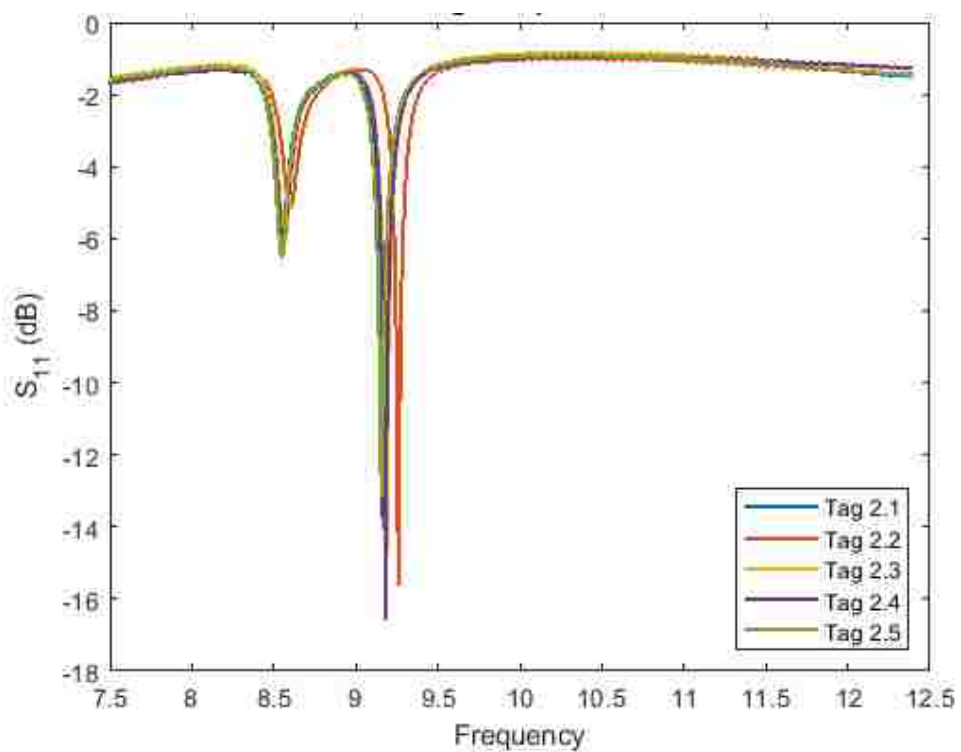


Figure 4.75. Comparison of processed measurements of five copies of Tag 2.

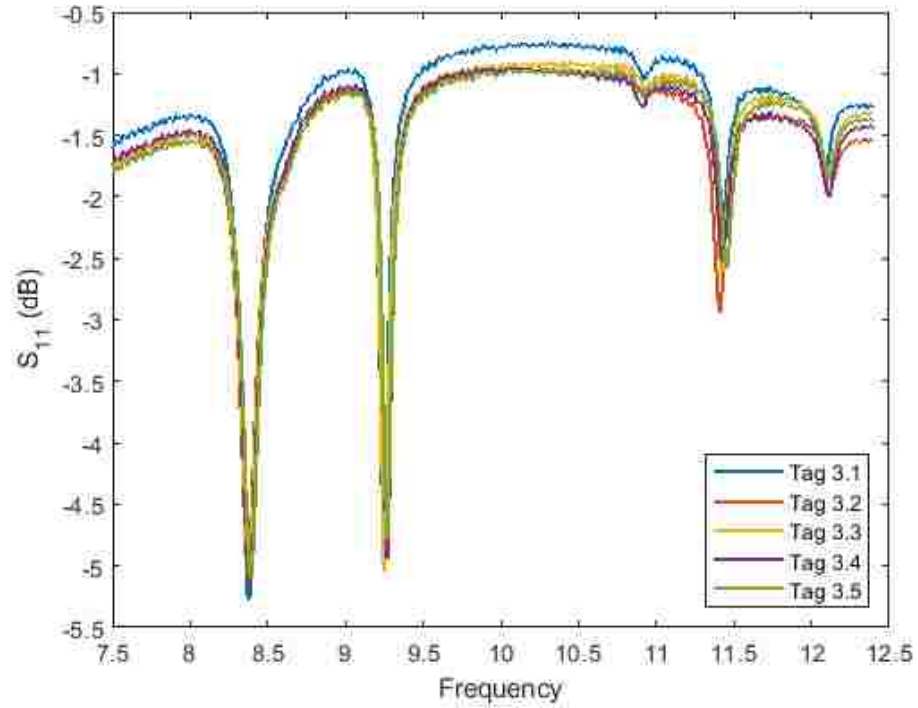


Figure 4.76. Comparison of processed measurements for five copies of Tag 3.

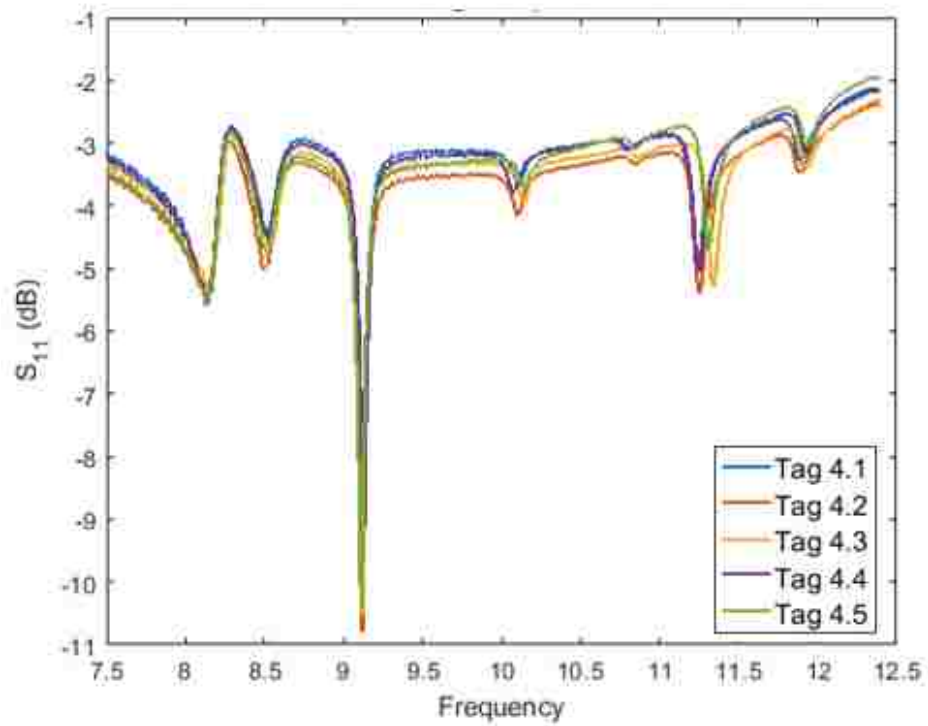


Figure 4.77. Comparison of processed measurements for five copies of Tag 4.

Figure 4.79 shows the response for this modified tag in comparison to the measurement and simulation for the intended tag. As can be seen, three of the spirals have their notches shift up in frequency showing that slight changes in length of the spirals could causes the mismatch between measurement and simulation seen for the eight spiral tag.

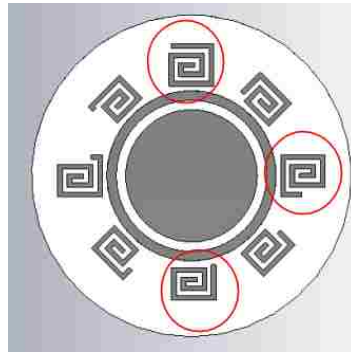


Figure 4.78. Spirals modified for simulation of manufacturing defects.

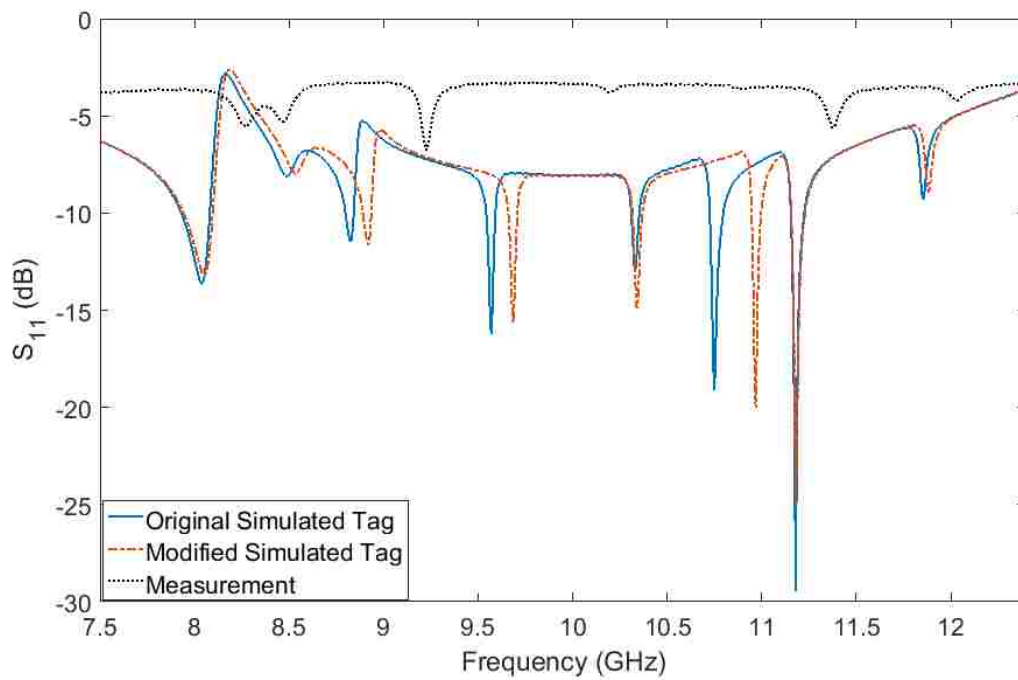


Figure 4.79. Simulation of modified tag in comparison to original tag simulation and measurement.

Following measurement of all four tags, their responses at a distance of 0.5 cm were compared to see how well the different responses could be distinguished from each other. Figure 4.80 compares the responses for the four tags. As can be seen, Tag 3 is missing a notch around 10 GHz that is present in the responses of Tags 1 and 4. This is expected based on the spiral that was removed and its associated notch. The response for Tag 4 has notches in similar locations to that of Tag 1, as is also expected. In this case, the removed spiral has its associated notch outside the frequency range of the measurements that were done.

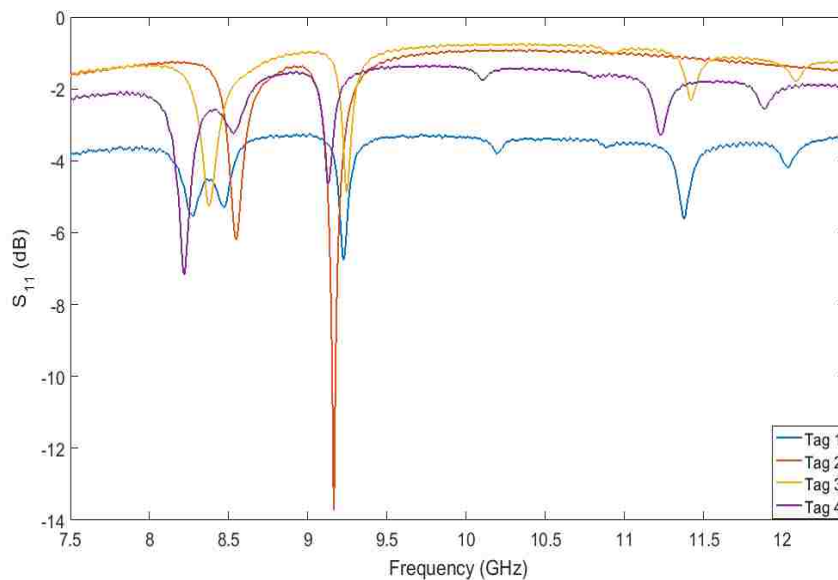


Figure 4.80. Comparison of measured responses of four tag configurations.

**4.7.1. Misalignment Simulations.** To examine the effects of misalignment, more simulations were conducted. Through these waveguide based  $S_{11}$  simulations, the effects of tag translation in the  $x$ ,  $y$ , and  $z$  directions were examined as well as the effects of tag

rotation about the  $x$ ,  $y$ , and  $z$  axes. The  $x$  direction is along the long  $a$  dimension (long dimension) of the rectangular waveguide, while the  $y$  direction is along the  $b$  dimension of the waveguide. In all cases, the eight spiral X-band tag was used. In order to overcome the effects of misalignment, a circularly polarized antenna could potentially be used [128, 129]. Another option for overcoming misalignment issues, is a polarization independent reading system like that proposed in [130], however, it comes at the cost of added complexity.

**4.7.1.1. X translation.** First, the tag was moved in both the  $-x$  and  $+x$  directions, which is along the ‘ $a$ ’ dimension of the waveguide, in 1 mm increments at a distance of 0.5 cm. The tag was only moved up to 5 mm in each direction to look at plausible misalignments that could happen in measurement. Figures 4.81 and 4.82 show the results of this translation. In both the case of  $+x$  and  $-x$  translation, it can be seen that the notches change in magnitude but do not shift in frequency.

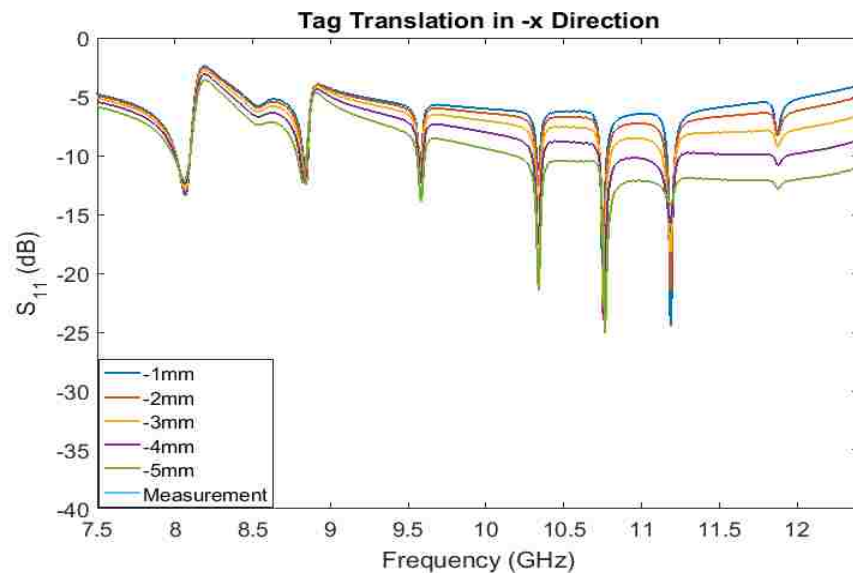


Figure 4.81. Translation of tag in  $-x$  direction.



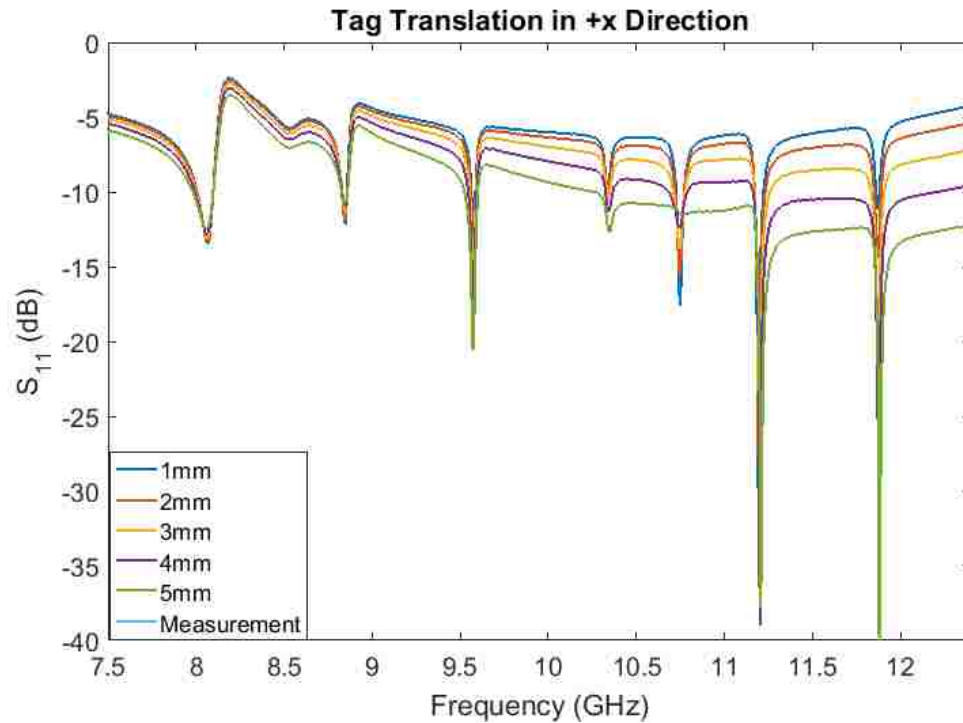


Figure 4.82. Translation of tag in +x direction.

**4.7.1.2. Y translation.** The second case investigated involved moving the tag in the  $-y$  and  $+y$  directions. For these cases, the tag was again moved in 1 mm increments at a distance of 0.5 cm from the waveguide aperture. Figures 4.83 and 4.84 show the results for translation in the  $-y$  and  $+y$  directions, respectively. From these figures it can be seen that for Y-direction translation, the  $S_{11}$  magnitude tends to change, but the notches do not shift in frequency. Thus, it can be concluded that Y-direction translation misalignment is not the causes of the shifted and missing notches in the measured response.

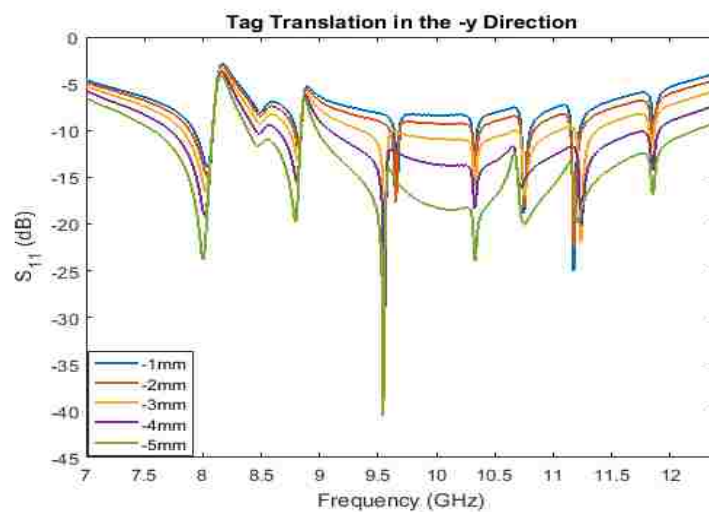


Figure 4.83. Translation of tag in  $-y$  direction.

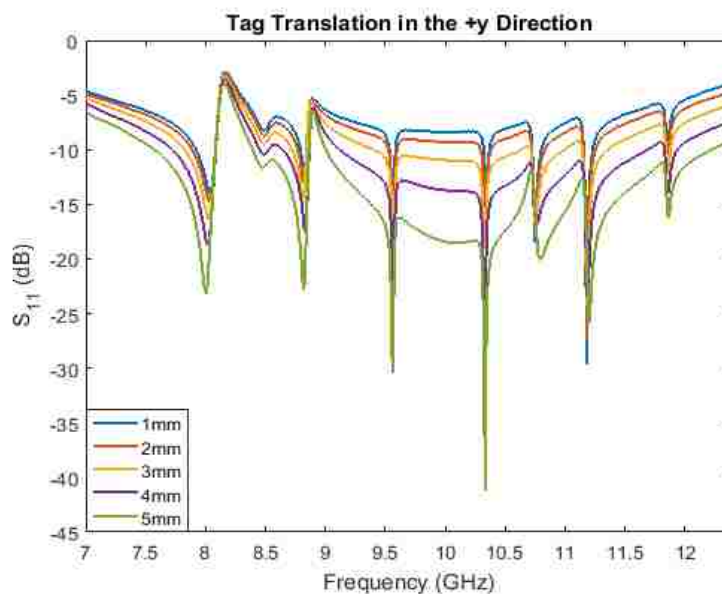


Figure 4.84. Translation of tag in  $+y$  direction.

**4.7.1.3. Z translation.** It is known that  $S_{11}$  measurements are distance dependent. To examine this dependence first, small  $z$ -direction translations were examined. For these, the tag was moved toward the waveguide 1 mm (-1 mm translation

for a distance of 4 mm from waveguide aperture to tag) and away from the waveguide 1 mm (+1 mm translation). The results in comparison to the measurement at a 5 mm distance are shown in Figure 4.85. From Figure 4.85 it can be seen that the -1 mm

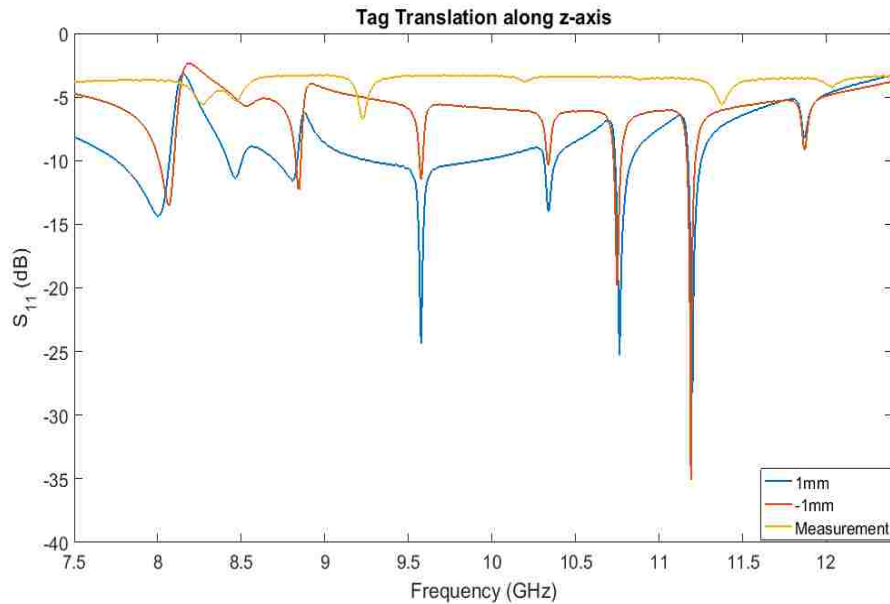


Figure 4.85. Translation of tag along  $z$ -direction.

translation produces a higher magnitude response. This makes sense because the tag is closer to the waveguide aperture. However, in both translation cases, the notches again do not shift much in frequency. While small errors in  $z$  distance between the tag and waveguide aperture could cause differences between the measurement and the simulation, this still does not account for the frequency shift of notches seen in the measurement.

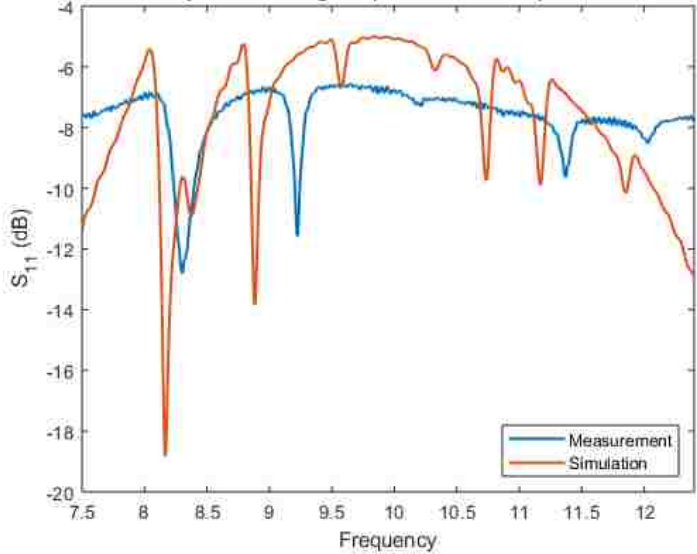
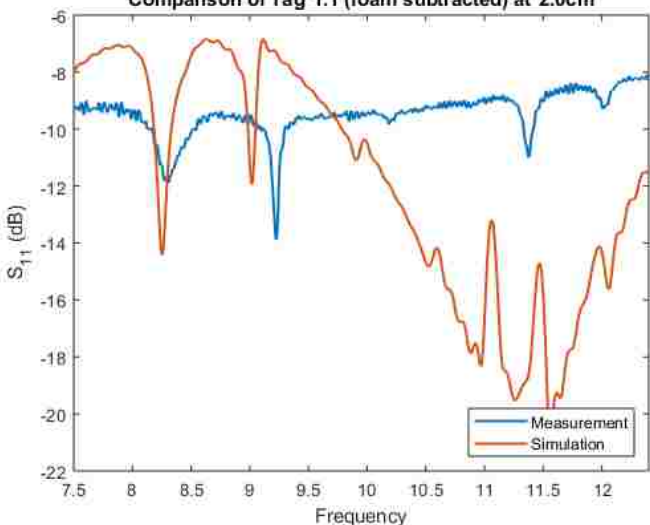
Next, a comparison was done greater  $z$ -direction translations. The tag was moved away from the waveguide aperture ( $+z$  direction) at 5 mm increments up to 20 mm for

both simulation and measurement. Only Tag 1.1 was used because as was shown in Figure 4.74, all five copies of Tag 1 produce similar responses. The results are reported in Table 4.4. From Table 4.4, it can be seen that the measurement and simulation results for

Table 4.4. Effect of  $z$ -direction translation on measurement and simulation.

Distance	Plot
5 mm	
10 mm	

Table 4.4. Effect of  $z$ -direction translation on measurement and simulation (cont.).

Distance	Plot
15 mm	
20 mm	

all four distances are in disagreement, but each distance also produces a different response. Because of this distance dependency, RCS measurements are often used for chipless RFID tags. However, as previously mentioned, RCS measurements are more

complex to make than  $S_{11}$  measurements. Section 6 will explore methods for making RCS measurements.

**4.7.1.4. X-axis rotation.** Next, the tag was rotated about the  $x$ -axis from  $-10^\circ$  to  $10^\circ$  in  $1^\circ$  increments. Figure 4.86 shows  $-10^\circ$  rotation of the tag with respect to the waveguide aperture. Figures 4.87, 4.88, and 4.89 show different cases of  $x$ -axis rotation. In Figure 4.87, the responses of the tag for  $-1^\circ$ ,  $0^\circ$ , and  $1^\circ$  are shown. As can be seen, each of these responses is different and the notches shift around as the tag is rotated. Figures 4.88 and 4.89 show more drastic rotation cases. By examining these three figures, it is observed that there is not symmetry between positive and negative rotation angles (i.e.,  $+1^\circ$  and  $-1^\circ$  of rotation do not produce the same response). In all cases, though, the notches tend to shift around. This means that  $x$ -axis rotation could be contributing to the difference between measurement and simulation of the tags seen in Figure 4.71.

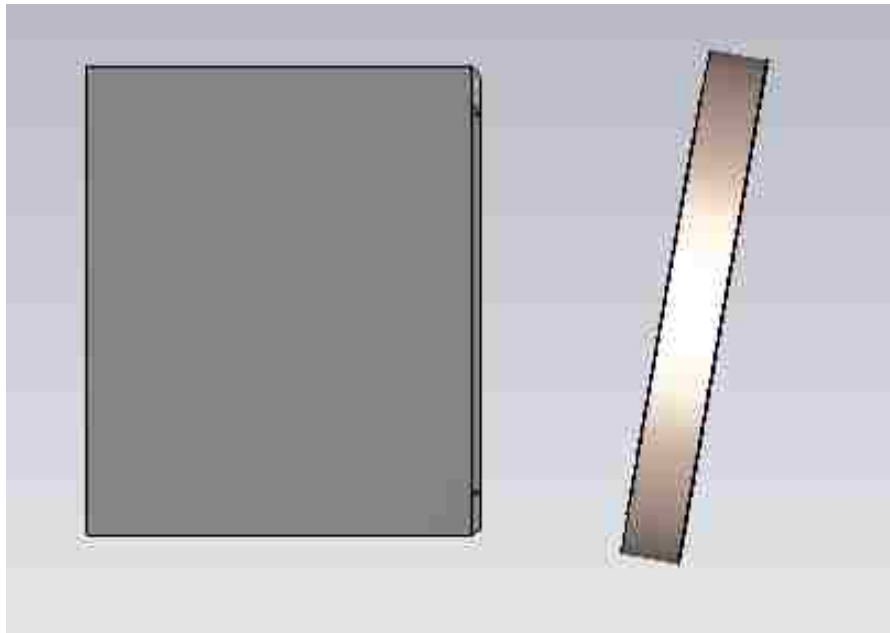


Figure 4.86. Depiction of  $x$ -axis rotation of tag.

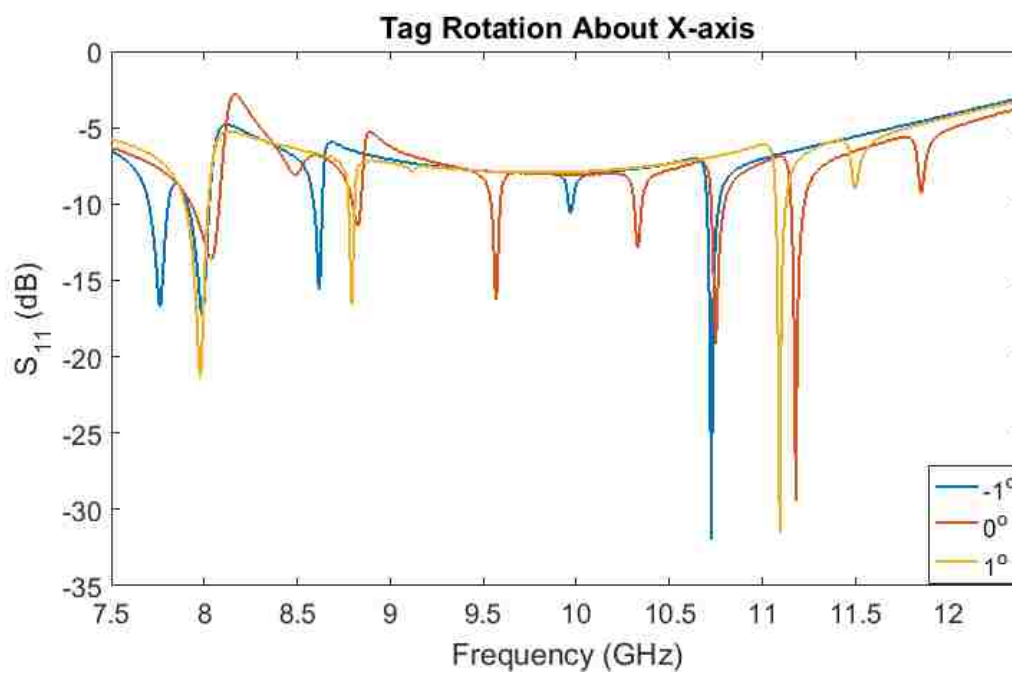


Figure 4.87.  $x$ -axis tag rotation for  $-1^\circ$ ,  $0^\circ$ , and  $1^\circ$ .

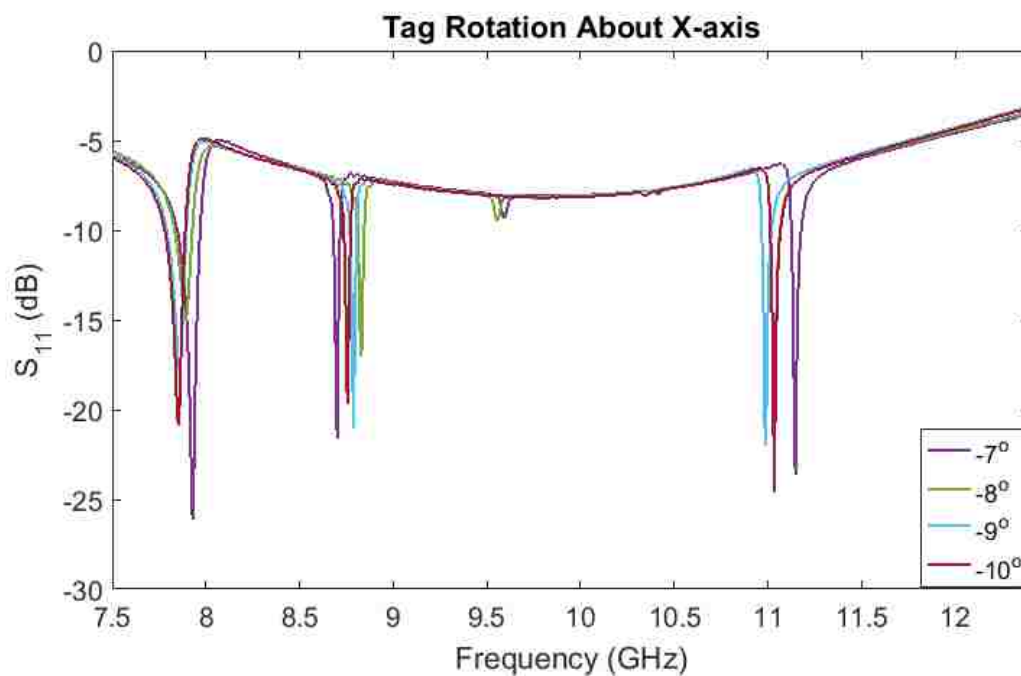


Figure 4.88.  $x$ -axis tag rotation for  $-10^\circ$  to  $-7^\circ$ .

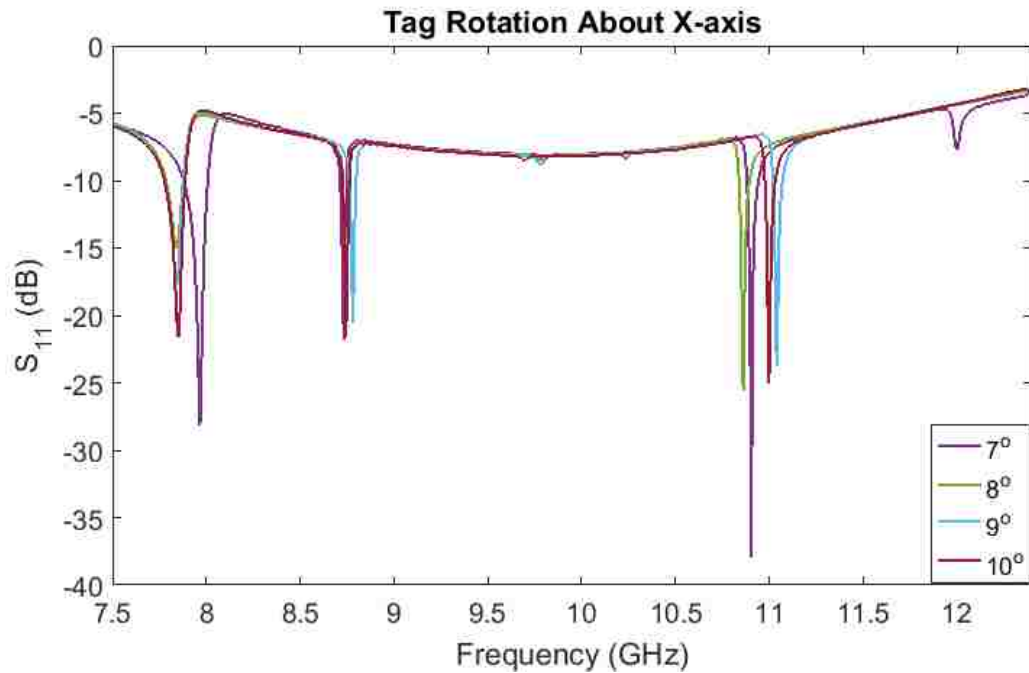


Figure 4.89.  $x$ -axis tag rotation for  $7^\circ$  to  $10^\circ$ .

**4.7.1.5. Y-axis rotation.** Rotation about the  $y$ -axis was examined next. In this case, the tag was again rotated from  $-10^\circ$  to  $10^\circ$  in  $1^\circ$  increments. Figure 4.90 shows  $-10^\circ$  of rotation of the tag about the  $y$ -axis. In Figures 4.91, 4.92, and 4.93 the same rotation cases as Figures 4.87, 4.88, and 4.89, respectively, are explored but for rotation about the  $y$ -axis rather than the  $x$ -axis. Similar to  $x$ -axis rotation,  $y$ -axis rotation produces different responses for each angle and positive and negative rotations of the same amount do not produce the same responses. Additionally, the notches shift in frequency again as the tag is rotated. This means that  $y$ -axis rotation could also contribute to the disagreement between measurement and simulation in Figure 4.71.



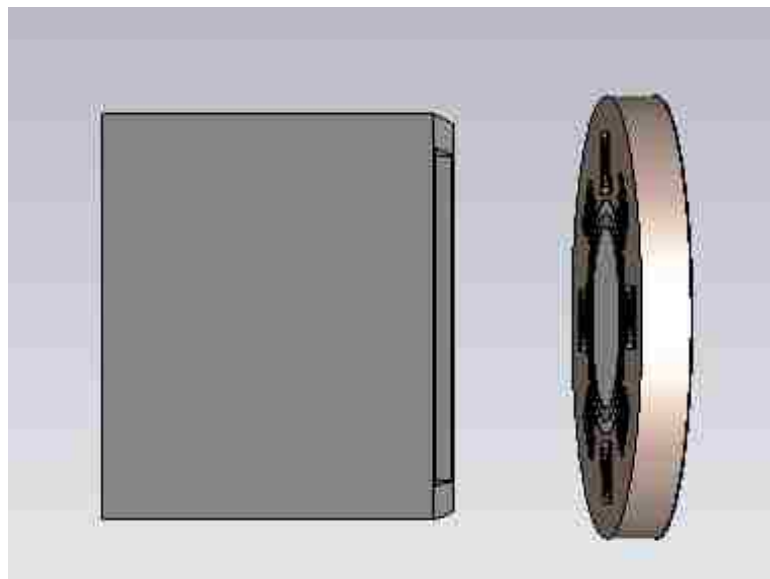


Figure 4.90. Depiction of tag rotation about y-axis.

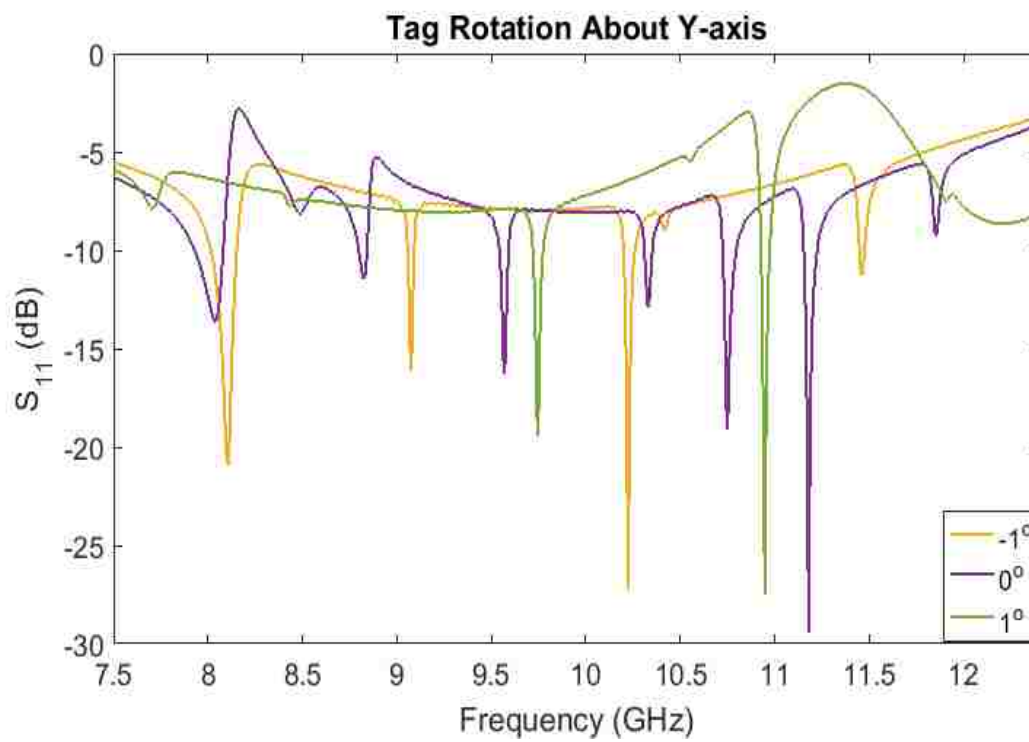


Figure 4.91. y-axis tag rotation for  $-1^\circ$ ,  $0^\circ$ , and  $1^\circ$ .

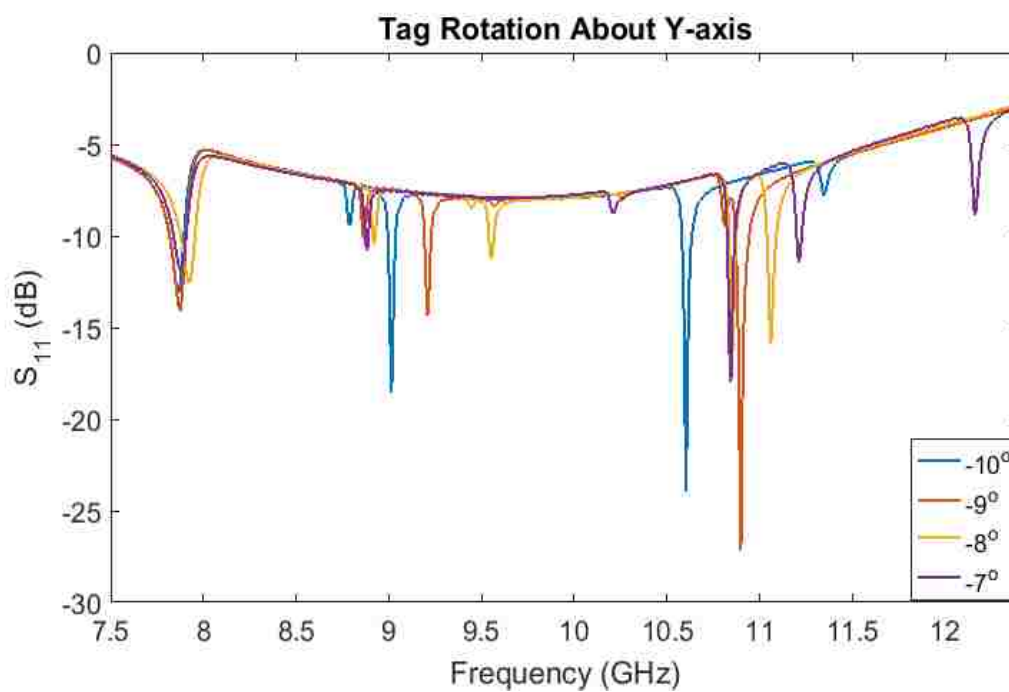


Figure 4.92. y-axis tag rotation for  $-10^\circ$  to  $-7^\circ$ .

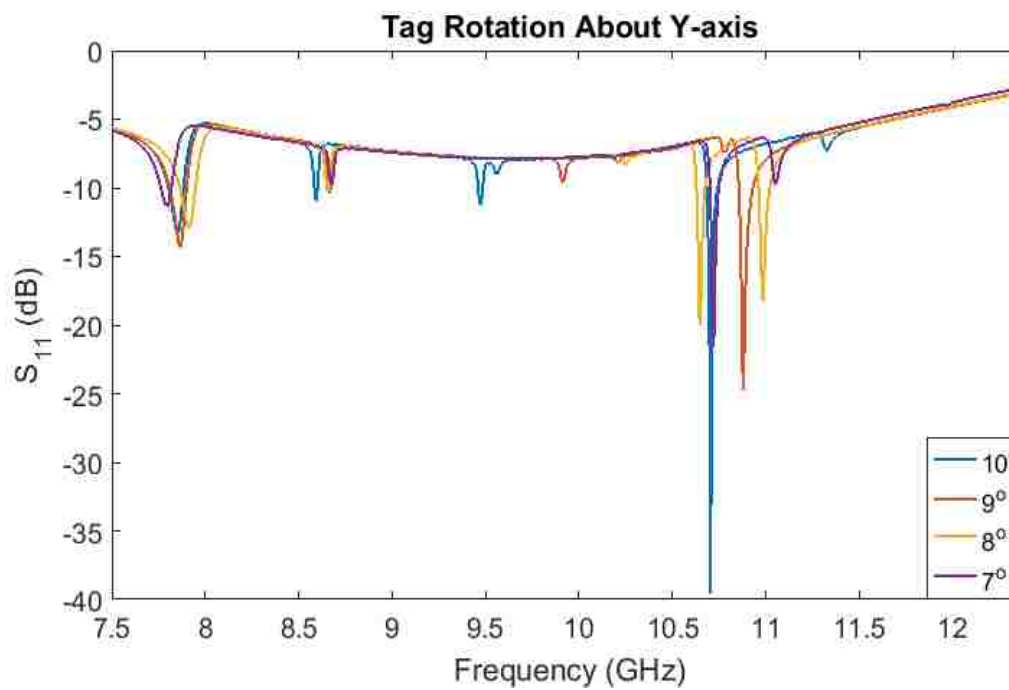


Figure 4.93. y-axis tag rotation for  $7^\circ$  to  $10^\circ$ .

**4.7.1.6. Z-axis rotation.** Lastly,  $z$ -axis rotation was examined. As previously discussed in Section 4.6.1, this tag in its four spiral configuration is very sensitive to rotation. In its eight spiral configuration it is still sensitive to rotation but less so than in its four spiral configuration. The angles provided are for counterclockwise rotation. In simulation, the tag was rotated in  $5^\circ$  increments from  $0^\circ$  to  $360^\circ$ . Both  $0^\circ$  and  $360^\circ$  were simulated as a check to ensure that the results made sense. Figure 4.94 shows results for  $90^\circ$  rotation increments. As can be seen  $0^\circ$ ,  $180^\circ$ , and  $360^\circ$  produce the same results (yellow curve) while  $90^\circ$  and  $270^\circ$  also produce the same results (green curve). These results were unexpected because the tag is not symmetrical, however, the electric field of the waveguide interacts with the tag in the same way for these  $180^\circ$  offsets. This phenomenon was also corroborated with measurement, shown in Figure 4.95 where results for  $0^\circ$  and  $180^\circ$  are exactly on top of each other in simulation and almost on top of each other in measurement.

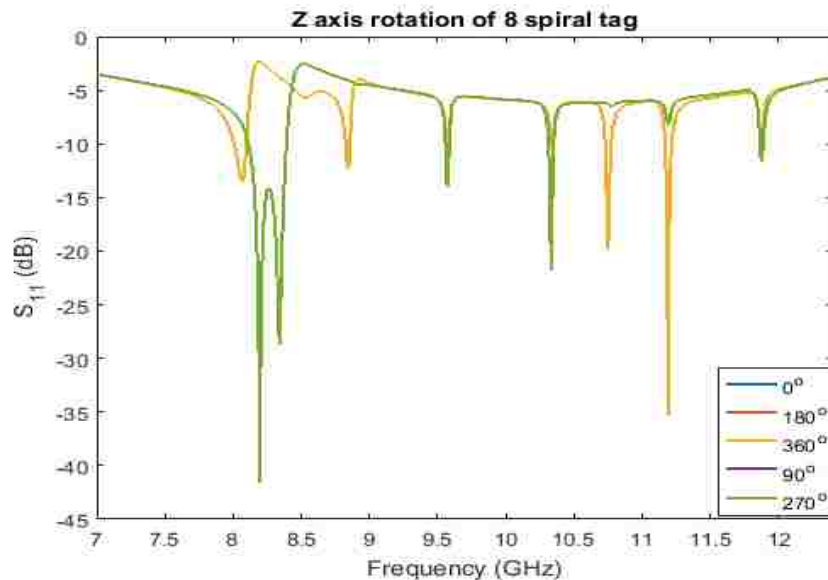


Figure 4.94. Simulation of  $z$ -axis tag rotation.

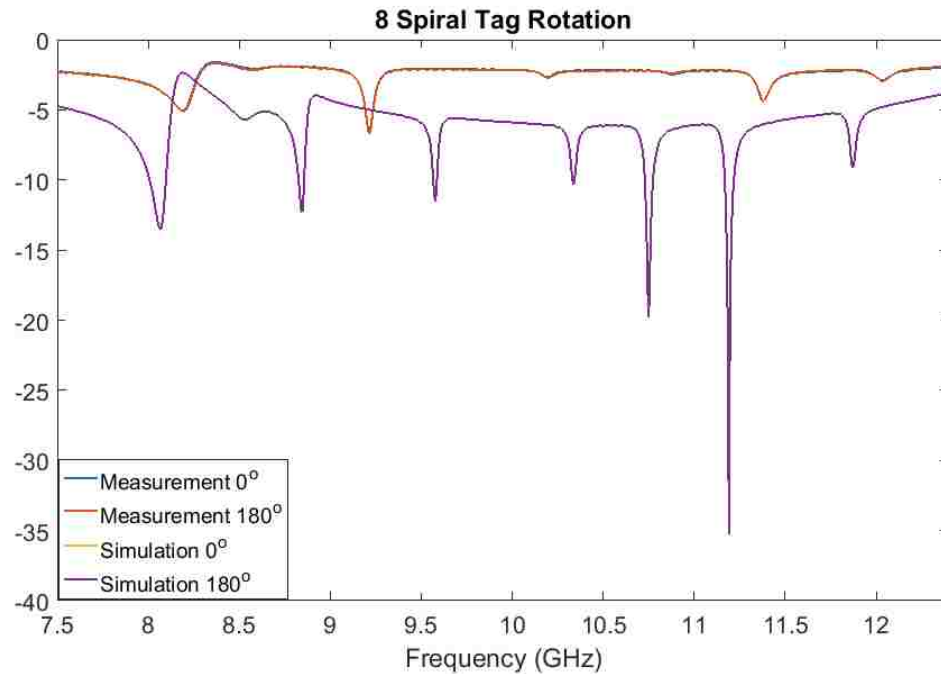


Figure 4.95. Comparison of simulation and measurement for  $z$ -axis tag rotation.

Next, the  $45^\circ$  increments were compared and this phenomena of  $180^\circ$  pairs producing the same response no longer holds. For the case of  $45^\circ$  and  $225^\circ$  and the case of  $135^\circ$  and  $315^\circ$ , shown in Figures 4.96 and 4.97 respectively, there is a slight difference between the two simulated responses. This is believed to be due to the lack of symmetry in the tag and how the electric field interacts with the spirals in these positions.

Lastly,  $5^\circ$  increments of rotation were examined. Figures 4.98 and 4.99 show these results. From these figures it can be seen that there are differences in response for  $5^\circ$  changes in rotation and differences depending on the direction of rotation (i.e.,  $+5^\circ$  of rotation produces a different response than  $-5^\circ$  of rotation). In all of these cases shifts in notches are seen, meaning that  $z$ -axis rotation could also contribute to the differences between measurement and simulation seen in Figure 4.71.

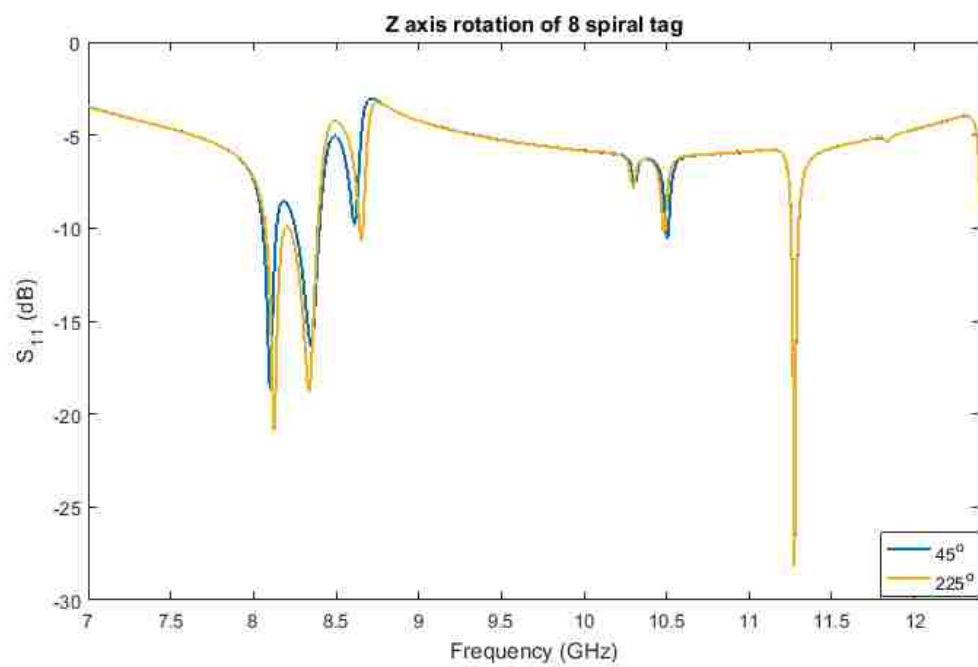


Figure 4.96.  $z$ -axis tag rotation for 45° and 225°.

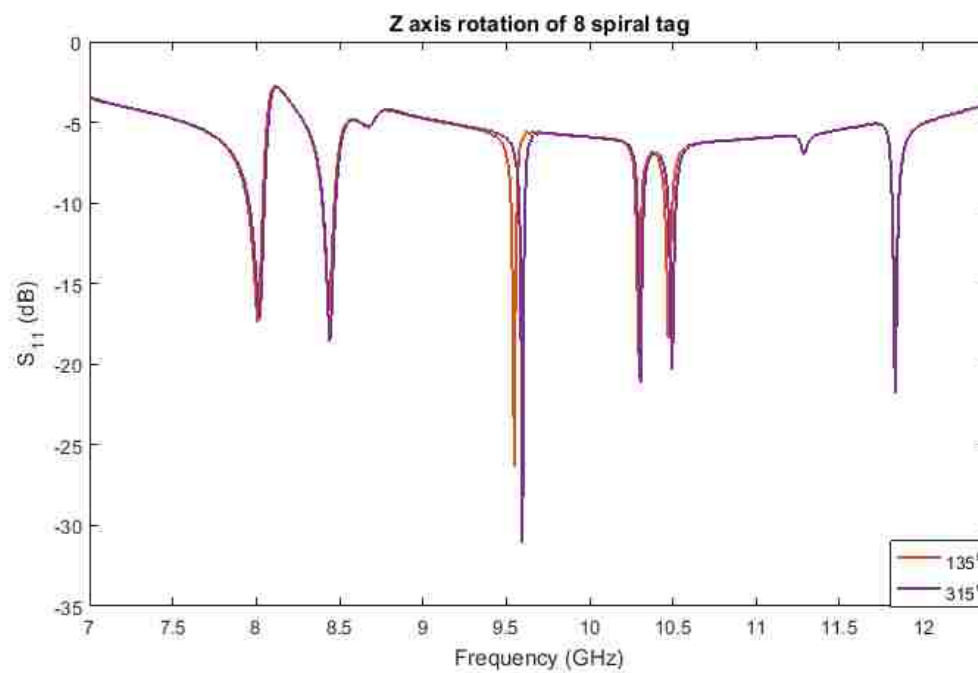
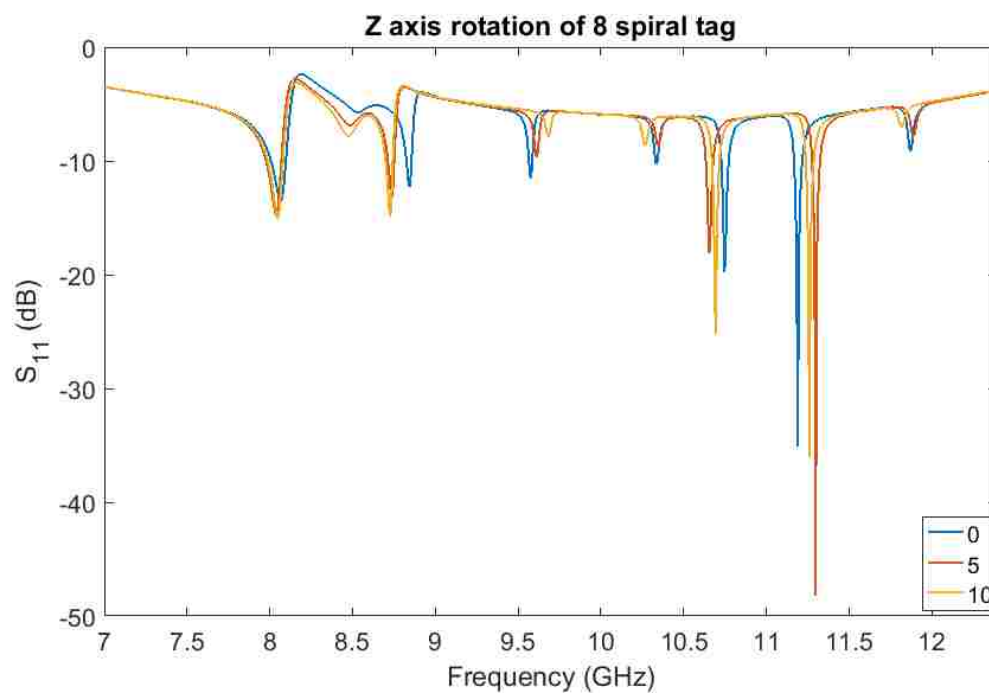
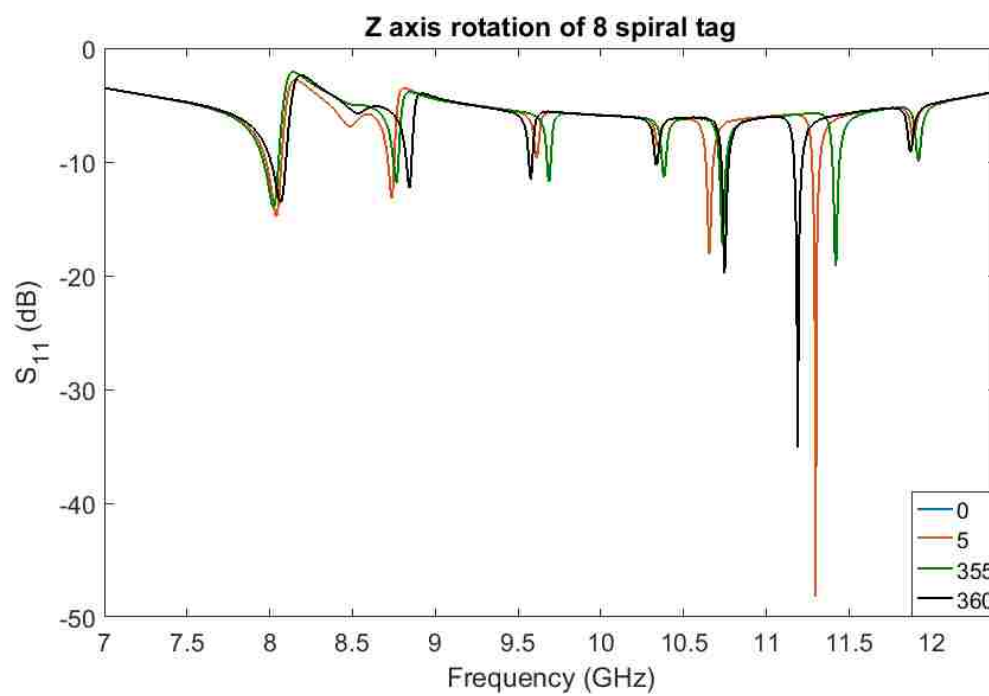


Figure 4.97.  $z$ -axis tag rotation for 135° and 315°.

Figure 4.98.  $z$ -axis tag rotation for  $0^\circ$  to  $10^\circ$ .Figure 4.99.  $z$ -axis tag rotation for  $-5^\circ$  to  $5^\circ$ .

## 4.8. DISCUSSION

In this section the work done in [104] and [108] was built on. To this end, a tag design methodology was presented and then utilized to develop a tag design. Design guidelines that can be used to adapt tags to different applications were then presented and utilized to optimize the tag for a different frequency range, rotation sensing, ID application, and embedded materials characterization. A method to associate tag geometry with response characteristics by using surface current density simulations was also discussed. Lastly, the tag of Section 4.3 was fabricated in four different configurations and measured. It was found that while the single spiral tag configuration agrees well with simulation results, the other three configurations do not. To this end, simulations were conducted to examine the effects of manufacturing defects and misalignment. It was found that slight changes in the length of spirals as well as slight rotations of the tag could cause the shift of notches like was seen in the measurement results. Additionally, translational errors in the  $xy$  directions can cause changes in the magnitude of the response, while translational errors in the  $z$  direction can cause the response to change shape. To mitigate some of these effects RCS measurements can be conducted, however, this comes at the cost of additional measurement complexity. RCS measurements will be explored further in Section 6.

## **5. INKJET-PRINTING AS A MEANS OF TAG MANUFACTURING**

### **5.1. PREMISE**

Inkjet-printing has gained a lot of attention in the chipless RFID community as a way to produce tags in a quick and inexpensive manner, making them easily deployable and potentially ubiquitous. While many chipless RFID tags claim to be “printable”, very few have actually been printed and measured. Many of these “printable” tags are for ID applications [21, 29, 35, 52, 54, 59, 68, 131]. However, there have been a few cases of printable and printed tags for sensing applications [50, 73, 132]. Additionally, there is a lack of consensus on the dielectric properties of common printing papers and a lack of information as to the conductivity that should be expected from inkjet-printing. This section seeks to expand the information available in both of these areas and examine how these printing parameters can be used in simulation to better predict the responses of printed tags. For this work, a Brother® desktop inkjet-printer (MFC-J680DW) is used with silver nano-particle ink (Mitsubishi NBSIJ-FD02). This printer was chosen based on previous work for its high dpi, ability to print conductive ink, relative inexpensiveness, and high ink deposition [40-43, 50, 98, 133, 134]. Work presented in this section is from [135], [136], and beyond.

### **5.2. PRINTING PAPER DIELECTRIC PROPERTIES**

The dielectric properties of printing papers must be known in order to properly simulate the EM properties of tags. Previously, the dielectric properties of some common printing papers have been measured using a variety of methods including ring resonators, T-resonators, co-planar waveguides, cavities, split ring resonators, and through-reflect



lines up to 12.5 GHz [42, 97, 98, 137-139]. These values have then been applied to applications up to 24 GHz, despite dielectric properties being frequency dependent [140]. Table 5.1 shows the previously reported dielectric properties of common inkjet-printing papers and their method of determination. In most of these cases, the type of photo paper used was not specified and the type of Mitsubishi paper used in [137] was not stated. Since all of these methods except the cavity used in [138], require that a resonator or coplanar waveguide be fabricated on the paper in order to measure the dielectric properties, manufacturing errors can also affect the results.

Table 5.1. Reported dielectric properties of printing papers.

Method	Paper Type	Dielectric Property Results	Frequency Range (GHz)	Reference
T-Resonator printed with Dimatix Printer using silver nanoparticle ink	Photo Paper	$\epsilon_r = 2.9 \text{ to } 3.2$	0.6 - 10	[42]
Co-planar waveguide printed with Epson printer using silver nanoparticle ink	Mitsubishi (NB-TP-3GU100) - PET	$\epsilon_r = 6.7$ $\tan\delta = 0.11$	0 - 3	[97]
	Mitsubishi (NB-RC-3GR120)	$\epsilon_r = 3.6$ $\tan\delta = 0.14$	0 - 3	
	HP Premium Plus Photo Paper	$\epsilon_r = 5.2$ $\tan\delta = 0.11$	0 - 3	

Table 5.1. Reported dielectric properties of printing papers (cont.).

Method	Paper Type	Dielectric Property Results	Frequency Range (GHz)	Reference
Ring resonator and Through-Reflect Lines made with copper adhesive laminate	Commercial paper with hydrophobic coating	$\epsilon_r = 3.28$ $\tan\delta = 0.061$	0 - 2	[98]
Ring resonator	Commercial paper with hydrophobic coating	$\epsilon_r = 3.2$ $\tan\delta = 0.077$	0.5 – 2.5	[44]
Value reported without method described or cited	Mitsubishi Photo Paper	$\epsilon_r = 2.9$ $\tan\delta = 0.061$	1	[137]
Transmission line made of conductive adhesive	Kodak Photo Paper	$\epsilon_r = 3.2$ $\tan\delta = 0.08$	Not specified	[141]
Damaskos Metallic cavity	Glossy paper	$\epsilon_r = 2.85$ $\tan\delta = 0.08$	5.8	[138]
T-resonator on multilayer substrate (paper layers bonded together), inkjet printed with 5 layers of silver nanoparticle ink	Photo Paper	$\epsilon_r = 2.8$	10	[41]
Split ring resonator printed with Dimatix printer	Commercial photo paper	$\epsilon_r = 2.9$ to 3.4 $\tan\delta = 0.06$	1 – 10	[139]

To the best of the author's knowledge, the dielectric properties of these papers have not been measured and reported above 12.5 GHz. To this end, measurements were conducted using the open-ended waveguide method of [95] to determine the dielectric properties of four different papers from X-band (8.2 – 12.4 GHz) through K-band (18 – 26.5 GHz). The four different papers are Mitsubishi® paper (NB-TP-3GU100), Mitsubishi® paper (NB-RC-3GR120), HP® Photo Paper (CR758A), and LD® Glossy Photo Sticker Paper (HYPSTICK100). The two types of Mitsubishi paper and the photo paper are common to inkjet printing, while the photo sticker paper is used because it advantageous to be able to easily adhere printed tags to structures when doing SHM. Table 5.2 tabulates the thickness of each paper, as this information is necessary for both calculation of dielectric properties and for simulation of printed tags.

Table 5.2. Printing paper thicknesses.

Paper	Thickness (mm)
Mitsubishi® Paper (NB-TP-3GU100)	0.135
Mitsubishi® Paper (NB-RC-3GR120)	0.177
HP® Photo Paper (CR758A)	0.267
LD® Photo Sticker Paper (HYPSTICK100)	0.279

The open-ended waveguide method described in [95] was used for measurement. This method has the benefit of not requiring a conductive circuit to be manufactured on the paper, which means that there are fewer sources of potential error. At X-band, Ku-band, and K-band, the  $S_{11}$  of papers of all 4 types were measured. The measurement

setup, shown in Figure 5.1, consists of a waveguide with a flange pointing towards the ceiling. For x-band and k-band, a modified flange, like that presented in [127] and shown in Figure 5.1, is used because it mimics an infinite flange. For Ku-band, an elliptical flange was used because it was what was available. For each paper measurement at each frequency band, multiple samples were measured multiple times. The side of the paper that is printed on was faced towards the aperture of the waveguide, since this is the side the waveguide would see of printed tags.



Figure 5.1. Setup for measurement of dielectric properties of paper.

An example of one of the measurements and the recalculated reflection coefficient used to determine the dielectric properties is shown in Figure 5.2. Figure 5.2 is for a Mitsubishi® paper (NB-TP-3GU100) sample at X-band. Table 5.3 tabulates the

dielectric properties for all four papers at the 3 different frequency bands. These results except for those for Mitsubishi® Paper (NB-RC-3GR120) were presented previously in [135].

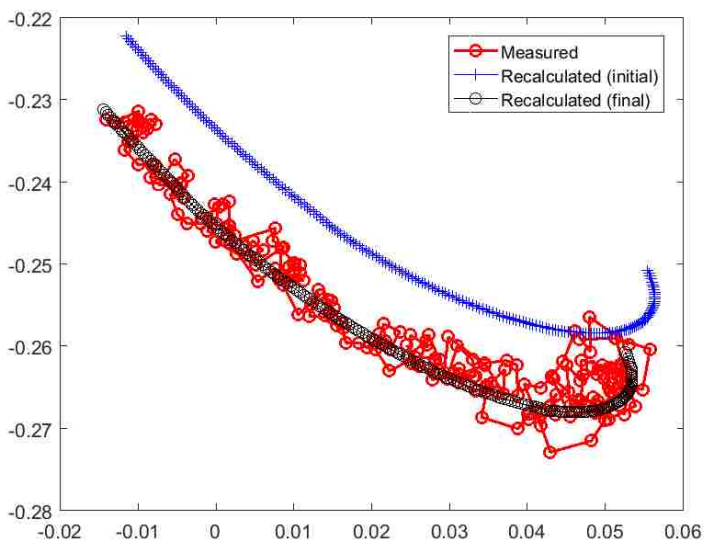


Figure 5.2. Measurement and recalculation for dielectric property determination.

Table 5.3. Dielectric properties of papers.

Paper	X-band	Ku-band	K-band
Mitsubishi® Paper (NB-TP-3GU100)	2.41-j0.16	2.348-j0.132	2.452-j0.192
Mitsubishi® Paper (NB-RC-3GR120)	2.47-j0.094	2.23-j0.032	2.23-j0.026
HP® Photo Paper	2.11-j0.12	1.92-j0.10	2.17-j0.09
LD® Photo Sticker Paper	2.14-j0.11	2.08-j0.29	2.14-j0.09

The results shown in Table 5.3 show that the relative permittivity of the Mitsubishi® paper (NB-TP-3GU100) is approximately 2.4. This is reasonable since it is made of polyethylene terephthalate (PET) which has a relative permittivity of about 2.3. Cellulose paper's relative permittivity tends to range from 2-3, so the reported values for the other papers, which are also cellulose based, are also reasonable. For these types of measurements, air gaps between the waveguide aperture and the material being measured can introduce some measurement inaccuracies. It should also be noted that these reported values are lower than those reported previously in Table 5.1.

### **5.3. CONDUCTIVITY DETERMINATION**

Understanding how the conductivity of printed tags affects their performance is also important. Previously, it has been demonstrated that reduced conductivity that is inherent to inkjet-printing, in comparison to traditional microstrip line, results in reduced magnitude of resonances [37]. This can make measuring the tag difficult and it can affect the binary code associated with the tag depending on the coding method used. To this end, two different experiments were conducted to evaluate the conductivity of inkjet-printed tags.

In the first experiment, a 4 cm x 4 cm square was printed. This square was then measured as a microwave short with an X-band waveguide and the result was compared to a calibration kit microwave short. The printed short is shown in Figure 5.3 and the results of this experiment are shown in Figure 5.4. From the results it can be seen that the printed short does not behave like a perfect short, however, it does behave similarly to the calibration kit short.



Figure 5.3. Printed microwave short.

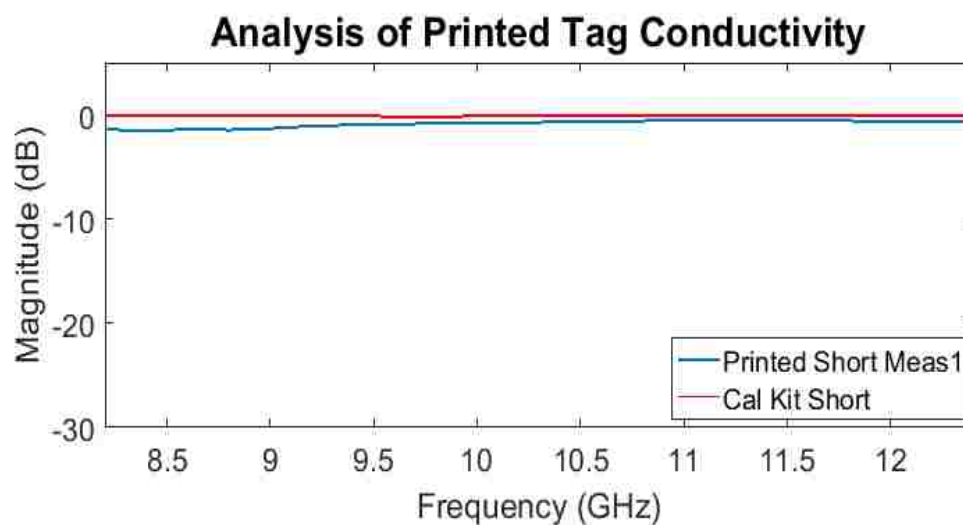


Figure 5.4. Comparison of printed short to calibration kit short.

The second experiment involved using a microwave X-band resonant cavity that was specifically optimized for measuring surface resistivity [142]. This method has a few advantages over four point probe methods, like those used in [42], such as being able to be used for bulk features rather than thin traces and not needing to touch the surface of the print with probes, as this can easily causes scratches on the print surface and affect

conductivity. This susceptibility to scratches and wear will be examined further in Section 5.3.1. When using this cavity, the method presented in [143] can be used to calculate the conductivity from the surface resistance of cavity lids using Equations (12) and (13) below:

$$R_s = \frac{1}{\alpha} \left( \frac{1}{Q^i} - \frac{1}{Q^{ref}} \right) + R_s^{ref} \quad (12)$$

$$\sigma = \frac{\pi \mu_0 f}{(R_s)^2} \quad (13)$$

In Equation (12),  $R_s$  is the surface resistance,  $Q^i$  is the measured Q-factor of the material under test (MUT),  $Q^{ref}$  is the measured Q-factor of the reference material, and  $\alpha$  is a constant that is related to the mode the cavity is operated in and the dimensions of the cavity.  $\alpha$  can be derived from [144] and [145] and expressed mathematically as Equation (14):

$$\alpha = \frac{2}{ka\eta} \quad (14)$$

In Equation (14)  $a$  is the radius of the cavity,  $\eta$  is the intrinsic impedance, and  $k$  is the wave number. Equations (15) and (16) express the intrinsic impedance and wave number, respectively, while Equation (17) expresses the resonant frequency for TE  $nml$  mode,

$f_{nml}$  :

$$\eta = \frac{377}{\sqrt{\epsilon_r}} \quad (15)$$

$$k = \frac{2\pi f_{nml} \sqrt{\epsilon_r}}{c} \quad (16)$$



$$f_{nml} = \frac{c}{2\pi\sqrt{\mu_r\epsilon_r}} \sqrt{\left(\frac{p'_{nm}}{a}\right)^2 + \left(\frac{l\pi}{d}\right)^2} \quad (17)$$

In Equation (17),  $p'_{nm}$  is the  $n$ th root of the Bessel function  $J'_n$  and  $d$  is the height of the cavity.

The cavity used is operated in the  $TE_{012}$  mode which has a resonant frequency of 11.45 GHz. The dimensions of the cavity are  $a=22.5$  mm and  $d=37.2$  mm. A CST Microwave Studio® model of the cavity is shown in Figure 5.5. The cavity is made to operate at the  $TE_{012}$  mode since at this mode, the fields circulate around the cavity as is illustrated in Figure 5.6. This allows for small gaps between the lid and cavity body to not be an issue while also providing maximum interaction between the fields and the surface of the lid. This allows for sensitivity to surface resistance and therefore conductivity. The  $S_{21}$  response of the cavity is shown in Figure 5.7 for two different lid materials – aluminum and perfect electrical conductor (PEC). The two different lid types were

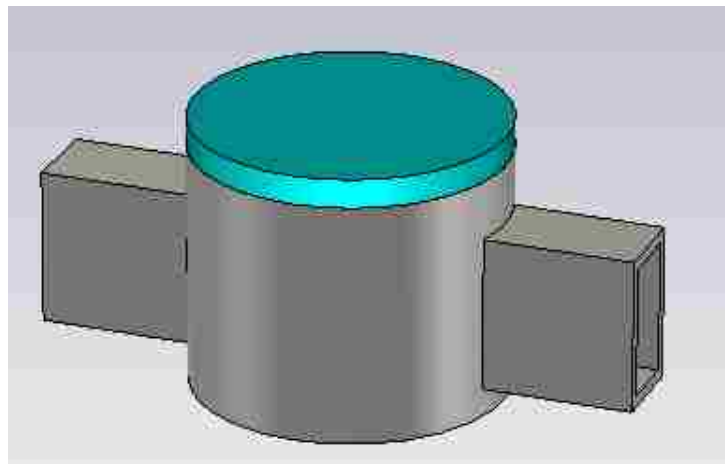


Figure 5.5. CST Microwave Studio® model of resonant cavity.

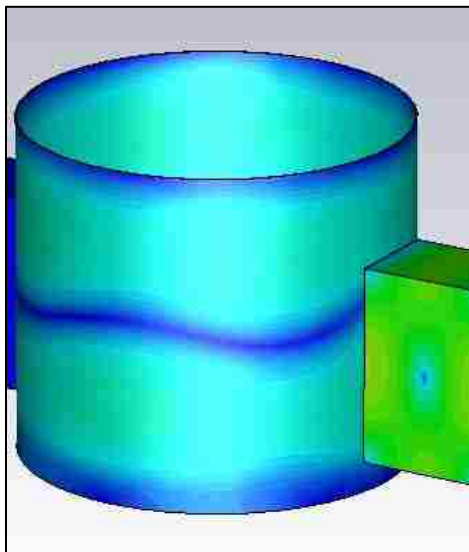


Figure 5.6. Operation of cavity at  $TE_{012}$  mode.

simulated to verify that the aluminum lid of the physical cavity would be sufficient for these measurements. From Figure 5.7, agreement between the aluminum and PEC lids can be seen around the 11.45 GHz frequency range where the cavity was to be operated.

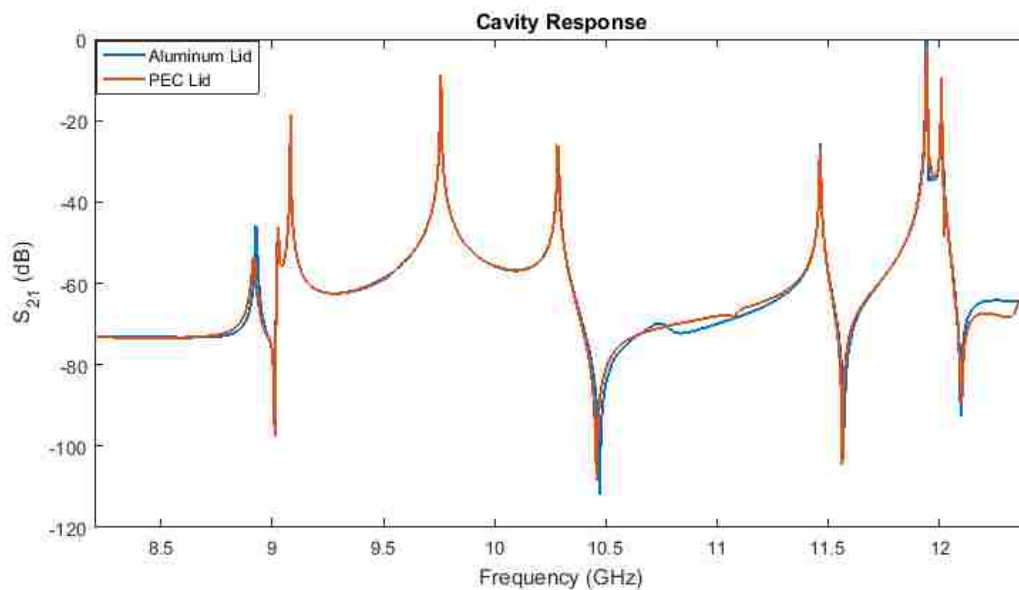


Figure 5.7. Simulated  $S_{21}$  response of resonant cavity.

To show further cause for using this approach for measuring conductivity, additional simulations were conducted. In these simulations, the conductivity of the cavity lid was changed and the Q-factor of the resonance at 11.45 GHz was examined. Figure 5.8 shows these results for three different conductivities. As can be seen, as the conductivity increases, so does the Q-factor of the resonance. The results of further simulations with different conductivities are summarized in Figure 5.9.

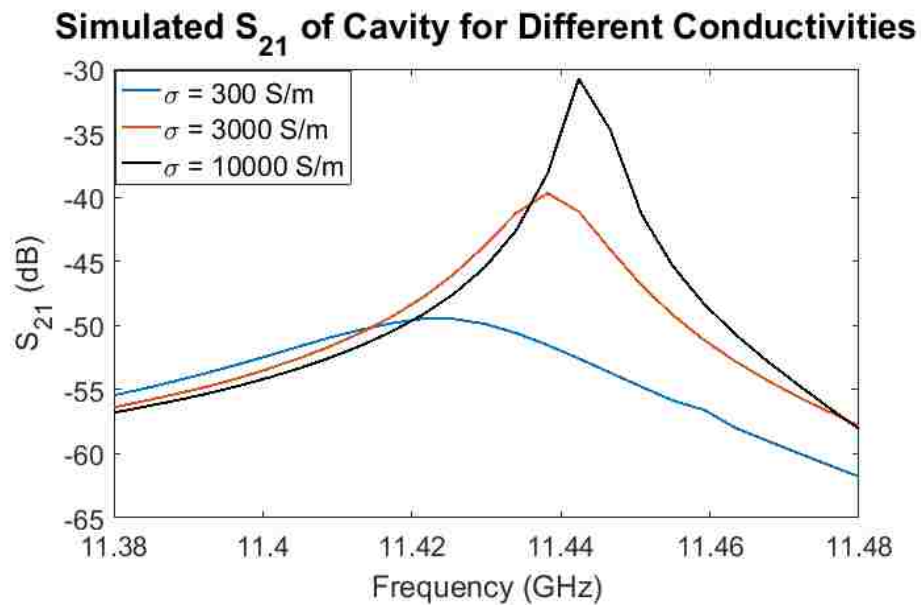


Figure 5.8. Simulated effect of conductivity on Q-factor.

Following verification of this measurement approach through simulation, measurements were conducted. For these measurements a set of samples were printed with a Brother® inkjet printer. The samples (6 cm diameter circles to fit the cavity lid) were printed on Mitsubishi® paper (NB-TP-3GU100), subsequently referred to as simply Mitsubishi® paper, HP® photo paper, and LD® photo sticker paper with the photo vivid

setting, as this setting has been shown to deposit to the most ink and lead to the most conductive prints [134]. Both single layer and two-layer prints were also prepared and multiple samples of each combination of paper and layer number were produced. Examples of printed samples are shown in Figure 5.10. The samples were then adhered to the cavity lid with double-stick tape and  $S_{21}$  was measured with a VNA. For the measurements the VNA was set up to operate from 11.3 to 11.6 GHz with 10001 frequency points to best capture high Q-factor resonances. Figure 5.11 shows the measurement setup used.

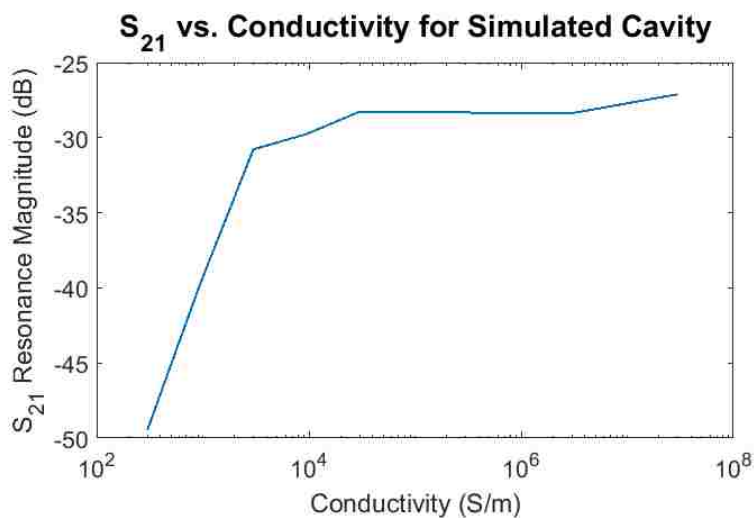


Figure 5.9.  $S_{21}$  as a function of conductivity.

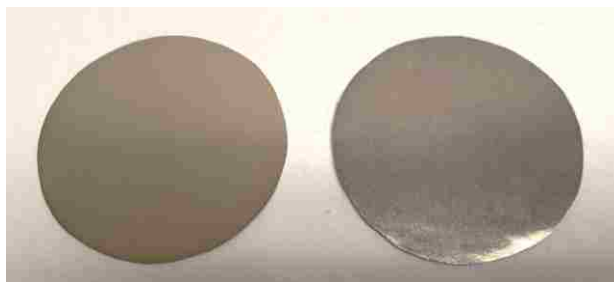


Figure 5.10. Examples of printed samples for conductivity measurement.



Figure 5.11. Measurement setup for conductivity measurements.

In performing the measurements, the aluminum cavity lid was used as the reference measurement and then multiple measurements were made with each sample. Figure 5.12 shows a comparison of Mitsubishi® paper and photo paper single layer prints with the aluminum lid. As can be seen, the aluminum lid has the highest Q-factor resonance of the three cases, as expected. Table 5.4 shows a comparison of measurements for the three different printing papers for both single layer and two-layer prints. This table demonstrates that for single layer prints, photo sticker paper has the highest Q-factor, but the resonance in this case is also shifted down in frequency from where it is supposed to be. When another print layer is added, the Q-factor for both the Mitsubishi® paper and photo paper increases, while that of the photo sticker paper decreases. However, the resonance of the photo sticker paper shifts back up in frequency to closer to where it is supposed to occur. This shift of resonance is believed to be attributed to the skin depth of

the print being larger than the print thickness, meaning that microwaves see through the print to the paper substrate. This effect will be investigated further later in this section. These Table 5.4 results show that increasing the number of layers does not always result in higher conductivity. Additionally, different papers with the same print settings can result in different conductivities, which is possibly a result of how well the paper coating causes the ink to adhere to the paper.

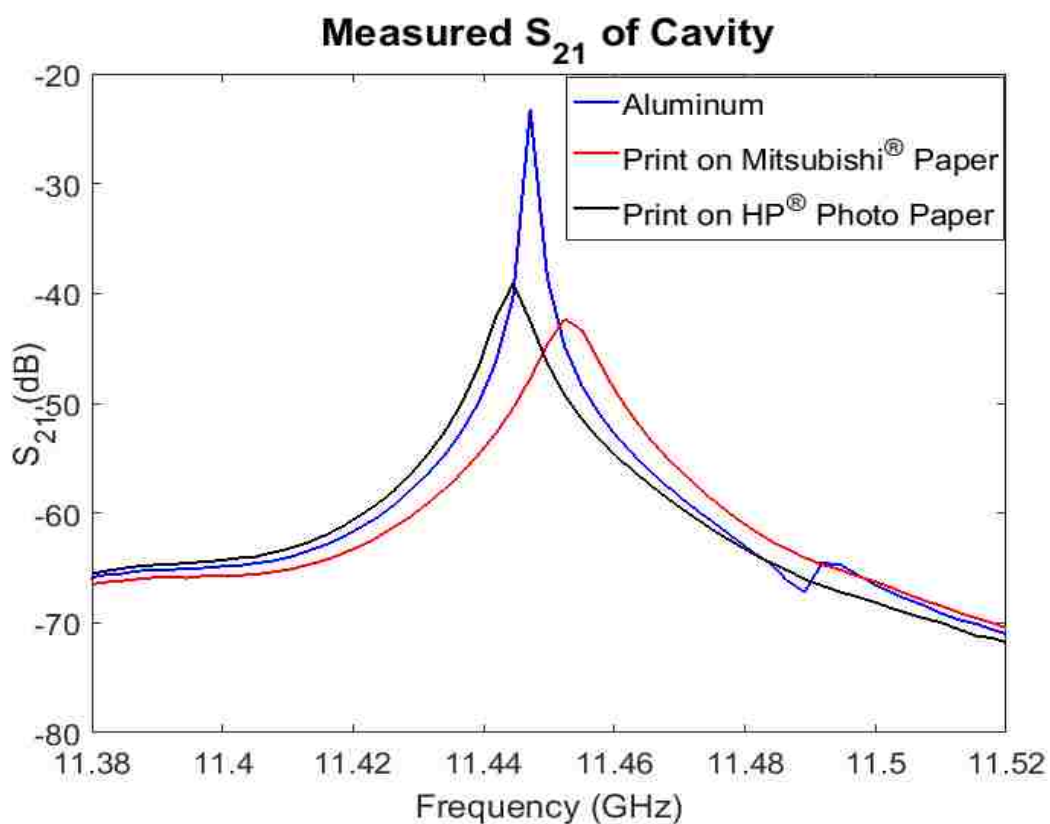
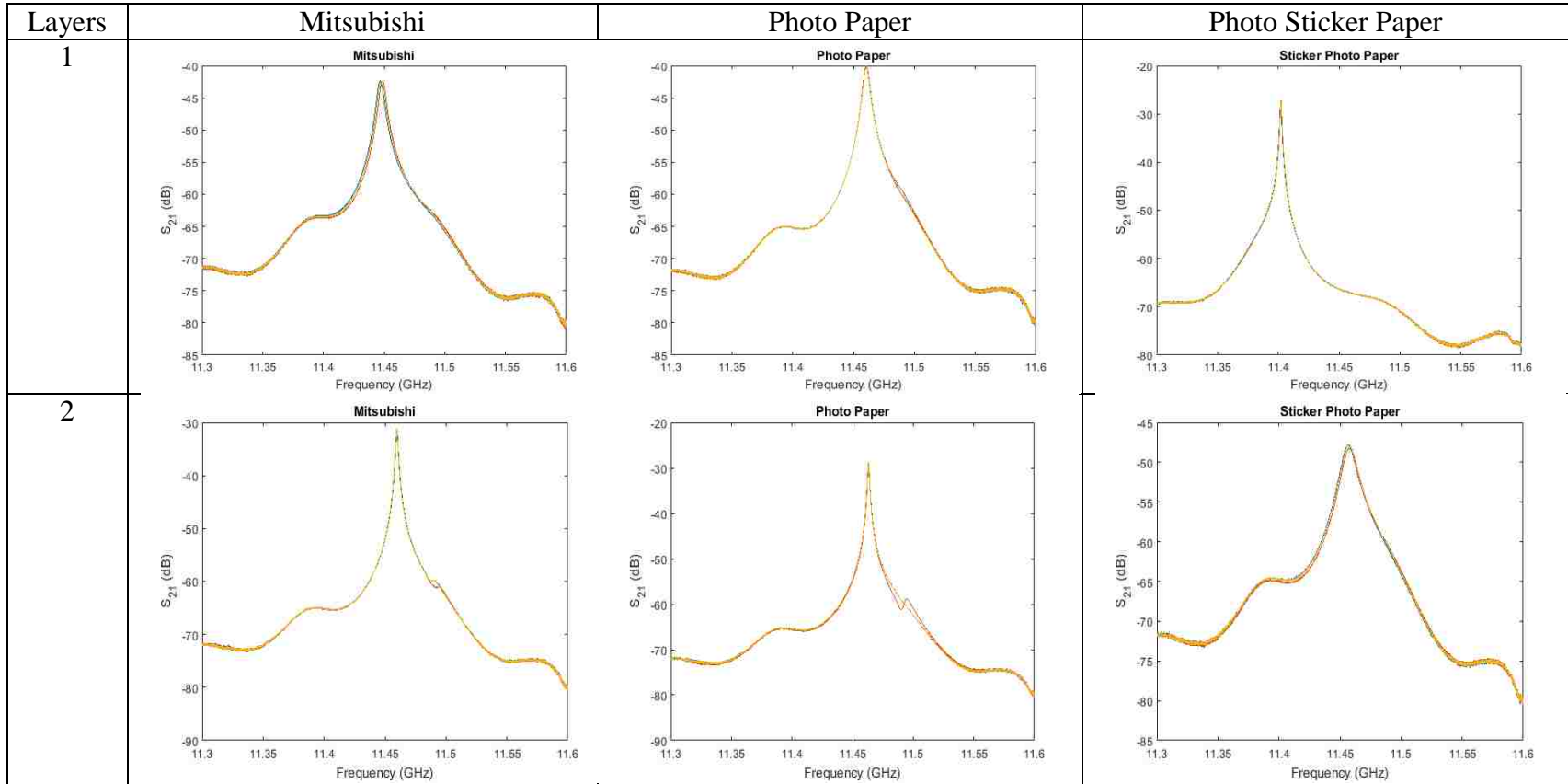


Figure 5.12. Measurement comparison of different papers with reference.

Table 5.4. Measured  $S_{21}$  of different inkjet-printed samples.



The results of Table 5.4 and the other measurement sets gathered are summarized in Table 5.5. In Table 5.5 there is a range for both Q-factor and calculated conductivity for each type of sample. These ranges show that even samples produced with the same settings can have widely varying conductivities. This quality control issue could not be tolerated in production, as tags with different conductivities will perform very differently. Table 5.5 also shows that single layer photo sticker paper prints have the highest conductivity, while adding another print layer increases the conductivity for Mitsubishi® and photo paper.

Table 5.5. Summary of conductivity measurement results.

<b>Type</b>	<b>Q range</b>	<b>Conductivity Range (S/m)</b>
Aluminum Lids	1389 - 1429	
Mitsubishi Paper: 1 layer, photo vivid	64.23 - 163.15	198.42 - 1494.9
Mitsubishi Paper: 2 layer, photo vivid	495.07 - 512.82	25909 - 28941
Photo Paper: 1 layer, photo vivid	183.82 - 210.54	1958.1 - 2696.5
Photo Paper: 2 layer, photo vivid	581.55 - 649.51	43886.8 - 65156.4



Table 5.5. Summary of conductivity measurement results (cont.).

<b>Type</b>	<b>Q range</b>	<b>Conductivity Range (S/m)</b>
Sticker Paper: 1 layer, photo vivid	746.35 - 1010.1	113386 - 597624
Sticker Paper: 2 layer, photo vivid	77.28 - 78.44	293.14 - 302.63

**5.3.1. Influences on Conductivity.** In handling samples, additional influences on conductivity were observed. It has previously been reported that bending or stretching of inkjet-printed features causes micro-cracking in the conductor. This effect has then been exploited for creating one time use strain sensors [73, 132]. To examine the effect of handling, one of the photo paper samples was smeared slightly. This effect is visible in Figure 5.13 in comparing the un-smeared sample on the left to the smeared sample on the right. The smeared sample was then measured again using the resonant cavity. The results are reported in Table 5.6. As can be seen from this table, there is a dramatic decreases in conductivity after smearing of the sample. These results do not bode well for using printed tags for structural health monitoring, as the tags would need to be handled to be installed on a structure. Sealants could be used to protect the prints, but one has to ensure that the sealant will not affect the scattering abilities of the tag or cause a change in tag response [134].



Figure 5.13. Effect of handling samples. Left: un-smearred. Right: Smearred.

Table 5.6. Effect of handling prints on conductivity.

<b>Type</b>	<b>Q-factor</b>	<b>Conductivity</b>
Aluminum Lid	1389-1429	
Photo Paper, 1 layer	183.82 – 210.54	1958.1 – 2696.5
Photo Paper, 1 layer, smearred	43.81 – 55.19	89.25 – 144.15

Print conductivity can also influence skin depth and therefore performance. As seen previously in Table 5.4, there was a shift in the resonance frequency for the single layer photo sticker paper prints. This is believed to be an effect of skin depth in relation to print thickness. Typical prints with silver nano-particle ink vary from 300 to 500 nm thick depending on the printer used [42, 134]. Skin depth is a figure of merit that describes to what extent microwaves penetrate a conductor. Mathematically, it is described as Equation (18):

$$\delta = \sqrt{\frac{2}{\omega\mu\sigma}} \quad (18)$$

As can be seen from Equation (18), skin depth is dependent on both frequency ( $\omega$ ) and conductivity ( $\sigma$ ). Figure 5.14, shows how skin depth varies for measured conductivities over a frequency range of 4 to 15 GHz. At the lowest conductivity (measured for the smeared print) the skin depth is approximately 0.85 mm at 4 GHz, which is 1700 times larger than the thickest typical single layer print. As the conductivity increases, the skin depth decreases. As previously mentioned, skin depth is a figure of merit rather than a microwave penetration cutoff point. This means that even for small skin depths or thick prints, the substrate behind the conductor can still play a role in performance.

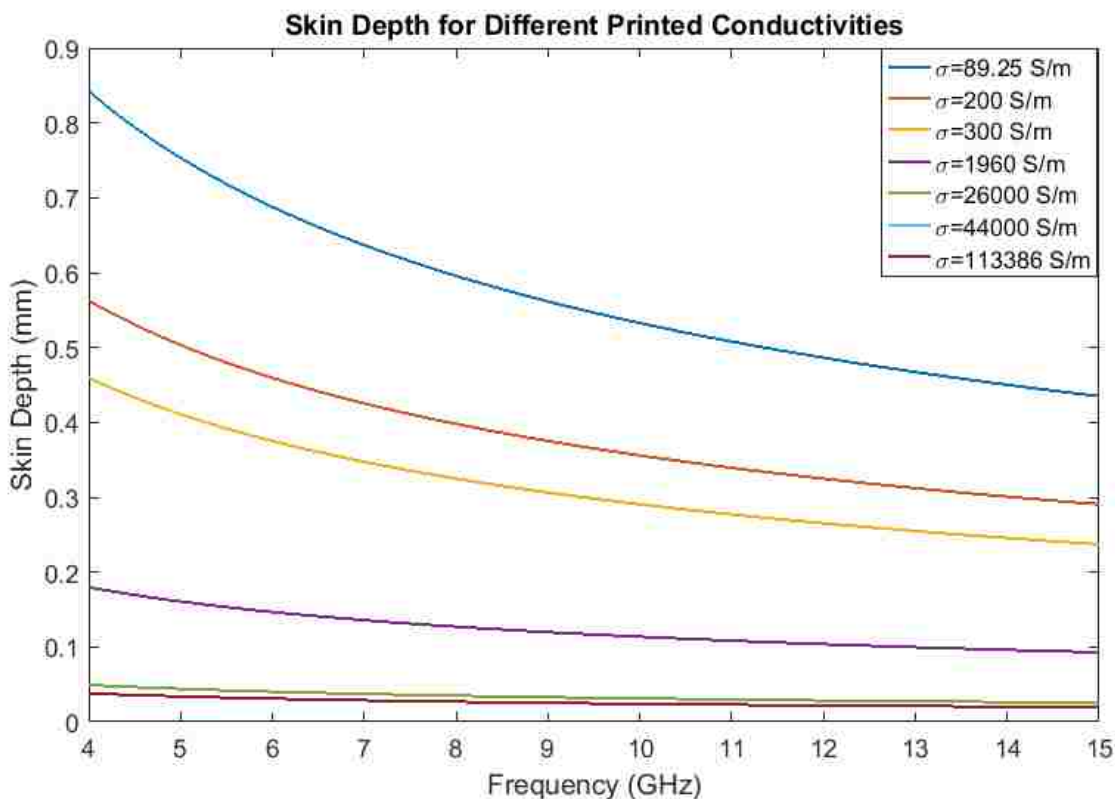


Figure 5.14. Effect of conductivity on skin depth.

**5.3.2. Improving Conductivity.** There are a variety of methods that can be used to improve conductivity. The two primary methods are sintering and multi-layer printing. Multi-layer printing has been used by [41], [42], [134], [146], and [147]. As was previously shown, though, printing multiple layers does not always result in higher conductivity. Additionally, it can be difficult to obtain alignment between printed layers which can then affect performance [134]. In terms of sintering, there are a variety of methods that can be employed.

**5.3.2.1. Thermal sintering.** Thermal sintering is one of the simpler, less expensive sintering methods that can be employed. This method, however, requires that a specific temperature profile be maintained over time and care must be taken so that the substrate is not harmed during the sintering process. Many paper- and PET- based substrates have their thermal degradation point below the temperatures that are required to break down the polymers that surround the silver nano-particles (i.e., the temperatures needed for sintering). This leads to plastic deformations and stresses of the substrate [147-153]. Figure 5.15 shows an attempt at sintering with imprecisely controlled temperature conditions. As can be seen, the sintered print on Mitsubishi® paper curled and became unusable. The print sintered on photo paper was still usable and was also viewed under a microscope. These microscope images are shown in Figure 5.16 and show that sintering provides better connectivity between the silver nano-particle ink droplets which in turn should result in better conductivity. Substrates that are more stable at higher temperatures can be used to combat this, but these substrates are more expensive, more difficult to print on, and need to be characterized before use.



Figure 5.15. Sintered prints. Left: photo paper. Right: Mitsubishi paper.

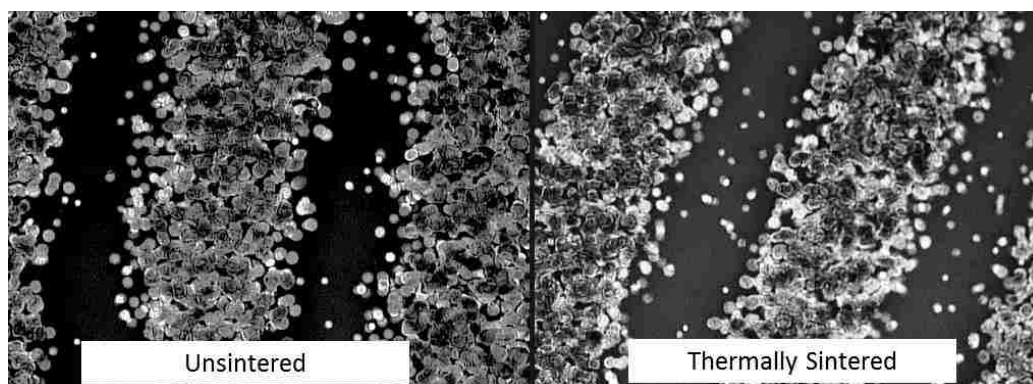


Figure 5.16. Microscope images of effect of thermal sintering.

**5.3.2.2. Laser and photonic sintering.** Laser sintering can be used to selectively thermally sinter prints. In this process the laser heats the print locally as it moves over the print. In [151] multiple laser powers and scanning speeds were tested and it was found that silver nano-particle inks require high power and fast scanning speed in order to avoid harming the substrate in the sintering process. Photonic sintering is a similar process. In photonic sintering, UV to IR pulsed light sources are used to rapidly increase the temperature locally. This method has the caveat of only working for transparent substrates that will allow the energy from the source to only be absorbed by

the ink. It is not clear opaque substrates can be used effectively with this sintering method [151].

**5.3.2.3. Electrical sintering.** Electrical sintering is one of the less common techniques. It involves applying a voltage directly to printed features with a controlled DC power supply. As voltage is applied, the current going through the print causes sintering to occur. This process takes approximately 3 ms for traces that are ~60um wide and 900 nm thick [152].

**5.3.2.4. Plasma sintering.** In [151] and [153] plasma sintering was explored as a means to increase conductivity. This method is considered to be a selective sintering technique that causes sintering to occur gradually from the top to the bottom of the print. Because of this top down process, if the print is not sintered long enough, poor adhesion between the print and the substrate can occur. Though plasma sintering, increased connectivity of silver nano-particles can be seen through microscope images, but cracks also sometimes appear in the conductor due to substrate deformation or shrinkage. This method has been shown to be effective for increasing conductivity, but it requires a plasma chamber, which is an expensive piece of equipment. This expensiveness and complexity counteracts some of the advantages of inkjet-printing with desktop inkjet printers.

## **5.4. SIMULATION WITH PRINTING PARAMETERS**

The paper dielectric properties and print conductivity results measured in the previous sections can be applied to EM models to better simulate printed tags. An example of a printable tag (i.e., a tag without a ground plane) is shown in Figure 5.17 and

its RCS vs. frequency response is shown in Figure 5.18. This tag was presented previously in [103] and this Figure 5.17 response is for when the tag is manufactured as a PCB (i.e., FR-4 substrate of 0.5mm thickness).

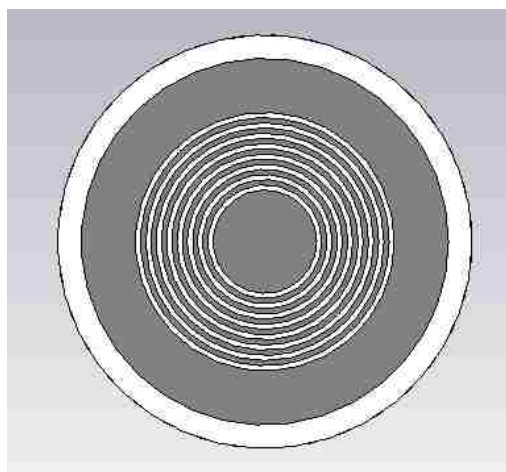


Figure 5.17. Example of printable tag.

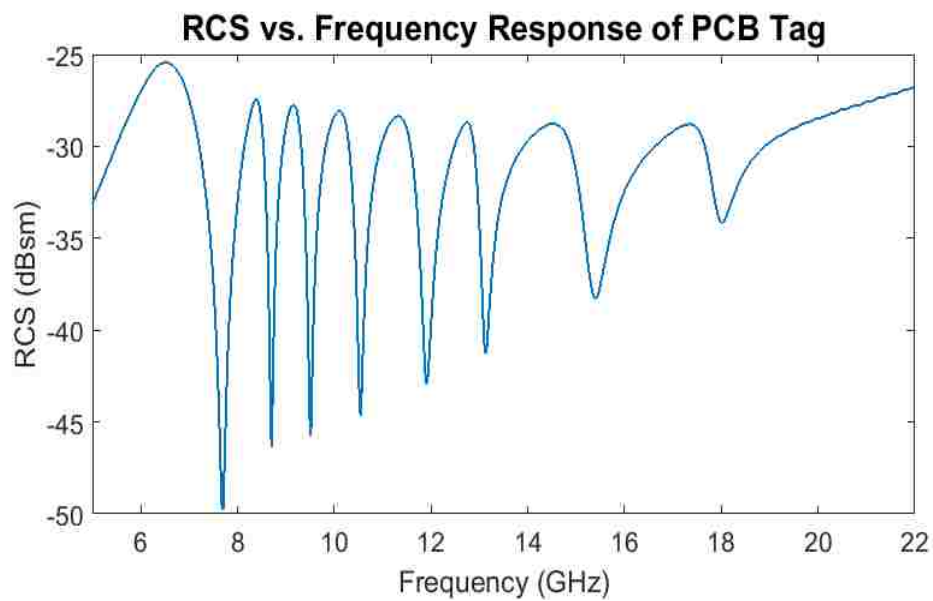


Figure 5.18. Response of printable tag.

The substrate of this tag can then be manipulated so that the tag is simulated as if it is printed on the papers that previously had their dielectric properties measured. Figure 5.19 shows the RCS vs. frequency response for when the tag is simulated on Mitsubishi® paper, photo paper, and photo sticker paper. In these cases, the substrate thickness is manipulated to be that of the paper used and the conductor is set as PEC. As these papers have similar dielectric properties, the responses in Figure 5.19 do not vary much.

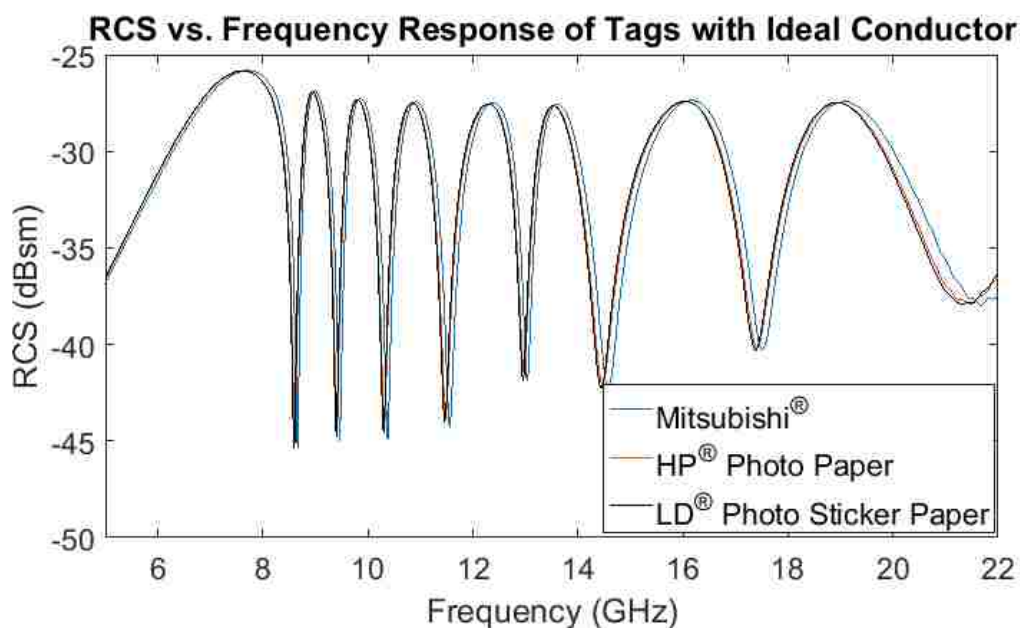


Figure 5.19. Response of tag on different printing substrates.

Following this simulation case, the conductor was also manipulated to be not ideal. Here it was set to have a conductivity of 3000 S/m and the tag was simulated for the same three papers. The results are shown in Figure 5.20. As can be seen, the notches in the response are no longer distinguishable. This effect also happens when PCB substrates are used. To illustrate this, the tag from Figure 4.51 was simulated with



varying conductivity of the conductor. From Figure 5.21 it can be seen that as the conductivity is reduced, the notches become less defined until they are no longer distinguishable. This further justifies the need for employing techniques to enhance conductivity.

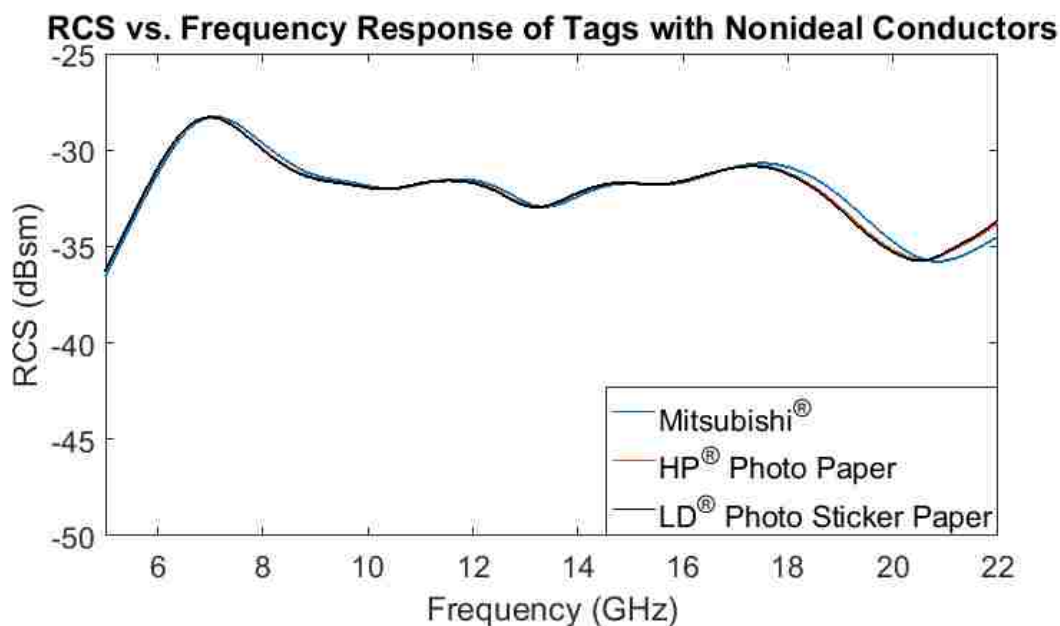


Figure 5.20. Response of simulated printed tag with non-ideal conductor.

Next, the non-idealness of print features was examined. Due to the raster scanning nature of printers, circular features are printed on a grid resulting in them not being perfectly circular. This effect was examined in [118] and [37], and is re-examined here. In Figure 5.22 a discretized circular slot resonator is featured. This discretized slot resonator tag was then simulated and its response was compared to an ideal circular slot resonator of similar dimensions, shown in Figure 5.23. The responses of these two slot resonators are shown in Figure 5.24. As can be seen, the responses are not the same; there

is a difference in resonance frequency between the two. This effect could cause measured responses to not agree with simulation and therefore it is important to consider when considering printing for a manufacturing method.

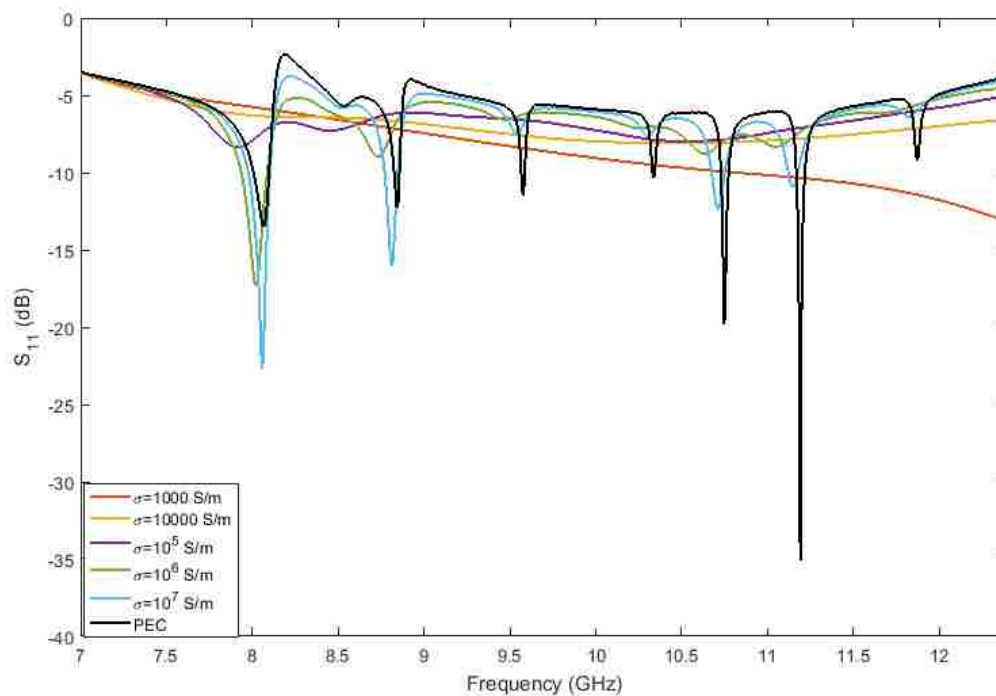


Figure 5.21. X-band spiral tag response with variable conductivity.

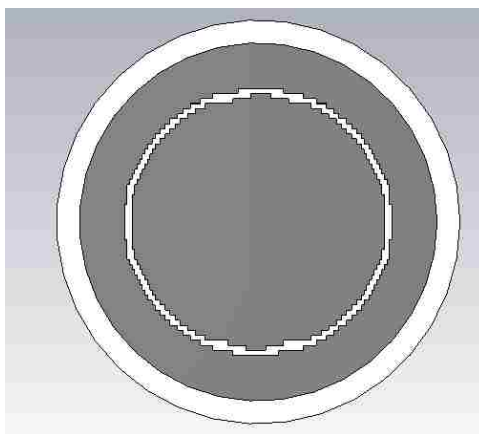


Figure 5.22. Discretized circular slot resonator.

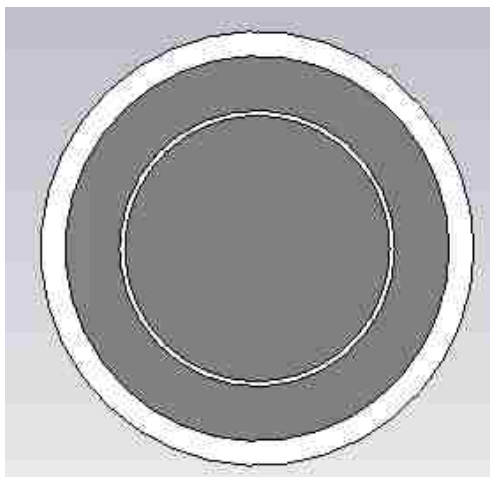


Figure 5.23. Ideal circular slot resonator.

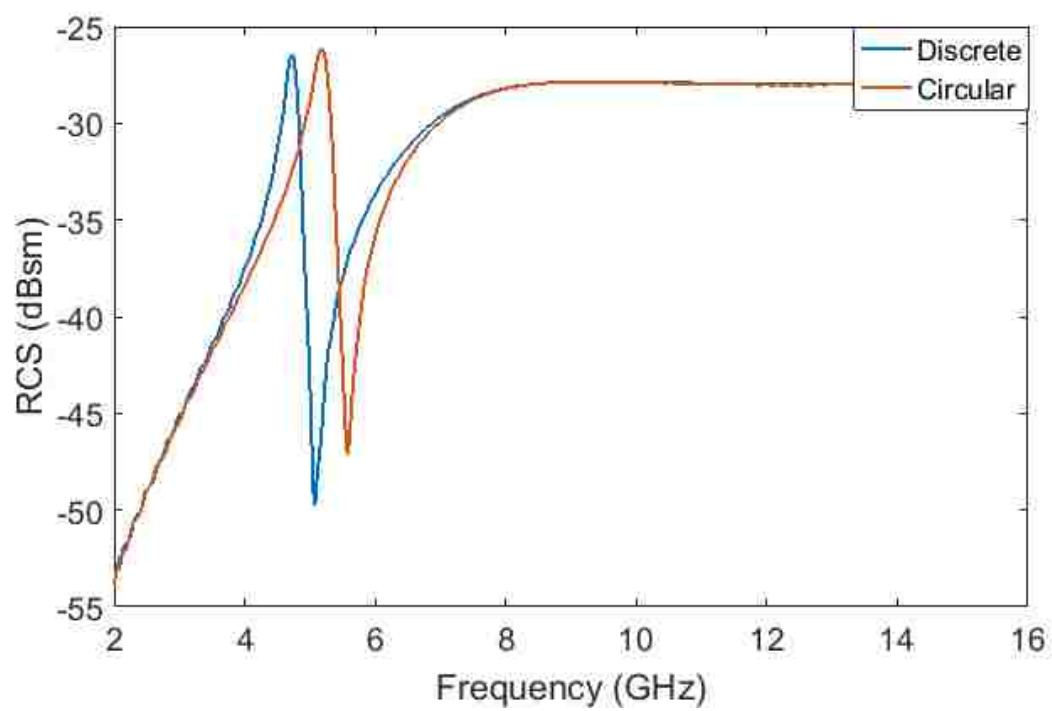


Figure 5.24. Comparison of response for discretized and ideal circular slot resonator.

## 5.5. MEASUREMENT OF PRINTED TAGS

Measurement was also done to compare the performance of PCB and inkjet-printed tags. For these measurements, an X-band waveguide with an elliptical flange was used to measure  $S_{11}$  and the tag was placed on the aperture with the conductive side facing the aperture. This measurement setup and the PCB and printed tags used are shown in Figure 5.25. This measurement setup was also simulated for PCB and printed tags. The printed tags in this simulation use a conductivity of 3000 S/m and the measured dielectric properties for the substrates. The simulation setup is shown in Figure 5.26 and the simulation results are shown in Figure 5.27. As can be seen from Figure 5.27, the simulated responses for the printed tags do not have distinguishable notches. This is also reflected in the measurement results shown in Figure 5.28. Overall, the printed tags in both simulation and measurement do not produce useful responses. That is, notches are not distinguishable making it impossible to assign binary codes. Until conductivity of printed tags can be increased, they are not practical for this work. Thus, measurements in subsequent sections will use PCB tags.

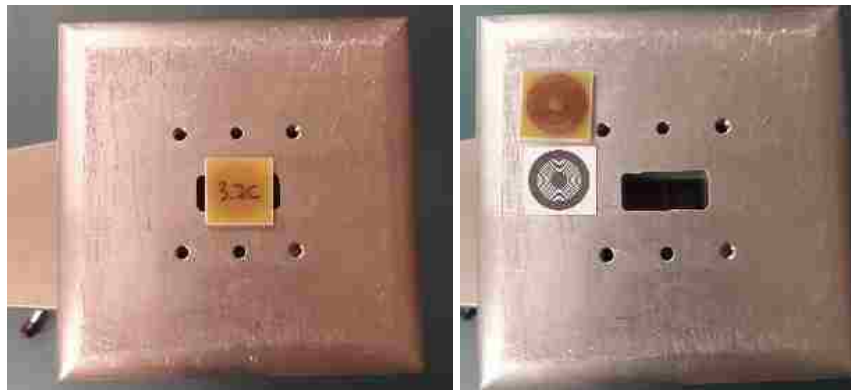


Figure 5.25. Measurement setup for measurement of PCB and printed tags.

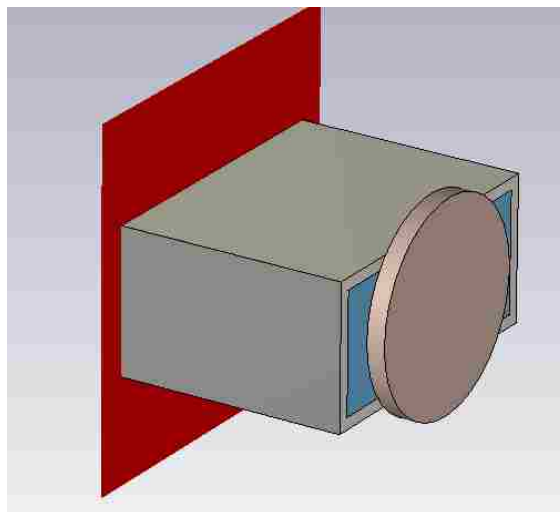


Figure 5.26. Simulation setup for tag  $S_{11}$ .

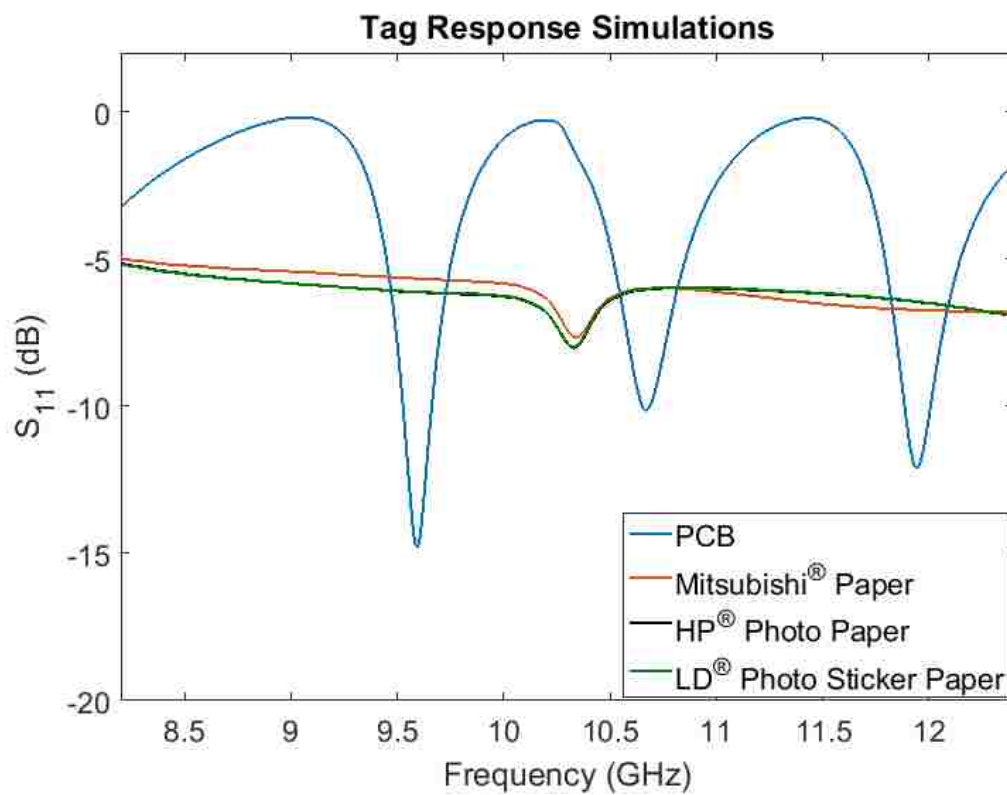


Figure 5.27. Simulated  $S_{11}$  responses of PCB and printed tags.

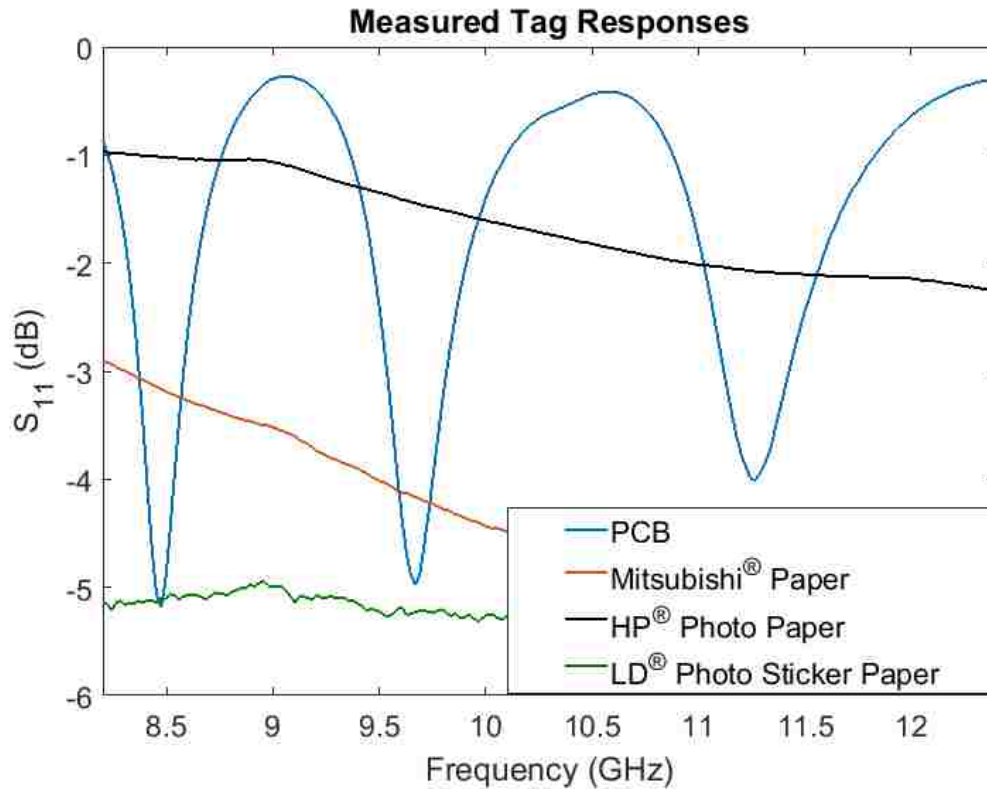


Figure 5.28. Measurement results of PCB and printed tags.

## 5.6. DISCUSSION

Inkjet-printing has the potential to allow tags to be produced quickly and inexpensively. However, when using this manufacturing method printing parameters, such as the dielectric properties of the paper, the conductivity of the print, and the resolution of the printer, need to be understood so that the tag to be printed can be accurately simulated. Additionally, having an understanding of these parameters and how they affect tag performance is necessary in order to evaluate if inkjet-printing is a suitable manufacturing method for a particular application.

## 6. TAG MEASUREMENT METHODS

### 6.1. MOTIVATION

Currently, there is a push to increase the read range, the distance a tag can be measured from, for chipless RFID tags. Traditional RFID allows for read ranges of upwards of 20 m, but many systems that operate at low powers have read ranges on the order of a few meters [7, 154, 155]. Chipless RFID tags, on the other hand, tend to have read ranges less than 10 cm. Read range is a function of both the characteristics of the reader antenna used (i.e., beamwidth, gain, etc.) and the scattering ability of the tag [129, 156]. In traditional RFID systems, the tag modulates the interrogation signal resulting in a backscattered signal that can be isolated from the static reflections [7, 157, 158]. However, chipless tags do not have this capability. To this end, depolarizing tags have been proposed, but these tend to have lower bit densities and less versatile responses than backscatter- and Tx/Rx- based tags [29, 30, 75, 86, 89, 90, 102, 128, 159, 160]. While work is being done to increase the bit density and customizability of depolarizing tags, many measurement and notch detection methods have also been proposed. Some of these measurement techniques were employed for measuring the previously presented tags. The theory behind these measurement techniques and measurement results will be presented in subsequent sections. Additionally, new methods like microwave thermography and embedded measurements for materials characterization will be discussed.

## 6.2. RADAR CROSS-SECTION (RCS) MEASUREMENTS

The RCS of a target is a far-field quantity that is defined as the portion of the scattering cross-section for a specified polarization component of a scattered wave. This definition assumes that a plane-wave is incident [161, 162]. The value for the RCS, expressed as an area, is dependent on the direction of arrival of the incident wave and the direction of observation. Mathematically, the RCS can be described as follows:

$$\sigma = 4\pi R^2 \frac{|E_{scattered}|^2}{|E_{incident}|^2} \quad (19)$$

In Equation (19),  $E_{scattered}$  and  $E_{incident}$  are electric fields. As previously mentioned, RCS is an area, but it is often expressed in dB square meter or dBsm. It should also be noted that RCS is frequency and polarization dependent and the definition of RCS assumes that the target is in free-space without multipath reflections [162-165]. In general, RCS can be reported as a function of frequency (as is done in CST Microwave Studio® simulations), as a single area value, as a pattern in the two principal planes, or as a far-field 3D pattern. It should also be mentioned that differential RCS is a quantity that is often discussed in the RFID field. However, it is defined as the RCS difference between two different RFID chip impedance states and is therefore not an applicable quantity to chipless RFID [166, 167].

As previously discussed, RCS measurements have the benefit of being distance independent. However, they require a more complex measurement process than S-parameter measurements do. At small read ranges, S-parameter measurements produce similar results to RCS measurements, as was shown in Section 2.3. However, as distance increases, the measured S-parameter response can change dramatically, as was illustrated



in the  $S_{11}$  measurements in Section 4.7.1.3. Thus, performing RCS measurements is necessary.

**6.2.1. RCS Determination Methods.** A variety of RCS measurement methods have been proposed. In the following sections, six of these methods are discussed. Then, in Section 6.2.2 Method 6 is employed to determine the RCS of tags from both simulation and measurement.

**6.2.1.1. Method 1.** One method of RCS measurement, described in [165] and [168], involves employing the radar range equation. This equation is as follows:

$$P_r = \frac{P_t G_t G_r \sigma_{target} \lambda^2}{(4\pi)^3 R^4} \quad (20)$$

In Equation (20),  $P_r$  is received power,  $P_t$  is transmitted power,  $G_r$  is the receiver antenna gain,  $G_t$  is the transmitter antenna gain, and  $\sigma_{target}$  is the RCS of the target. By rearranging Equation (20), the RCS can be solved for. A VNA can then be used with time domain analysis and time gating to simulate a pulsed radar and measure the needed parameters to find the RCS. In performing measurements, the full polarization matrix, depicted in Equation (21) is measured:

$$S = \begin{pmatrix} S_{vv} & S_{hv} \\ S_{vh} & S_{hh} \end{pmatrix} \quad (21)$$

Each entry in the matrix in Equation (21) is a combination of different transmit and receive polarizations. Note, only linear polarization is supported by this method and it assumed that a bistatic configuration or monostatic dual-polarized antenna configuration is used for the measurements. Through further calculation, the RCS can be expressed similarly to Equation (21) and then the RCS can be expressed in terms of measured received and transmitted powers (Equation (23)).

$$\sigma = \begin{pmatrix} \sqrt{\sigma_{vv}} & \sqrt{\sigma_{hv}} \\ \sqrt{\sigma_{vh}} & \sqrt{\sigma_{hh}} \end{pmatrix} \quad (22)$$

$$\sigma = \frac{P_{rv} + P_{rh}}{P_t} \quad (23)$$

In Equation (23)  $P_{rv}$  and  $P_{rh}$  refer to the power received in the vertical and horizontal polarizations, respectively.

In performing the measurements, calibration can be performed by measuring the  $S_{21}$  of a standard reference target with a known RCS, such as a metal plate or a metal sphere. This measurement can then be transformed to the time domain where it is then range gated. The magnitude of the peak that is associated with the target that appears in the time domain data is recorded. Then,  $S_{21}$  measurements can be taken of the target and calibration standard in order to calculate the RCS by the following equations derived from the radar range equation:

$$\frac{P_{std}}{P_t} = 10 \frac{S_{21}^{std}}{10} \quad (24)$$

$$\frac{P_{tgt}}{P_t} = 10 \frac{S_{21}^{tgt}}{10} \quad (24)$$

$$\frac{P_{tgt}}{P_{std}} = \frac{\sigma_{tgt}}{\sigma_{std}} = 10 \left( \frac{S_{21}^{tgt} - S_{21}^{std}}{10} \right) \quad (25)$$

In Equation (25)  $\sigma_{std}$  (used in  $m^2$ ) is typically a theoretical value that has been calculated.

This method has been shown to take into account polarization dependence, however, it does not take into account frequency dependence. In [165] and [168] this method was used to determine a single value for the RCS rather than the RCS over frequency. Though it was not shown, by using the  $S_{21}$  measurements of the target and

standard reference target over a frequency range, it could be possible to calculate the RCS as a function of frequency.

**6.2.1.2. Method 2.** The second method of RCS measurement from [169], designed for determining the RCS of antennas, involves utilizing an equation for the received signal power. This equation is a combination of the antenna-mode scattered, structural-mode scattered, relative phase, and leakage signals. By combining these parameters, the equation for the received power can be represented as a regression model that takes into account the interference between scattered signals and leakage signals and observation error. This regression model can then be solved by using minimum mean square error estimation. Lastly, the solution is used with observed responses for short, open, and load conditions to find RCS parameters. This method has been shown to produce more accurate results than Method 1, however, it comes at the cost of more complex processing. Additionally, this method also only provides a single value for the RCS rather than the RCS over a frequency range [169].

**6.2.1.3. Method 3.** Method 3 from [170] provides a 12-term error correction procedure that utilizes a single reference target and isolation measurement. This is in contrast to other 12-term error correction procedures which require three independent reference targets [171]. In this method, the relationship between S-parameters and the RCS is described as follows:

$$\underline{[S]} = \frac{1}{\sqrt{4\pi R_o^2}} \underline{[\sqrt{\sigma}]} \quad (26)$$

In Equation (26), underlined matrices refer to the entries of the matrices being complex and  $R_o$  is defined as a “fixed reference radius for the target,” however, it is not clear what

exactly this dimension refers to. Equation (26) is used as the basis for extracting the RCS from S-parameter measurements in this method. While this method provides the RCS as a function of frequency and is simpler than a traditional 12-term error correction procedure, it still requires some complex post processing of S-parameter data in order to reconstruct the RCS [170].

**6.2.1.4. Method 4.** Method 4 of [158] and [172] was specifically designed for measuring the RCS of UHF RFID tags. For this measurement procedure, first an isolation measurement is made. This isolation measurement is the  $S_{11}$  of an anechoic chamber. Then, the  $S_{11}$  of the tag in the anechoic chamber is measured. These measurements are then subtracted coherently. The result of this subtraction,  $S'_{11}$ , is then approximated in terms of the power transmitted and received, which is shown in Equation (27):

$$|S'_{11}|^2 \approx \frac{P_r}{P_t} \quad (27)$$

By combining Equation (27) with the radar range equation, Equation (28) can be derived to express RCS:

$$\sigma = |S'_{11}|^2 \frac{(4\pi)^3 R^4}{G_t^2 \lambda^2} \quad (28)$$

This method has the benefits of being able to utilize a monostatic measurement configuration and requiring simple processing.

**6.2.1.5. Method 5.** In [106] two different methods for RCS measurement for millimeter wave passive RFID are presented. The first method, which is similar to Methods 1 and 4, uses the radar range equation. Using the radar range equation, the backscattered power,  $P_b$ , of the tag can be represented by Equation (29):

$$P_b = P_t G^2 \frac{\lambda}{(4\pi)^3 R^4} \sigma_{target} \left(1 - |S_{11}^{Tx/Rx}|^2\right)^2 \quad (29)$$

$$PT = \left(1 - |S_{11}^{Tx/Rx}|^2\right) \quad (30)$$

In Equation (29),  $G$  is the gain of the reader antenna which is often a horn antenna. The power transfer factor,  $PT$ , is often excluded in RCS measurement procedures that are based on the radar range equation since its value is very close to one. However, it is included here because it has been shown to play a role when the frequencies get into the millimeter wave range. The final equation used to calculate the RCS from measurements is Equation (31):

$$\sigma = |S_{11}^{target} - S_{11}^{mount}|^2 \frac{(4\pi)^3 R^4}{G^2 \lambda^2 (1 - |S_{11}^{Tx/Rx}|^2)^2} \quad (31)$$

This method has the advantage of being simple and not requiring any reference targets. However, in order for it to produce accurate results, the  $S_{11}$  measurements and system parameters like the gain of the reader antenna must be well known [106]. The second method presented in [106] is based on the method presented in [25] and [173], except it uses a monostatic setup rather than a bistatic setup. This method will be presented as Method 6.

**6.2.1.6. Method 6.** Method 6 from [25] and [173] uses a bistatic setup to measure the RCS of chipless RFID tags. It should be noted that this is the first measurement method presented that is designed specifically for chipless RFID. This method has also become standard for determining the RCS of chipless tags. Figure 6.1 shows a diagram on which this method is based. From the diagram, it can be seen that

this model takes into account the coupling between the two reader antennas, the free-space path losses, the VNA, and the support the tag will be mounted on [173].

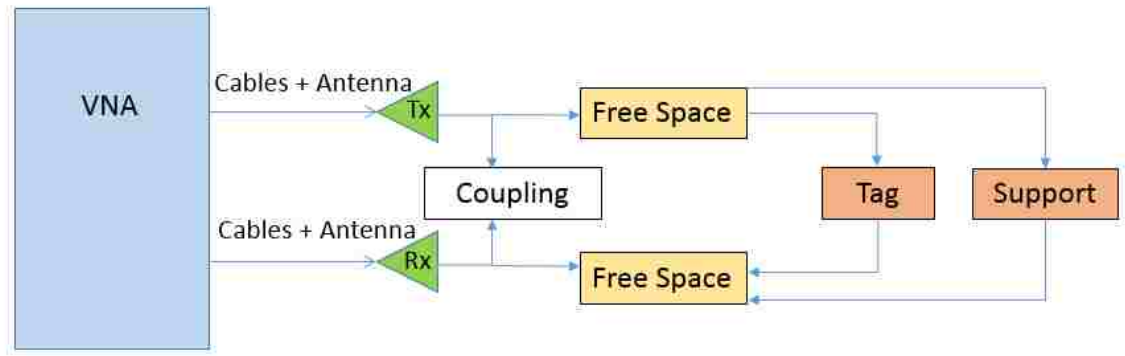


Figure 6.1. Diagram of RCS measurement model for Method 6.

By using the model in Figure 6.1, and bringing in the Friis Transmission equation and an approximation for the definition RCS (Equation (32)), a formula for the RCS of a tag can be derived. This formula, shown in Equation (33), requires the measurement of one reference target, such as a plate or a sphere, and knowing the value of the RCS of the reference target ( $\sigma_{ref}$ ).

$$\sigma \approx 4\pi R^2 |S_{21}|^2 \quad (32)$$

$$\sigma_{tag} = \left[ \frac{S_{21}^{tag} - S_{21}^{support}}{S_{21}^{ref} - S_{21}^{support}} \right]^2 \sigma_{ref} \quad (33)$$

This method has become very popular for measuring the RCS of chipless RFID tags [25, 52, 53, 55, 58, 62, 91]. An example of RCS measured with this method is shown in Figure 6.2. As can be seen, this method tends to produce less clean responses than RCS simulations (e.g., Figure 2.2). However, these reconstructed RCS responses do follow the general shape of the simulated responses.

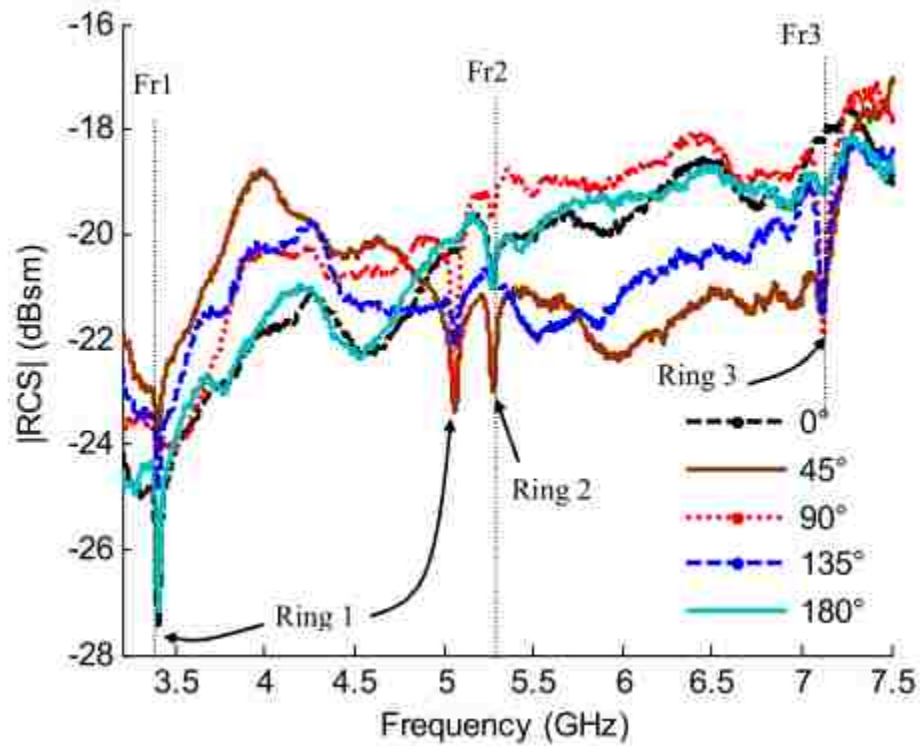


Figure 6.2. Measured RCS for a split ring resonator based tag [91].

**6.2.2. Employment of Method 6.** Due to its popularity, Method 6 was used in its monostatic configuration from [106] (shown in Equation (34) which is similar to Equation (33)) for reconstructing the RCS of the eight spiral X-band tag shown in Section

$$\sigma_{tag} = \left[ \frac{S_{11}^{tag} - S_{11}^{support}}{S_{11}^{ref} - S_{11}^{support}} \right]^2 \sigma_{ref} \quad (34)$$

4.5 from measurements of the tag. To begin with, simulations were conducted to determine the best approach for measuring the RCS of the tag with this method (i.e. what distances to measure at, what to mount the tag on during the measurement, and what to use for a reference target). For these simulations, an X-band waveguide was used as the reader antenna and the  $S_{11}$  of the tag on a foam support, a metal plate, and just the foam support were simulated at a distance of 5 cm between the object and the waveguide

aperture. The simulation setup is depicted in Figure 6.3. Three different metal plates of different sizes were used as reference targets in the simulations to determine what would be appropriate for the experiments. In using Equation (34) for the purpose of verifying it for the spiral tag and plate reference,  $S_{11}^{tag}$  is the simulated  $S_{11}$  of the tag on the foam support (see Figure 6.3),  $S_{11}^{support}$  is the simulated  $S_{11}$  of just the foam support, and  $S_{11}^{ref}$  is the simulated  $S_{11}$  of the different size metal plates. For the  $\sigma_{ref}$  both calculated and simulated values were used. For the calculated values, Equation (35) was used:

$$\sigma_{plate} = 4\pi \frac{S^2}{\lambda^2} \quad (35)$$

In Equation (35),  $S$  is the area of the plate [106]. For the simulated  $\sigma_{plate}$  CST Microwave Studio® was used to conduct a monostatic RCS simulated with a plane-wave excitation and RCS probe interrogation. From this, the plate RCS as a function of frequency was found. Figure 6.4 shows the simulated  $S_{11}$  response of the tag at a distance of 5 cm. As can be seen, the notches are not very defined for the tag at this distance. Figures 6.5, 6.6, and 6.7 then show the reconstructed RCS (using Equation (34)) when a plate of different sizes is used as the reference target, which affects  $S_{11}^{ref}$  and  $\sigma_{ref}$  in Equation (34). In these three figures, the reconstructed RCS is shown for both the scenario where the value for  $\sigma_{ref}$  is calculated using Equation (35) and where the value of  $\sigma_{ref}$  is simulated using CST Microwave Studio® to compare their results. The three different plate sizes that are used are 8 x 8 cm (Figure 6.5), 20 x 20 cm (Figure 6.6), and 30 x 30 cm (Figure 6.7). From these figures it can be seen that the reconstructed RCS from  $S_{11}$  simulations for the two different  $\sigma_{ref}$  determination methods, provide similar results (i.e., the notches are in the same locations, but amplitudes are slightly different).



In all cases the reconstructed RCS shows a slight downshift in frequency from the simulated RCS response and a higher magnitude. The higher magnitude is due to the multiplication of  $\sigma_{ref}$  in Equation (34). As the plate gets larger, it increases the value of  $\sigma_{ref}$  in accordance to Equation (35) and increases the magnitude of the reconstructed RCS. The downshift seen could be due to the foam used in the simulations to support the tag.

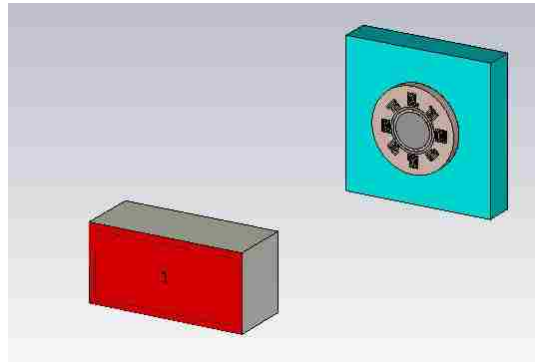


Figure 6.3. Simulation setup for RCS calculation.

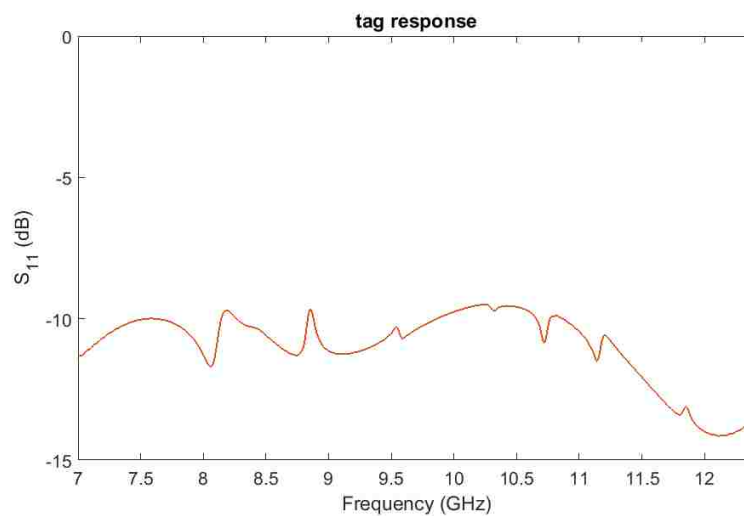


Figure 6.4.  $S_{11}$  of the tag at a distance of 5 cm.

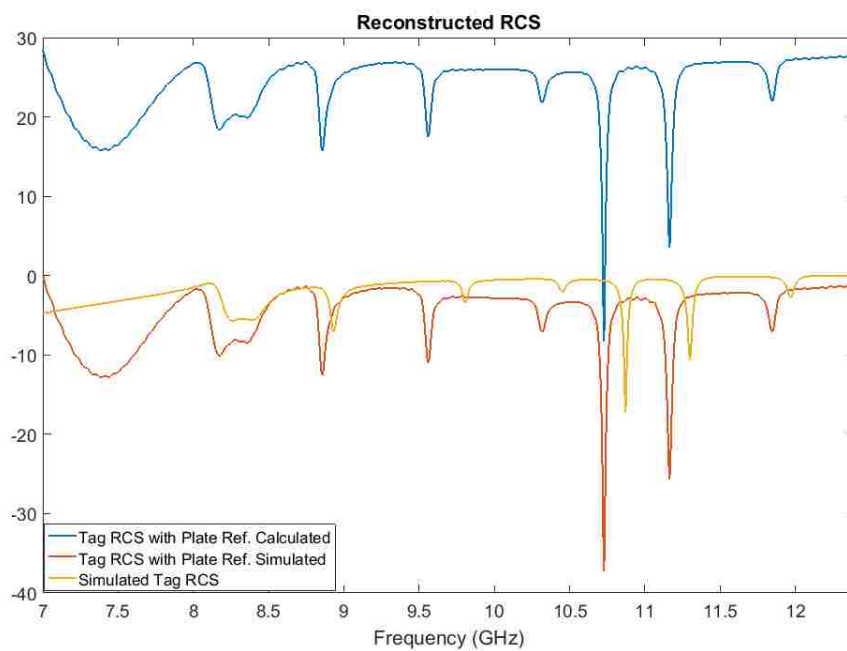


Figure 6.5. Reconstructed RCS of tag from simulation data using 8 x 8 cm plate as reference.

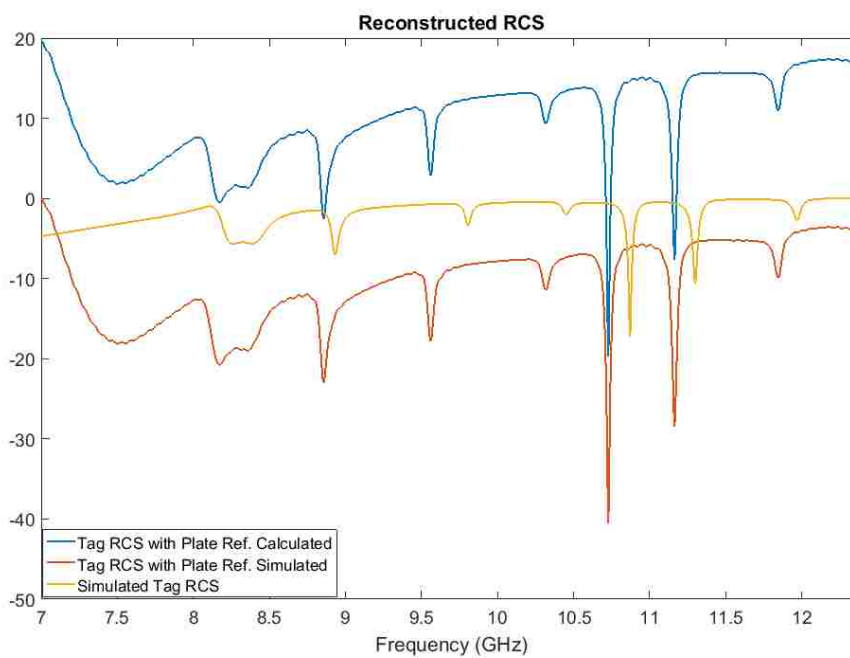


Figure 6.6. Calculated RCS of tag from simulation data using 20 x 20 cm plate as reference.

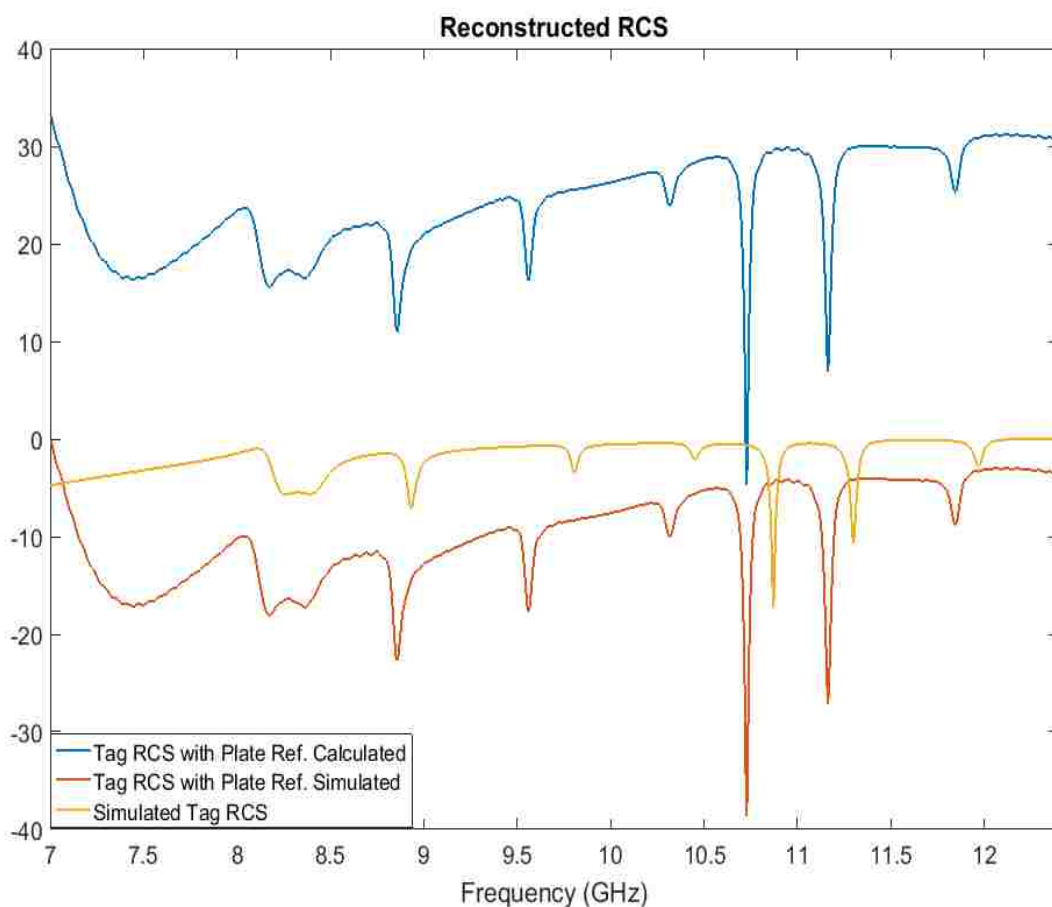


Figure 6.7. Calculated RCS of tag from simulation data using 30 x 30 cm plate as reference.

Having shown that this method can reconstruct the RCS for this tag via simulation, measurements were then conducted. For these measurements, the setup used previously for tag measurements was used. This setup is shown in Figure 4.69. A metal plate that was 20 x 20 cm was used as the reference target. Measurements were taken at 0.5 cm increments from 0.5 cm to 6 cm. The results of tag measurement at the various distances are shown in Table 6.1 and the results of RCS reconstruction are shown in Table 6.2 for the different distances. For the results in Table 6.2, a measurement of the

plate was used for  $S_{11}^{ref}$  and  $\sigma_{ref}$  was calculated using Equation (35).  $S_{11}^{tag}$  was measured as the tag on the foam support and  $S_{11}^{support}$  was measured as just the foam used to support the tag as was done in simulation.

Table 6.1.  $S_{11}$  of eight spiral tag for different distances.

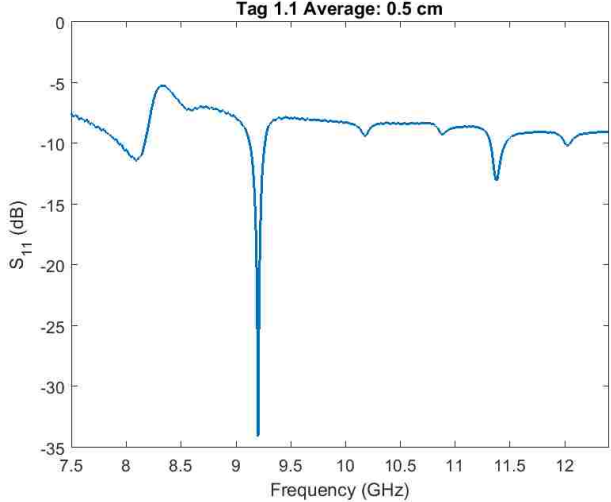
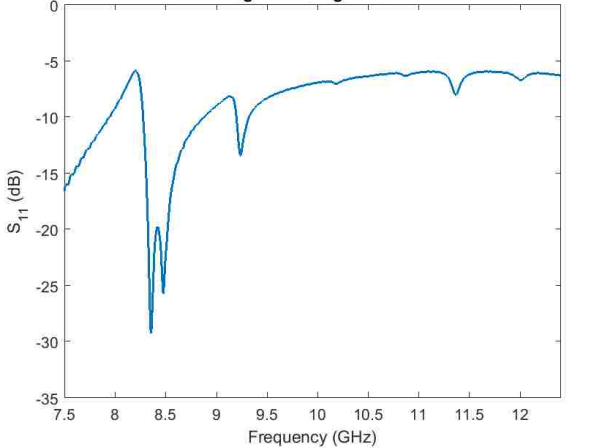
Distance (cm)	$S_{11}$
0.5	 <p>Tag 1.1 Average: 0.5 cm</p>
1	 <p>Tag 1.1 Average: 1 cm</p>

Table 6.1.  $S_{11}$  of eight spiral tag for different distances (cont.).

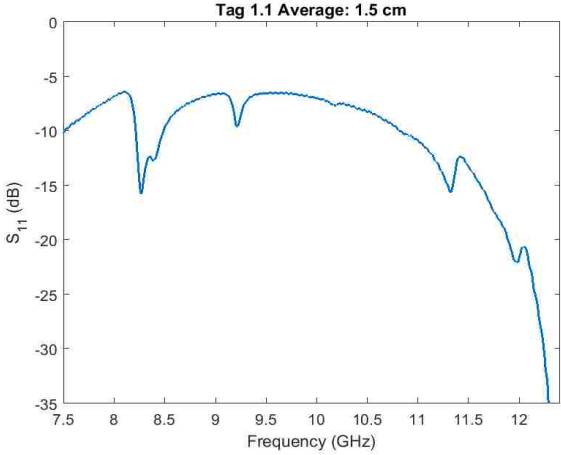
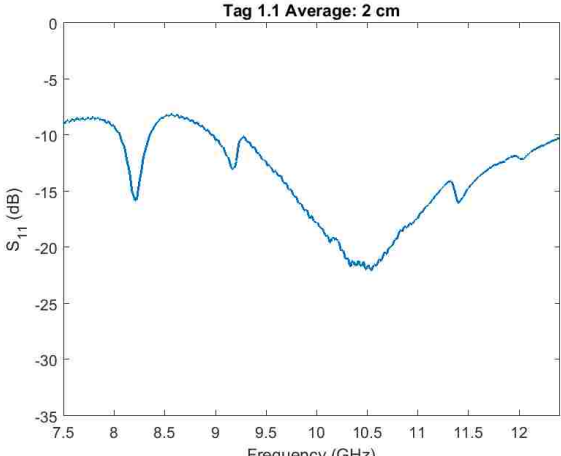
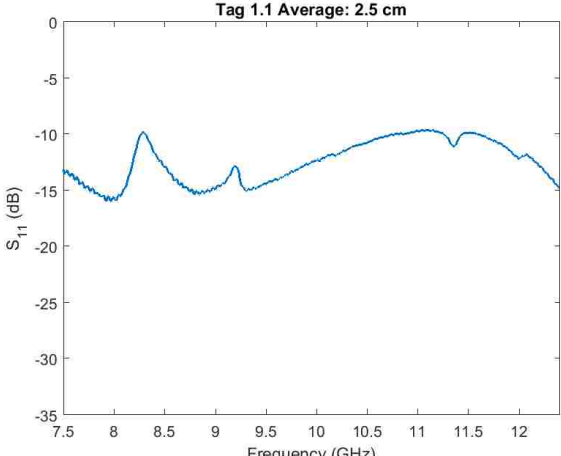
Distance (cm)	$S_{11}$
1.5	 <p>Tag 1.1 Average: 1.5 cm</p>
2	 <p>Tag 1.1 Average: 2 cm</p>
2.5	 <p>Tag 1.1 Average: 2.5 cm</p>

Table 6.1.  $S_{11}$  of eight spiral tag for different distances (cont.).

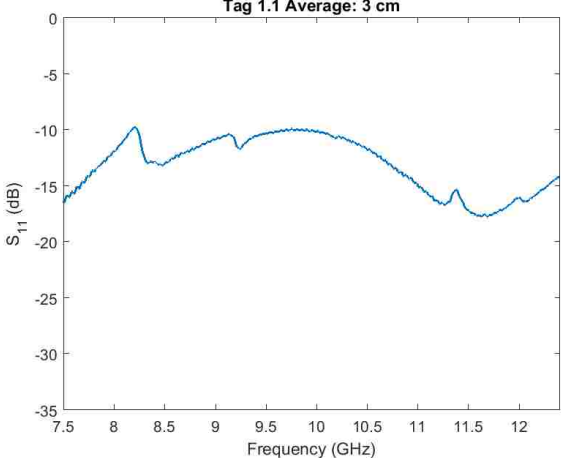
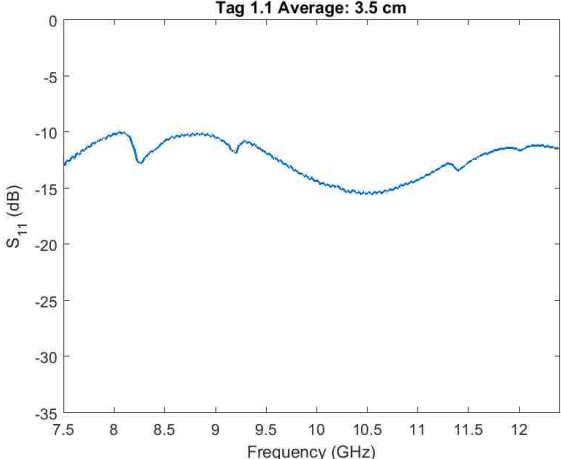
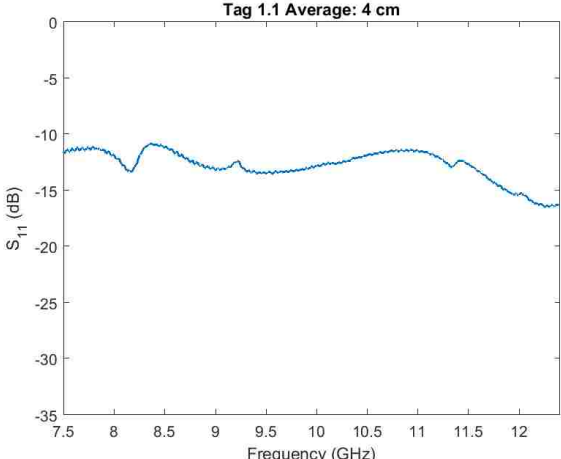
Distance (cm)	$S_{11}$
3	 <p>Tag 1.1 Average: 3 cm</p>
3.5	 <p>Tag 1.1 Average: 3.5 cm</p>
4	 <p>Tag 1.1 Average: 4 cm</p>

Table 6.1.  $S_{11}$  of eight spiral tag for different distances (cont.).

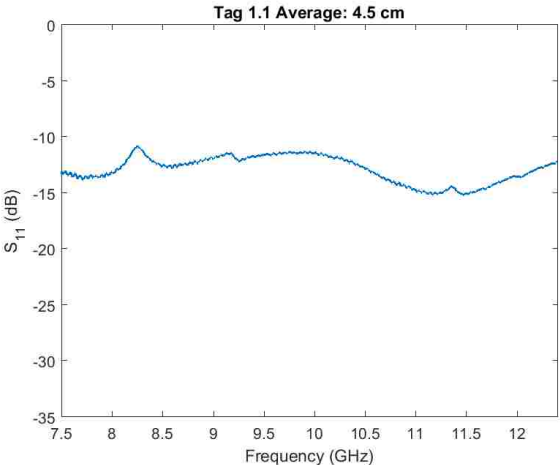
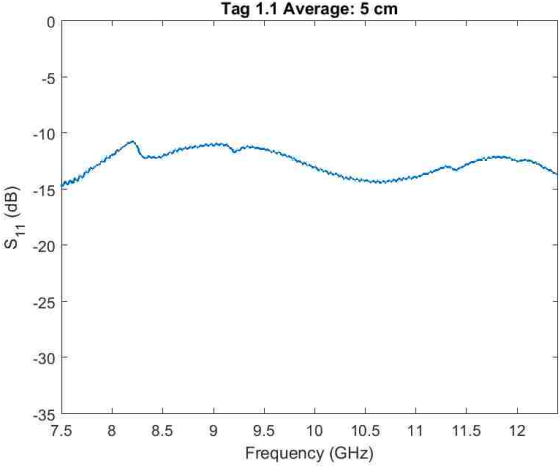
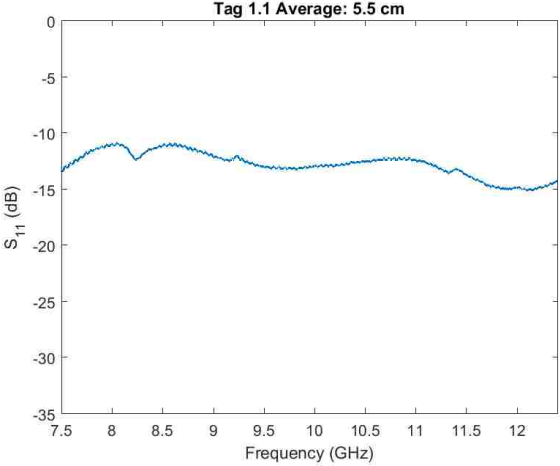
Distance (cm)	$S_{11}$
4.5	 <p>Tag 1.1 Average: 4.5 cm</p>
5	 <p>Tag 1.1 Average: 5 cm</p>
5.5	 <p>Tag 1.1 Average: 5.5 cm</p>

Table 6.1.  $S_{11}$  of eight spiral tag for different distances (cont.).

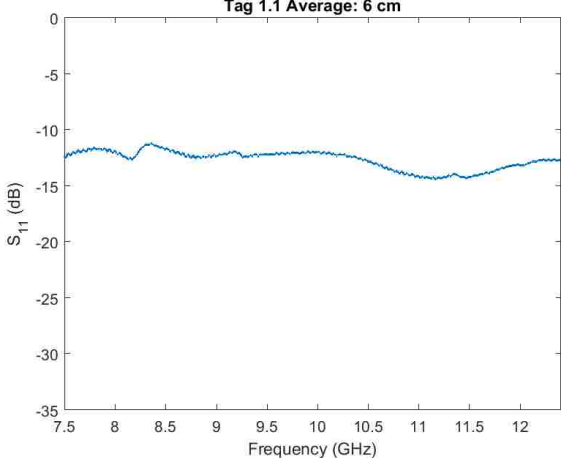
Distance (cm)	$S_{11}$
6	 <p>Tag 1.1 Average: 6 cm</p> <p>The plot shows the reflection coefficient <math>S_{11}</math> in dB versus Frequency in GHz. The y-axis ranges from 0 to -35 dB, and the x-axis ranges from 7.5 to 12 GHz. The data points are connected by a blue line, showing a relatively flat response around -15 dB with minor fluctuations.</p>

Table 6.2. Reconstructed RCS for measured plate reference target.

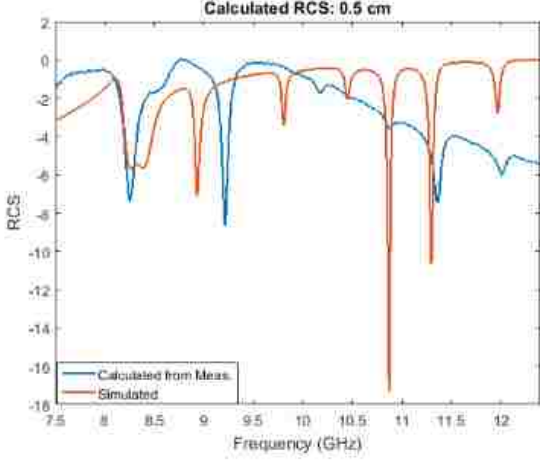
Distance (cm)	RCS
0.5	 <p>Calculated RCS: 0.5 cm</p> <p>The plot shows the Reconstructed RCS versus Frequency in GHz. The y-axis ranges from 2 to -16, and the x-axis ranges from 7.5 to 12 GHz. Two data series are plotted: 'Calculated from Meas.' (blue line) and 'Simulated' (orange line). Both series show several sharp resonance dips, with the simulated data showing deeper and more distinct dips than the measured data.</p>



Table 6.2. Reconstructed RCS for measured plate reference target (cont.).

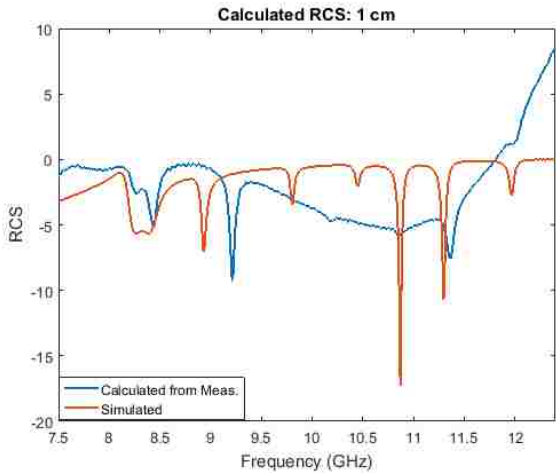
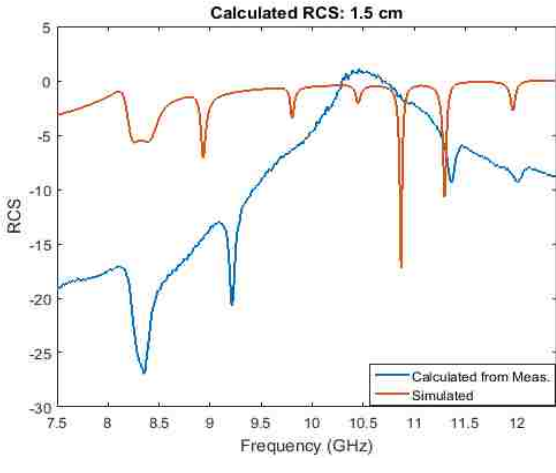
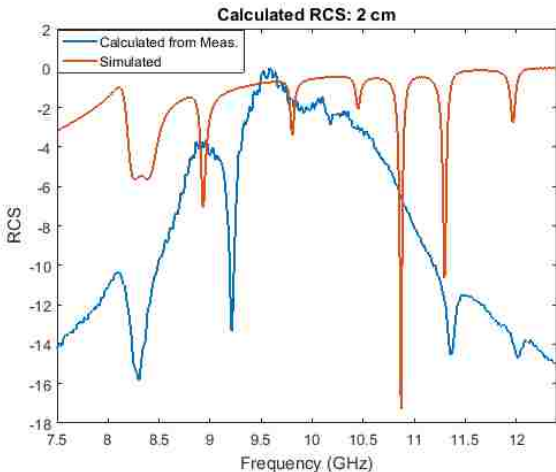
Distance (cm)	RCS
1	
1.5	
2	

Table 6.2. Reconstructed RCS for measured plate reference target (cont.).

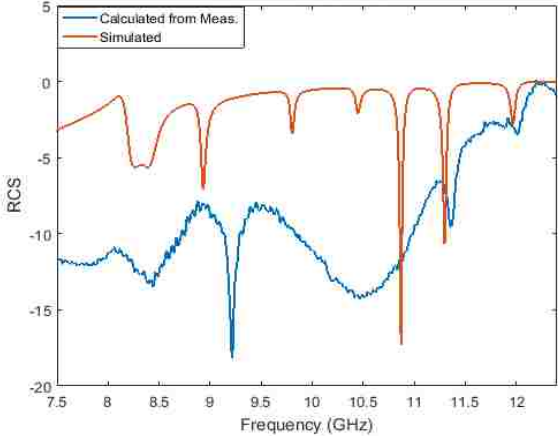
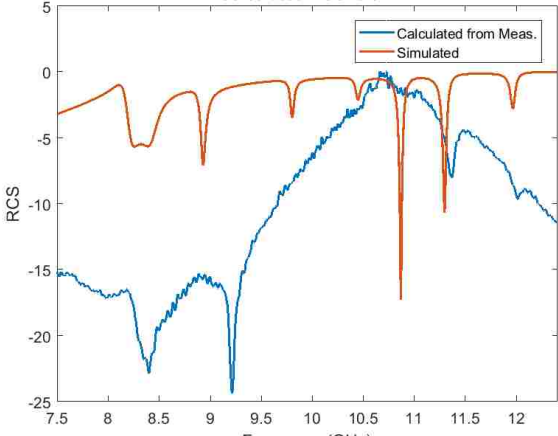
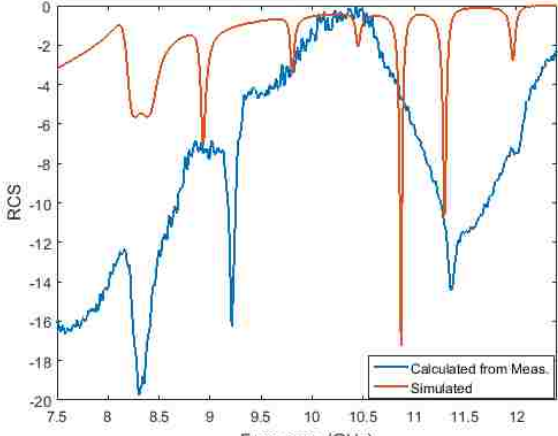
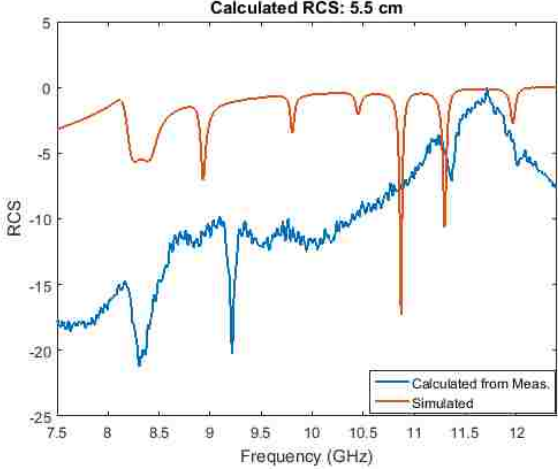
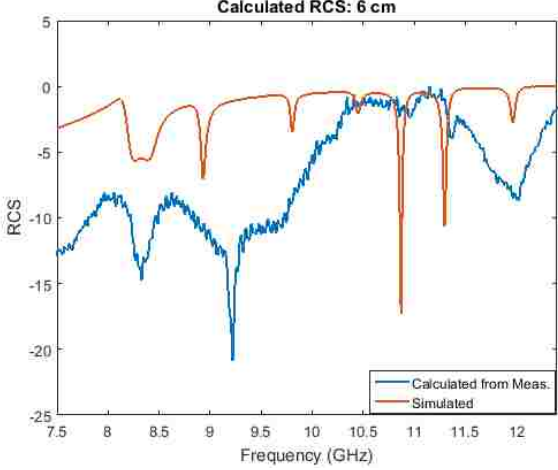
Distance (cm)	RCS
2.5	<p style="text-align: center;"><b>Calculated RCS: 2.5 cm</b></p>  <p>The plot shows RCS vs Frequency (GHz) for a 2.5 cm distance. The y-axis ranges from -20 to 5, and the x-axis ranges from 7.5 to 12 GHz. Two data series are shown: 'Calculated from Meas.' (blue line) and 'Simulated' (orange line). Both series exhibit several sharp nulls, with the most prominent ones occurring at approximately 9.2 GHz, 10.8 GHz, and 11.2 GHz. The simulated data shows a relatively flat baseline near 0 dB, while the measured data shows a significant dip to -18 dB at 9.2 GHz.</p>
3	<p style="text-align: center;"><b>Calculated RCS: 3 cm</b></p>  <p>The plot shows RCS vs Frequency (GHz) for a 3 cm distance. The y-axis ranges from -25 to 5, and the x-axis ranges from 7.5 to 12 GHz. Two data series are shown: 'Calculated from Meas.' (blue line) and 'Simulated' (orange line). The simulated data shows a flat baseline near 0 dB with several sharp nulls. The measured data shows a broad peak around 10.5 GHz and a deep null at approximately 9.2 GHz.</p>
3.5	<p style="text-align: center;"><b>Calculated RCS: 3.5 cm</b></p>  <p>The plot shows RCS vs Frequency (GHz) for a 3.5 cm distance. The y-axis ranges from -20 to 0, and the x-axis ranges from 7.5 to 12 GHz. Two data series are shown: 'Calculated from Meas.' (blue line) and 'Simulated' (orange line). The simulated data shows a flat baseline near 0 dB with several sharp nulls. The measured data shows a broad peak around 10.5 GHz and a deep null at approximately 9.2 GHz.</p>

Table 6.2. Reconstructed RCS for measured plate reference target (cont.).

Distance (cm)	RCS
4	<p>Calculated RCS: 4 cm</p>
4.5	<p>Calculated RCS: 4.5 cm</p>
5	<p>Calculated RCS: 5 cm</p>

Table 6.2. Reconstructed RCS for measured plate reference target (cont.).

Distance (cm)	RCS
5.5	
6	

From Table 6.2, it can be seen that reconstructing the RCS from measurements does not lead to perfect agreement between the measured and simulated RCS. However, it does allow notches that were not discernable from the  $S_{11}$  measurements to be seen, especially at distances greater than 3 cm. Additionally, the reconstructed RCS varies with distance. It was suspected that these variations had to do with inaccuracies in the plate measurement and the manufacturing inaccuracies that were seen through

measurements of the tag in Section 4.7. To this end,  $S_{11}$  simulation data for the plate was substituted for the plate  $S_{11}$  measurement into Equation (33). Table 6.3 shows the results tabulated for this variation of the reconstruction method.

Table 6.3. Reconstructed RCS with plate simulation for reference.

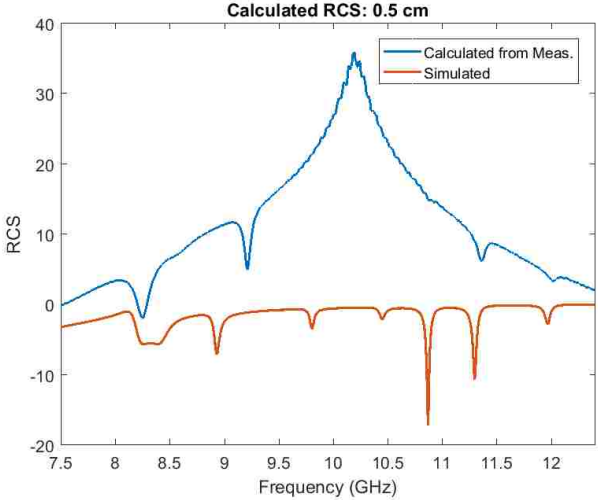
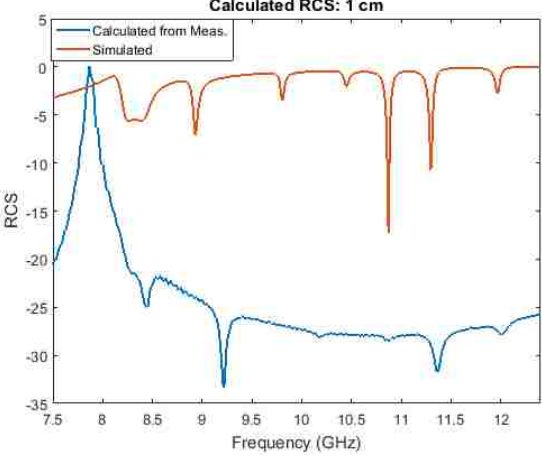
Distance (cm)	RCS (dBsm)
0.5	
1	

Table 6.3. Reconstructed RCS with plate simulation for reference (cont.).

Distance (cm)	RCS (dBsm)
1.5	<p>Calculated RCS: 1.5 cm</p>
2	<p>Calculated RCS: 2 cm</p>
2.5	<p>Calculated RCS: 2.5 cm</p>

Table 6.3. Reconstructed RCS with plate simulation for reference (cont.).

Distance (cm)	RCS (dBsm)
3	
3.5	
4	

Table 6.3. Reconstructed RCS with plate simulation for reference (cont.).

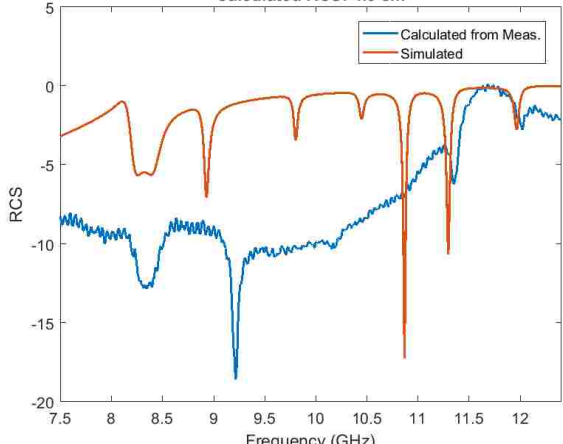
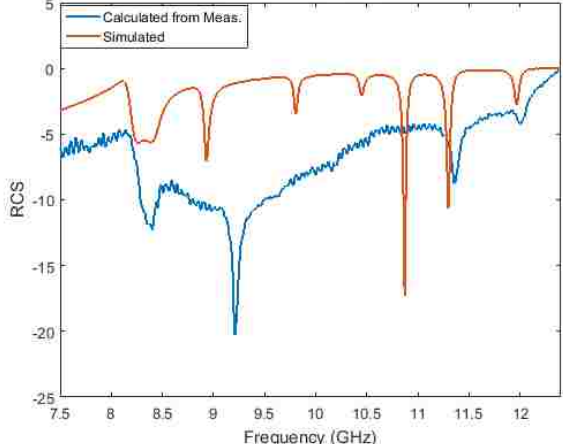
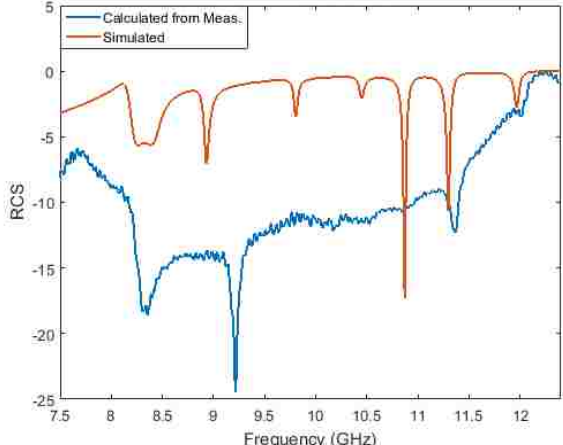
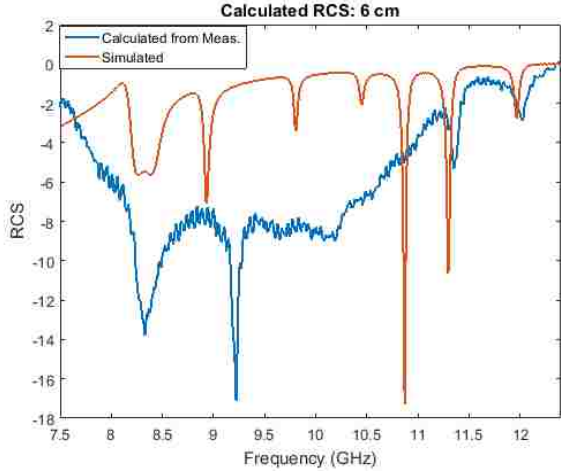
Distance (cm)	RCS (dBsm)
4.5	<p style="text-align: center;"><b>Calculated RCS: 4.5 cm</b></p> 
5	<p style="text-align: center;"><b>Calculated RCS: 5 cm</b></p> 
5.5	<p style="text-align: center;"><b>Calculated RCS: 5.5 cm</b></p> 



Table 6.3. Reconstructed RCS with plate simulation for reference (cont.).

Distance (cm)	RCS (dBsm)
6	

As can be seen from Table 6.3, when the plate simulation is used the reconstructed and simulated RCS responses still do not completely agree. However, at distances above 3 cm, the reconstructed RCS maintains a similar shape. This provides evidence for the theory that the plate measurements being inaccurate are contributing to the disagreement between the simulated and reconstructed responses. Additionally, it is still believed that the manufacturing inaccuracies of the tag are contributing to the disagreement seen in Tables 6.2 and 6.3. Furthermore, inaccuracies in the tag measurement (i.e., tag/reader misalignment like what was shown in Section 4.7.1) could also contribute.

While performing RCS measurement can theoretically remove the distance dependency of chipless RFID measurement, in practice it is difficult to accurately measure the RCS. This difficulty mostly comes from the challenges associated with measuring a reference target. Additionally, these methods do not translate well from a lab setting to a practical setting. In the field, one would not necessarily be able to accurately

measure a reference targets and it would also be difficult to place the reference target in the same location as the tag in some applications (e.g., SHM applications where a tag would be attached to or embedded in a structure). These issues limit the practicality of RCS measurement in the field.

### 6.3. BISTATIC MEASUREMENTS

Bistatic measurements are often used in chipless RFID tag measurements. Thus, a limited set of bistatic measurements were also conducted. For these measurements, two horn antennas that operate from 6.5 – 14 GHz were used and they were placed 18 cm from the tag. The measurement setup is shown in Figure 6.8. The tag measured was the eight circular slot resonator tag that was used for measurements in Section 5.5. This tag was used in a 4 x 4 array configuration for both PCB and inkjet-printing manufacturing methods to raise the signal level so that no post processing would need to be done on the measurement [107]. A 4 x 4 configuration was used after it was seen that the response of a single tag configuration couldn't be seen with this measurement setup when operating in the far-field of the horn antennas. The tags used are shown in Figure 6.9. Figure 6.10 shows the simulated response of the 4 x 4 PCB tag. As can be seen, it is very similar to the response of a single eight circular slot resonator tag like is shown in Figure 2.2. Figure 6.11 then shows the measurement results for the PCB tag and Figure 6.12 and 6.13 show the unsintered and sintered inkjet-printed tag responses, respectively. From Figure 6.11, it can be seen that the measured response for the PCB 4 x 4 tag array is very similar to the simulated response. The responses for the unsintered and sintered tags, however, do not agree well with the simulated response. In these measured responses no notches

are discernable and sintering does not produce a definite improvement in the response. These indistinguishable responses are most likely due to low conductivity of prints as was discussed in Section 5.

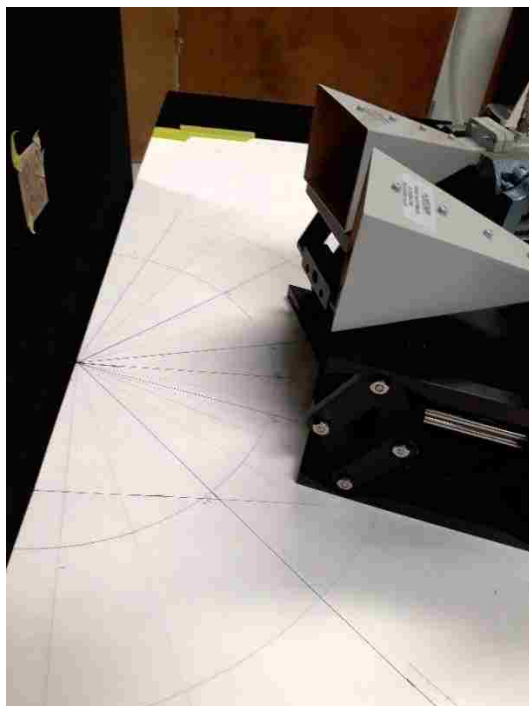


Figure 6.8. Bistatic measurement setup.

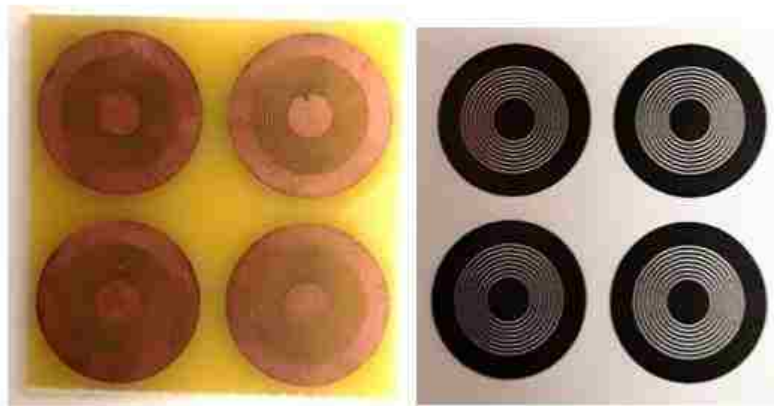


Figure 6.9. PCB and inkjet-printed tag arrays.

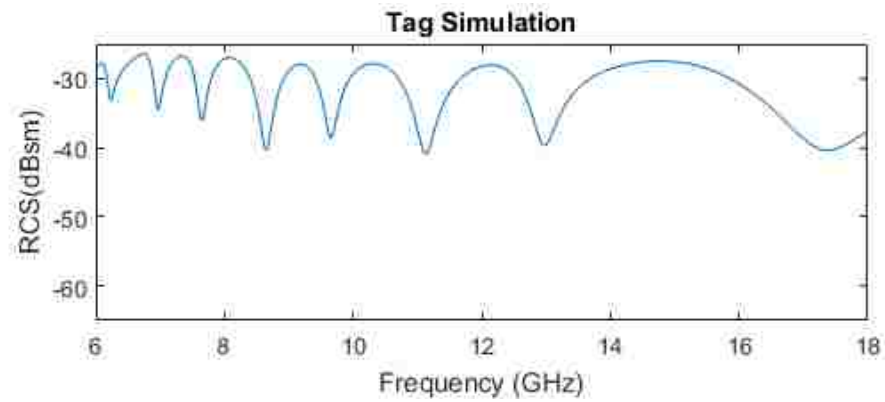


Figure 6.10. Simulated response of 4 x 4 PCB tag array.

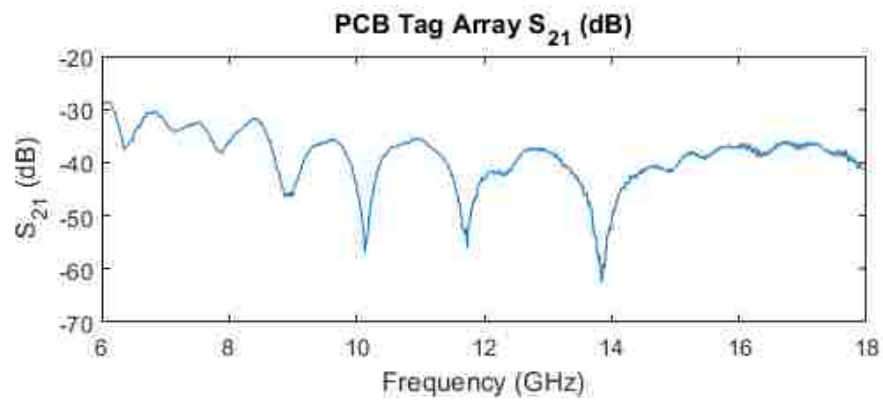


Figure 6.11. Measured response of 4 x 4 PCB tag array.

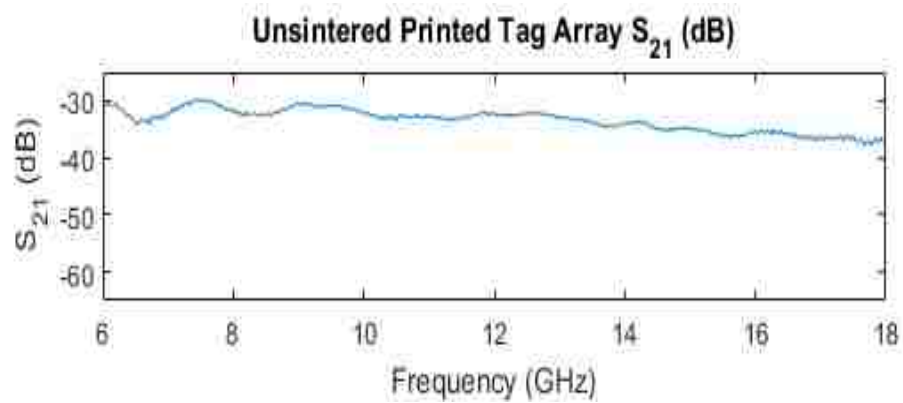


Figure 6.12. Measured response of 4 x 4 unsintered inkjet-printed tag array.

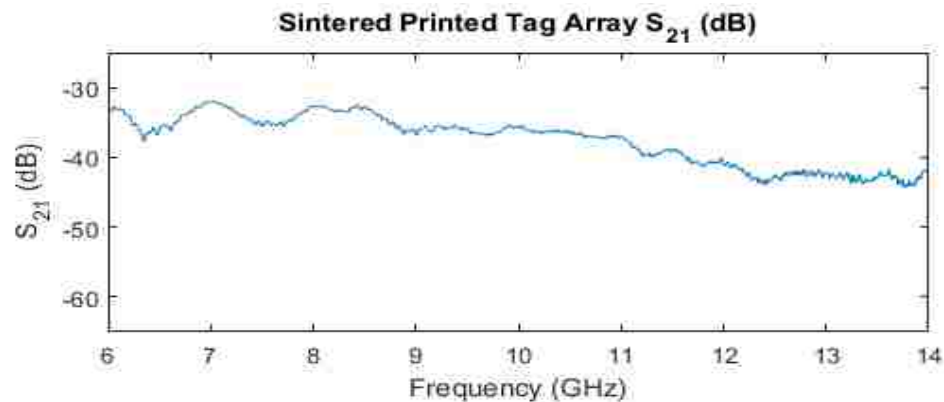


Figure 6.13. Measured response of 4 x 4 sintered inkjet-printed tag array.

#### 6.4. MICROWAVE THERMOGRAPHY

After conducting the measurements in Section 4.7 and seeing how the measured tag response did not agree with the simulated tag response, microwave thermography was employed in an attempt to determine if manufacturing inaccuracies of the tag were the root cause of the disagreement. Microwave thermography involves heating an object or structure selectively with microwaves and then using a thermal camera to examine how the heating occurs [174-176]. Based on the surface current density simulations conducted in Section 4.5, it was believed that microwave thermography could be used to show a higher heat concentration on tag features where one would expect a high surface current density for a certain frequency. To this end, a microwave source connected to an amplifier and a horn antenna was used to interrogate the eight spiral and single spiral tags at different frequencies corresponding to notches in the tags' responses. A Flir IR camera was then used to see if the expected features of the tag were heating up. Figure 6.14 shows the images taken with the thermal camera when the tag was interrogated with 8

GHz and 9.2 GHz, which correspond to two notches in the tag's response. In Figure 6.14a, the center circular patch is the brightest element when one would expect for the ring to be the brightest. In Figure 6.14b, the spiral on the right (the spiral in location 1 of the tag), is the brightest. In this case, the thermal image results match what would be expected from the RCS response and surface current density simulations. However, for frequencies of other notches in the response, no one spiral stood out as brighter than the others. This may be related to the other notches in the response not being as deep as the notch associated with the first spiral and the temperature raise not being sufficient.

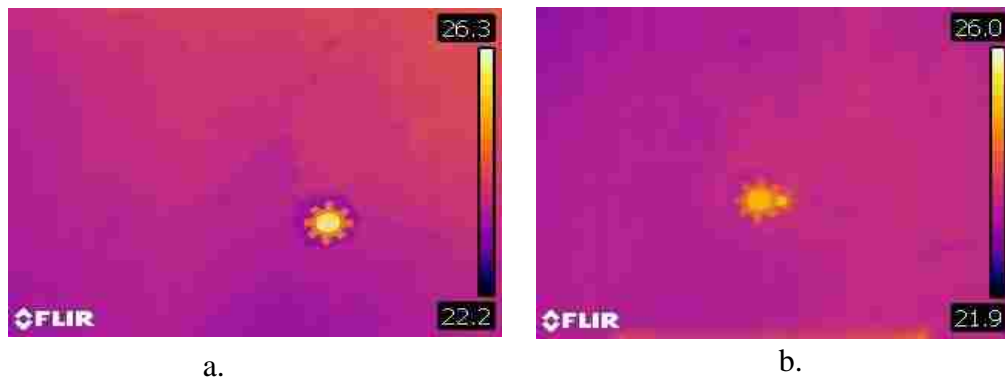


Figure 6.14. 8 spiral tag microwave thermography results. a) Thermal camera image for 8 GHz. b) Thermal camera image for 9.2 GHz.

To further examine this method, the single spiral tag was also examined. Figure 6.15 shows the thermal camera images for 8.7 and 9.25 GHz which correspond to the notch and spiral resonances in the response. In both images in Figure 6.15 the whole tag seems to glow when interrogated rather than a single feature. Referring back to the results in Figure 4.56, it was seen that both the spiral and the ring have high surface current density at these two frequencies and therefore both features contribute to the two notches

in the response in the 8 – 10 GHz frequency range. Based on this information, the images seen in Figure 6.15 could corroborate the surface current density simulations, however, the results are not consistent enough to prove the utility of this method for identifying manufacturing inaccuracies in tags.

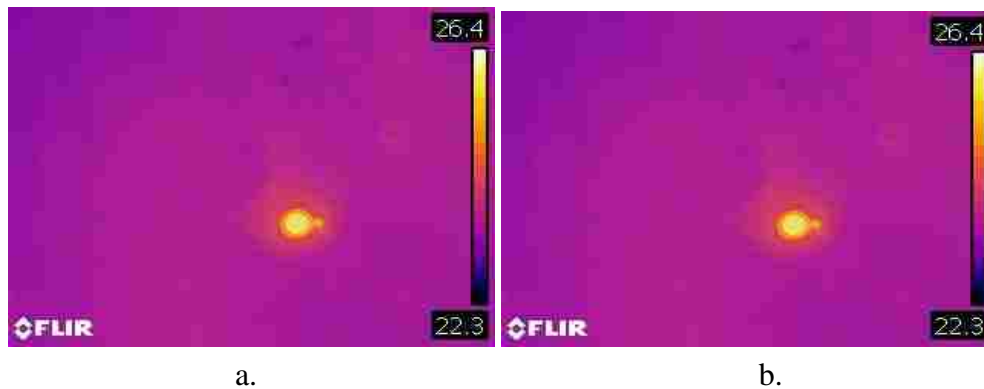


Figure 6.15. Single spiral tag microwave thermography results. a) Thermal camera image for 8.7 GHz. b) Thermal camera image for 9.25 GHz.

## 6.5. EMBEDDED TAG MEASUREMENTS

The last phase of this work revolved around completing additional embedded measurements with the eight spiral tag. For these measurements, the tag was placed on a dowel rod in a container. Due to the tag having a ground plane, the dowel rod is not seen and does not affect the measurements. The waveguide was then placed 1 cm from the tag. The measurement setup is shown in Figure 6.16. The tag was then measured both with and without the container filled with materials. When materials were added to the container, the container was filled so that material came to the surface of the tag (embedded 0 cm) and covered the tag by 0.5 cm (embedded 0.5 cm). The materials used

for these measurements were canola oil and sand. An example of the measurement setup with added material is shown in Figure 6.17.  $S_{11}$  measurements were then done of just the material without the tag and of the tag with the material. The measurement for just the material was subtracted from that of the tag, as was done in Section 2.3, in an attempt to isolate the response of the tag. The results for the two different embedding depths are shown in Figures 6.18 and 6.19. At the 0 cm embedded depth shown in Figure 6.18, a shift in response is seen for the two materials in comparison to the tag with no material.



Figure 6.16. Embedded tag measurement setup.





Figure 6.17. Embedded tag measurement setup for tag embedded 0 cm in oil.

Canola oil has a permittivity of  $\sim 2.9$  and sand is  $\sim 3.5$ . This would explain why the response for sand is downshifted further than that for oil. In Figure 6.19, when the tag is embedded 0.5cm below the surface of the material, the responses for oil and sand are indistinguishable. In the oil response, one notch at  $\sim 8$  GHz could potentially be said to be present. This would be a downshift from the free-space response. A reason for the sand response not having defined notches could be that the sand was slightly damp which would make it lossy. Additionally, because the tag is so small, its scattered signal is small in comparison to the tag that was used in Section 2.3. This makes it more difficult to discern the tag's response from that of the background even when background subtraction is done in post processing. By the notches not being discernable, a code cannot be assigned to these measured responses. Thus, materials characterization cannot be performed based on these measurements. Overall, these results show that some measurement challenges need to be overcome in order for this method be used for sensing purposes.

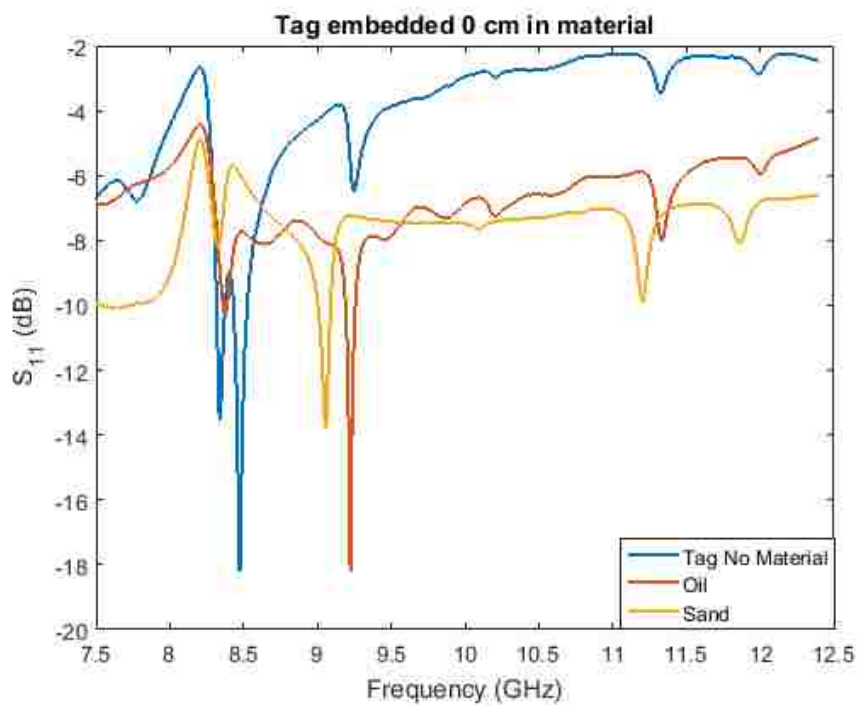


Figure 6.18. Responses for tag embedded 0 cm in free-space, oil, and sand.

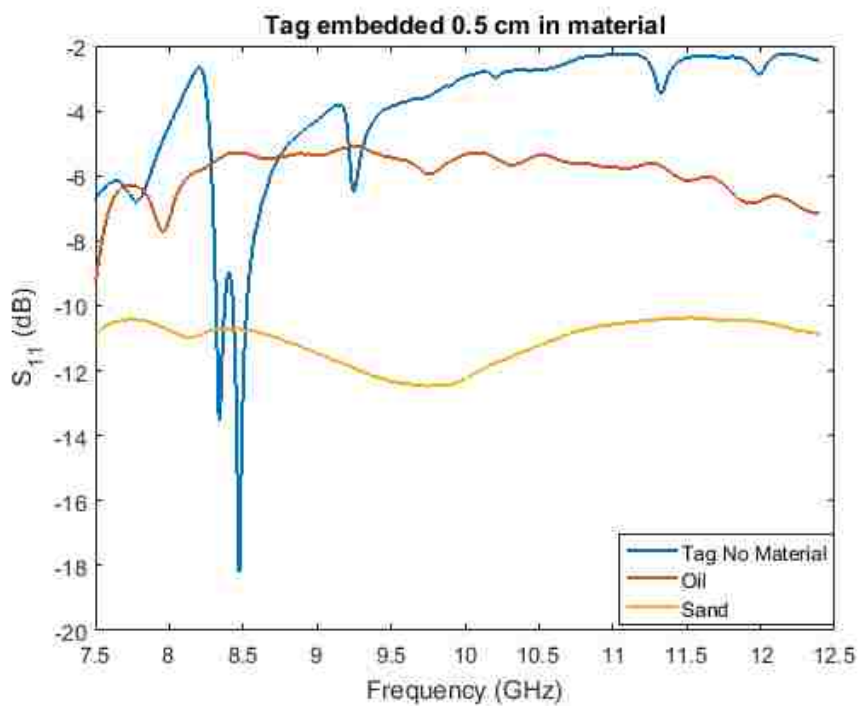


Figure 6.19. Responses for tag embedded 0.5 cm in free-space, oil, and sand.

## **7. SUMMARY AND FUTURE WORK**

### **7.1. BACKGROUND**

Chipless RFID is a relatively new, yet versatile technology that has great potential in both the identification and sensing application spaces. Tags have been developed for many different sensing purposes, but until this work, using chipless RFID tags for embedded materials characterization has yet to be explored. The goal of this thesis was to explore the utility of embedded materials characterization with chipless RFID and develop a tag design methodology so that tags could be created for this sensing application. Inkjet-printing was also explored as a method for manufacturing in order to create tags in an inexpensive quick manner. Though addressing these goals, the foundation for a new nondestructive testing method was laid.

### **7.2. MATERIALS CHARACTERIZATION METHODOLOGY**

In Section 2, a proof of concept was conducted to show that embedded chipless RFID tags could be used to perform microwave materials characterization. In this proof of concept, both simulation and measurement were conducted and it was shown that the tag response changes as a function of the material it is embedded in. As permittivity increases the response tends to shift down in frequency and compress and as the loss tangent increases the response tends to distort more. By assigning a binary code to the response, one can observe how this code changes as the material the tag is embedded in changes. However, previously presented coding methods are designed for ID applications where the response is rather stable and predictable. Thus, the codes produced by these methods do not capture shifts and distortions in response well. For this reason a new

coding method was developed and demonstrated in Section 3. Through examples it was shown that the bandwidth coded and the threshold chosen can both have a large effect on the codes that are produced. Therefore, the code assigner needs to select these on a tag by tag basis.

Lastly, additional embedded measurements were conducted in Section 6.5. These measurements showed that there are still some measurement challenges that need to be overcome in order for embedded chipless RFID materials characterization to be a practical method.

### **7.3. APPLICATION-ADAPTABLE DESIGN METHODOLOGY**

Many chipless RFID tags consist of a single type of resonator which limits their versatility. By combining multiple types of resonators, a greater variety of responses can be achieved which then allows tags to be used for more purposes. In Section 4, a methodology for designing tags by combining multiple types of resonators was developed. This methodology relies on design guidelines such as equations, equivalent circuits, and design curves to allow for manipulation of tag geometry in a purposeful manner. This then allows the tag designer to engineer their tag's response rather than develop it through trial and error. This methodology can then be coupled with surface current density simulations in the manner described in Section 4.5 to gain greater insight into how different tag designs will perform. Furthermore, tags can easily be adapted for different applications by employing this process.

The developed tag design methodology was then used to create a tag that combines ring and spiral resonators. By doing so, this tag achieves a very high bit

density. The tag can then be adapted to work for a variety of applications including ID and materials characterization and to operate in different frequency ranges. It can also be adapted for different manufacturing techniques, such as inkjet-printing which was the subject of Section 5.

In Section 5, inkjet-printing for chipless RFID tags was explored. Different popular printing papers had their dielectric properties determined and the conductivity of printed features were determined. These printing parameters were then fed into simulations to predict how printed tags would perform and explain why measurements of prints were not showing the expected response characteristics. Through this investigation of inkjet-printing, it was found that while this method does have many advantages like being quick and inexpensive, it tends to suffer from low conductivity. The low conductivity can prevent tags from being measurable. Thus, it is important for conductivity enhancing methods like sintering and multi-layer printing to be investigated so that this method can be employed in the chipless RFID field.

#### **7.4. FUTURE WORK**

While the utility of the embedded materials characterization methodology presented in this work was shown, there are many aspects of this method that could be refined and improved. First, the coding method could be further optimized so that it is more sensitive to small changes in dielectric properties while only the needed number of bits are used so that the codes do not become too long and unwieldy. Next, the measurement method could be refined so that changes in material are detected correctly. Doing this would involve further investigation into different measurement setups, such as

using a bistatic setup or different reader antenna, and also looking at different post processing methods. Furthermore, more materials with a wider variety of dielectric properties could be used for embedded tag measurements. This information could then be fed into a model or database, with the goal of creating a system that could determine dielectric properties from the code associated with the tag response.

Another aspect of the future work would be to address some of the issues associated with inkjet-printing as a manufacturing method. More specifically, techniques for increasing the conductivity without counteracting the advantages of inkjet-printing being quick and inexpensive would have to be developed. To this end, different inks and sintering methods could be explored. Sealants for printed tags could also be investigated in order to increase their durability. Additionally, more printing substrates could be characterized so that tags can be better simulated.

Finally, measurement challenges associated with chipless RFID need to be addressed. These include increasing the read range, overcoming the need for precise tag/reader alignment, minimizing the effects the background can have on tag responses, and avoiding distance dependency. These issues could be addressed by employing different reader antennas, such as ones with high gain and circular polarization, and by refining the RCS measurement process to make it both more accurate and easier to use in the field. Furthermore, new post processing methods could be developed to address these issues.

**BIBLIOGRAPHY**

- [1] K. M. Donnell, M. A. Abou-Khousa, M. Belayneh, and R. Zoughi, "Dual-Loaded Modulated Dipole Scatterer as an Embedded Sensor," *IEEE Transactions on Instrumentation and Measurement*, vol. 60, pp. 1884-1892, 2011.
- [2] R. Zoughi, J. R. Gallion, and M. T. Ghasr, "Accurate Microwave Measurement of Coating Thickness on Carbon Composite Substrates," *IEEE Transactions on Instrumentation and Measurement*, vol. 65, pp. 951-953, 2016.
- [3] A. Abedi, "Battery free wireless sensor networks: Theory and applications," in *2014 International Conference on Computing, Networking and Communications (ICNC)*, 2014, pp. 287-291.
- [4] D. Sleight, T. Sreekantamurthy, D. Kosareo, R. Martin, T. Johnson, and R. Martin, "Structural Design of Ares V Interstage Composite Structure," in *52nd AIAA/ASME/ASCE/AHS/ASC Structures, Structural Dynamics and Materials Conference*, ed: American Institute of Aeronautics and Astronautics, 2011.
- [5] G. Gardiner. (2015). *Structural health monitoring: NDT-integrated aerostructures*. Available: <https://www.compositesworld.com/articles/structural-health-monitoring-ndt-integrated-aerostructures-enter-service>
- [6] H. Liu, M. Bolic, A. Nayak, and I. Stojmenovic, "Taxonomy and Challenges of the Integration of RFID and Wireless Sensor Networks," *IEEE Network*, vol. 22, pp. 26-35, 2008.
- [7] E. Perret, *Radio Frequency Identification and Sensors: From RFID to Chipless RFID*. : Wiley, 2014.
- [8] J. Cho, Y. Shim, T. Kwon, Y. Choi, S. Pack, and S. Kim, "SARIF: A novel framework for integrating wireless sensor and RFID networks," *IEEE Wireless Communications*, vol. 14, pp. 50-56, 2007.
- [9] D. Jayawardana, S. Kharkovsky, R. Liyanapathirana, and X. Zhu, "Measurement System With Accelerometer Integrated RFID Tag for Infrastructure Health Monitoring," *IEEE Transactions on Instrumentation and Measurement*, vol. 65, pp. 1163-1171, 2016.
- [10] A. W. Nagpurkar and S. K. Jaiswal, "An overview of WSN and RFID network integration," in *2015 2nd International Conference on Electronics and Communication Systems (ICECS)*, 2015, pp. 497-502.

- [11] EPC, "EPC™ Radio-Frequency Identity Protocols Generation-2 UHF RFID," ed. Brussels, 2018.
- [12] S. Preradovic and N. Karmakar, *Multiresonator-Based Chipless RFID Barcode of the Future*: Springer 2012.
- [13] S. Mukherjee, "Chipless Radio Frequency Identification (RFID) Device," in *2007 1st Annual RFID Eurasia*, 2007, pp. 1-4.
- [14] D. Dardari and R. D. Errico, "Passive Ultrawide Bandwidth RFID," in *IEEE GLOBECOM 2008 - 2008 IEEE Global Telecommunications Conference*, 2008, pp. 1-6.
- [15] C. Herrojo, J. Mata-Contreras, F. Paredes, and F. Martín, "Microwave Encoders for Chipless RFID and Angular Velocity Sensors Based on S-Shaped Split Ring Resonators," *IEEE Sensors Journal*, vol. 17, pp. 4805-4813, 2017.
- [16] A. Ramos, A. Lazaro, and D. Girbau, "Time-coded chipless sensors to detect quality of materials in civil engineering," in *2015 9th European Conference on Antennas and Propagation (EuCAP)*, 2015, pp. 1-4.
- [17] S. Preradovic, I. Balbin, N. C. Karmakar, and G. Swiegers, "A Novel Chipless RFID System Based on Planar Multiresonators for Barcode Replacement," in *2008 IEEE International Conference on RFID*, 2008, pp. 289-296.
- [18] S. Preradovic and N. Karmakar, "Chipless millimeter wave identification (MMID) tag at 30 GHz," in *2011 41st European Microwave Conference*, 2011, pp. 123-126.
- [19] A. Habib, M. A. Afzal, H. Sadia, Y. Amin, and H. Tenhunen, "Chipless RFID tag for IoT applications," in *2016 IEEE 59th International Midwest Symposium on Circuits and Systems (MWSCAS)*, 2016, pp. 1-4.
- [20] V. Sharma and M. Hashmi, "Chipless RFID tag based on open-loop resonator," in *2017 IEEE Asia Pacific Microwave Conference (APMC)*, 2017, pp. 543-546.
- [21] M. Khaliel, A. Fawky, A. El-Awamry, A. E. Mahmoud, and T. Kaiser, "Printable, high coding capacity chipless RFID tags for low-cost item tagging," in *2017 IEEE 14th International Conference on Networking, Sensing and Control (ICNSC)*, 2017, pp. 351-355.
- [22] Y. Liu and X. Yang, "Chipless Radio Frequency Identification Tag Design with Modified Interdigital Hairpin Resonators," in *2018 International Conference on Intelligent Transportation, Big Data & Smart City (ICITBS)*, 2018, pp. 645-648.



- [23] M. A. Islam, Y. Yap, N. Karmakar, and A. K. M. Azad, "Orientation independent compact chipless RFID tag," in *2012 IEEE International Conference on RFID-Technologies and Applications (RFID-TA)*, 2012, pp. 137-141.
- [24] N. Javed, A. Habib, Y. Amin, and H. Tenhunen, "Miniaturized flexible chipless RFID tag for IoT market," in *2017 International Conference on Communication, Computing and Digital Systems (C-CODE)*, 2017, pp. 71-74.
- [25] A. Vena, E. Perret, and S. Tedjini, "High-Capacity Chipless RFID Tag Insensitive to the Polarization," *IEEE Transactions on Antennas and Propagation*, vol. 60, pp. 4509-4515, 2012.
- [26] F. Costa, S. Genovesi, and A. Monorchio, "A Chipless RFID Based on Multiresonant High-Impedance Surfaces," *IEEE Transactions on Microwave Theory and Techniques*, vol. 61, pp. 146-153, 2013.
- [27] A. Vena, E. Perret, and S. Tedjini, "Chipless RFID Tag Using Hybrid Coding Technique," *IEEE Transactions on Microwave Theory and Techniques*, vol. 59, pp. 3356-3364, 2011.
- [28] D. H. Nguyen, M. Zomorodi, and N. C. Karmarka, "Spatial-Based Chipless RFID System," *IEEE Journal of Radio Frequency Identification*, pp. 1-1, 2019.
- [29] M. Khaliel, M. El-Hadidy, and T. Kaiser, "Printable depolarizing chipless RFID tag based on DGS resonators for suppressing the clutter effects," in *2015 9th European Conference on Antennas and Propagation (EuCAP)*, 2015, pp. 1-5.
- [30] H. Bao and X. Liu, "A depolarizing chipless RFID tag with quasi-loop resonators," in *2017 IEEE International Symposium on Antennas and Propagation & USNC/URSI National Radio Science Meeting*, 2017, pp. 2513-2514.
- [31] M. M. Khan, F. A. Tahir, and H. M. Cheema, "High capacity polarization sensitive chipless RFID tag," in *2015 IEEE International Symposium on Antennas and Propagation & USNC/URSI National Radio Science Meeting*, 2015, pp. 1770-1771.
- [32] O. Necibi, S. Naoui, and A. Gharsallah, "Design of a chipless RFID TAG based on the frequency shift technique for K band," in *2016 2nd International Conference on Advanced Technologies for Signal and Image Processing (ATSIP)*, 2016, pp. 816-819.
- [33] F. Zheng, Y. Chen, T. Kaiser, and A. J. H. Vinck, "On the Coding of Chipless Tags," *IEEE Journal of Radio Frequency Identification*, vol. 2, pp. 170-184, 2018.

- [34] M. Khaliel, A. El-Awamry, A. F. Megahed, and T. Kaiser, "A Novel Design Approach for Co/Cross-Polarizing Chipless RFID Tags of High Coding Capacity," *IEEE Journal of Radio Frequency Identification*, vol. 1, pp. 135-143, 2017.
- [35] M. M. Khan, F. A. Tahir, M. F. Farooqui, A. Shamim, and H. M. Cheema, "3.56-bits/cm Compact Inkjet Printed and Application Specific Chipless RFID Tag," *IEEE Antennas and Wireless Propagation Letters*, vol. 15, pp. 1109-1112, 2016.
- [36] M. Mumtaz, S. F. Amber, A. Ejaz, A. Habib, S. I. Jafri, and Y. Amin, "Design and analysis of C shaped chipless RFID tag," in *2017 International Symposium on Wireless Systems and Networks (ISWSN)*, 2017, pp. 1-5.
- [37] M. A. Islam and N. C. Karmakar, "Real-World Implementation Challenges of a Novel Dual-Polarized Compact Printable Chipless RFID Tag," *IEEE Transactions on Microwave Theory and Techniques*, vol. 63, pp. 4581-4591, 2015.
- [38] M. Svanda, J. Havlicek, J. Machac, and M. Polivka, "Polarisation independent chipless RFID tag based on circular arrangement of dual-spiral capacitively-loaded dipoles with robust RCS response," *IET Microwaves, Antennas & Propagation*, vol. 12, pp. 2167-2171, 2018.
- [39] K. Kalantar-zadeh, *Sensors: An Introductory Course*: Springer US, 2013.
- [40] J. Mujal, E. Ramon, E. Díaz, J. Carrabina, C. Á, R. Martínez, *et al.*, "Inkjet printed antennas for NFC systems," in *2010 17th IEEE International Conference on Electronics, Circuits and Systems*, 2010, pp. 1220-1223.
- [41] B. S. Cook and A. Shamim, "Inkjet Printing of Novel Wideband and High Gain Antennas on Low-Cost Paper Substrate," *IEEE Transactions on Antennas and Propagation*, vol. 60, pp. 4148-4156, 2012.
- [42] S. Kim, B. Cook, T. Le, J. Cooper, H. Lee, V. Lakafosis, *et al.*, "Inkjet-printed antennas, sensors and circuits on paper substrate," *IET Microwaves, Antennas & Propagation*, vol. 7, pp. 858-868, 2013.
- [43] M. M. Tentzeris, "Inkjet-Printed Nanotechnology-Enabled Zero-Power Wireless Sensor Nodes for Internet-of-Things (IoT) and M2M Applications " Georgia Tech, Presentation.
- [44] L. Yang, A. Rida, R. Vyas, and M. M. Tentzeris, "RFID Tag and RF Structures on a Paper Substrate Using Inkjet-Printing Technology," *IEEE Transactions on Microwave Theory and Techniques*, vol. 55, pp. 2894-2901, 2007.

- [45] B. Shao, Q. Chen, Y. Amin, R. Liu, and L.-R. Zheng, "Chipless RFID tags fabricated by fully printing of metallic inks," *annals of telecommunications - annales des télécommunications*, vol. 68, pp. 401-413, 2013/08/01 2013.
- [46] S. Khan, L. Lorenzelli, and R. S. Dahiya, "Technologies for Printing Sensors and Electronics Over Large Flexible Substrates: A Review," *IEEE Sensors Journal*, vol. 15, pp. 3164-3185, 2015.
- [47] R. Nair, M. Barahona, D. Betancourt, G. Schmidt, M. Bellmann, D. Höft, *et al.*, "A fully printed passive chipless RFID tag for low-cost mass production," in *The 8th European Conference on Antennas and Propagation (EuCAP 2014)*, 2014, pp. 2950-2954.
- [48] D. Betancourt, R. Nair, K. Haase, G. Schmidt, M. Bellmann, D. Höft, *et al.*, "Square-shape fully printed chipless RFID tag and its applications in evacuation procedures," in *2015 9th European Conference on Antennas and Propagation (EuCAP)*, 2015, pp. 1-5.
- [49] B. Shao, Q. Chen, R. Liu, and L.-R. Zheng, "Design of fully printable and configurable chipless RFID tag on flexible substrate," *Microwave and Optical Technology Letters*, vol. 54, pp. 226-230, 2012/01/01 2012.
- [50] M. Borgese, F. A. Dicandia, F. Costa, S. Genovesi, and G. Manara, "An Inkjet Printed Chipless RFID Sensor for Wireless Humidity Monitoring," *IEEE Sensors Journal*, vol. 17, pp. 4699-4707, 2017.
- [51] S. Preradovic, I. Balbin, N. C. Karmakar, and G. F. Swiegers, "Multiresonator-Based Chipless RFID System for Low-Cost Item Tracking," *IEEE Transactions on Microwave Theory and Techniques*, vol. 57, pp. 1411-1419, 2009.
- [52] A. Vena, E. Perret, and S. Tedjini, "A Fully Printable Chipless RFID Tag With Detuning Correction Technique," *IEEE Microwave and Wireless Components Letters*, vol. 22, pp. 209-211, 2012.
- [53] L. Xu and K. Huang, "Design of Compact Trapezoidal Bow-Tie Chipless RFID Tag " *International Journal of Antennas and Propagation*, vol. 2015, 23 July 2014 2014.
- [54] M. A. Islam, Y. Yap, and N. Karmakar, "' $\Delta$ ' slotted compact printable orientation insensitive chipless RFID tag for long range applications," in *2016 9th International Conference on Electrical and Computer Engineering (ICECE)*, 2016, pp. 283-286.

- [55] M. Polivka, J. Havlicek, M. Svanda, and J. Machac, "Improvement in Robustness and Recognizability of RCS Response of U-Shaped Strip-Based Chipless RFID Tags," *IEEE Antennas and Wireless Propagation Letters*, vol. 15, pp. 2000-2003, 2016.
- [56] K. Yang, D. Forte, and M. M. Tehranipoor, "UCR: An unclonable chipless RFID tag," in *2016 IEEE International Symposium on Hardware Oriented Security and Trust (HOST)*, 2016, pp. 7-12.
- [57] H. Huang and L. Su, "A Compact Dual-Polarized Chipless RFID Tag by Using Nested Concentric Square Loops," *IEEE Antennas and Wireless Propagation Letters*, vol. 16, pp. 1036-1039, 2017.
- [58] J. Havlicek, M. Svanda, M. Polivka, J. Machac, and J. Kracek, "Chipless RFID Tag Based on Electrically Small Spiral Capacitively Loaded Dipole," *IEEE Antennas and Wireless Propagation Letters*, vol. 16, pp. 3051-3054, 2017.
- [59] H. ANAM, A. HABIB, S. I. JAFRI, Y. AMIN, and H. TENHUNEN, "Directly Printable Frequency Signed Chipless RFID Tag for IoT Applications " *RADIOENGINEERING*, vol. 26, 2017.
- [60] S. Zeb, J. A. Satti, A. Habib, Y. Amin, and H. Tenhunen, "Dual-polarized data dense chipless RFID tag towards IoT applications," in *2017 International Symposium on Wireless Systems and Networks (ISWSN)*, 2017, pp. 1-5.
- [61] M. Narula and A. Kumar, "Miniaturized chipless RFID tag using multiple microstrip resonators," in *2017 International Conference on Nextgen Electronic Technologies: Silicon to Software (ICNETS2)*, 2017, pp. 101-104.
- [62] M. Polivka, M. Scanda, J. Havlicek, and J. Machac, "Detuned Dipole Array Backed by Rectangular Plate Applied as Chipless RFID Tag," *Progress In Electromagnetics Research Symposium Proceedings*, 2017.
- [63] J. Song, X. Li, and H. Zhu, "A 16-bit chipless RFID tag with quasi-complementary structure," in *2017 Sixth Asia-Pacific Conference on Antennas and Propagation (APCAP)*, 2017, pp. 1-3.
- [64] H. T. Abbas, H. H. Abdullah, M. A. H. Mohanna, H. A. Mansour, and G. S. Shehata, "High RCS compact orientation independent chipless RFID tags based on slot ring resonators (SRR)," in *2018 35th National Radio Science Conference (NRSC)*, 2018, pp. 69-76.
- [65] T. Cheng, L. Wang, P. Cheong, S. Ho, W. Choi, G. Yang, *et al.*, "Design of UWB Chipless RFID Tag using Microstrip and Slot Cross-shaped Resonators," in *2018 International Flexible Electronics Technology Conference (IFETC)*, 2018, pp. 1-4.

- [66] G. C. Wan, Y. K. Kuang, Q. Xu, and M. S. Tong, "A Novel Chipless RFID Tag Based on Backscattering Principle," in *2018 Progress in Electromagnetics Research Symposium (PIERS-Toyama)*, 2018, pp. 1295-1298.
- [67] R. Figueiredo, J. Louro, S. Pereira, J. Gonçalves, and N. B. Carvalho, "Design of Narrow Band Single-Layer Chipless RFID Tag," in *2018 2nd URSI Atlantic Radio Science Meeting (AT-RASC)*, 2018, pp. 1-4.
- [68] W. M. Adbulkawi and A. A. Sheta, "Printable Chipless RFID Tags for IoT Applications," in *2018 1st International Conference on Computer Applications & Information Security (ICCAIS)*, 2018, pp. 1-4.
- [69] S. Shrestha, R. P. Yerramilli, and N. C. Karmakar, "Spatially efficient chipless RFID tag, Screen-printed on flexible substrate," in *12th European Conference on Antennas and Propagation (EuCAP 2018)*, 2018, pp. 1-4.
- [70] V. Sharma, S. Malhotra, and M. Hashmi, "Slot Resonator Based Novel Orientation Independent Chipless RFID Tag Configurations," *IEEE Sensors Journal*, pp. 1-1, 2019.
- [71] A. Lázaro, R. Villarino, F. Costa, S. Genovesi, A. Gentile, L. Buoncristiani, *et al.*, "Chipless Dielectric Constant Sensor for Structural Health Testing," *IEEE Sensors Journal*, vol. 18, pp. 5576-5585, 2018.
- [72] S. Dey and N. C. Karmakar, "Chipless RFID strain sensors: A novel feasibility analysis in terms of conventional patch antennas," in *2015 IEEE MTT-S International Microwave and RF Conference (IMaRC)*, 2015, pp. 72-75.
- [73] A. Vena, M. Tedjini, T. Björninen, L. Sydänheimo, L. Ukkonen, and M. M. Tentzeris, "A novel inkjet-printed wireless chipless strain and crack sensor on flexible laminates," in *2014 IEEE Antennas and Propagation Society International Symposium (APSURSI)*, 2014, pp. 1294-1295.
- [74] E. Perret, "Micrometric displacement sensor based on chipless RFID," in *2017 IEEE MTT-S International Microwave Symposium (IMS)*, 2017, pp. 605-608.
- [75] S. Genovesi, F. Costa, M. Borgese, F. A. Dicandia, A. Monorchio, and G. Manara, "Chipless RFID sensor for rotation monitoring," in *2017 IEEE International Conference on RFID Technology & Application (RFID-TA)*, 2017, pp. 233-236.
- [76] R. Khalifeh, M. S. Yasri, B. Lescop, F. Gallée, E. Diler, D. Thierry, *et al.*, "Development of Wireless and Passive Corrosion Sensors for Material Degradation Monitoring in Coastal Zones and Immersed Environment," *IEEE Journal of Oceanic Engineering*, vol. 41, pp. 776-782, 2016.

- [77] L. Yang, R. Zhang, D. Staiculescu, C. P. Wong, and M. M. Tentzeris, "A Novel Conformal RFID-Enabled Module Utilizing Inkjet-Printed Antennas and Carbon Nanotubes for Gas-Detection Applications," *IEEE Antennas and Wireless Propagation Letters*, vol. 8, pp. 653-656, 2009.
- [78] P. Kalansuriya, R. Bhattacharyya, S. Sarma, and N. Karmakar, "Towards chipless RFID-based sensing for pervasive surface crack detection," in *2012 IEEE International Conference on RFID-Technologies and Applications (RFID-TA)*, 2012, pp. 46-51.
- [79] R. Suwalak, C. Phongcharoenpanich, D. Torrungrueng, and P. Akkaraekthalin, "Dielectric material determination using the radar equation in RFID sensor applications," in *2015 IEEE Conference on Antenna Measurements & Applications (CAMA)*, 2015, pp. 1-4.
- [80] E. Perret, "Permittivity characterization based on Radar Cross measurements," in *2016 URSI International Symposium on Electromagnetic Theory (EMTS)*, 2016, pp. 457-460.
- [81] R. Suwalak, K. Lertsakwimarn, C. Phongcharoenpanich, and D. Torrungrueng, "Dual-band chipless RFID sensor for a material quality monitoring application," in *2016 International Symposium on Antennas and Propagation (ISAP)*, 2016, pp. 1004-1005.
- [82] M. Martinez and D. v. d. Weide, "Chipless RFID temperature threshold sensor and detection method," in *2017 IEEE International Conference on RFID (RFID)*, 2017, pp. 61-66.
- [83] N. Javed, A. Habib, Y. Amin, and H. Tenhunen, "Towards Moisture Sensing Using Dual-Polarized Printable Chipless RFID Tag," in *2017 International Conference on Frontiers of Information Technology (FIT)*, 2017, pp. 189-193.
- [84] M. Yang, W. Zhang, L. Li, L. Han, X. Chen, R. Yang, *et al.*, "A Resistance-Type Sensor Based on Chipless RFID," *IEEE Transactions on Antennas and Propagation*, vol. 65, pp. 3319-3325, 2017.
- [85] P. Schumacher, C. Schuster, A. Jiménez-Sáez, M. Schüßler, and R. Jakoby, "Passive chipless wireless pressure sensor for Harsh and reflective environments," in *2018 11th German Microwave Conference (GeMiC)*, 2018, pp. 227-230.
- [86] F. Costa, A. Gentile, S. Genovesi, L. Buoncristiani, A. Lazaro, R. Villarino, *et al.*, "Non-contact Material Monitoring by Using Depolarizing Chipless RFID Tags," in *2018 IEEE International Symposium on Antennas and Propagation & USNC/URSI National Radio Science Meeting*, 2018, pp. 1497-1498.

- [87] S. Deif, L. Harron, and M. Daneshmand, "Out-of-Sight Salt-Water Concentration Sensing Using Chipless- RFID for Pipeline Coating Integrity," in *2018 IEEE/MTT-S International Microwave Symposium - IMS*, 2018, pp. 367-370.
- [88] D. Girbau, A. Lázaro, and R. Villarino, "Passive wireless permittivity sensor based on frequency-coded chipless RFID tags," in *2012 IEEE/MTT-S International Microwave Symposium Digest*, 2012, pp. 1-3.
- [89] S. Fan, T. Chang, X. Liu, Y. Fan, and M. M. Tentzeris, "A Depolarizing Chipless RFID Tag with Humidity Sensing Capability," in *2018 IEEE International Symposium on Antennas and Propagation & USNC/URSI National Radio Science Meeting*, 2018, pp. 2469-2470.
- [90] A. M. J. Marindra, R. Sutthaweekul, and G. Y. Tian, "Depolarizing Chipless RFID Sensor Tag for Characterization of Metal Cracks Based on Dual Resonance Features," in *2018 10th International Conference on Information Technology and Electrical Engineering (ICITEE)*, 2018, pp. 73-78.
- [91] A. Vena, E. Perret, and S. Tedjini, "A compact chipless RFID tag using polarization diversity for encoding and sensing," in *2012 IEEE International Conference on RFID (RFID)*, 2012, pp. 191-197.
- [92] R. Zoughi, *Microwave Non-Destructive Testing and Evaluation Principles*: Springer Netherlands, 2000.
- [93] U. Inan, A. Inan, and R. Said, *Engineering Electromagnetics and Waves*, 2 ed. Upper Saddle River, NJ: Pearson, 2015.
- [94] J. Baker-Jarvis, C. Jones, B. Riddle, M. Janezic, R. G. Geyer, J. H. Grosvenor Jr., et al., *Dielectric and magnetic measurements: A survey of nondestructive, quasi-nondestructive, and process-control techniques* vol. 7: Springer, 1995.
- [95] M. T. Ghasr, D. Simms, and R. Zoughi, "Multimodal Solution for a Waveguide Radiating Into Multilayered Structures—Dielectric Property and Thickness Evaluation," *IEEE Transactions on Instrumentation and Measurement*, vol. 58, pp. 1505-1513, 2009.
- [96] K. J. Bois, L. F. Handjojo, A. D. Benally, K. Mubarak, and R. Zoughi, "Dielectric plug-loaded two-port transmission line measurement technique for dielectric property characterization of granular and liquid materials," *IEEE Transactions on Instrumentation and Measurement*, vol. 48, pp. 1141-1148, 1999.
- [97] C. Z. Beisteiner, Bernhard G., "Dielectric Permittivity Measurement of Paper Substrates Using Commercial Inkjet Printers," *30th Eurosensors Conference Proceedings*, vol. 168, pp. 995-998, 2016.

- [98] A. Rida, L. Yang, R. Vyas, and M. M. Tentzeris, "Conductive Inkjet-Printed Antennas on Flexible Low-Cost Paper-Based Substrates for RFID and WSN Applications," *IEEE Antennas and Propagation Magazine*, vol. 51, pp. 13-23, 2009.
- [99] F. Costa, E. Perret, S. Genovesi, S. Tedjini, A. Lazaro, D. Girbau, *et al.*, "Progress in green chipless RFID sensors," in *2017 11th European Conference on Antennas and Propagation (EUCAP)*, 2017, pp. 3917-3921.
- [100] T. P. Marsland and S. Evans, "Dielectric measurements with an open-ended coaxial probe," *IEE Proceedings H - Microwaves, Antennas and Propagation*, vol. 134, pp. 341-349, 1987.
- [101] P. A. Bernard and J. M. Gautray, "Measurement of dielectric constant using a microstrip ring resonator," *IEEE Transactions on Microwave Theory and Techniques*, vol. 39, pp. 592-595, 1991.
- [102] F. Costa, A. Gentile, S. Genovesi, L. Buoncristiani, A. Lazaro, R. Villarino, *et al.*, "A Depolarizing Chipless RF Label for Dielectric Permittivity Sensing," *IEEE Microwave and Wireless Components Letters*, vol. 28, pp. 371-373, 2018.
- [103] K. Brinker and R. Zoughi, "Embedded chipless RFID measurement methodology for microwave materials characterization," in *2018 IEEE International Instrumentation and Measurement Technology Conference (I2MTC)*, 2018, pp. 1-6.
- [104] K. Brinker, M. Vaccaro, and R. Zoughi, "Application-Adaptable Chipless RFID Tag: Design Methodology, Metrics, and Measurements."
- [105] F. Costa, S. Genovesi, and A. Monorchio, "Reading chipless RFID located on metallic platforms by using cross-polar scattering," in *2014 XXXIth URSI General Assembly and Scientific Symposium (URSI GASS)*, 2014, pp. 1-4.
- [106] D. Hotte, R. Siragusa, Y. Duroc, and S. Tedjini, "Radar cross-section measurement in millimetre-wave for passive millimetre-wave identification tags," *IET Microwaves, Antennas & Propagation*, vol. 9, pp. 1733-1739, 2015.
- [107] E. Çetin, M. B. Sahin, and E. Ö, "Array Strategies for Improving the Performances of Chipless RFID Tags," in *2018 IEEE International Symposium on Antennas and Propagation & USNC/URSI National Radio Science Meeting*, 2018, pp. 2015-2016.
- [108] K. Brinker and R. Zoughi, "Application-Adaptable Chipless RFID Tag," in *Proceedings of the IEEE International Symposium on Antennas and Propagation (AP-S)*, Boston, MA, 2018, pp. 1493-1494.



- [109] G. T. Santos-Souza, A. A. d. C. Alves, L. L. Bravo-Roger, and H. E. Hernandez-Figueroa, "Numerical determination of frequency guard band resonances for Chipless RFID Tags," in *2014 IEEE Brasil RFID*, 2014, pp. 10-12.
- [110] L. d. S. Araújo and A. J. B. d. Oliveira, "The square spiral resonator: Investigating its electromagnetic performance for filter design," in *2015 SBMO/IEEE MTT-S International Microwave and Optoelectronics Conference (IMOC)*, 2015, pp. 1-6.
- [111] T. Jiang, F. Lai, and Y. Chen, "Investigation of the bandwidth of resonators for frequency-coded chipless radio-frequency identification tags," in *2018 27th Wireless and Optical Communication Conference (WOCC)*, 2018, pp. 1-4.
- [112] C. Saha and J. Y. Siddiqui, "A comparative analysis for split ring resonators of different geometrical shapes," in *2011 IEEE Applied Electromagnetics Conference (AEMC)*, 2011, pp. 1-4.
- [113] O. B. Kobe, J. Chuma, R. Jamisola, and M. Chose, "A review on quality factor enhanced on-chip microwave planar resonators," *Engineering Science and Technology, an International Journal* pp. 460-466, 2017.
- [114] D. S. La, S. Q. Jia, and X. L. Ma, "Compact wideband band-pass filter using regular hexagon ring resonator," in *2015 Asia-Pacific Microwave Conference (APMC)*, 2015, pp. 1-3.
- [115] K. Fertas, F. Ghanem, M. Challal, M. Ouahdi, F. Fertas, and R. Aksas, "Design and implementation of a novel tri-band bandstop filter based on hexagonal metamaterials split ring resonators," in *2017 5th International Conference on Electrical Engineering - Boumerdes (ICEE-B)*, 2017, pp. 1-4.
- [116] K. Song, Y. Zhu, M. Zhao, M. Fan, and Y. Fan, "Miniaturized bandpass filter using dual-mode hexagonal loop resonator," *International Journal of Microwave and Wireless Technologies*, vol. 9, pp. 1003-1008, 2017.
- [117] A. Gupta and B. Garg, "Multilayer Butterworth Third Order Lowpass Filter Based on Spiral Hexagon Ring Resonator," *International Journal of Scientific Research Engineering & Technology (IJSRET)*, vol. 4, 2015.
- [118] M. Martinez and D. v. d. Weide, "Compact slot-based chipless RFID tag," in *2014 IEEE RFID Technology and Applications Conference (RFID-TA)*, 2014, pp. 233-236.
- [119] A. Habib, M. A. Azam, Y. Amin, and H. Tenhunen, "Chipless slot resonators for IoT system identification," in *2016 IEEE International Conference on Electro Information Technology (EIT)*, 2016, pp. 0341-0344.

- [120] K. Yang, U. Botero, H. Shen, D. Forte, and M. Tehranipoor, "A split manufacturing approach for unclonable chipless RFIDs for pharmaceutical supply chain security," in *2017 Asian Hardware Oriented Security and Trust Symposium (AsianHOST)*, 2017, pp. 61-66.
- [121] R. Hopkins and C. Free, "Equivalent circuit for the microstrip ring resonator suitable for broadband materials characterisation," *IET Microwaves, Antennas & Propagation*, vol. 2, pp. 66-73, 2008.
- [122] J. Joubert, "Spiral microstrip resonators for narrow-stopband filters," *IEE Proceedings - Microwaves, Antennas and Propagation*, vol. 150, pp. 493-496, 2003.
- [123] Q. Gu, G. C. Wan, C. Gao, and M. S. Tong, "Frequency-coded chipless RFID tag based on spiral resonators," in *2016 Progress in Electromagnetic Research Symposium (PIERS)*, 2016, pp. 844-846.
- [124] Y. Ki-Cheol, L. Hyun-Wook, P. Jung-Geun, and L. Jong-Chul, "Design of a high-Q resonator for satellite broadcasting application," in *2008 IEEE Antennas and Propagation Society International Symposium*, 2008, pp. 1-4.
- [125] J. Zunfu, P. S. Excell, and Z. M. Hejazi, "Calculation of distributed capacitances of spiral resonators," *IEEE Transactions on Microwave Theory and Techniques*, vol. 45, pp. 139-142, 1997.
- [126] Z. M. Hejazi, P. S. Excell, and Z. Jiang, "Accurate distributed inductance of spiral resonators," *IEEE Microwave and Guided Wave Letters*, vol. 8, pp. 164-166, 1998.
- [127] M. Kempin, M. T. Ghasr, J. T. Case, and R. Zoughi, "Modified Waveguide Flange for Evaluation of Stratified Composites," *IEEE Transactions on Instrumentation and Measurement*, vol. 63, pp. 1524-1534, 2014.
- [128] M. Martinez and D. v. d. Weide, "Circular polarization on depolarizing chipless RFID tags," in *2016 IEEE Radio and Wireless Symposium (RWS)*, 2016, pp. 145-147.
- [129] M. A. Islam and N. C. Karmakar, "A 4 x 4 Dual Polarized mm-Wave ACMPA Array for a Universal mm-Wave Chipless RFID Tag Reader," *IEEE Transactions on Antennas and Propagation*, vol. 63, pp. 1633-1640, 2015.
- [130] M. Garbati, A. Ramos, R. Siragusa, E. Perret, and C. Halopé, "Chipless RFID reading system independent of polarization," in *2016 IEEE MTT-S International Microwave Symposium (IMS)*, 2016, pp. 1-3.

- [131] C. Herrojo, J. Mata-Contreras, F. Paredes, A. Núñez, E. Ramon, and F. Martín, "Near-Field Chipless-RFID System With Erasable/Programmable 40-bit Tags Inkjet Printed on Paper Substrates," *IEEE Microwave and Wireless Components Letters*, vol. 28, pp. 272-274, 2018.
- [132] J. Kim, Z. Wang, and W. S. Kim, "Stretchable RFID for Wireless Strain Sensing With Silver Nano Ink," *IEEE Sensors Journal*, vol. 14, pp. 4395-4401, 2014.
- [133] R. Singh, E. Singh, and H. S. Nalwa, "Inkjet printed nanomaterial based flexible radio frequency identification (RFID) tag sensors for the internet of nano things," *RSC Advances*, vol. 7, pp. 48597-48630, 2017.
- [134] Y. H. Kawahara, Steve; Cook, Benjamin S.; Zhang, Cheng; Abowd, Gregory D. , "Instant Inkjet Circuits: Lab-based Inkjet Printing to Support Rapid Prototyping of UbiComp Devices," *ACM*, September 8-12, 2013 2013.
- [135] K. Brinker and R. Zoughi, "Measurement of Inkjet-Printing Parameters for Accurate Chipless RFID Tag EM Simulation," in *IEEE International Instrumentation and Measurement Technologies Conference*, Auckland, New Zealand, 2019.
- [136] K. Brinker and R. Zoughi, "Microwave Measurement of Conductivity of Inkjet-Printed Wireless Passive Sensors for Structural Health Monitoring (SHM)," American Society of Nondestructive Testing Research Symposium 2019.
- [137] C. Mariotti, F. Alimenti, L. Roselli, and M. M. Tentzeris, "High-Performance RF Devices and Components on Flexible Cellulose Substrate by Vertically Integrated Additive Manufacturing Technologies," *IEEE Transactions on Microwave Theory and Techniques*, vol. 65, pp. 62-71, 2017.
- [138] A. Vena, E. Perret, S. Tedjini, G. E. P. Tourtollet, A. Delattre, F. Garet, *et al.*, "Design of Chipless RFID Tags Printed on Paper by Flexography," *IEEE Transactions on Antennas and Propagation*, vol. 61, pp. 5868-5877, 2013.
- [139] G. Shaker, S. Safavi-Naeini, N. Sangary, and M. M. Tentzeris, "Inkjet Printing of Ultrawideband (UWB) Antennas on Paper-Based Substrates," *IEEE Antennas and Wireless Propagation Letters*, vol. 10, pp. 111-114, 2011.
- [140] F. Alimenti, V. Palazzi, C. Mariotti, M. Virili, G. Orecchini, L. Roselli, *et al.*, "24-GHz CW radar front-ends on cellulose-based substrates: A new technology for low-cost applications," in *2015 IEEE MTT-S International Microwave Symposium*, 2015, pp. 1-4.
- [141] F. Alimenti, P. Mezzanotte, M. Dionigi, M. Virili, and L. Roselli, "Microwave Circuits in Paper Substrates Exploiting Conductive Adhesive Tapes," *IEEE Microwave and Wireless Components Letters*, vol. 22, pp. 660-662, 2012.

- [142] F. J. Tischer and F. Jalali, "Resonant cavities for the measurement of the surface resistance of conductors at millimeter wavelengths " *Review of Scientific Instruments*, vol. 46, 1974.
- [143] A. Hernandez, E. Martin, J. Margineda, and J. M. Zamarro, "Resonant cavities for measuring the surface resistance of metals at X-band frequencies," *Journal of Physics E: Scientific Instruments*, vol. 19, p. 222, 1986.
- [144] D. M. Pozar, *Microwave Engineering*, 4 ed.: Wiley, 2012.
- [145] S. Ramo, J. R. Whinnery, and T. V. Duzer, *Fields and Waves in Communication Electronics*, 2 ed.: Wiley, 1984.
- [146] B. Shao, Y. Amin, Q. Chen, R. Liu, and L. Zheng, "Directly Printed Packaging-Paper-Based Chipless RFID Tag With Coplanar LC Resonator," *IEEE Antennas and Wireless Propagation Letters*, vol. 12, pp. 325-328, 2013.
- [147] A. Vena, A. A. Babar, L. Sydänheimo, M. M. Tentzeris, and L. Ukkonen, "A Novel Near-Transparent ASK-Reconfigurable Inkjet-Printed Chipless RFID Tag," *IEEE Antennas and Wireless Propagation Letters*, vol. 12, pp. 753-756, 2013.
- [148] Z. Radiovojevic, K. Andersson, K. Hashizume, M. Heino, M. Mantysalo, P. Mansikkamaki, *et al.*, "Optimised Curing of Silver Ink Jet Based Printed Traces," in *12th International Workshop on Thermal investigations of ICs - THERMINIC 2006*, Nice, France, 2006.
- [149] K. Changjae, N. Masaya, and S. Katsuaki, "Electrical conductivity enhancement in inkjet-printed narrow lines through gradual heating," *Journal of Micromechanics and Microengineering*, vol. 22, p. 035016, 2012.
- [150] T. Nge, M. Nogi, and K. Suganuma, "Electrical functionality of inkjet-printed silver nanoparticle conductive tracks on nanostructured paper compared with those on plastic substrates," *Journal of Materials Chemistry C* 2013.
- [151] J. Niittynen, R. Abbel, M. Mäntysalo, J. Perelaer, U. S. Schubert, and D. Lupo, "Alternative sintering methods compared to conventional thermal sintering for inkjet printed silver nanoparticle ink," *Thin Solid Films*, vol. 556, pp. 452-459, 2014/04/01/ 2014.
- [152] L. A. Mark, A. Mikko, M. Tomi, A. Ari, O. Kimmo, S. Mika, *et al.*, "Electrical sintering of nanoparticle structures," *Nanotechnology*, vol. 19, p. 175201, 2008.
- [153] J. Perelaer, R. Jani, M. Grouchko, A. Kamyshny, S. Magdassi, and U. S. Schubert, "Plasma and Microwave Flash Sintering of a Tailored Silver Nanoparticle Ink, Yielding 60% Bulk Conductivity on Cost-Effective Polymer Foils," *Advanced Materials*, vol. 24, pp. 3993-3998, 2012/08/02 2012.

- [154] C. Miozzi, S. Nappi, S. Amendola, C. Occhiuzzi, and G. Marrocco, "A General-Purpose Configurable RFID Epidermal Board With a Two-Way Discrete Impedance Tuning," *IEEE Antennas and Wireless Propagation Letters*, vol. 18, pp. 684-687, 2019.
- [155] M. Longhi, Z. Taylor, M. Popović, J. Nieto, G. Marrocco, and R. Siegwart, "RFID-Based Localization for Greenhouses Monitoring Using MAVs," in *2018 IEEE-APS Topical Conference on Antennas and Propagation in Wireless Communications (APWC)*, 2018, pp. 905-908.
- [156] R. Koswatta and N. C. Karmakar, "Investigation into antenna performance on read range improvement of chipless RFID tag reader," in *2010 Asia-Pacific Microwave Conference*, 2010, pp. 1300-1303.
- [157] S. Capdevila, L. Jofre, J. Bolomey, and J. Romeu, "RFID Multiprobe Impedance-Based Sensors," *IEEE Transactions on Instrumentation and Measurement*, vol. 59, pp. 3093-3101, 2010.
- [158] K. V. S. Rao, P. V. Nikitin, K. V. S. Rao, and P. V. Nikitin, "Theory and measurement of backscattering from RFID tags," *IEEE Antennas and Propagation Magazine*, vol. 48, pp. 212-218, 2006.
- [159] A. Ramos, E. Perret, O. Rance, S. Tedjini, A. Lázaro, and D. Girbau, "Temporal Separation Detection for Chipless Depolarizing Frequency-Coded RFID," *IEEE Transactions on Microwave Theory and Techniques*, vol. 64, pp. 2326-2337, 2016.
- [160] A. Vena, E. Perret, and S. Tedjni, "A Depolarizing Chipless RFID Tag for Robust Detection and Its FCC Compliant UWB Reading System," *IEEE Transactions on Microwave Theory and Techniques*, vol. 61, pp. 2982-2994, 2013.
- [161] "IEEE Standard Definitions of Terms for Antennas," *IEEE Std 145-1993*, pp. 1-32, 1993.
- [162] D. W. Hess, "Introduction to RCS measurements," in *2008 Loughborough Antennas and Propagation Conference*, 2008, pp. 37-44.
- [163] R. B. Dybdal, "Radar cross section measurements," *Proceedings of the IEEE*, vol. 75, pp. 498-516, 1987.
- [164] R. Norland, "Multipath scattering from complex targets," *IEE Proceedings - Radar, Sonar and Navigation*, vol. 148, pp. 343-347, 2001.
- [165] M. Grace, "Measurement of Radar Cross Section Using the "VNA Master" Handheld VNA: Application Note," Anritsu2011.

- [166] P. V. Nikitin, K. V. S. Rao, and R. D. Martinez, "Differential RCS of RFID tag," *Electronics Letters*, vol. 43, pp. 431-432, 2007.
- [167] S. Skali, C. Chantepy, and S. Tedjini, "On the measurement of the delta Radar Cross Section ( $\Delta$ RCS) for UHF tags," in *2009 IEEE International Conference on RFID*, 2009, pp. 346-351.
- [168] "New Network Analyzer Methodologies in Antenna/RCS Measurements," 2004.
- [169] S. Shrestha, M. D. Balachandran, M. Agarwal, L. Zou, and K. Varahramyan, "A Method to Measure Radar Cross Section Parameters of Antennas," *IEEE Transactions on Antennas and Propagation*, vol. 56, pp. 3494-3500, 2008.
- [170] W. Wiesbeck and D. Kahny, "Single reference, three target calibration and error correction for monostatic, polarimetric free space measurements," *Proceedings of the IEEE*, vol. 79, pp. 1551-1558, 1991.
- [171] W. Wiesbeck and S. Riegger, "A complete error model for free space polarimetric measurements," *IEEE Transactions on Antennas and Propagation*, vol. 39, pp. 1105-1111, 1991.
- [172] A. Pouzin, T. Vuong, S. Tedjini, J. Perdereau, and L. Dreux, "Measurement of Radar Cross Section for Passive UHF RFID Tags," in *The Second European Conference on Antennas and Propagation, EuCAP 2007*, 2007, pp. 1-6.
- [173] A. Vena, "Contribution au développement de la technologie RFID sans puce à haute capacité de codage," Université de Grenoble, 2014.
- [174] A. Foudazi, K. M. Donnell, and M. T. Ghasr, "Application of Active Microwave Thermography to delamination detection," in *2014 IEEE International Instrumentation and Measurement Technology Conference (I2MTC) Proceedings*, 2014, pp. 1567-1571.
- [175] H. Zhang, R. Yang, Y. He, A. Foudazi, L. Cheng, and G. Tian, "A Review of Microwave Thermography Nondestructive Testing and Evaluation," *Sensors (Basel, Switzerland)*, vol. 17, p. 1123, 2017.
- [176] P. H. B. Koch and H. Oertel, "Microwave thermography," *Proceedings of the IEEE*, vol. 55, pp. 416-418, 1967.

## VITA

Katelyn Rose Brinker is from Highland IL. In 2013 she graduated from Highland High School and in 2017 she received her Bachelors of Science degrees in Electrical Engineering and Computer Engineering from Missouri University of Science and Technology (Missouri S&T). She graduated Summa Cum Laude.

In Fall of 2017 she began her Master's of Science degree in Electrical Engineering at Missouri S&T with the support of a NASA Space Technology Research Fellowship. Her research was conducted at the Applied Microwave Nondestructive Testing Laboratory (*amntl*).

While an undergraduate student at Missouri S&T, she was involved with the Mars Rover Design Team, the Missouri S&T IEEE Student Branch, and the Eta Kappa Nu (HKN) Gamma Theta Chapter. She was also the Undergraduate Representative of the IEEE Instrumentation and Measurement Society from 2016-2018. As a graduate student she was involved with the Missouri S&T IEEE Student Branch and HKN chapter. Additionally, she served as the Graduate Representative of the IEEE Instrumentation and Measurement Society and as a Student Governor to the HKN Board of Governors.

She received her MS degree in Electrical Engineering from Missouri S&T in July of 2019.